Unravelling giant molecular clouds

Fuheng Liang (梁 赋珩)

St Cross College

University of Oxford

A thesis submitted for the degree of

Doctor of Philosophy

Trinity 2024

本博士论文献给
我的母亲与父亲：缪应忠、梁西广。

This thesis is dedicated to
my mother and father, Yingzhong Miao and Xiguang Liang.

Acknowledgements

When I started this DPhil[1] programme, it was the best of times, it was the worst of times. The COVID-19 pandemic started to hit hard in early 2020 when I was going through applications for doctoral programmes. The abnormal era witnessed and influenced decision-making, travel, matriculation, and the start of my degree. Be it abnormal or ordinary, it would always have been special to me, as the DPhil has surely been a once-in-a-lifetime journey.

I would like to first express my love and gratitude to my parents, grandparents, and other close relatives. You have always been fundamental in my life, my pursuit of knowledge, and my scientific research career, spiritually and materialistically. I am extremely lucky to have such family support around me.

I thank my Oxford DPhil supervisor, Prof. Martin Bureau, with my great appreciation and admiration. You once said the key to supervision is being a role model, and indeed, I have learnt so much from you, both scientifically and personally. I am sure I will benefit from your art of perfectionism and prioritisation throughout my career. Similarly, I thank my supervisors at the European Southern Observatory (ESO), Dr. Ashley Barnes and Prof. Eric Emsellem, ESO mentor Dr. Melanie Kaasinen, WISDOM project PI Reader Timothy Davis, and other collaborators. None of my achievements would have been possible without your help. There is a long list of people who have backed me up for my completion of the programme, from the enrolment stage to the day-to-day life and year-to-year progression, such as Prof. Patrick Roche, Prof. Lance Miller, Ms. Ashling Gordon, Ms. Nelma Silvia, Dr. Chiara Spiniello, Prof. Michele Cappellari, etc., as well as my examiner Prof. Amélie Saintonge. On a formal note, I acknowledge the precious support from the Subdepartment of Astrophysics at Oxford, the Scatcherd European Scholarship of the University of Oxford, and the ESO Studentship Programme.

Now it is time for my beloved friends. Foremost is the special squad in the mythological ancient accelerator tower ('The Tower'): Curro, Jaime, Kc, Mads, and Alex, as well as honorary associates Lauren and James. You guys are such an amazing group to work on science with and to hang out with. Meanwhile, it has also been a great pleasure to have the company of all my other friends in Oxford, Munich/Garching, China, and

[1] I cannot help but note the historical origin of this rare abbreviation of the degree. Despite the vast amount of use of Latin at the University of Oxford, 'DPhil', short for 'Doctor of Philosophy', is the English modernisation of its Latin companion 'PhD' (short for 'philosophiae doctor'). See https://www.alumni.ox.ac.uk/quad/article/100-years-dphil.

other places in the world. Among them, special thanks go to Mads for bestowing the Apple mouse upon me and to Ryan and Yangfan for the melatonin, all of which greatly benefited the writing of this thesis.

Last but not least, I thank my air-conditioners, which ensured me alive over the long warm days in Oxford and Munich. I also thank my colourful life and numerous hobbies, without which this thesis would have been finished much earlier; however, they are the very things that help make me who I am.

Software, tools, and data used in this thesis are acknowledged in the respective chapters and/or the corresponding journal publications. Specifically for the thesis, the Oxford thesis LaTeX template[2] and `bibtex-tidy`[3] were used.

[2] https://github.com/mcmanigle/OxThesis

[3] https://flamingtempura.github.io/bibtex-tidy/

Abstract

Giant molecular clouds (GMCs) provide the fuel for star formation and bear various feedbacks. Thus, they are key to our understanding of galaxy evolution and the baryon cycle. In this thesis, I study the cold molecular gas content in the nearby universe, including three megamaser-host galaxies, one early-type galaxy, and the central molecular zone (CMZ) of the Milky Way (MW). The spatial scales probed by the analyses range from kpc-scale gas discs (i.e. the environment GMCs reside in) to sub-pc clumps within GMCs.

I start with analysing the distribution and kinematics of the molecular gas of three megamaser galaxies: NGC 1194, NGC 3393, and NGC 5765B. I present Atacama Large Millimeter/sub-millimeter Array (ALMA) ^{12}CO(2-1) observations with resolutions of $\approx$ 100 pc. Every galaxy has an extended rotating molecular gas disc but all also have non-axisymmetric features. I explore the tentative correlation between the existence of megamasers and these features in the gas discs. I also examine the potential for using ^{12}CO(2-1) as a dynamical tracer in these galaxies to measure the supermassive blackhole masses.

Next, I investigate resolved GMCs of the lenticular galaxy NGC 1387, exploiting high-resolution (14 pc) ^{12}CO(2-1) observations from ALMA. I analysed the fundamental properties of 1285 individual GMCs. Unusually for an ETG, the GMCs of NGC 1387 follow scaling relations very similar to those of the MW disc, and most are virialised. A subset of GMCs have their angular momenta aligned with the large-scale galactic rotation.

Finally, in the MW CMZ, I study the gas-structure dendrogram across a large dynamical range (1–100 pc), primarily with ALMA HNCO(4-3) observations at 0.7 pc resolution. I discuss the dynamical state of the gas structures and identify galactic shear and magnetic fields as potential physical drivers of their morphologies.

Overall, this thesis has studied cold molecular gas (clouds) in special systems (megamaser hosts, the ETG, and the MW centre) with unprecedented physical resolutions. It enriches our understanding of molecular gas properties in the context of galaxy evolution.

Statement of Originality

I carried out the work presented in this thesis as a student at the Sub-department of Astrophysics, Department of Physics, University of Oxford, between October 2020 and August 2024 under the supervision of Prof. Martin Bureau. I also conducted research at the European Southern Observatory (ESO; Garching) from August 2023 to August 2024, supervised by Prof. Eric Emsellem and Dr. Ashley Barnes, supported by the ESO Studentship Programme and the Scatcherd European Scholarship of the University of Oxford. I hereby declare that no part of this thesis has been accepted or submitted in support of another degree, diploma or other qualification at the University of Oxford or other higher learning institutions. Except where otherwise stated or where reference is made to the work of others, the work in this thesis is entirely my own.

The work presented in Chapter 2 has been published by Liang et al. (2024). As the first author of the paper, I carried out the ALMA data reduction, analysed the data products, and wrote the manuscript, while the co-authors contributed to securing the observations through proposals, carried out the James Clerk Maxwell Telescope data reduction, and provided comments.

The work presented in Chapter 3 is summarised in a paper undergoing team internal review and will be submitted to a refereed journal soon. As the first author of the draft, I carried out the ALMA data reduction, cloud identification and measurements, analysed the results, and wrote the manuscript, while the co-authors contributed to securing the observations through proposals and provided comments.

The work presented in Chapter 4 is summarised in a paper undergoing team internal review and will be submitted to a refereed journal soon. As the first author of the draft, I carried out the gas structure identification and measurements, analysed the results, and wrote the manuscript, while the co-authors contributed to securing the observations through proposals, reduced the ALMA data, and provided comments.

Contents

List of Figures

List of Tables

List of Abbreviations

1D, 2D, 3D . . . one-, two-, three-dimensional

ACA . . . . . ALMA Compact Array

ACES . . . . . ALMA CMZ Exploration Survey

AGN . . . . . active galactic nucleus

ALMA . . . . . Atacama Large Millimeter/submillimeter Array

ALMaQUEST . ALMA-MaNGA QUEnching and STar formation

APEX . . . . . Atacama Pathfinder EXperiment

CGM . . . . . circumgalactic medium

CMZ . . . . . Central Molecular Zone

EDGE-CALIFA Extragalactic Database for Galaxy Evolution survey–Calar Alto Legacy Integral Field Area

ETG . . . . . early-type galaxy

FIR . . . . . far-infrared

FoV . . . . . field of view

FT . . . . . Fourier transform

FWHM . . . . . full width at half maximum

GALEX . . . . . *Galaxy Evolution Explorer*

GMC . . . . . giant molecular cloud

HST . . . . . *Hubble Space Telescope*

IMF . . . . . initial mass function

IR . . . . . infrared

ISM . . . . . interstellar medium

JCMT . . . . . James Clerk Maxwell Telescope

JWST . . . . . *James Webb Space Telescope*

LoS . . . . . line of sight

LINER . . . . . low-ionisation nuclear emission-line region

LTG . . . . . late-type galaxy

M . . . . . Messier

MaNGA . . . . Mapping Nearby Galaxies at Apache Point Observatory

MUSE . . . . . Multi-Unit Spectroscopic Explorer

MW . . . . . Milky Way

NGC . . . . . New General Catalogue of Nebulae and Clusters of Stars

PB . . . . . primary beam

PHANGS . . . . Physics at High Angular resolution in Nearby GalaxieS

PVD . . . . . position-velocity diagram

RMS . . . . . root mean square

Sgr . . . . . Sagittarius

SDSS . . . . . Sloan Digital Sky Survey

SFE . . . . . star formation efficiency

SFR . . . . . star formation rate

SMA . . . . . Submillimeter Array

SMBH . . . . . supermassive black hole

sSFR . . . . . specific star formation rate

UV . . . . . ultraviolet

VLT . . . . . Very Large Telescope

WISDOM . . . mm-Wave Interferometric Survey of Dark Object Masses

xCOLD GASS . extended CO Legacy Database for *GALEX* Arecibo SDSS Survey

xGASS . . . . . extended *GALEX* Arecibo SDSS Survey

1 Introduction

Contents

1.1 Galaxy formation and evolution

Galaxies are one of the fundamental building blocks of our universe. Within a galaxy, there is a complex interplay between stars, gas, dust, magnetic fields, cosmic rays, dark matter, etc. At scales larger than an individual galaxy, the universe can be seen as organised in a hierarchy of galaxy groups, clusters, and larger-scale structures, all embedded in a certain space-time geometry, the most popular model of which is the so-called ‘Lambda–Cold

Dark Matter' (ΛCDM) model. As an intermediate scale in this ladder, galaxies involve almost all (baryonic) physical processes and constitute one of the major research topics of contemporary astronomy and astrophysics. To help disentangle the physics of galaxy formation and evolution, this thesis focuses on a specific component of galaxies — cold molecular gas, typically in the form of giant molecular clouds.

1.1.1 Stars and the baryon cycle

In the framework of ΛCDM, the beginning of our universe is a hot plasma of ionised hydrogen, helium, and lithium, with almost perfect homogeneity and isotropy. However, tiny quantum fluctuations of the mass density field grow due to gravity and give rise to the structures seen today, including galaxies. As dark matter dominates the total gravitational mass of the universe and because it does not experience radiation pressure, it drives the formation of local overdensities called 'dark matter haloes' through gravity.

As for baryonic matter,[1] shortly after the initial ionised phase, it goes through the so-called 'epoch of recombination',[2] becomes neutral, and generates the cosmic microwave background (Peebles, 1968). These neutral baryons, decoupled from radiation pressure, are attracted to and accumulate in dark matter haloes due to the gravitational potential wells. They then become the seeds of the luminous components of galaxies (e.g. White & Rees, 1978). As local overdensities grow and gravitational potential wells deepen, the density of this neutral gas rises while its temperature drops due to radiation cooling. Neutral gas clouds are formed during this process, providing the major sites and fuel for subsequent star formation.

After a cloud reaches a critical density (as a function of the scale and sound speed of the system), the Jeans instability starts to dominate, predicting runaway gravitational collapse (e.g. Jeans, 1902; Bonnor, 1957). This leads to a rapid increase of the temperature

[1] As this thesis does not stress the difference between baryons and leptons, and to follow the convention in modern astronomy and astrophysics, terms such as 'baryonic matter', 'baryons', and the like include both baryons and leptons (such as electrons), unless explicitly specified otherwise. In other words, these terms are used interchangeably with 'ordinary matter', as opposed to dark matter.

[2] It is worth noting that the 'epoch of recombination' is a misnomer because atoms in the universe had never been in a neutral or combined state before. At the time of discovery and naming of this epoch, it was believed that the universe started in a neutral state, thus the subsequent 'recombination'. This is no longer believed to be the case.

at the centre of the cloud and ultimately (if the cloud is massive enough) ignition of nuclear fusion. This leads to the formation of the first (Population[3] (Pop)-III[4]) stars (e.g. Hartquist & Cameron, 1977). Such an isolated concentration of stars situated at the centre of a dark matter halo constitutes a galaxy.

The formation of a star is one of the most influential physical processes in the universe. The onset of star formation appears to be simply described by the Jeans instability. However, it is extremely difficult to understand and predict star formation in real galaxy environments. Moreover, star formation is fundamental to our understanding of galaxies, as it is an important driver of the baryon cycle. Without stars, the universe would be in a nearly static state, with few exceptions such as radiation (and cooling) and the release of gravitational potential energy (and heating). The birth of stars is transformative, making a multitude of additional baryonic physical processes influential in galaxy evolution.

The material between stars in a galaxy is called the interstellar medium (ISM). Stars play a major role in driving the evolution of the ISM properties. Inside a star, new chemical elements are created through nuclear fusion (called 'metals' in astronomy, referring to any element heavier than helium). These metals are returned to the ISM at the end of the star's life, through stellar winds and/or supernova explosions. Although metals make up less than two per cent of the baryonic content of the universe (Calura & Matteucci, 2004), they play a major role in numerous physical mechanisms. A special metal compound is dust, also formed by certain stars, primarily asymptotic giant branch stars and explosions of supernovae (Schneider & Maiolino, 2024). Dust has complicated chemical compositions and efficiently absorbs light. All metals, especially dust, greatly influence the properties of the ISM and future generations of stars (e.g. Maiolino & Mannucci, 2019). Photons and energetic particles are emitted from stars towards the ISM. They ionise the star's immediate surroundings and create an H II[5] region in the ISM, as well as ionise much of the intergalactic medium (IGM). The latter process constitutes another major cosmic

[3]In this thesis, only the capitalised 'Population' refers to the specific classification of stars in the context of the grand cosmic history. Other lower-case uses (or where grammar requires an upper case) of 'population' generally mean 'a coeval group of'.

[4]The numeric III in the name was chosen retrospectively, after the two distinct populations of stars in the Milky Way (e.g. Baade, 1944).

[5]H II refers to singly ionised hydrogen while H I refers to neutral hydrogen. The same numeric rule applies to other elements and ionisation states.

epoch after recombination, referred to as the 'epoch of reionisation' (e.g. Shapiro, 1995). Overall, stars play a major role in shaping galaxies, similar to the engine in an automobile.

From the perspective of the ISM, once a galaxy is formed, individual particles follow a so-called 'baryon cycle'. First, the spatial extents of galaxies as defined by their luminous contents encompass only a small fraction of all baryonic matter. The majority of the baryons ($\approx$ 90%; e.g. Shull et al. 2012) are located outside galaxies. However, due to the galaxies' gravitational attraction, the remaining cold atomic baryons (the so-called 'pristine gas') accrete onto them (e.g. Giavalisco et al., 2011). Next, with the aid of dust grains (and except for the Pop-III star era), the atomic gas forms molecules. The molecular gas then goes through the aforementioned process of gravitational collapse until stars form in the highest-density cores of molecular clouds. Then, upon the onset of star formation, ionising photons and stellar winds of energetic particles disperse and/or destroy the parent molecular clouds. A significant fraction of these baryons thus changes to the ionised state. Some baryons have large momenta and kinetic energy and are blown out of the host galaxies (see Chevance et al., 2023, for a review), forming the circumgalactic medium (CGM; Tumlinson et al., 2017). Some fall back onto the galaxy and/or condense to the neutral state, thus continuing the baryon cycle. Overall, in this scenario, stars are again the central driver, turning nuclear potential energy into ionising photons and kinetic energy. Stars act like the heart in a body, driving and coordinating the baryon cycle to make a galaxy alive.

This thesis focuses on the cold molecular phase to study galaxy evolution, the stage both fostering star formation and bearing the feedback from stars to the ISM. Under the scope of giant molecular clouds, this thesis put constraints on the molecular gas properties both shortly before and immediately after star formation.

When studying the molecular gas, common questions arise. What determines the conditions within molecular clouds? What triggers star formation within them? What affects the properties of the resultant stellar systems? Different theories concerning the gas density, turbulence, Mach number, magnetic field, etc., have been extensively studied using simulations and observations (e.g. Kennicutt, 1998; Ballesteros-Paredes et al., 2007; Federrath & Klessen, 2012), yet there is still no consensus on a comprehensive theory

of star formation. Below the cloud scale (< 1 pc), high-density molecular cores are the sites and units of star formation. Much tighter correlations between dense gas and star formation have been found than those of low-density gas (Gao & Solomon, 2004b). Many studies have also tried to constrain the core mass function (e.g. Alves et al., 2007) and connect it to the stellar initial mass function (IMF; e.g. Salpeter, 1955; Offner et al., 2014). As most stars — if not all — form in clusters (Lada & Lada, 2003), the theory of 'integrated galaxy-wide IMF' has been proposed to connect the star cluster mass function of the galaxy and the IMF of each cluster (e.g. Yan et al., 2017).

It is however still challenging to apply these theories to understand star formation in the context of galaxy evolution as a whole. Surveys such as ALMAQuest (Lin et al., 2020) and EDGE-CALIFA (Bolatto et al., 2017) have provided rich datasets and extensive analyses of the star formation efficiency (SFE; the ratio between the star formation rate, SFR, and the cold molecular gas mass, $M_{\rm mol}$), with decent numbers of spatially resolved galaxies in the nearby universe. Studies of individual Local Group galaxies at even higher spatial resolutions have also yielded some fundamental observational constraints (e.g. Bolatto et al., 2008). These will be discussed in Section 1.3.

1.1.2 Galaxies in the nearby universe

Throughout cosmic history, galaxies have drastically changed in morphology and other properties. With the design goal of detecting the 'first galaxies' at cosmic dawn, the *James Webb Space Telescope* (*JWST*) has already revealed some of the highest-redshift (z) galaxies ever discovered, at $z \gtrsim 10$ (e.g. Robertson et al., 2023; Carniani et al., 2024). Using photometric modelling, studies have revealed that disc galaxies dominate the galaxy population at $4 < z < 10$ (Lee et al., 2024).

Closer to us, the physical resolutions of observations of the stellar and gaseous components are good enough to reveal more details. Galaxies around cosmic noon ($z \approx 2$) appear to be clumpy (Förster Schreiber et al., 2011) and have high gas mass fractions ($\mu_{\rm gas} \approx 80\%$, defined as the ratio of the gas mass over the stellar mass; Tacconi et al., 2020). They also exhibit the highest star formation rates (Madau & Dickinson, 2014) and black hole accretion rates (the origin of active galactic nucleus, AGN, activities)

across cosmic history (e.g. Wolf et al., 2003; Aird et al., 2015; Florez et al., 2021). Förster Schreiber & Wuyts (2020) elaborate on more properties of these cosmic-noon galaxies and their evolution since.

In the low-redshift regime ($z \lesssim 0.5$ or distances $D \lesssim 1900$ Mpc) and the nearby universe ($z \lesssim 0.15$ or $D \lesssim 600$ Mpc), galaxy morphology has changed once again. The huge (kpc-scale) clumps at $z \approx 2$ are absent and galaxies are more symmetric. Yet, the whole galaxy population still has a high morphological diversity. This epoch of the evolutionary history of galaxies is the epoch that has been observed and studied the most by humankind, and is the epoch that this thesis focuses on. Below I summarise our understanding of nearby galaxies from a historical perspective.

The modern study of external galaxies started about the time when Edwin Hubble determined the distance of the Andromeda Galaxy (M31) to be 285 kpc (Hubble 1925; updated to 724 kpc in recent years, Ngeow et al. 2015). This is far beyond the known extent of our own Galaxy and thus proves that M31 is an external galaxy. Figure 1.1 shows the glass-plate photograph of M31 where Hubble found one of the Cepheids used to measure the distance of M31. Ever since, galaxies have not only been observed and studied in a wealth of details but they have also been used as tracers of cosmic geometry, for example revealing the expansion history of the universe (e.g. Alam et al., 2021).

Starting from several tens of galaxies in the Local Group ($D \lesssim 1.5$ Mpc), many catalogues of galaxies across larger cosmic volumes were created during the past eight decades or so, including the famous Messier catalogue (preceding the formal discovery of external galaxies; Messier, 1781), the New General Catalogue of Nebulae and Clusters of Stars (NGC; Dreyer, 1953), the Sloan Digital Sky Survey (SDSS; Abazajian et al. 2009), etc. With optical images of these galaxies, a few morphological classification schemes have been widely used. Generally speaking, the purposes of any classification are (i) to summarise what is seen and (ii) to ask (and attempt to answer) why such things are seen. The first purpose is the foundational step while the second purpose is the ultimate goal. The two steps are entangled, in that the method used to summarise already embeds the question and potentially (part of) the answer.

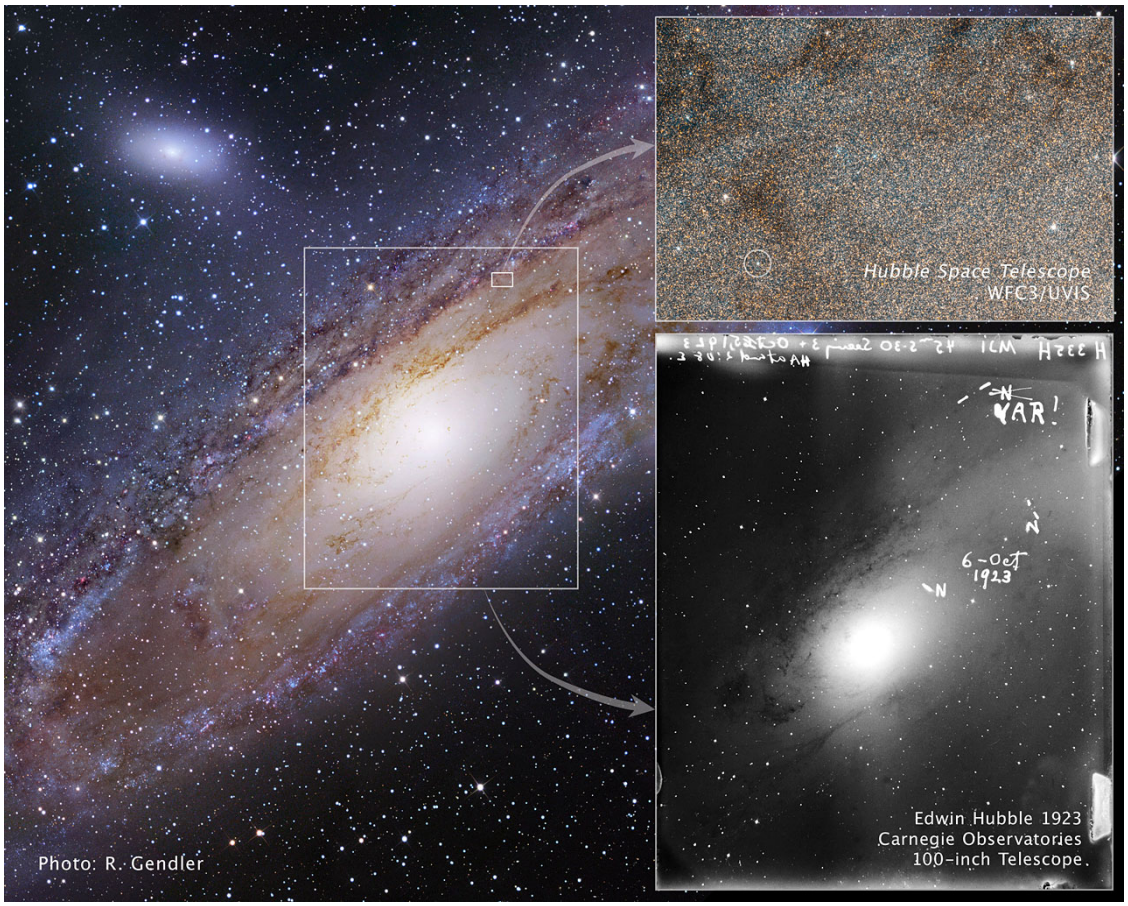

Figure 1.1: Cepheid in the Andromeda Galaxy. Image from Space Telescope Science Institute. *Left:* Andromeda Galaxy photo courtesy of R. Gendler. *Upper right:* zoom-in with *Hubble Space Telescope* (*HST*) Wide Field Camera 3. At the centre of the white circle is the Cepheid Edwin Hubble discovered. *Lower right:* zoom-in of Hubble's glass-plate photograph from the 100-inch Hooker telescope on 6 October 1923. 'VAR' stands for 'variable star' while the crossed-out 'N' stands for 'nova'.

Edwin Hubble first proposed the tuning-fork classification (also known as the Hubble sequence; top panel of Figure 1.2) and noted that the sequence of early-type galaxies (ETGs) and late-type galaxies (LTGs) did not indicate any evolutionary path (Hubble, 1926, 1936). However, for a long time, a popular belief was that one type evolved into the other. For example, Jeans (1928) proposed a theory of galaxy evolution from ETGs to LTGs through continuous collapse. Later, many believed that ETGs form from LTGs through hierarchical and consecutive mergers (e.g. Toomre, 1977; Schweizer, 1990). In recent years, chemical and kinematic analyses of stellar population observations from advanced observing facilities have revealed a more complex picture. The galaxy morphology dichotomy in the present-day universe may not indicate an evolutionary relation between

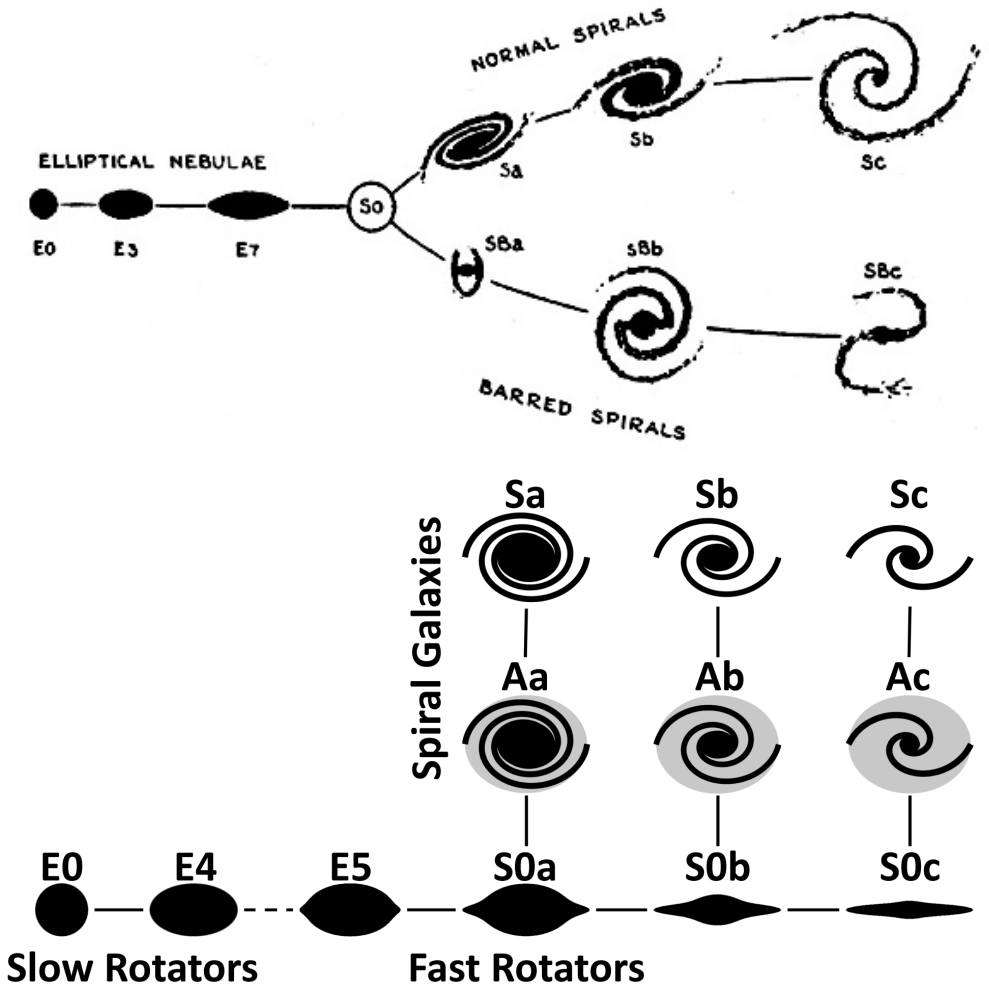

Figure 1.2: Galaxy classification schemes. *Top:* Hubble sequence (Hubble, 1936). *Bottom:* comb diagram from the ATLAS^{3D} survey (Cappellari et al., 2011).

present-day ETGs and LTGs, but rather may be more related to different formation channels at high redshifts. In addition, the two sub-categories of ETGs, elliptical galaxies and lenticular galaxies (also denoted 'S0'), may have formed differently (Matteucci, 2012).

The large-scale environment, such as galaxy groups and clusters, also plays a major role in galaxy evolution (Vollmer, 2013). Apart from galaxy mergers, high-density environments affect the distribution and physical state of the gas present, as well as the potential future accretion of (pristine) gas. For example, lenticular galaxies may have evolved from LTGs through the quenching and suppression of star formation, and in turn the loss of spiral arms (e.g. Loni et al., 2023). From this perspective, both LTGs and lenticular galaxies are categorised as disc galaxies. van den Bergh (1976) first alluded to such an

evolutionary path by adding a sequence of 'anaemic spirals' in between the sequence of spirals and lenticulars to the Hubble classification scheme. Anaemic spirals are defined by their less prominent spiral arms and redder colours than normal spirals, while these arms are still detectable and the colours are still bluer as compared to lenticulars. Following that, the nearby volume-limited ETG survey ATLAS^{3D} updated this scheme into a 'comb' diagram, explicitly pointing out the correlation of the gas fraction and star formation rate with other (new) properties of the stellar kinematics (Cappellari et al., 2011).

At this point, it is worth re-visiting the two steps of galaxy classification (i.e. 'what is seen' and 'why such things are seen') as a stepping stone to understand galaxy formation and evolution. Though I largely follow the terminology of early classifications in this thesis, I also try to stress the importance of other galaxy properties derived from multi-wavelength observations and not considered in the early classifications. There are three major galaxy types (ellipticals, lenticulars, and spirals) plus the dwarf type. Although dwarfs dominate the overall galaxy population by number in the nearby universe, I only discuss the other three (giant galaxy) morphological types in detail given the scope of this thesis. Below, I discuss their main morphological, stellar population, and gas content differences, and then in Section 1.1.3, their nuclear activity differences.

Using the stellar morphology definition at optical wavelengths, elliptical galaxies have largely featureless ellipsoidal stellar distributions; lenticular galaxies are disc galaxies with neither spiral arms nor large-scale dust features; spiral galaxies have stellar discs with spiral arms. Lenticulars and spirals may also have bars and/or bulges in the central regions.

A bar is usually a boxy/peanut-shaped distribution of stars, with its longest axis in the plane of the stellar disc and its axis perpendicular to the stellar disc longer than the disc thickness. In the range of galactocentric radii covered by the bar, there is usually a deficit of both stars and gas outside the bar itself. Thus, a (stellar) bar forms a non-axisymmetric gravitational potential well, leading to shocks in the gas, loss of angular momentum, and gas inflows toward the galactic centre along the leading edges of a bar (see e.g. Athanassoula, 1992; Athanassoula & Beaton, 2006; Kim & Stone, 2012).

A bulge is a central spheroid of stars, also extending beyond the stellar disc in the vertical direction. In the literature, such a bulge is also referred to as a classical bulge,

while another stellar component sometimes referred to as a pseudo-bulge is defined as an excess surface brightness in galactic centres above that of the inward extrapolation of the outer exponential radial profile, without geometric bulging out of the disc (see Kormendy & Kennicutt, 2004, for a review). Some secondary morphological components include nuclear bars, nuclear discs, nuclear star clusters, stellar haloes, rings, etc. Galactic components other than stars and observations at wavelength ranges other than the optical often reveal other features, such as filamentary structures, shells, and bubbles in the gas (e.g. Barnes et al., 2023). It is one of the fundamental goals of galaxy studies to understand how each feature forms and whether/how galaxies evolve across morphological types.

In terms of stellar populations and dynamics, ellipticals typically have stars of the oldest ages, highest metallicities, and largest alpha-element[6] abundances, and have pressure-supported dynamics. Spirals have the youngest stars with mixed metallicities and alpha-element abundances, and the discs are supported by ordered rotation. Lenticulars are usually intermediate in these properties. The total stellar masses of ellipticals are on average the highest while their specific star formation rates (sSFRs), defined as the ratio of the SFR to the stellar mass (M_*), are on average the lowest. Again, spirals are usually the opposite and lenticulars intermediate. Therefore, ellipticals are mostly located in the so-called 'red sequence' of galaxies in the colour-magnitude diagram, equivalently in the 'quiescent' galaxies separated from the star formation main sequence (SFMS) in the SFR–M_* diagram.

As hinted above, metallicity is an important property of stellar populations. Though stellar metallicity and gas-phase metallicity are defined in slightly different ways, both reflect the fraction of metals in the baryons and they correlate well with each other on galaxy scales. Overall galaxy metallicity correlates positively with total galaxy stellar mass and with morphological type. Elliptical galaxies thus tend to be at the high-mass high-metallicity end of the mass–metallicity relation while spirals tend to be at the lower ends (Tremonti et al., 2004; Griffith et al., 2019). These statements concern galaxies as a whole. However, different components in a galaxy can vary significantly. In spirals, the (pseudo-)bulges and thick discs, if any, are usually older, have lower sSFRs, are redder

[6]Alpha elements are defined as elements with integer increments of alpha particles, from carbon to titanium.

in colour, and have higher metallicities than the thin discs. Thus, these components are somewhat similar to elliptical and lenticular galaxies.

To study the evolution of the stellar populations of galaxies in more depth, metallicity can be further sub-divided into the abundance of each element. In particular, each alpha element approximately forms a layer in a post-main-sequence high-mass star, so alpha elements in the ISM (and, in turn, in subsequent generations of stars) are mainly contributed to by type-II supernovae. Distinct from those, iron in the ISM (and in subsequent stars) mainly arises from type-I supernovae (see McWilliam, 1997; Matteucci & Chiappini, 2005, for reviews). As the timescales of the two types of supernovae are different, the formation timescale of each stellar population can be constrained by measuring the ratio of the alpha elements and iron abundances. For example, the Wallerstein–Tinsley diagram of [α/Fe] vs. [Fe/H] (where the brackets indicate a logarithmic scale with respect to solar) has been used to distinguish the thick and thin discs of the MW, also indicating different formation paths (Wallerstein, 1962; Lian et al., 2020).

Even for a given morphological component, variations are significant across different galaxies, probably because of the different evolutionary stages of each galaxy. Specifically, the thin discs of LTGs vary in terms of gas fraction and stellar population colour (Bell & de Jong, 2000, see also Section 1.3.1). The thick discs of LTGs evolve in terms of specific angular momentum (Hu et al., 2023). Based on results from the ATLAS^{3D} survey, the comb diagram was proposed, to explain these variations as a result of galaxy evolution (bottom panel of Figure 1.2; Cappellari et al., 2011). Briefly, galaxies first follow a sequence of decreasing sSFR due to a combination of decreasing gas fraction and decreasing SFE (Lin et al., 2022), then a sequence of decreasing specific angular momentum. The former sequence classifies galaxies into traditional spirals, anaemic spirals, and lenticulars; the latter characterises the transition from lenticulars to ellipticals as a transition from fast rotators to slow rotators. Later studies have further demonstrated that the gas fraction and other gas properties (including the SFE) are indeed the driver of galaxy evolution (see Saintonge & Catinella, 2022, for a review). The gas properties of nearby galaxies are discussed in more detail in Section 1.3.

1.1.3 Galactic centres

The previous sections describe the phenomenological properties exhibited by galaxies. To understand the physical mechanisms behind these properties, galactic centres are a key region to study. The centres of galaxies are not just the peaks of the density and luminosity distributions. Indeed, these environments are so extreme as to actively drive the evolution of galaxies.

The presence of a supermassive black hole (SMBH) has been confirmed in almost every galaxy with a bulge (Ho, 1999). These SMBHs are usually within the mass range 10^6–10^{10} $M_\odot$, which is typically one-hundredth to one-thousandth of their host galaxy's stellar mass, and they occupy a negligible volume. Yet, substantial evidence supports a tight correlation between SMBH mass and galaxy properties, indicating a regulated co-evolution (e.g. Wang et al., 2023). One proposed mechanism for such co-evolution is AGN feedback. AGNs harbour SMBHs, radiate brightly at optical and most other wavelength ranges, and have winds and jets of particles arising from the loss of gravitational potential energy of the infalling/accreting material. Such radiative and kinetic feedbacks have been proposed to influence galaxy evolution, including causing the exponential decrease at the high-mass end of the galaxy stellar-mass function.

In addition to stars, AGNs are thus another important driver of the baryon cycle and galaxy evolution. Cold molecular gas from either the galactic disc (e.g. Izumi et al., 2023) or the CGM (Rose et al., 2019) and hot gas accretion via the Bondi process (e.g. Narayan & Fabian, 2011) are major contributors to AGN accretion, although the relative importance among these is still under debate. The emitted radiation and material are in the form of energetic photons, ionised gas, and cosmic rays. Thus, it is essential to fully understand AGN accretion and feedback to understand galaxy evolution. Cold molecular gas around AGNs is feeding AGN accretion and being affected by AGN feedback.

In general, the nuclear activity of galaxies is a complex and active field of research (see Padovani et al., 2017, for a review). Observationally, AGNs have various types and a few of them are discussed below. Seyfert (Sy) 1 exhibits broad emission lines with velocity widths of ≈ 1000 km s^{-1} while Sy 2 only have much narrower lines. Both Sy types are mostly present in spiral galaxies and are quiet at radio wavelengths due to the absence

of (relativistic) jets. ETGs, on the other hand, usually host radio-loud AGNs and low-ionisation nuclear emission-line regions (Heckman, 1980). Quasars have been identified up to $z = 7.64$ (Wang et al., 2021). They were historically thought to be point sources but are now known to also be AGNs, which, unlike local AGNs, do not have detectable stellar components surrounding them due to the faintness of stars at such far distances. In the theoretical framework of a unified AGN model, all observational types are interpreted to be results of different viewing angles (see Antonucci, 1993, for a review). The unified AGN model has an SMBH at the centre, surrounded by an accretion disc, a spheroidal broad-line region, a narrow-line region (outside the broad-line region), a dust torus (coplanar with the accretion disc), and optionally relativistic jets perpendicular to the accretion disc.

Apart from (potentially active) central SMBHs, the central regions of galaxies have various other unusual properties, including high densities of stars, gas, radiation, pressure, etc. Many properties are significantly different from those elsewhere in nearby galaxies, but interestingly are analogous to those of high-redshift galaxies (Kruijssen & Longmore, 2013). Due to these extreme conditions, galactic centres are unique laboratories to test theories of star formation as well as to understand galaxy properties at earlier cosmic epochs (Henshaw et al., 2023). This thesis mostly focuses on galactic centres, to disentangle the interplay of the different physical mechanisms behind the molecular gas properties.

1.2 Cold molecular gas

As argued in Section 1.1.1, the cold molecular phase of the ISM fosters star formation and bears its feedback. Thus, this thesis focuses on cold molecular gas to try to understand galaxy evolution. In this section, I will first review the origin and destruction of the main molecular species used in this thesis (Section 1.2.1), then describe the emission from molecular gas and the physical properties derived from it (Section 1.2.2), and finally introduce the technology used to observe cold molecular gas (Section 1.2.3).

1.2.1 Formation and destruction

Molecular hydrogen is the simplest and most abundant species of cold molecular gas. Its dominant formation takes place on the surface of dust grains, known as grain catalysis.

Two hydrogen atoms are adsorbed onto a grain surface, encounter each other through diffusion (i.e. random walk), synthesise a hydrogen molecule, and desorb from the surface (see Wakelam et al., 2017, for a review).

The second most abundant molecule in the ISM is carbon monoxide (CO), about 10^{-4} that of molecular hydrogen by number (Lacy et al., 1994). Its formation channels are much more complex. In diffuse molecular clouds, the majority of gas-phase carbon is in the form of C^+ while that of hydrogen is H_2. The primary formation channel of CO is thus a series of reactions, from the radiative association of C^+ and H_2, via CH_2^+ and CH, eventually to the neutral-neutral exchange reaction of CH and oxygen (Solomon & Klemperer, 1972; Draine, 2011). Many other reactions can affect the abundance of CO to second order, such as the recombination of HCO^+ (Liszt, 2007) and the reaction of C^+ with the OH radical (Oppenheimer & Dalgarno, 1975).

The formation mechanisms get more complicated and uncertain when it comes to nitrogen-bearing molecules, such as diazenylium (N_2H^+) and isocyanic acid (HNCO). N_2H^+ is primarily formed from the interaction of H_3^+ and N_2 in the gas phase (Lee et al., 2004). For HNCO, various formation channels have been proposed, both in the gas phase (Turner et al., 1999; Iglesias, 1977) and on grain surfaces (Allen & Robinson, 1977; Garrod et al., 2008). It is also possible that the main source of gas-phase HNCO is the breakdown of more complex species (Tideswell et al., 2010). Nevertheless, despite all these studies the origin of HNCO is still largely an open question (e.g. see the recent work by Hernández-Gómez et al., 2019).

The destruction of molecules is just as important as their formation, as it results from (stellar) feedback and forms part of the baryon cycle. The main destruction process of molecular hydrogen is photodissociation ($H_2 + h\nu \rightarrow H + H$). Newborn stars emit photons that excite hydrogen molecules, and $\approx 15\%$ of the excited molecules decay into the so-called vibrational continuum, which is effectively an unbound state of the two hydrogen atoms (Draine, 2011). This process creates a 'photodissociation region' (defined as the interface between the H II region and the molecular cloud), and more specifically a photodissociation front (defined as the surface where half the hydrogen mass is in atoms and the other half in molecules). Other molecules are also efficiently photodissociated

in photodissociation regions, but each has a distinct photodissociation front. A recent review of this active field of research is provided by Wolfire et al. (2022).

The main chemical channel of N_2H^+ destruction is via reactions with CO. It is therefore more abundant when CO freezes out onto dust grains at low temperatures. This anti-correlation between N_2H^+ and CO was studied by e.g. Jørgensen et al. (2004). The CO molecule is primarily chemically destructed by He^+ (Liszt, 2007). Aside from destruction, the interstellar radiation field can also excite and/or ionise molecules and ions, discussed further below (Section 1.2.2).

1.2.2 Tracers and observables

To observe molecules, both emission and absorption of radiation are used. Molecular gas is mostly cold ($\lesssim$ 100 K), primarily because its formation channels are efficient only at such low temperatures. Cold temperatures are also a requirement for the gravitational contraction and/or collapse of giant molecular clouds, that ultimately lead to star formation. Despite comprising the bulk of the cold molecular gas, molecular hydrogen does not have any transition at these low temperatures, as it is symmetric and does not have a dipole moment. Only warm molecular hydrogen emits, e.g. the $\lambda = 28.22$ μm line in the far-infrared (FIR) with an upper-level energy of 510 K (Dabrowski, 1984). Cold molecular hydrogen thus cannot be observed via emission or absorption, and other tracers must be used to probe it.

CO is the most widely used such tracer, due to its high abundance and brightness. Cosmic CO was first detected by Wilson et al. (1970). When a CO molecule is excited by collision with other particles, primarily H_2, or by an ultraviolet (UV) photon, the CO molecule can de-excite to various rotational-vibrational levels. The lifetimes of all vibrationally excited levels (denoted by $v > 1$) are too small for collisions to play a significant role in their (de)excitation. With the spontaneous decay toward lower vibrationally excited levels, the majority of the molecules remain in the ground vibrational state ($v = 0$). On the other hand, rotationally excited states (denoted by $J > 1$) have critical densities (for collision effects to be significant) comparable to the typical ISM density. Thus, the partition function characterised by the (rotation-)excitation temperature ($T_{\rm ex}$) is

coupled to the gas temperature. The spontaneous decay of these rotationally excited states creates line emission. Under the condition $T_{\rm ex} \gg 2.77\,J(J+1)$ K, the J state is populated and the line emission of the $J \rightarrow J-1$ transition is bright (Bolatto et al., 2013).

The most commonly used CO line is $J = 1 \rightarrow 0$[7] at a rest frequency of $\nu_{\rm rest}$ = 115.271 GHz. This line has been widely mapped in the MW (e.g. Dame et al., 1987) and external galaxies (e.g. Young et al., 1995), and it is used as the main tracer of the molecular gas distribution, kinematics, and physical properties. In recent years, CO(2-1) at a rest frequency of $\nu_{\rm rest}$ = 230.538 GHz has increasingly been used, as it provides a good balance between brightness and angular resolution (inversely proportional to the frequency). Large surveys such as PHANGS (Leroy et al., 2021) and WISDOM (Davis et al., 2022) have primarily used CO(2-1).

Apart from CO, this thesis also makes use of a few other important molecules, including N_2H^+ and HNCO. Cosmic N_2H^+ was first detected by Turner (1974) and identified by Green et al. (1974). It has been used to trace the high-density regions of molecular clouds as (i) the formation of N_2H^+ favours higher densities ($\gtrsim 10^4$ cm^{-3}; Priestley et al. 2023) than the formation of CO ($\gtrsim 10^2$ cm^{-3}; Shetty et al. 2011) and (ii) CO freezes out onto dust grains in such environments and thus becomes fainter (Whitworth & Jaffa, 2018). Cosmic HNCO is a more recently used dense molecular gas tracer (Jackson et al., 1984), even though it was first detected by Snyder & Buhl (1972).

Cold molecular gas observations most often take the form of spectra, i.e. line flux density as a function of wavelength λ or frequency ν (or velocity v, once converted using the line rest frequency $\nu_{\rm rest}$ and observed Doppler shift[8]). The unnormalised 0$^{\rm th}$ moment of a spectrum yields the total (or integrated) flux. The normalised 1$^{\rm st}$ moment of a spectrum is the average line-of-sight (LoS) velocity of the target, which can be used to pin down the location of a Galactic cloud and the redshift of an extragalactic target. The square root of the normalised 2$^{\rm nd}$ moment (with respect to the average LoS velocity) quantifies the linewidth of the emitter and is also called velocity dispersion. It has contributions from both ordered bulk motions (such as converging/diverging gas flows and ordered rotation

[7]For simplicity, such rotational transition lines are abbreviated as e.g. CO(1-0).

[8]I follow the radio convention throughout this thesis: $v/c \equiv 1 - \nu/\nu_{\rm rest} = 1 - \lambda_{\rm rest}/\lambda$, where c is the speed of light, $\lambda_{\rm rest}$ the rest wavelength, and other variables already introduced.

about galactic centres) and random motions (including thermal and turbulent broadening). Spatially resolved observations (see Section 1.2.3 for details) produce spectra along multiple LoSs. This usually forms a three-dimensional (3D; position-position-velocity) datacube. Each of the moments then becomes a two-dimensional (2D; position-position) map revealing the distribution and motions of gas.

Particularly for CO(1-0), a conversion factor $X_{\rm CO} \approx 2 \times 10^{20}$ cm^{-2} (K km s^{-1})$^{-1}$ is used to convert CO(1-0) luminosity (or intensity) into hydrogen molecule number (or number surface density). CO(1-0) is almost always optically thick in molecular clouds, and variations of $X_{\rm CO}$ arise due to the effects of environment, geometry, excitation, dynamics, etc., especially on small spatial scales. Bolatto et al. (2013) presented a review of $X_{\rm CO}$ and Teng et al. (2024) recently proposed a simple empirical prescription to determine $X_{\rm CO}$ using the CO line width. For practical convenience, another conversion factor $\alpha_{\rm CO(1-0)}$ is defined to convert CO(1-0) luminosity (or intensity) into total molecular gas mass (or mass surface density), including the mass contribution from molecules other than H_2. The commonly used value $X_{\rm CO} = 2 \times 10^{20}$ cm^{-2} (K km s^{-1})$^{-1}$ corresponds to $\alpha_{\rm CO(1-0)} = 4.3$ M$_\odot$ pc^{-2} (K km s^{-1})$^{-1}$.

Apart from the spectrum and its moments, a few more aspects can be probed using molecular gas observations. With multiple molecular lines, radiative transfer modelling can be carried out to derive molecular gas properties such as temperature and density (Teng et al., 2022). Magnetic field properties can be derived from molecular line emission using the velocity gradient technique (González-Casanova & Lazarian, 2017; Zhao et al., 2024), polarisation observations (Cortes et al., 2008), and/or Zeeman splitting (e.g. Crutcher et al., 1993; Koley et al., 2022).

When molecular line emission is too faint to be detected, molecular absorption lines can be used as alternative, more sensitive tracers. When a gaseous system is located along the LoS to a continuum source, cold molecular gas creates an absorption feature. The background continuum source can be a distant AGN (e.g. Combes et al., 2019; Klitsch et al., 2023) or the AGN of the galaxy itself (e.g. Rose et al., 2020).

Last but not least, dust has also been used to trace molecular gas, more specifically dust continuum emission and dust extinction of stellar light. Dust continuum emission is

simply the thermal radiation described by a modified blackbody model (Scoville et al., 2014), from which the dust mass and temperature can be derived. To distinguish dust continuum emission from other continuum sources (mainly free-free and synchrotron emission), the spectral index (i.e. the power-law index of the continuum spectrum) can be measured across a range of frequencies and compared with the characteristic indices of known radiative processes (≈ 2.0 for dust emission; Paradis et al. 2010). It is also possible to convert the derived dust mass into a cold molecular gas mass using a dust-to-gas ratio. This provides an independent method to cross-calibrate $X_{\rm CO}$ (e.g. Berta et al., 2016; Popesso et al., 2020). A dust extinction map, derived from the stellar light at optical and IR wavelengths, also traces the amount of cold molecular gas (Concas & Popesso, 2019). Compared to the CO emission line, using dust continuum emission and/or extinction as tracers usually requires much less observing time, but it does not provide any kinematic information as no velocity can be derived from a continuum source.

1.2.3 Observational technologies

As mentioned above, molecular line emission is typically in the (sub-)millimetre (100 GHz corresponds to 3 mm) regime. This belongs to the (high-frequency end of) radio wavelengths, with which it shares many observational technology similarities. Conversely, the high-frequency end of the sub-millimetre regime ($\approx$ 1 THz or 0.3 mm) blends with the FIR regime. Heterodyne receivers are most commonly used for (sub-)millimetre observations. They measure both the intensity and phase of the electromagnetic radiation, critical for the interferometric technique discussed below.

The Earth's atmosphere is partially transparent at (sub-)millimetre wavelengths, as shown in Figure 1.3 (adapted from Remijan et al., 2019). The major absorption features in the transmission curves are created by water vapour and oxygen. As a result, the Atacama Large Millimeter/submillimeter Array (ALMA), despite the site dryness thanks to the high altitude of 5000 m, only covers 77% of the frequencies within 50–950 GHz. The ten ALMA bands are colour-shaded areas in Figure 1.3. In addition to the deep 'trenches' in the transmission curves dictating ALMA band boundaries, the average transparency of the high-frequency bands of ALMA (~30%) is lower than that of the

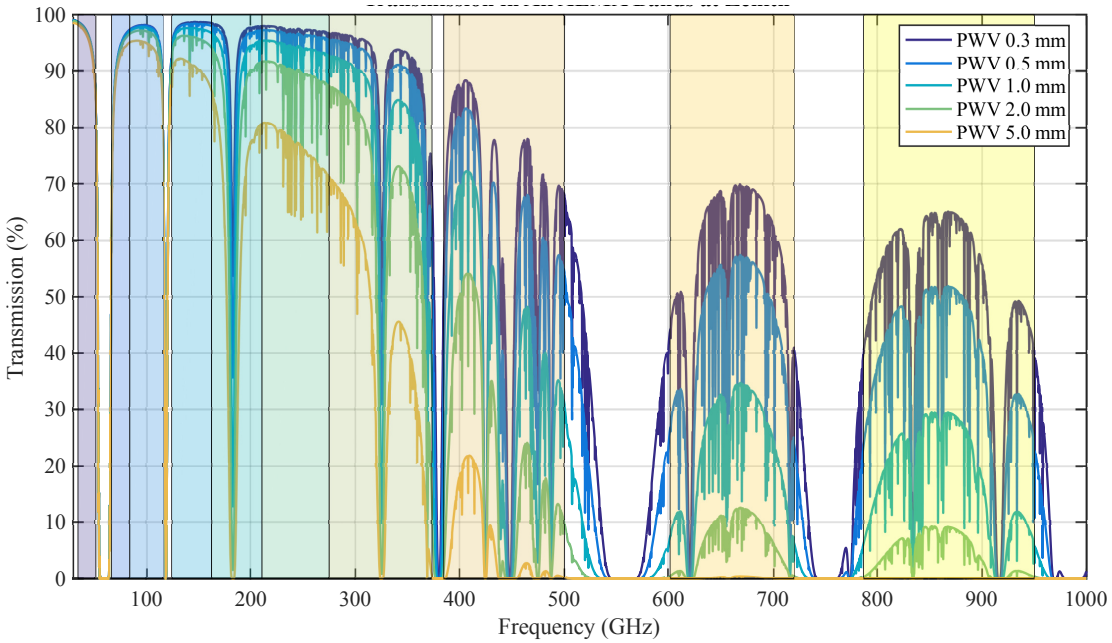

Figure 1.3: Atmospheric transmission percentage as a function of GHz frequencies (equivalent to (sub-)millimetre wavelengths), measured at the ALMA site zenith. Curves with different colours correspond to different precipitable water vapour (PWV) levels indicated in the top-right corner. Colour-shaded rectangles show the wavelength coverages of different ALMA bands. Adapted from Remijan et al. (2019).

low-frequency bands (≈95%). Generally speaking, ground-based observations are still largely feasible and have the general advantages (compared to space missions) of larger mirrors, lower cost, lower risks, easier maintenance, and a longer lifespan. The majority of (sub-)millimetre facilities are therefore ground-based. Nonetheless, a few FIR/sub-millimetre space missions have also made remarkable contributions to this field, most recently the *Herschel Space Observatory*.

In the 1940s, the Nobel prize-winning[9] interferometry technique started to be developed and implemented in radio/(sub-)millimetre astronomy, and transformed the field. In a nutshell, single-dish telescopes measure the on-sky brightness distribution of an astronomical target using multiple pointings and/or arrays of receivers, while interferometers connect multiple telescopes to form an array and measure the brightness distribution in Fourier space.

Interferometry is achieved by correlating the signal received from every pair of telescopes in the array, also referred to as a baseline. Using two telescopes separated

[9] https://www.nobelprize.org/prizes/physics/1974/speedread/

by a distance vector $\boldsymbol{b}$ as an example, Figure 1.4 illustrates the process. The centre of the source (often used as the phase centre as well) is at an angle θ from the normal to the ground in a direction denoted by the unit vector $\boldsymbol{s}_0$, while a variable unit vector $\boldsymbol{s}$ is defined to point to any specific location in the source plane with a variable angle α with respect to $\boldsymbol{s}_0$. Due to the large distances of astronomical targets, $\boldsymbol{s}_0$ remains approximately parallel for all antennae (and so does $\boldsymbol{s}$). Without loss of generality, the voltage outputs V_1 and V_2 (at any given frequency) from the two antenna receivers can be expressed as as

$$\begin{aligned} V_1 &\equiv \int_\Omega \sqrt{I_s A_s}\cos(\omega t + \tau) \\ V_2 &\equiv \int_\Omega \sqrt{I_s A_s}\cos(\omega t) \\ \tau &= 2\pi \frac{\boldsymbol{s}\cdot\boldsymbol{b}}{\lambda} \ , \end{aligned}$$

where Ω is the solid angle spanned by the source, i.e. the set of all possible $\boldsymbol{s}$, I_s the intensity along the LoS to $\boldsymbol{s}$, A_s the response function,[10] τ the phase difference, ω the angular frequency of the observation, and λ the wavelength of the observation.

A correlator multiplies these two voltages and takes their time average, with the output

$$R_{12,\cos} \equiv < V_1 V_2 >= \frac{1}{2}\int_\Omega I_s A_s \cos\tau .$$

Similarly, by manually introducing a time delay corresponding to a phase difference of -90° to V_1, the correlator output becomes

$$\begin{aligned} R_{12,\sin} &\equiv < V_{1,\mathrm{del}} V_2 > \\ &= \int_\Omega I_s A_s < \cos(\omega t + \tau - \frac{\pi}{2})\cos(\omega t) > \\ &= \frac{1}{2}\int_\Omega I_s A_s \sin\tau \ . \end{aligned}$$

Combining $R_{12,\cos}$ and $R_{12,\sin}$, the observable called complex visibility $\mathcal{V}$ is defined as

$$\mathcal{V} \equiv 2(R_{12,\cos} - iR_{12,\sin}) = \int_\Omega I_s A_s e^{-\tau} \ .$$

[10] A_s encompasses the telescope collecting area and primary beam response, the receiver electronic gain, and multiple other factors, and is considered known through calibration.

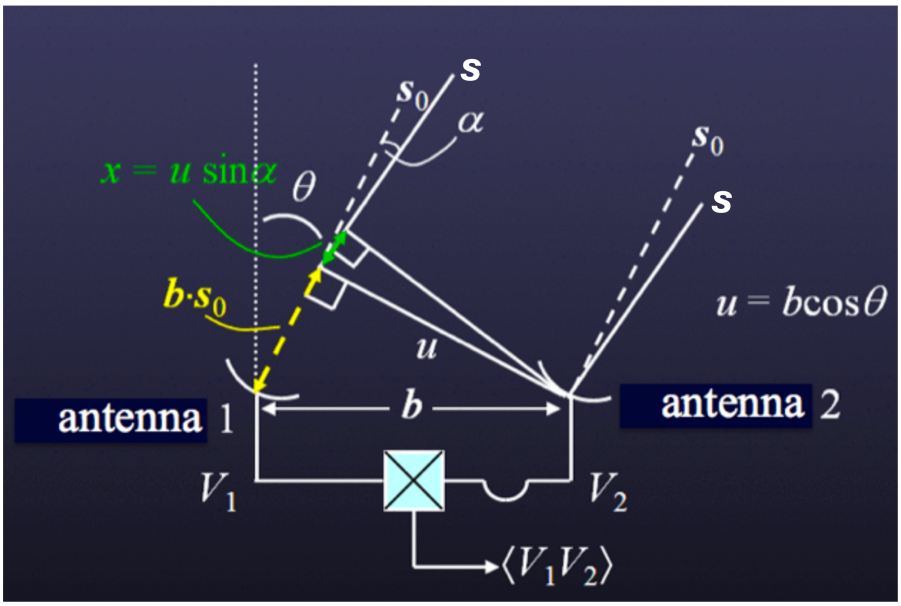

Figure 1.4: Schematic diagram of interferometry. Two antennae a distance $\boldsymbol{b}$ apart receive signals from a target. The centre of the target is along the unit vector $\boldsymbol{s}_0$ at an angle θ with respect to the vertical direction, while the on-sky spatial extension of the target is described by the unit vector $\boldsymbol{s}$ at an angle α to $\boldsymbol{s}_0$. The signals received are in the form of the voltages V_1 and V_2 and are processed using a correlator. See Section 1.2.3 for details. Adapted from Remijan et al. (2019).

In practice, another manual time delay is introduced to offset the geometrical delay caused by $\boldsymbol{s}_0$, so that $\tau' = 2\pi \frac{|\boldsymbol{b}| \sin\alpha}{\lambda}$ if $\boldsymbol{b}$, $\boldsymbol{s}$, and $\boldsymbol{s}_0$ are coplanar. To generalise to 2D (for both the baseline and the source), u and v are defined as the projected lengths of $\boldsymbol{b}$ in two orthogonal directions (conventionally east-west and north-south, respectively) in the unit of λ, and l and m are defined as the direction cosines of $\boldsymbol{s}$ in the same coordinate system. The visibility $\mathcal{V}$ then becomes

$$\mathcal{V} = \int \int I_s A_s e^{-2\pi(ul+vm)} \mathrm{d}l \mathrm{d}m \ ,$$

the exact Fourier transform (FT) of $I_s A_s$. Therefore, the inverse FT of the observed $\mathcal{V}$ yields the desired on-sky brightness distribution I_s. In practice, there are many more details involved in interferometry, and interested readers are referred to Thompson et al. (2017) and Remijan et al. (2019).

The angular resolution of a single-dish telescope is determined by the diffraction pattern size of its primary mirror. However, for interferometry, this primary beam size determines the field of view (FoV) and is not related to the spatial resolving power. The angular resolution of interferometry is determined by the longest baseline b_{max}, which corresponds

to the highest spatial frequency and in turn the shortest source separation. Specifically, the angular resolution is proportional to $\frac{\lambda}{b_{\max}}$, and the factor of the proportionality is typically in the range of 0.7–1.2 depending on the weighting applied to $\mathcal{V}(u, v)$ in the inverse FT. In terms of angular resolution (but not sensitivity), an interferometric array is thus effectively a single-dish telescope with a diameter equal to the longest baseline.

One major deviation of actual observations from the ideal case described above is the incomplete coverage of the uv plane. Although most observations are long enough that the rotation of the earth helps to populate the uv plane, the plane is still sparsely sampled in most cases. In particular, the innermost part of the uv plane is restricted by the shortest baseline available (and thus ultimately the physical size of the telescopes). These $\mathcal{V}(u, v)$ are the lowest spatial frequencies of the brightness distribution and correspond to the flux level of the most extended emission. Thus, interferometric observations (alone) often miss (or resolve out) flux, and they can be supplemented by single-dish observations of the total flux to help remedy this problem.

Another issue caused by the incomplete uv plane sampling is interferometric artefacts. A point source has constant $\mathcal{V}$ in the uv plane. Thus, an inverse FT of the interferometric array pattern directly predicts the observed point source. This point source image is called the point spread function in optical astronomy and the (dirty) synthesised beam in radio interferometry. Due to the incomplete sampling of the uv plane, apart from the central main lobe this synthesised beam has many sidelobes and negative bowls, thus the name 'dirty'. An interferometric observation thus yields a convolution of the real source brightness distribution and this dirty beam, generally called a dirty image or a dirty cube. Deconvolution is thus desired, and popular algorithms are usually variations of the original CLEAN algorithm Högbom (1974). In brief, 'cleaning' iteratively selects the peak intensity of the dirty image (or one channel of a dirty cube), regards a few per cent of the peak as a point source, stores this fictitious point source into a so-called model image (initially blank), and subtracts the dirty beam pattern corresponding to that point source from the dirty image. The dirty image after such an extraction is called the residual image. The iterative extraction stops when the highest intensity in the residual image is below a user-set threshold, usually 1–3 times the observational noise. Finally,

the model image is convolved and added back to the residual image to create a so-called clean image. The convolution kernel is usually the Gaussian function best fitting the central lobe of the dirty beam, also called the 'clean beam'.

Before the imaging (i.e. the inverse FT) and cleaning steps, the data reduction procedures of both single-dish and interferometric observations primarily include: (i) flagging out bad data, (ii) bandpass (both phase and amplitude of $\mathcal{V}$) calibration, (iii) gain (both phase and amplitude) calibration, and (iv) absolute flux scale calibration. The major purpose of these calibration steps is to remove time- and frequency-dependent atmospheric and instrumental variations. This is usually achieved by observing calibrator sources near the scientific target, sometimes repeatedly at fixed time intervals, during one observing run. For interferometric observations, if the scientific source is bright enough, itself can be used as a gain calibrator, a.k.a. the self-calibration technique.

Prominent (sub-)millimetre interferometers include the ALMA located in Chile, the Northern Extended Millimeter Array (NOEMA) in France, and the Submillimeter Array (SMA) in Hawaii. Specifically, ALMA is a state-of-the-art facility with capabilities unmatched by other interferometers. It is a large collaboration involving Europe, North America, East Asia, and Chile, and started scientific observations in 2011. ALMA consists of two arrays located on the Chajnantor plateau at 5000-m altitude: (i) the main array of 50 12-m antennae and (ii) the ALMA Compact Array (ACA; also called the Morita Array) of 12 7-m antennae (called the 7-m Array) and four 12-m antennae (for single-dish observations; called the Total Power Array). The frequency coverage is 35–950 GHz, with various modes and spectral set-ups to suit the needs of different projects. The data used in this thesis primarily come from ALMA.

1.3 Cold molecular gas as a galaxy component

Cold molecular gas is the fuel for and the site of star formation, and is thus key to galaxy evolution. To understand the physical mechanisms associated with cold molecular gas, a multi-scale hierarchical view is essential. Using the terminology of the review of Schinnerer & Leroy (2024), I discuss the properties of the molecular gas on the following scales below: the whole galaxy scale ($\sim$ 10 kpc), the resolved galaxy scale (0.5–2 kpc),

the cloud scale (≈ 100 pc), and the resolved cloud scale (∼ 10 pc). The term 'giant molecular cloud' (GMC) often refers to the massive (and large-size) end of the molecular cloud distribution, of radius ≈ 20–80 pc. A thorough understanding of GMC properties of all types of galaxies is essential to effectively tackle a range of related questions regarding star formation and quenching, stellar feedback, turbulence, etc.

At the whole galaxy scale, single-dish telescopes are often used to conduct large surveys of galaxies. Among them, the extended CO Legacy Database for *GALEX* Arecibo SDSS Survey (xCOLD GASS) targeted an unbiased large sample of galaxies with $0.01 < z < 0.05$ and stellar mass $M_*/\mathrm{M}_\odot > 10^9$ (Saintonge et al., 2017). It constitutes a reference for the distributions of and correlations among fundamental galaxy properties related to molecular gas and star formation in galaxies. The mean CO(2-1)/CO(1-0) line ratio (in brightness temperature unit) is 0.79 ± 0.23; the molecular gas fraction μ_{gas} is typically in the range of 0.01–0.1; the molecular gas depletion time ($t_{\mathrm{dep}} \equiv M_{\mathrm{mol}}/SFR = 1/SFE$) is $\log(t_{\mathrm{dep}}/\mathrm{yr}) = 8.98 \pm 0.27$. Both μ_{gas} and t_{dep} correlate most strongly with sSFR (or equivalently the offset from the SFMS).

Below, we explore the molecular gas properties of individual galaxy morphological types on smaller physical scales.

1.3.1 Late-type galaxies

Nearby LTGs occupy the molecular gas–rich and high-SFE ends of the aforementioned distributions. Whenever an LTG has young stellar populations (true for most LTGs), it always has cold molecular gas associated with them. The cold molecular gas masses of LTGs are, on average, ≈ 5% of their stellar masses and this mean fraction is approximately constant across spiral subtypes. Nonetheless, the scatter is as large as a factor of five to both directions for individual galaxies. This range of molecular gas mass fraction has been established by Young & Scoville (1991, and references therein) and validated by the *Herschel* Reference Survey (Boselli et al., 2014), the EDGE-CALIFA survey (Bolatto et al., 2017), and the xGASS survey (Catinella et al., 2018, using the proximity to the SFMS and low central stellar mass surface density as proxies of LTG morphologies). The mass of cold atomic gas is, on average, four times that of the cold molecular gas (Boselli

et al., 2014). There are also systematic variations across the sub-types of LTGs and as a function of total stellar mass. In early-type spirals (i.e. Sa and Sb) and high-mass spirals, the ratio of atomic to molecular gas mass is lower (as low as 0.1) while for late-type spirals (i.e. Sc and Sd) and low-mass spirals, this ratio is higher (as high as 100) (Young & Scoville, 1991; Obreschkow & Rawlings, 2009; Blanton & Moustakas, 2009).

At the resolved galaxy scale, the molecular gas of LTGs has similar spatial extent and morphological structures as the optical components (Stuber et al., 2023a), although the radial profile of the molecular gas mass surface density usually declines (toward the galaxy outskirt) faster than the stellar component (Saintonge & Catinella, 2022, and references therein). The CO distributions also have larger clumpiness and asymmetries (quantified by e.g. the Gini coefficient), as seen toward the upper-left of Figure 1.5 (Davis et al., 2022). The kinematics of the molecular gas are often disturbed due to AGNs, bars, and/or intense star formation (see Section 2.6). Many studies have also investigated kpc-scale molecular gas inflows from the galaxy outskirts to the central regions, affecting both star formation (e.g. Chown et al., 2019) and SMBHs/AGNs (e.g. Querejeta et al., 2016; Lelli et al., 2022).

At cloud and sub-cloud scales, early studies of the MW Disc GMCs established the so-called Larson relations among the GMC properties such as radius, velocity dispersion and molecular gas mass (or equivalently molecular gas mass surface density; Larson 1981; Solomon et al. 1987). Subsequent studies within Local Group galaxies (exclusively LTGs and dwarfs) and nearby spirals reported similar relations despite minor methodological differences (e.g. Blitz et al., 2007; Bolatto et al., 2008; Donovan Meyer et al., 2013; Colombo et al., 2014). Beyond the Local Group, Sun et al. (2018, 2020a) also reported similar results for molecular gas probed on a pixel-by-pixel basis (that is without identifying individual clouds) at a spatial scale of $\approx$ 100 pc, using a large sample of LTGs from the Physics at High Angular resolution in Nearby GalaxieS (PHANGS) survey.

In the meantime, such studies pointed out that galactic centres tend to be outliers of global trends in terms of linewidth, pressure, SFE, etc., as are bars (Freeman et al., 2017; Sun et al., 2018, 2020b; Choi et al., 2023, 2024) and AGNs (Lu et al., 2022). Given these deviations from the Larson relations and the somewhat subjective identification of individual cloud structures, the Hayer-Keto relation/diagram of $\sigma/\sqrt{R}$ vs. $\sqrt{\Sigma}$ (σ the

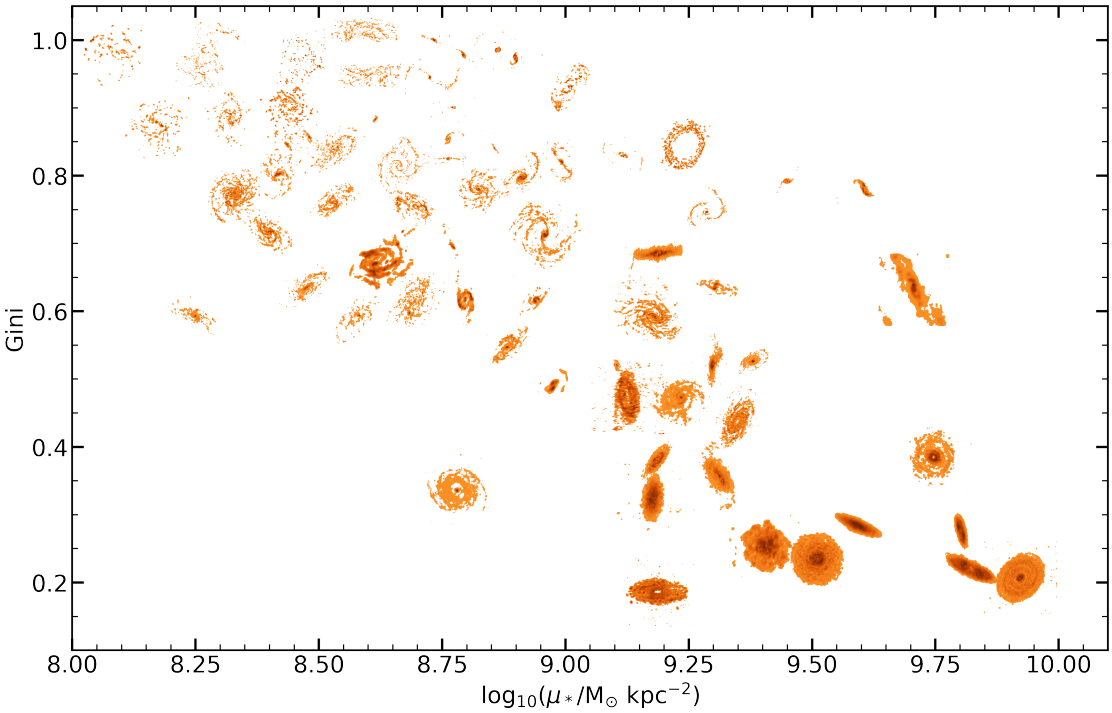

Figure 1.5: Molecular gas morphologies in the parameter space of the Gini coefficient and central stellar mass surface density (μ_*), from Davis et al. (2022). The latter is a proxy for galaxy Hubble type, larger μ_* corresponding to earlier types. All distributions are scaled to the same size on the figure, and are thus not to (physical) scale.

linewidth, R the radius, Σ the molecular gas mass surface density of clouds) has been proposed as a replacement of the Larson relations to gauge the dynamical state of clouds (Keto & Myers, 1986; Heyer et al., 2009; Schinnerer & Leroy, 2024).

1.3.2 Early-type galaxies

Drastically different from that of LTGs, the cold molecular gas content (and our knowledge of it) of ETGs is rather scarce. Only about a quarter of ETGs harbour a significant molecular gas reservoir, the fraction being larger for lenticulars than for ellipticals (Combes et al., 2007; Sage et al., 2007). For these, the total molecular gas mass is typically $\approx 0.1\%$, with a range of 0.01%–5%, of the stellar mass (Young et al., 2011). The origin of this molecular gas is unclear but is most likely either internally recycled stellar mass loss or external accretion (Young et al., 2008; Davis et al., 2011).

The spatial extent of the molecular gas of ETGs is usually much smaller than that of the stellar component, and is usually constrained to the stellar spheroid (Saintonge & Catinella,

2022; Davis et al., 2022), though the molecular gas still forms a thin disc. Due to the deep gravitational potentials of ETGs (that have higher central stellar mass densities than typical LTGs), shear and tidal effects are strong and the dynamical timescales (the times required to complete one circular orbit) are very short ($\sim$ 10 Myr). The molecular gas nevertheless forms dynamically cold and geometrically thin discs, as in LTGs, but the discs are rather smooth and featureless (Davis et al., 2022), as shown toward the lower-right of Figure 1.5.

Despite these important findings, most early studies of molecular gas in galaxies either were confined to the Local Group or lacked the resolution to spatially and spectrally resolve individual GMCs. The former studies suffer from a limited diversity of galaxy types (exclusively LTGs and dwarfs), while the latter lead to difficulties interpreting empirical relations derived from unresolved gas structures. With the advent of ALMA, in the past ten years or so cloud-scale and cloud-resolving observations beyond the Local Group have become feasible for a large number of galaxies. This has greatly benefited our understanding of molecular gas in ETGs.

On cloud scales, deviations from the typical LTG gas properties are significant, particularly in terms of elevated linewidths and virial parameters (Williams et al., 2023; Lu et al., 2024). Also, the smoothness of the ETG discs leads to the non-detection of cloud-like overdensities, e.g. in NGC 524. Even at a resolution of 37 pc, nearly sufficient to resolve the majority of the clouds observed in other galaxies, very few GMCs or gas sub-structures can be identified (Lu et al., 2024). These unusual behaviours are largely attributed to the extreme conditions in the centres of ETGs, particularly the gas dynamics.

The first resolved GMC catalogue of an ETG, NGC 4526 (distance 16.4 Mpc), was created from the Combined Array for Research in Millimeter-wave Astronomy observations by Utomo et al. (2015). The properties of the NGC 4526 GMCs deviate from those of the MW Disc clouds, with much larger linewidths and luminosities (or equivalently molecular gas masses) at a given radius and no size–linewidth correlation. Liu et al. (2021) studied another ETG with ALMA, NGC 4429 (distance 16.5 Mpc), and the properties of its GMCs also deviate from those of the MW Disc clouds. These two galaxies are the only ETGs with GMC populations studied in a spatially (and spectrally) resolved manner so far, apart from NGC 5128 with its highly disturbed and externally

accreted gas (Miura et al. 2021; see also Section 3.7). It is then natural to ask whether the GMC properties of all ETGs systematically differ from those implied by the Larson relations, originally established for MW Disc and Local Group LTG clouds.

1.3.3 Central Molecular Zone of Milky Way

As discussed in Sections 1.1.3, 1.3.1 and 1.3.2, galactic centres are unusual and extreme galactic environments. They have large stellar mass densities, gas densities, pressures, metallicities, temperatures, radiation fields, turbulence, magnetic fields, cosmic ray fluxes, and shear and tidal forces, and small dynamical timescales. Their star formation can either be as large as that of starbursts or as low as that of quiescent galaxies/regions. All of these extreme properties can be the cause or the effect of one another. To disentangle such complex interplay, highly detailed observations are required. The one galactic centre we can systematically observe with much better physical resolution and a greater amount of detail is that of our own MW, due to its closeness to us ($\approx$ 8 kpc; Gravity Collaboration et al. 2019).

The molecular gas at the centre of the MW forms a ring-like structure in the innermost 300 pc (in galactocentric radius), with a radial width of $\sim$ 10 pc (Ferrière et al., 2007; Ridley et al., 2017), named the central molecular zone (CMZ), the properties of which appear representative of many CMZs in nearby galaxies (Schinnerer & Leroy, 2024). Below I review these properties and pending puzzles of the MW CMZ, as well as observational campaigns that have contributed to our knowledge of it.[11]

The total molecular gas mass of the MW CMZ is estimated to be 2–6 $\times$ 10^7 $M_\odot$ (Ferrière et al., 2007), 3–10% of all molecular gas in the MW (Roman-Duval et al., 2016), concentrated in $\sim$ 0.1% of the MW surface area and with a current SFR of $\approx$ 0.07 $M_\odot$ yr^{-1} (Henshaw et al., 2023). This yields a gas depletion time of $<$ 1 Gyr, shorter than that of typical spiral galaxies. However, when dense gas is considered, the SFR is $\approx$ 2 dex lower than the predicted SFR from the general trend (SFR vs. dense gas mass) of star-forming galaxies (see Figure 1.5 of Barnes, 2018).

[11] A catalogue of CMZ observations is available at: https://github.com/CentralMolecularZone/DataSets.

The CMZ was first probed by surveys in the 1970s (e.g. Bania, 1977), and it is complex in geometry and kinematics. Up until now, the general consensus is that bar-driven gas inflows along the dust lanes formed the ring-like structure, as is observed in many other nearby spiral galaxies (see Henshaw et al., 2023, for a review). However, difficulties in determining the exact 3D geometry of the CMZ arise from its edge-on orientation in the sky, and competing models include 'two spiral arms' (Ridley et al., 2017), 'a closed elliptical orbit' (e.g. Molinari et al., 2011), and 'open streams' (e.g. Kruijssen et al., 2015). Regarding the kinematics, gas overshooting the dust lanes gives rise to the parallelogram in the classic CMZ molecular gas position-velocity diagram (Hatchfield et al., 2021), while decelerating gas forms multiple extended velocity features.

To understand the properties of the gas under such an extreme environment and the physical processes behind the lower-than-expected star formation rate (considering the dense gas), a detailed examination of the clouds, clumps, and cores in the CMZ is necessary.

The dust continuum emission has been mapped by e.g. the *Herschel* Infrared Galactic Plane Survey (Molinari et al., 2010), the MUSTANG Galactic Plane Survey (Ginsburg et al., 2020), and the SMA CMZoom survey (Battersby et al., 2020). With dust spectral energy distribution modelling from FIR to mm wavelengths, the dust temperatures are constrained to be in the range 20–25 K, a factor of 2–3 higher than those in comparable-density MW Disc cores. The typical column densities of molecular hydrogen are $\sim 10^{23}$ cm^{-2}, peaking at $> 10^{24}$ cm^{-2} in the Sagittarius (Sgr) B2 region. There is also an anti-correlation between molecular hydrogen column density and dust temperature.

As for line observations, to avoid confusion with MW Disc clouds along the LoS, dense gas tracers are more often used than ^{12}CO. Examples include the MOPRA CMZ survey (Jones et al., 2012, see Section 4.2.1), APEX CMZ survey (Ginsburg et al., 2016), Nobeyama Radio Observatory surveys (Tanaka et al., 2018), and the ongoing ALMA large programme ALMA CMZ Exploration Survey (ACES; see Section 4.2.2). It is believed that CMZ clouds are denser than MW Disc ones on pc scale, but the comparison of their sub-pc density distributions is not settled. The CMZ gas is also warmer (30–300 K) than the MW Disc gas (10–50 K; Sakamoto et al. 1997). Such

temperatures higher than those of the CMZ dust suggest that the gas and dust are not thermally coupled in the CMZ (Henshaw et al., 2023).

The turbulence level of the CMZ clouds is significantly higher than that of the MW Disc clouds, as revealed by the higher normalisation (i.e. higher linewidth at a given radius) and potentially steeper slope of the size–linewidth relation (e.g. Shetty et al., 2012; Kauffmann et al., 2017). Nonetheless, one weakness of all past works is the limited spectral resolution and resulting confusion between multiple clouds along the same LoS. Strong galactic shear may also substantially contribute to the linewidth of a cloud by creating an apparent bulk velocity gradient, especially at limited spatial and spectral resolution, thus lowering the true contribution of turbulence to the linewidth (Federrath et al., 2016). Other mechanisms such as gravitational collapse, colliding flows, cloud-cloud collisions, supernova interactions, etc., can also contribute to the linewidths (Henshaw et al., 2023).

To advance our understanding of the relative importance of these mechanisms, observations with better spatial and spectral resolutions and a larger dynamic range are critical. ACES is specifically designed for this purpose. It has a spatial resolution of 0.1 pc, a spectral resolution of 0.2 km s^{-1}, continuous coverage of all scales from one beam to 200-pc (in Galactic Longitude), and a velocity range of -130 to 140 km s^{-1} (see Section 4.2.2). It will not only lead to important improvements in the size-linewidth relation and other properties of molecular clouds, but it will also yield unprecedented insights into the following big questions in CMZ studies: which physical mechanism(s) drive mass flows; how is the gas structured in 3D; and what determines the spatial distribution, efficiency, and chemistry of star formation.

1.4 Thesis outline

This thesis aims to study the physical mechanisms that drive the distribution, morphology, kinematics, and dynamics of molecular gas (clouds). Along this line, further implications of such properties are also discussed, such as to use molecular gas as a dynamical tracer to measure supermassive blackhole masses, to explain star formation activities, etc. After the introduction on galaxies and cold molecular gas (clouds) in the current chapter, Chapter 2 studies the large-scale molecular gas distribution and kinematics of three Sy-2 galaxies at

a physical resolution of ≈ 100 pc, extending the knowledge of Section 1.3.1. Chapter 3 investigates the resolved cloud properties (at 14 pc resolution) of the early-type (lenticular) galaxy NGC 1387 along the lines discussed in Section 1.3.2. Chapter 4 probes the molecular cloud/clump properties of the MW CMZ at 0.7 pc resolution in the context of Section 1.3.3. Each of Chapters 2–4 probes a different sample of galaxies at a different physical scale. With them combined, this thesis intends to extend the knowledge on molecular gas properties in nearby galaxies in a representative way. Lastly, I summarise the findings and outline a few directions for future work in Chapter 5.

2

Molecular gas distributions and kinematics of three megamaser galaxies

Contents

2.1 Introduction

The co-evolution of galaxies and supermassive black holes (SMBHs) underpins our understanding of galaxy evolution, but different methods to measure SMBH masses have

only infrequently been cross-checked. We attempt to identify targets to cross-check two of the most accurate methods, megamaser and cold molecular gas dynamics. Three promising galaxies are selected from all those with existing megamaser SMBH mass measurements. We present Atacama Large Millimeter/sub-millimeter Array (ALMA) ^{12}CO(2-1) and 230-GHz continuum observations with angular resolutions of $\approx 0\farcs5$. Every galaxy has an extended rotating molecular gas disc and 230-GHz continuum source(s), but all also have irregularities and/or non-axisymmetric features: NGC 1194 is highly inclined and has disturbed and lopsided central ^{12}CO(2-1) emission; NGC 3393 has a nuclear disc with fairly regular but patchy ^{12}CO(2-1) emission with little gas near the kinematic major axis, faint emission in the very centre and two brighter structures reminiscent of a nuclear ring and/or spiral; NGC 5765B has a strong bar and very bright ^{12}CO(2-1) emission concentrated along two bisymmetric offset dust lanes and two bisymmetric nuclear spiral arms. ^{12}CO(2-1) and ^{12}CO(3-2) observations with the James Clerk Maxwell Telescope are compared with the ALMA observations. Because of the disturbed gas kinematics and the impractically long integration times required for higher angular resolution observations, none of the three galaxies is suitable for a future SMBH mass measurement. Nonetheless, increasing the number of molecular gas observations of megamaser galaxies is valuable, and the ubiquitous disturbances suggest a link between large-scale gas properties and the existence of megamasers.

This chapter is arranged as follows. In Section 2.2, the significance and past research of SMBH mass measurements are reviewed. In Section 2.3, we present a compilation of existing maser SMBH mass measurements and the three targets selected here for further study. In Section 2.4, we describe new intermediate-resolution ALMA as well as James Clerk Maxwell Telescope (JCMT) observations of the molecular gas and mm-continuum emission of those three galaxies, along with standard data products. The potential for SMBH mass measurements using CO observations at higher angular resolutions is discussed in Section 2.5. We discuss the link between molecular gas disc properties and maser emission with an enlarged sample in Section 2.6. Finally, we summarise and conclude in Section 2.7.

2.2 Molecular gas as a dynamic tracer for SMBH mass

Over the past few decades, tight empirical scaling relations have suggested that supermassive black holes (SMBHs) in galaxy centres co-evolve with their host galaxies across cosmic time (see e.g. Kormendy & Ho 2013 and D'Onofrio et al. 2021 for reviews). The tightest correlation is between SMBH mass and stellar velocity dispersion ($M_{\rm BH}$ – $\sigma_\star$ relation; e.g. Gebhardt et al. 2000; Ferrarese & Merritt 2000; Beifiori et al. 2012; van den Bosch 2016). Numerous studies have probed potential SMBH and host galaxy self-regulating growth mechanisms through feedback from active galactic nuclei (AGN; see e.g. Alexander & Hickox 2012 for a review). Understanding SMBH properties (mass, growth history, feedback, etc.) is thus critical to our understanding of galaxy evolution.

These scaling relations are however built from no more than $\approx$ 160 SMBHs with reliable direct (i.e. dynamical) mass measurements. Moreover, these come from a variety of measurement methods such as stellar dynamics, ionised-gas dynamics, megamaser (hereafter 'maser' for short) dynamics and more recently cold molecular gas dynamics, each with different limitations and potential biases. First and for most measurements of $M_{\rm BH}$ in ETGs, stellar dynamical modelling has been used, which suffers from unresolved numeric issues (see e.g. Cretton & Emsellem, 2004). Second, the dynamical modelling of ionised gas applies to a wider range of galaxies, but the ionised gas is often affected by non-gravitational forces (e.g. Ho et al., 2002; Verdoes Kleijn et al., 2000; Cappellari et al., 2002b). Thus, modelling is complicated by the unknown nature of the large observed line width. Third, masers suitable for such dynamical measurements are very rare ($\approx$ 1% of objects searched) and so far have only been detected in Seyfert 2 galaxies (e.g. Kuo et al., 2011b). On the other hand, the recently developed molecular gas dynamics method is generally applicable to both active and non-active galaxies. This method is conceptually simple and has yielded very small uncertainties (e.g. Barth et al., 2016a; Boizelle et al., 2021a; Onishi et al., 2015b; Ruffa et al., 2023a).

Therefore, increasing reliably measured SMBHs, and most importantly the number of measuring methods, is of great importance. Since most methods are only applicable to certain galaxy types, only a few of the measurements have been cross-checked (see Walsh

et al. 2013 for an earlier summary). These include: (i) 'stars vs. ionised gas' in IC 1459 (Cappellari et al., 2002a), NGC 3379 (Shapiro et al., 2006), Centaurus A (Neumayer et al., 2007; Cappellari et al., 2009), NGC 3998 (Walsh et al., 2012), NGC 4335 (Verdoes Kleijn et al., 2002) and M81 (Devereux et al., 2003); (ii) 'stars vs. ionised gas vs. direct imaging' in M87 (Gebhardt & Thomas, 2009; Gebhardt et al., 2011; Walsh et al., 2013; Jeter et al., 2019; Event Horizon Telescope Collaboration et al., 2019; Jeter & Broderick, 2021; Broderick et al., 2022; Liepold et al., 2023; Simon et al., 2024); (iii) 'stars vs. ionised gas vs. reverberation mapping' in NGC 3227 and NGC 4151 (Davies et al., 2006; Onken et al., 2007; Hicks & Malkan, 2008); (iv) 'stars vs. masers' in NGC 4258 (Siopis et al., 2009; Drehmer et al., 2015); (v) 'ionised gas vs. masers' in NGC 4258 (Pastorini et al., 2007); and (vi) 'stars vs. proper motions' in the Milky Way (Sagittarius A*; Feldmeier-Krause et al. 2017). Many of these cross-checking attempts were however affected by disturbed ionised-gas kinematics and/or other issues, and thus were not particularly decisive.

Across these methods, maser dynamics is generally regarded as providing the most accurate and precise SMBH mass measurements, as it measures with high accuracy the gas kinematics close to the SMBHs, yielding a typical mass uncertainty of $\lesssim 10\%$ dominated by the galaxy distance (e.g. Herrnstein et al., 2005). This method spatially resolves the Keplerian rotation of the parsec-scale discs in which the masers are located, within the spheres of influence (SoIs) of the SMBHs. The origin of maser emission is the stimulated emission from certain molecules such as water (H_2O) and hydroxyl (OH). They occur in high–gas density (10^7 cm^{-3} $\lesssim n(H_2) \lesssim 10^{11}$ cm^{-3}; the upper limit is set by the threshold for collisional de-excitation to dominate) and radiation-intense regions, necessary for population inversion to happen. Detectable maser sources also require a sufficiently long path length (with velocity coherence) for the amplification to be high enough. The intense radiation source for megamasers are usually AGNs or starbursts. See more details on (mega)masers in the review by Lo (2005).

Given the rigorous conditions for masers, maser galaxies are rare, requiring edge-on masing discs and a particular type of nuclear activity mostly present in late-type disc galaxies (i.e. a Seyfert 2 AGN), with a narrow range of SMBH masses ($\sim 10^7$ M$_\odot$). Nonetheless, maser measurements offer valuable benchmarks for cross-checks (and

potentially cross-calibration) with other methods, as stressed in many works (e.g. van den Bosch et al., 2016). However, maser SMBH mass measurements seem to systematically lie below (i.e. at smaller SMBH masses than) the $M_{\rm BH} - \sigma_\star$ relation, even when controlling for morphological type (e.g. Greene et al., 2016), and therefore may not follow the general trend defined by all other measurements. This may reveal intrinsic scatter in the $M_{\rm BH} - \sigma_\star$ relation, but it may also arise from systematic effects across the different methods. Cross-checks of individual SMBH measurements are thus imperative.

Due to the high angular resolutions afforded by current mm/sub-mm interferometers, cold molecular gas (particularly CO) dynamics have recently been used to weigh SMBHs. Following the first measurement in NGC 4526 (Davis et al., 2013b), new measurements mostly using the exquisite sensitivity and angular resolution of the Atacama Large Millmeter/sub-millimeter Array (ALMA) have been made by the millimetre-Wave Interferometric Survey of Dark Object Masses (WISDOM; Davis et al. 2017, 2018, 2020; Onishi et al. 2017; Smith et al. 2019, 2021; North et al. 2019; Lelli et al. 2022; Ruffa et al. 2023b) and others (e.g. Onishi et al., 2015a; Barth et al., 2016b; Boizelle et al., 2019, 2021b; Nagai et al., 2019; Ruffa et al., 2019b; Nguyen et al., 2020, 2021, 2022; Cohn et al., 2021; Kabasares et al., 2022). Many of these observations probe CO emission on the same spatial scales as those probed by masers, and the latest in fact does better (Zhang et al., 2024). This method has only weak biases toward particular galaxy types and is conceptually very simple, mainly constrained by the size of each SMBH SoI and the existence of a central regularly rotating molecular gas disc. Given its increasing popularity, cross-checking CO and maser (as well as other methods) SMBH dynamical measurements is highly desirable.

This chapter thus aims to identify promising targets for future CO SMBH mass measurements (utilising higher resolution follow-up observations), from galaxies with existing maser measurements. Simultaneously, this chapter reveals the molecular gas properties of several maser host galaxies at $\sim$ 100 pc scale, essential to probe the cold interstellar medium (ISM) conditions required for masing.

2.3 Targets

2.3.1 Candidate selection

To cross-check cold molecular gas and maser dynamical SMBH mass measurements, we must first identify galaxies with existing maser measurements that also appear promising for molecular gas measurements. We use the compilation of SMBH mass measurements of van den Bosch (2016) as our starting point, including all maser measurements in their Tables 2 and 3. We update the galaxy distances when better determinations are now available, including those from maser monitoring programmes (NGC 6264, NGC 6323, NGC 5765B and UGC 3789), part of the Megamaser Cosmology Project (MCP; see Braatz et al. 2009 and Table 2.1), and adjust the SMBH masses accordingly ($M_{\rm BH} \propto D$ for all dynamical mass measurements, where D is the galaxy distance). We remove NGC 1386, as there is no refereed source for its SMBH mass and its ^{12}CO(1-0)[1] has already been imaged with ALMA by Ramakrishnan et al. (2019) and Zabel et al. (2019). We also correct the SMBH mass of IC 2560 quoted in van den Bosch (2016; $\log(M_{\rm BH}/{\rm M}_\odot) = 7.64 \pm 0.05$) back to the original mass reported by Yamauchi et al. (2012; $\log(M_{\rm BH}/{\rm M}_\odot) = 6.54 \pm 0.06$). This megamaser parent sample is summarised in Table 2.1.

[1]Hereafter we omit the carbon atomic mass number and refer to the ^{12}CO isotope simply as CO.

Table 2.1: Predicted SMBH SoIs and selection criteria of maser galaxies.

Galaxy	Distance (Mpc)	$\log(M_{\rm BH}/{\rm M}_\odot)$	$\sigma_\star$ (km s^{-1})	$R_{\rm SoI}$ (pc)	$\theta_{\rm SoI}$ (mas)	SoI	Dust	Dec.	References
(1)	(2)	(3)	(4)	(5)	(6)	(7)	(8)	(9)	(10)
Circinus	2.8 ± 0.5	6.06 ± 0.07	158 ± 18	0.20 ± 0.06	15 ± 5	✓	✓	✓	(1)
ESO 558-009	108 ± 6	7.23 ± 0.03	170 ± 20	2.5 ± 0.6	4.9 ± 1.2	-	✓	✓	(2)
IC 1481	79 ± 6	7.11 ± 0.13	95 ± 27	6.1 ± 3.9	16 ± 10	✓	-	✓	(3)
IC 2560	31 ± 13	6.54 ± 0.06	141 ± 10	0.90 ± 0.18	6.0 ± 2.8	-	-	✓	(4)
J0437+2456	65 ± 4	6.46 ± 0.05	110 ± 13	1.03 ± 0.27	3.3 ± 0.9	-	-	-	(2)
Mrk1029	121 ± 7	6.28 ± 0.12	132 ± 15	0.47 ± 0.17	0.8 ± 0.3	-	-	✓	(2)
NGC 1068	16 ± 9	6.95 ± 0.02	151 ± 7	1.67 ± 0.17	22 ± 13	✓	-	✓	(5)
NGC 1194	58 ± 6	7.85 ± 0.02	148 ± 24	14 ± 5	50 ± 17	✓	✓	✓	(6)
NGC 1320	34.2 ± 1.9	6.74 ± 0.21	141 ± 16	1.2 ± 0.7	7 ± 4	-	-	✓	(2)
NGC 2273	29.5 ± 1.9	6.93 ± 0.02	145 ± 17	1.8 ± 0.4	12.3 ± 3.0	✓	✓	-	(6)
NGC 2960	67 ± 7	7.03 ± 0.02	151 ± 7	2.01 ± 0.21	6.2 ± 0.9	-	✓	✓	(6)
NGC 3079	15.9 ± 1.2	6.36 ± 0.09	145 ± 7	0.47 ± 0.11	6.1 ± 1.5	-	✓	-	(7)
NGC 3393	49 ± 8	7.3 ± 0.4	148 ± 10	3.6 ± 2.5	15 ± 11	✓	✓	✓	(3), (8)
NGC 4258	7.3 ± 0.5	7.58 ± 0.03	115 ± 11	12.4 ± 2.4	351 ± 73	✓	-	-	(9), (10)
NGC 4388	16.5 ± 1.6	6.86 ± 0.01	107 ± 7	2.7 ± 0.4	34 ± 6	✓	-	✓	(6)
NGC 4945	3.58 ± 0.22	6.13 ± 0.18	135 ± 6	0.32 ± 0.14	18 ± 8	✓	-	✓	(10), (11)
NGC 5495	96 ± 5	7.04 ± 0.08	166 ± 19	1.7 ± 0.5	3.7 ± 1.1	-	-	✓	(2)
NGC 5765B	112 ± 5	7.61 ± 0.04	158 ± 18	7.0 ± 1.7	13 ± 3	✓	✓	✓	(12)
NGC 6264	144 ± 19	7.49 ± 0.06	158 ± 15	5.3 ± 1.2	7.6 ± 2.0	-	✓	-	(13)
NGC 6323	107 ± 36	6.97 ± 0.14	158 ± 26	1.6 ± 0.7	3.1 ± 1.7	-	-	-	(14)
UGC 3789	50 ± 5	7.06 ± 0.05	107 ± 12	4.3 ± 1.1	18 ± 5	✓	-	-	(15)
UGC 6093	152 ± 15	7.41 ± 0.03	155 ± 18	4.6 ± 1.1	6.3 ± 1.6	-	-	✓	(16)

Notes: Column 1: galaxy name. Column 2: distance. Column 3: maser-derived SMBH mass. Column 4: stellar velocity dispersion measured within one effective radius, using a variety of methods (van den Bosch, 2016). Columns 5 and 6: SMBH SoI physical radius and angular radius. Columns 7 – 9: selection criterion fulfillment. Column 10: maser SMBH mass measurement references: (1) Greenhill et al. 2003, (2) Gao et al. 2017, (3) Huré et al. 2011, (4) Yamauchi et al. 2012, (5) Lodato & Bertin 2003, (6) Kuo et al. 2011a, (7) Yamauchi et al. 2004, (8) Kondratko et al. 2008, (9) Herrnstein et al. 2005, (10) Kormendy & Ho 2013, (11) Greenhill et al. 1997, (12) Gao et al. 2016, (13) Kuo et al. 2013, (14) Kuo et al. 2015, (15) Reid et al. 2013 and (16) Zhao et al. 2018. We note that the maser emission in some galaxies may be dominated or contaminated by non-disc maser sources, such as masers in outflows/jets; see Pesce et al. (2015) for a clean subset with pure disc-maser galaxies and Keplerian rotation.

Table 2.2: Properties of our target galaxies.

Galaxy	Right ascension (J2000)	Declination (J2000)	$z^{1}_{\rm helio}$	Hubble type	Nuclear activity
NGC 1194	$03^{\rm h}03^{\rm m}49\overset{\rm s}{.}10870^{2}$	$-01°06'13\overset{''}{.}4720^{2}$	0.01363	S0-[3]	Sy2[4]
NGC 3393	$10^{\rm h}48^{\rm m}23\overset{\rm s}{.}4659^{5}$	$-25°09'43\overset{''}{.}477^{5}$	0.01251	SBa[6]	Sy2[4,7]
NGC 5765B	$14^{\rm h}50^{\rm m}51\overset{\rm s}{.}51884^{8}$	$+05°06'52\overset{''}{.}2501^{8}$	0.02754	Sab[9]	Sy2[10]

Notes: (1) Heliocentric redshifts are taken from Albareti et al. (2017) for NGC 1194 and NGC 5765B and from Pesce et al. (2015) for NGC 3393. (2) Average position of the masers at the systemic velocity of the galaxy (see Tables 1 and 3 of Kuo et al. 2011a). (3) Nair & Abraham (2010). (4) Oh et al. (2018). (5) Average position of the masers at the systemic velocity of the galaxy (see Section 4 of Kondratko et al. 2008). (6) de Vaucouleurs et al. (1991). (7) Baumgartner et al. (2013). (8) Best-fitting dynamical centre (see Table 7 of Gao et al. 2016). (9) Pjanka et al. (2017). (10) Toba et al. (2014).

We then apply the following selection criteria to retain the best cold molecular gas measurement candidates. Whether each galaxy fulfils each criterion is listed in Table 2.1.

1. SMBH SoI angular radius $\theta_{\rm SoI} \equiv R_{\rm SoI}/D > 0\overset{''}{.}01$, where the SMBH SoI physical radius $R_{\rm SoI} \equiv GM_{\rm BH}/\sigma^{2}_{\star}$, so that the SoI can be spatially resolved using ALMA's longest baselines at CO(2-1) (band 6).

2. *Hubble Space Telescope* (*HST*) imaging (available for all galaxies) showing a regular central dust disc, suggesting a central molecular gas disc in ordered rotation.

3. Declination $-66° < \delta < +20°$, to ensure a fairly round ALMA synthesised beam and minimise shadowing.[2]

The only galaxies to satisfy all these requirements are Circinus, NGC 1194, NGC 3393 and NGC 5765B. Cold molecular gas in Circinus has already been observed with ALMA at high angular resolution ($\approx 0\overset{''}{.}2$) and it is reported to have a disturbed velocity field (Izumi et al., 2018; Tristram et al., 2022). This galaxy is therefore not suited to cold gas dynamical modelling to derive an SMBH mass, and it is not considered further in this chapter. The basic properties of the other three galaxies, for which we obtained and present new ALMA data here, are listed in Table 2.2. We also discuss each galaxy in more detail below.

[2]We note that even if we relax this criterion to $-90° \leq \delta \leq +47°$, to reach the absolute declination limit of ALMA, the final sample of galaxies meeting all of our selection criteria does not change.

2.3.2 NGC 1194

NGC 1194 is a lenticular galaxy harbouring a Seyfert 2 AGN (Oh et al., 2018), for which we adopt a distance $D = 58 \pm 6$ Mpc. This distance was estimated from NGC 1194's Local Group-centric redshift (Karachentsev & Makarov, 1996) by Kormendy & Ho (2013) and Saglia et al. (2016) assuming a cosmology derived from the *Wilkinson Microwave Anisotropy Probe* (*WMAP*) 5-year data (Komatsu et al., 2009). NGC 1194 was first reported to harbour H_2O megamasers by Greenhill et al. (2008) and is part of the MCP. It has a relatively large maser disc with an inner radius of 0.51 pc and an outer radius of 1.33 pc. It hosts the most massive SMBH derived using the maser method to date, $M_{BH} = (7.1 \pm 0.3) \times 10^7$ $M_\odot$ at our adopted distance above (Kuo et al., 2011a). The maser disc has an inclination $i \approx 85°$ with a kinematic position angle[3] $PA_{kin} = 337°$, while the galaxy's overall inclination is $\approx 50°$ with a morphological position angle $PA_{mor} = 145°$, as determined from an r-band image from the Sloan Digital Sky Survey (SDSS; Adelman-McCarthy et al. 2008). No warp is detected in the maser disc.

Previous studies have reported atomic hydrogen out to a galactocentric radius of $\approx 120''$ (≈ 4 kpc; Sun et al., 2013) and patchy warm molecular hydrogen on a scale of $1''.6$ (450 pc), limited by the telescope field of view (FoV; Greene et al. 2014). Ionised gas has been detected through K-band emission lines (e.g. Brγ, [Si VI] and [Ca VIII]) at the galaxy centre by Greene et al. (2014) and through the [O III] optical emission line over a slightly more extended region (700×470 pc^2; Schmitt et al. 2003). Koss et al. (2021) did not detect cold molecular gas using the Atacama Pathfinder Experiment, with a CO(2-1) 3σ upper limit of 2×10^7 K km s^{-1} pc^2 (9 Jy km s^{-1}), consistent with (i.e. larger than) our detected flux reported in Section 2.4.3.

2.3.3 NGC 3393

NGC 3393 is an SBa galaxy (de Vaucouleurs et al., 1991) at an adopted distance $D = 49 \pm 8$ Mpc. This distance was again estimated from the Local Group-centric redshift (Karachentsev & Makarov, 1996) by Kormendy & Ho (2013) and Saglia et al.

[3]The kinematic (morphological) position angle is measured from north through east until the largest receding velocity (photometric major axis) is reached.

(2016) assuming the cosmology derived from *WMAP* 5-year data (Komatsu et al., 2009). NGC 3393 has a large-scale stellar bar ($PA_{\rm mor} \approx 160°$), extended radio jets (e.g. Cooke et al., 2000) and a Seyfert 2 nucleus (Baumgartner et al., 2013). A nuclear bar ($PA_{\rm mor} \approx 145°$) has also been posited (e.g. Läsker et al., 2016). The presence of two compact X-ray sources separated by $\approx$ 130 pc suggests there are two SMBHs in the nuclear region (Fabbiano et al., 2011), but these may be due to noise (Koss et al., 2015) and subsequent radio, near-infrared, optical, UV and hard X-ray observations are all consistent with a single point source (Imanishi & Saito, 2014; Koss et al., 2015).

H_2O megamasers were discovered using the National Aeronautics and Space Administration (NASA) Deep Space Network (Kondratko et al., 2006), and mapped with very long baseline interferometry (VLBI) to infer a central SMBH mass $M_{\rm BH} = (3.0 \pm 0.2) \times 10^7$ $M_\odot$ at our adopted distance above (Kondratko et al., 2008). With the same dataset, Huré et al. (2011) inferred a different SMBH mass of $M_{\rm BH} = 0.58 \times 10^7$ $M_\odot$ (at our adopted distance above) using different dynamical modelling. We therefore adopt the mean of these two measurements for the NGC 3393 SMBH mass, and half the difference as the uncertainty, as done by Kormendy & Ho (2013). The maser disc is large, with an outer radius of 1.5 pc, and was assumed to be edge-on with a tentative warp and $PA_{\rm kin} \approx 326°$, perpendicular to both the kiloparsec-scale radio jet and the axis of the narrow-line region (see Kondratko et al. 2008 and references therein). The overall inclination of the galaxy is $i = 44°$ with $PA_{\rm mor} \approx 160°$, as determined from a Two Micron All Sky Survey (2MASS) $K_{\rm s}$-band image (Skrutskie et al., 2006).

CO(2-1) emission was recently mapped with ALMA by Finlez et al. (2018). They presented two sets of maps with different imaging parameters, one with a $0\farcs56$ synthesised beam[4] and 2.5 km s^{-1} channels, the other with a $0\farcs68$ synthesised beam and 10 km s^{-1} channels. Very little CO(2-1) emission is detected in the very centre, which they attribute to either molecular gas destruction by the jet or high molecular gas densities/temperatures not detected in the $J = 2 - 1$ CO transition (see e.g. Mukherjee et al., 2018a,b; Ruffa et al., 2022). Our new observations slightly improve the angular resolution and sensitivity of these observations (see Table 2.3). Finlez et al. (2018) also provided a sophisticated

[4]Beam sizes quoted in this thesis are all full-widths at half-maxima, FWHM.

analysis of the ionised-gas kinematics, exploiting abundant optical emission lines. In addition to a regularly rotating component, there is a jet-driven outflow along the jet axis and an equatorial outflow perpendicular to it. Reynolds et al. (2022) reported an extended H I disc with a diameter of 226″ (54 kpc) and a total mass of 6.4×10^9 $M_\odot$ (scaled to our adopted distance above).

Table 2.3: Properties of our ALMA CO(2-1) and 230-GHz continuum observations. NGC 3393 includes the properties of Finlez et al.'s (2018) observations for reference.

Galaxy	Property	Value
NGC 1194:	Baseline range (m)	19 – 1808
	Maximum recoverable scale (arcsec)	2.7
	On-source time (min.)	19.75
	Pixel scale (arcsec pix^{-1})	0.05
	CO channel width (km s^{-1})	10
	CO synthesised beam (arcsec)	0.30×0.23
	CO synthesised beam (pc)	84×65
	CO RMS noise (mJy beam^{-1} chan^{-1})	0.41
	CO integrated flux[1] (Jy km s^{-1})	6.1 ± 0.1
	Integrated molecular gas mass[2] ($M_\odot$)	$(5.3 \pm 0.1) \times 10^7$
	Cont. rest-frame frequency (GHz)	232.1
	Cont. synthesised beam (arcsec)	0.31×0.22
	Cont. synthesised beam (pc)	87×62
	Cont. RMS noise (mJy beam^{-1})	0.020
NGC 3393:[3]	Baseline range (m)	15 – 1100
	Maximum recoverable scale (arcsec)	5.1
	On-source time of (min.)	49.07
	Pixel scale (arcsec pix^{-1})	0.1
	CO channel width (km s^{-1})	10
	CO synthesised beam (arcsec)	0.56×0.45
	CO synthesised beam (pc)	136×107
	CO RMS noise (mJy beam^{-1} chan^{-1})	0.37
	CO integrated flux[1] (Jy km s^{-1})	81.8 ± 0.4
	Integrated molecular gas mass[2] ($M_\odot$)	$(5.14 \pm 0.02) \times 10^8$
	Cont. rest-frame frequency (GHz)	238.7
	Cont. synthesised beam (arcsec)	0.58×0.47
	Cont. synthesised beam (pc)	138×112
	Cont. RMS noise (mJy beam^{-1})	0.017
NGC 3393:[4]	Baseline range (m)	15 – 629
	Maximum recoverable scale (arcsec)	5.3
	On-source time (min.)	28.33
	CO channel width (km s^{-1})	10

Continued on the next page

Galaxy	Property	Value
	CO synthesised beam (arcsec)	0.73×0.62
	CO synthesised beam (pc)	174×148
	CO RMS noise (mJy beam^{-1} chan^{-1})	0.45
	Cont. rest-frame frequency (GHz)	239.6
	Cont. synthesised beam (arcsec)	0.71×0.61
	Cont. synthesised beam (pc)	169×146
	Cont. RMS noise (mJy beam^{-1})	0.023
NGC 5765B:	Baseline range (m)	15 – 1124
	Maximum recoverable scale (arcsec)	3.5
	On-source time (min.)	22.25
	Pixel scale (arcsec pix^{-1})	0.06
	CO channel width (km s^{-1})	10
	CO synthesised beam (arcsec)	0.47×0.28
	CO synthesised beam (pc)	257×153
	CO RMS noise (mJy beam^{-1} chan^{-1})	0.48
	CO integrated flux[1] (Jy km s^{-1})	216.2 ± 0.4
	Integrated molecular gas mass[2] ($M_\odot$)	$(6.94 \pm 0.01) \times 10^9$
	Cont. rest-frame frequency (GHz)	232.5
	Cont. synthesised beam (arcsec)	0.47×0.28
	Cont. synthesised beam (pc)	257×153
	Cont. RMS noise (mJy beam^{-1})	0.028

[1] The CO integrated fluxes and associated integrated molecular gas masses are measured within the ALMA FoV only, and thus likely do not cover the full molecular gas extent of NGC 1194 and NGC 3393.
[2] A CO(2-1)/CO(1-0) line ratio of unity (in brightness temperature units) and a CO-to-molecule conversion factor of 4.3 $M_\odot$ pc^{-2} (K km s^{-1})$^{-1}$ are assumed to infer the molecular gas masses, that include the contribution of heavy elements.
[3] All the quantities listed in this segment are measured after combining the observations from programmes 2016.1.01553.S and 2015.1.00086.S.
[4] All the quantities listed in this segment are taken from Finlez et al. (2018).

2.3.4 NGC 5765B

NGC 5765B is an Sab galaxy (Pjanka et al., 2017) with a Seyfert 2 nucleus (Toba et al., 2014). It has a close companion, NGC 5765A, at an angular separation of 22.″5 ($\approx$ 12 kpc at our adopted distance below), beyond the FoV of our ALMA and JCMT observations. *HST* imaging reveals a bar, two rings (at radii of 1.″5 and 3.″5) and spiral features between these rings. Beyond the outer ring the galaxy is perturbed by interaction with its companion (Pjanka et al., 2017).

Central H_2O megamasers were detected with the Green Bank Telescope as part of the MCP and were monitored for over two years, yielding an angular diameter distance $D = 112 \pm 5$ Mpc (adopted here; Pesce et al. 2020) and a SMBH mass $M_{BH} = (4.0 \pm 0.4) \times 10^7$ $M_\odot$ (at this adopted distance; Gao et al. 2016). The maser disc (≈ 1.2 pc in radius) warps over an inclination range of $i = 94.^\circ5$ at the centre to $i = 73.^\circ3$ at the edge and over a kinetic position angle range of $PA_{kin} = 146.^\circ7$ at the centre to $PA_{kin} = 139.^\circ8$ at the edge, as determined through dynamical modelling (Gao et al., 2016). The overall galaxy inclination is $i = 26^\circ$ with $PA_{mor} = 10^\circ$, as determined from a 2MASS K_s-band image (Skrutskie et al., 2006).

Shirazi & Brinchmann (2012) studied the ionised gas of NGC5765B using an optical spectrum from SDSS. They reported strong nebular He II emission lines dominated by the AGN (i.e. without Wolf–Rayet features), along with other emission lines. The Arecibo Legacy Fast Arecibo L-band Feed Array survey (Haynes et al., 2018) derived a neutral hydrogen content of $(6.3 \pm 0.7) \times 10^9$ $M_\odot$ (at our adopted distance above). Davis et al. (2022) presented an ALMA CO(2-1) map and reported a total mass of $(1.2 \pm 0.1) \times 10^{10}$ $M_\odot$ (at our adopted distance above).

2.4 Observations

2.4.1 ALMA observations

Observations of the CO(2-1) line of our three target galaxies were carried out with ALMA as part of programme 2016.1.01553.S (PI: Bureau) on 24 October 2016 and 2, 3 and 15 May 2017. For NGC 3393, we combine another track from the ALMA programme 2015.1.00086.S (PI: Nagar) obtained on 3 May 2016.

For all our observations, the ALMA correlator was configured with one spectral window centred on the redshifted frequency of the CO(2-1) line (rest frequency ν_{rest} = 230.538 GHz.), with a bandwidth of 1.875 GHz (2438 km s^{-1} at $z = 0$) and 488-kHz channels (0.63 km s^{-1} at $z = 0$). The remaining three spectral windows were used to observe the continuum, if any, each with a bandwidth of 2 GHz and 15.625-MHz channels. The additional track for NGC 3393 also had one spectral window centred on

CO(2-1), with an additional spectral line window centred on CS(5-4) and two continuum spectral windows. Details of this track can be found in Finlez et al. (2018). The FoV of the ALMA 12-m array, i.e. the FWHM of the ALMA 12-m antennae primary beam, is $\approx 25''$ ($\approx$ 7.0, 6.0 and 15 kpc for NGC 1194, NGC 3393 and NGC 5765B, respectively) at the observed frequencies of CO(2-1). This FoV only extends to 1.1 R_e in NGC 1194 (H-band combined with K-band; Läsker et al. 2016), 1.3 R_e in NGC 3393 (H-band combined with I-band; Läsker et al. 2016) and 1.8 R_e in NGC 5765B (K_s-band; Davis et al. 2022), where R_e is the effective (i.e. half-light) radius. The ALMA FoV therefore covers the whole galaxy disc only in NGC 5765B, with more limited coverage in NGC 1194 and NGC 3393 (see Figure 2.1)

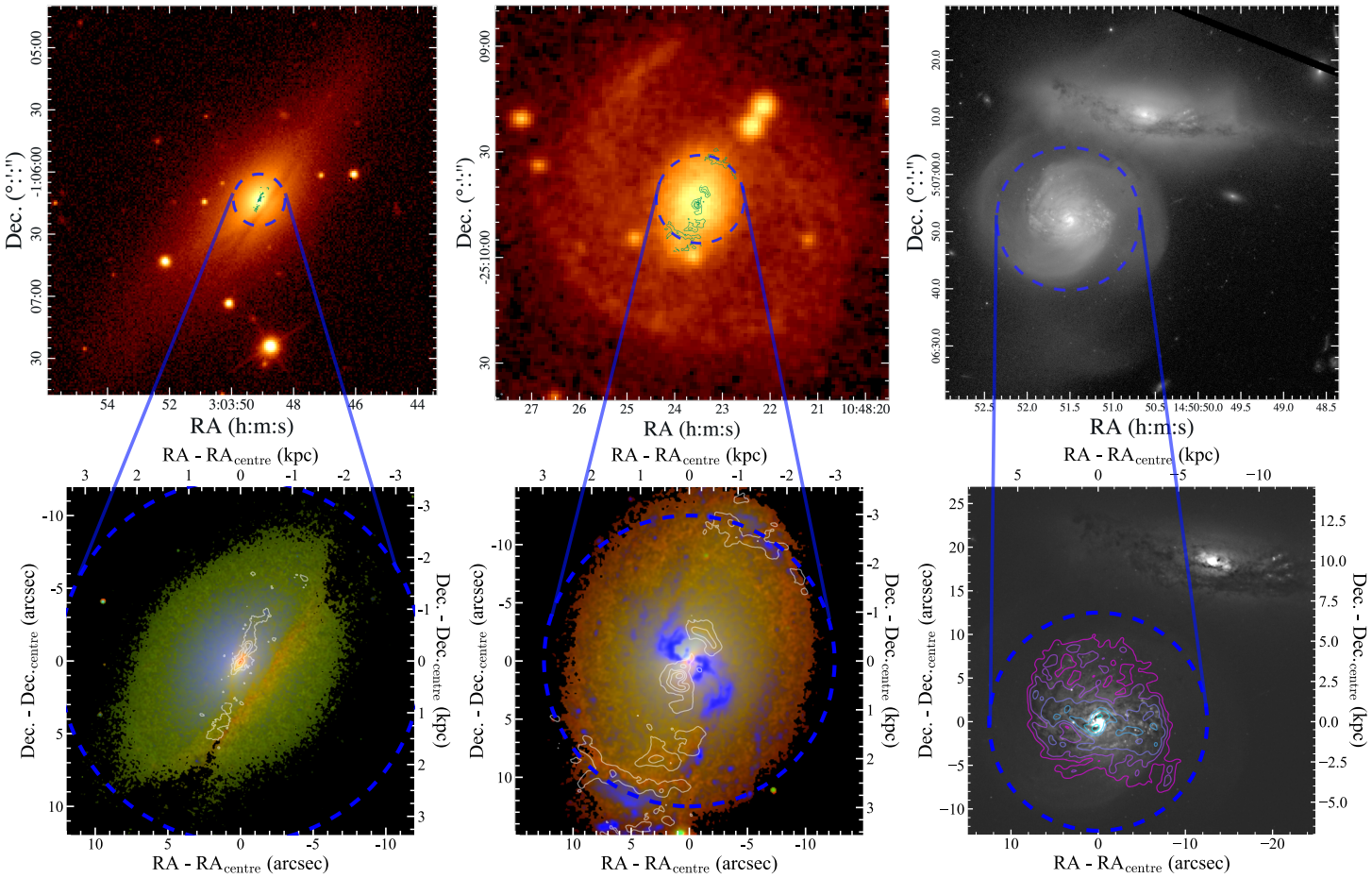

Figure 2.1: Optical images of our three target galaxies. In each panel, the ALMA CO(2-1) emission is overlaid as contours (except the upper-right panel) and the ALMA primary beam is shown as a blue dashed circle. The bottom row panels show zoom-in images. **Left column:** NGC 1194. Upper panel: SDSS *r*-band image of the whole galaxy. Lower panel: *HST* Wide-field Camera 3 (WFC3) F438W (blue), F814W (green) and F160W (red) composite of the central region. **Middle column:** NGC 3393. Upper panel: Digitized Sky Survey-2 red-band image of the whole galaxy. Lower panel: *HST*/WFC3 F336W (blue), F814W (green) and F160W (red) composite of the central region. **Right column:** NGC 5765B (in the bottom-left corner of each panel) and its companion NGC 5765A. Upper panel: *HST*/WFC3 F814W image. Lower panel: unsharp-masked *HST*/WFC3 F814W image.

The baseline ranges of the observations of NGC 1194, NGC 3393 and NGC 5765B were 19 – 1808, 15 – 1100 and 15 – 1124 m, respectively. The corresponding maximum recoverable scales were 2.″7 (0.86 kpc), 5.″1 (1.2 kpc) and 3.″5 (2.1 kpc), respectively. The data were calibrated using the standard ALMA pipeline, either through the European ALMA Regional Centre Calibrated Measurement Set (CalMS) service or by locally running `Common Astronomy Software Applications`[5] (`CASA`; CASA Team et al. 2022). CASA version 4.7 was used to calibrate the three tracks of 2016.1.01553.S and version 4.6 for the track of 2015.1.00086.S. For NGC 3393, the ALMA observations of Finlez et al. (2018) were combined with our higher-angular resolution observations to improve the *uv*-plane coverage and sensitivity (see Table 2.3). For both the line datacubes and the continuum images, the combined data improve the angular resolution (in one dimension) by ≈ 25% compared to Finlez et al. (2018). The following imaging steps all used CASA version 6.4.4.

First, for each galaxy, continuum emission was subtracted from the visibility data using linear fits and the CASA task `uvcontsub`. To produce datacubes with high sensitivity, we binned the channels to 10 km s^{-1} and used Briggs weighting with a robust parameter of 2.0 (close to natural weighting). The datacubes were then cleaned to a depth of 1.5 times the root-mean-square (RMS) noise of the line-free channels using the task `tclean` with the `MultiScale` algorithm (Cornwell, 2008) in the interactive mode and using a manually-defined three-dimensional mask. We note that varying these parameters does not significantly change any result of this chapter. A primary beam correction was then applied to the line datacubes.

Moment maps were generated using a smooth-masking technique (e.g. Dame 2011). A smoothed datacube (without primary-beam correction) was first generated by spatially convolving every channel with a two-dimensional (2D) square uniform kernel of side length equal to the synthesised beam width. As the channels are already binned to a width of 10 km s^{-1}, we did not smooth further spectrally. We then constructed a mask by first selecting all pixels of the smoothed datacube above a given flux density threshold (1.5 RMS) and then excluding pixels outside of the mask manually defined

[5]Available from `https://casa.nrao.edu/`.

during cleaning. Finally, the mask was adjusted channel by channel by (i) filling 'holes' of unselected pixels with areas smaller than two synthesised beams and (ii) removing 'islands' of selected pixels with areas smaller than one synthesised beam (both achieved using the Python package `scikit-image`[6]; van der Walt et al. 2014). This mask was then used to select the pixels of the original unsmoothed primary beam-corrected datacube that are used for the moment analysis.

The zeroth-moment (integrated flux), first-moment (intensity-weighted mean velocity) and second-moment[7] (intensity-weighted velocity dispersion) maps of NGC 1194, NGC 3393 and NGC 5765B are shown in the top rows of Figure 2.2, Figure 2.3 and Figure 2.4, respectively. The same mask was used to create the integrated spectrum (and to calculate the integrated flux) and the kinematic major-axis position-velocity diagram (PVD) of each galaxy, shown in the bottom-left and bottom-centre panels of each figure, respectively. As each channel has a different 2D masked region and spaxels near each other are strongly correlated, we applied the following procedure to estimate the uncertainty of the spatially integrated flux of each channel. For each line channel, we applied its 2D mask to every line-free channel of the datacube, calculated the sum of the flux densities of each of those line-free channels and adopted the RMS (around the mean) of these sums as the uncertainty of the integrated flux of the original line channel. Standard error propagation rules[8] were then used to calculate the uncertainty of the flux integrated over all channels (and in turn of the total molecular gas mass). Each PVD was generated by adopting a 2″-wide mock slit along the kinematic major axis, determined from a fit to the first-moment map using the `pafit` software[9] (Krajnović et al., 2006), except for NGC 3393 for which a rough kinematic major axis position angle was estimated by visual inspection due to the scarcity of gas along it. We used the astrometry from the existing VLBI observations to define the centre of each galaxy (see Table 2.2).

[6]Available from https://scikit-image.org.

[7]The second-moment requires at least two selected pixels along any line of sight, explaining the difference of spatial coverage between the second-moment map and other moment maps.

[8]Given the raw spectral resolution and the binned channel width, we safely assume no covariance between adjacent channels.

[9]Available from https://pypi.org/project/pafit/.

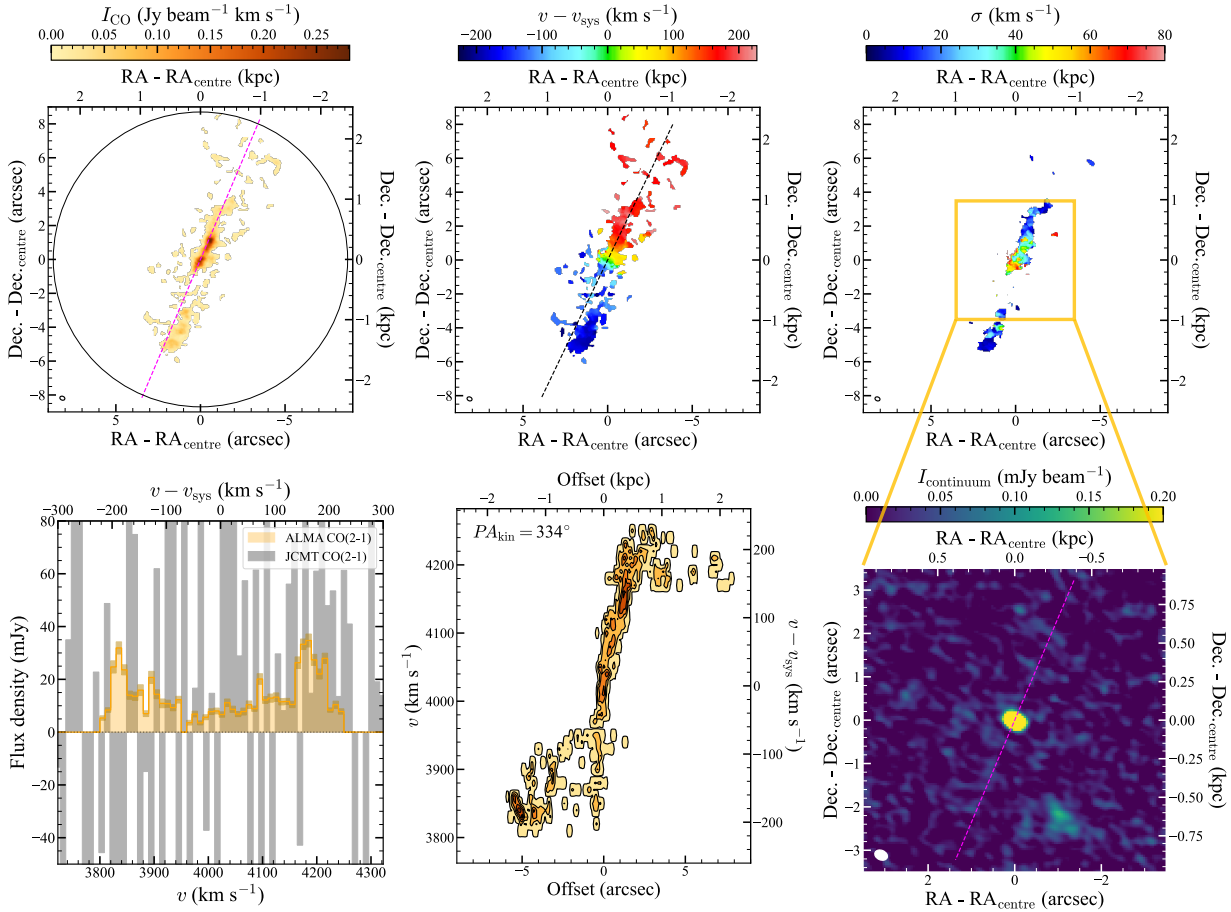

Figure 2.2: Data products of NGC 1194. **Top-left:** CO(2-1) zeroth-moment (integrated flux) map. The overlaid black solid circle shows the JCMT beam (assuming perfect pointing accuracy) at the same frequency. The magenta dashed line indicates the position angle of the maser disc (extrapolated in spatial extent). **Top-centre:** CO(2-1) first-moment (intensity-weighted mean velocity) map. The overlaid black dashed line shows the kinematic major axis. **Top-right:** CO(2-1) second-moment (intensity-weighted velocity dispersion) map. The upper limit of the colour bar slightly truncates the dynamic range of the map to dismiss heavily noisy and beam-smeared sight lines. **Bottom-left:** CO(2-1) integrated spectrum synthesised from the ALMA datacube (orange histogram, with uncertainties indicated as darker shades) and JCMT spectrum (grey histogram). **Bottom-centre:** CO(2-1) PVD along the kinematic major axis, whose position angle is listed in the top-left corner. **Bottom-right:** 230-GHz continuum map. The magenta dashed line again indicates the position angle of the maser disc (extrapolated in spatial extent). The spatial extent shown is smaller than that of the moment maps, as illustrated by the overlaid orange square. The synthesised beam is shown in the bottom-left corner of all the maps.

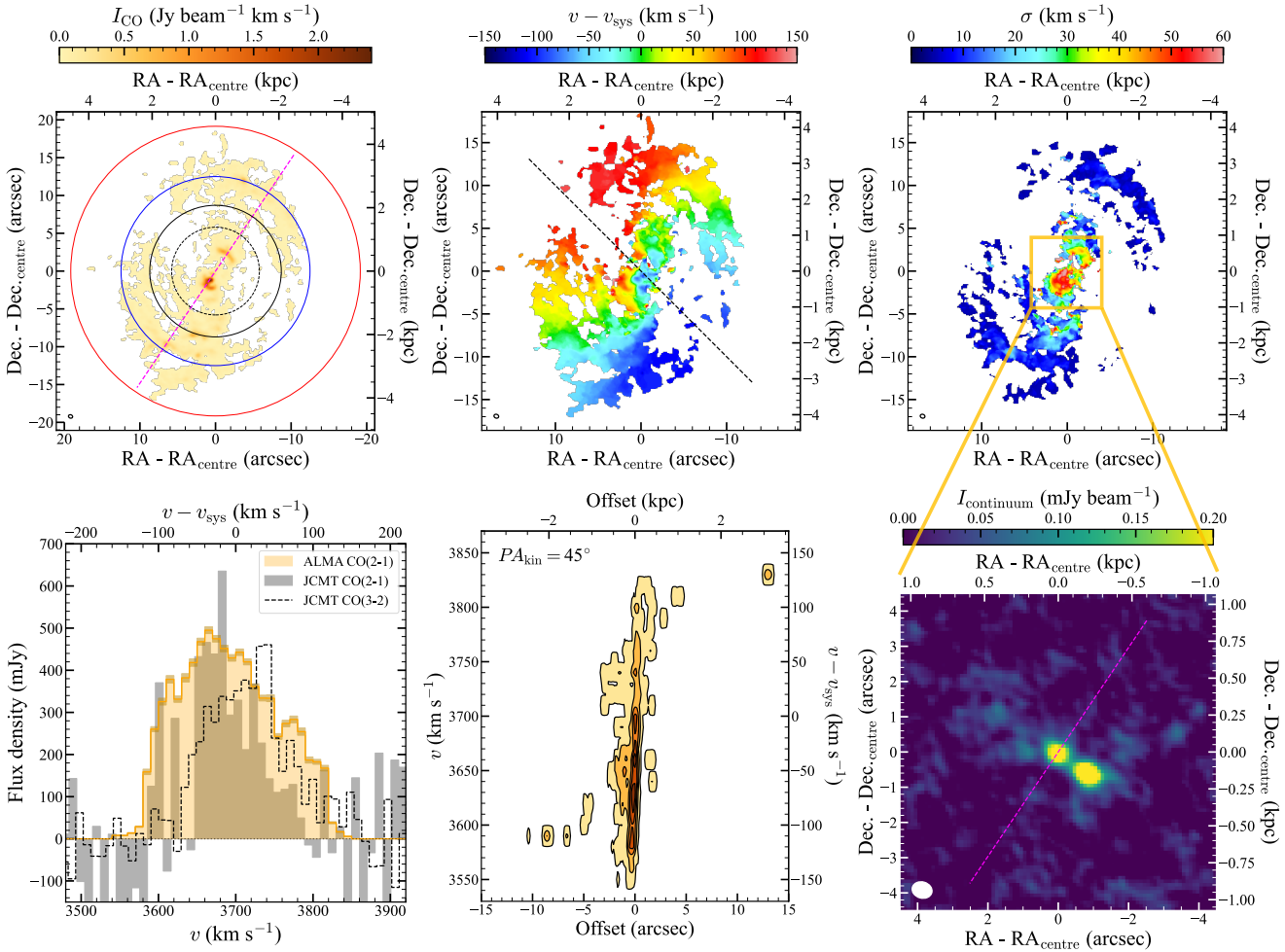

Figure 2.3: As Figure 2.2 but for NGC 3393. The JCMT beam (assuming perfect pointing accuracy) at the CO(3-2) frequency is also shown in the top-left panel as a black dashed circle, and the corresponding spectrum is shown in the bottom-left panel as a black dashed histogram. The ALMA CO(2-1) primary beam full width at 50% (i.e. the usual primary beam definition) and at 20% (the maximal extent of the datacube) of the maximum are also shown in the top-left panel as blue and red solid circles, respectively. Due to the scarcity of gas along the kinematic major axis, the kinematic position angle of 45° was estimated by eye rather than by a fit. The CO(2-1) emission reaches the edge of the ALMA FoV.

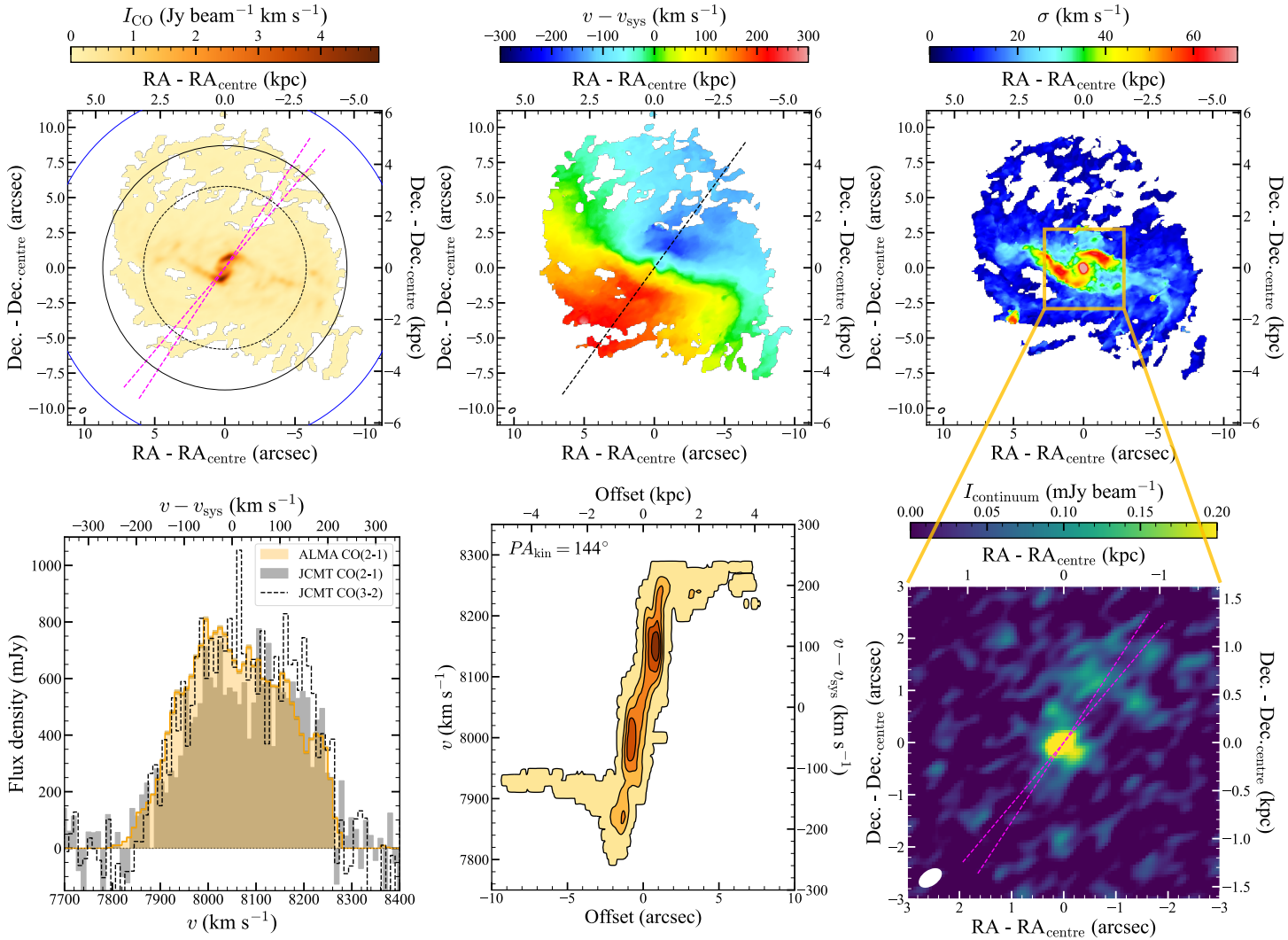

Figure 2.4: As Figure 2.3 but for NGC 5765B (although the red solid circle is not visible and the range of position angles of the maser disc due to its warp is indicated by two magenta dashed lines in the relevant panels).

For each galaxy, a continuum image was also produced from all spectral windows using only line-free channels. With the `tclean` task in the multi-frequency synthesis mode, we again adopted Briggs weighting with a robust parameter of 2.0 and cleaned to a depth of 1.5 times the RMS noise of the dirty image (measured in emission-free regions) in the interactive mode and using a manually-defined 2D mask. The primary beam correction was then applied to the continuum images.

The final angular resolution, sensitivity and other characteristics of each data product are listed in Table 2.3.

2.4.2 JCMT observations

Single-dish CO(2-1) observations of NGC 1194, NGC 3393 and NGC5765B were obtained with the JCMT on 18 – 23 October 2016, as part of Programme M16BP068 (PI: Gao), aiming to estimate the prevalence and abundance of molecular gas in the 15 disc galaxies known to harbour megamasers at the time and another 15 galaxies used as a control sample (Gao et al. in prep.). Follow-up CO(3-2) observations of NGC 3393 and NGC 5765B were carried out on 6 July 2017, 5 December 2017, 22 January 2018, 29 January 2018 and 24 December 2018, as part of Programme M17BP056 (PI: Gao).

The JCMT has a 15-m diameter antenna and therefore beams (i.e. FoVs) of 17.″4 and 11.″6 at the rest frequency of CO(2-1) and of CO(3-2), respectively, both of which are smaller than the ALMA primary beam in this work. Table 2.4 lists the basic properties of the JCMT observations, while the CO(2-1) and CO(3-2) JCMT beams are shown in Figures 2.2 – 2.4 as black solid and black dashed circles, respectively, overlaid on the zeroth-moment maps.

For the CO(2-1) observations, the RxA receiver was used with dual sidebands, with the Auto Correlation Spectral Imaging System (ACSIS) correlator configured to have a bandwidth of 1 GHz and channels of 1 MHz ($\approx$ 1.3 km s^{-1} at $z = 0$). The observations were conducted in standard position-switching mode with a total on-source integration time of $\approx$ 30 min per target. For the CO(3-2) observations, the 16-pixel Heterodyne Array Receiver Program (HARP) was used, with the ACSIS correlator configured to have a bandwidth of 1 GHz and channels of 0.488 MHz ($\approx$ 0.4 km s^{-1} at $z = 0$). The

Table 2.4: Properties of our JCMT CO(2-1) and CO(3-2) observations.

Galaxy	Property	Value
NGC 1194	Velocity range (km s^{-1})	3800 – 4300
	CO(2-1) RMS noise (mJy)	83
	CO(2-1) int. flux (Jy km s^{-1})	< 17.8
	$M_{\rm mol}$ (M$_\odot$)	$< 1.55 \times 10^8$
NGC 3393	Velocity range (km s^{-1})	3580 – 3900
	CO(2-1) RMS noise (mJy)	131
	CO(2-1) int. flux (Jy km s^{-1})	43 ± 10
	$M_{\rm mol}$ (M$_\odot$)	$(2.7 \pm 0.6) \times 10^8$
	CO(3-2) RMS noise (mJy)	71
	CO(3-2) int. flux (Jy km s^{-1})	52 ± 5
	JCMT CO(2-1)/CO(3-2) (K/K)	1.8 ± 0.5
NGC 5765B	Velocity range (km s^{-1})	7750 – 8400
	CO(2-1) RMS noise (mJy)	115
	CO(2-1) int. flux (Jy km s^{-1})	186 ± 16
	$M_{\rm mol}$ (M$_\odot$)	$(6.0 \pm 0.5) \times 10^9$
	CO(3-2) RMS noise (mJy)	67
	CO(3-2) int. flux (Jy km s^{-1})	207 ± 14
	JCMT CO(2-1)/CO(3-2) (K/K)	2.02 ± 0.22

Note: The integrated CO fluxes and associated integrated molecular gas masses and CO line ratios are only measured within the JCMT FoVs, which do not necessarily cover the full extent of the galaxies' molecular gas. The RMS noises were measured using a channel width of 10 km s^{-1}.

observations were conducted in beam-switching mode to achieve a better spectral baseline, with a total on-source integration time of $\approx$ 1 hr per target.

For both CO(2-1) and CO(3-2) data reduction, the standard ORAC data reduction pipeline (ORAC-DR; Jenness & Economou 2015) was used within the `Starlink` software package[10] (Currie et al., 2014). The spectra were first rebinned to channels of 10 km s^{-1} to match our ALMA data. A linear baseline fit to line-free channels was then subtracted from each spectrum, to remove any continuum emission and non-flat baseline. The spectra were then converted to a flux density scale $S_{\rm v} = 15.6\,T_{\rm A}^{\star}/\eta_{\rm A}$, where $T_{\rm A}^{\star}$ is the antenna temperature and $\eta_{\rm A} = 0.52$ is the JCMT antenna efficiency at both frequencies. The resulting spectra of NGC 1194, NGC 3393 and NGC 5765B are shown in the bottom-left panels of Figure 2.2, Figure 2.3 and Figure 2.4, respectively.

[10]Available from `https://starlink.eao.hawaii.edu/starlink`.

The integrated flux of each spectrum was obtained by integrating over the velocity range with clear emission (or a range estimated from the ALMA data in the case of NGC 1194, which is a non-detection), as listed in Table 2.4, while the integrated flux uncertainty is estimated using

$$\sigma = \Delta v \, \sigma_{\rm chan} \sqrt{N_{\rm line} \left(1 + \frac{N_{\rm line}}{N_{\rm noise}}\right)} \ , \tag{2.1}$$

where Δv is the channel width (10 km s^{-1}), $\sigma_{\rm chan}$ the noise per channel listed in Table 2.4, $N_{\rm line}$ the number of channels used for the integration and $N_{\rm noise}$ the number of channels used to estimate the noise (see Young et al., 2011). As for the ALMA data, the molecular gas mass of each galaxy was then calculated from the CO(2-1) line by assuming a CO(2-1)/CO(1-0) line ratio R_{21} of unity (in brightness temperature units) and a CO-to-molecule conversion factor $\alpha_{\rm CO} = 4.3$ M$_\odot$ pc^{-2} (K km s^{-1})$^{-1}$ (Bolatto et al., 2013), including the contribution of heavy elements, yielding

$$\frac{M_{\rm mol}}{\rm M_\odot} = \frac{2.63 \times 10^3}{1 + z_{\rm helio}} \left(\frac{F_{\rm CO(2\text{-}1)}}{\rm Jy \ km \ s^{-1}}\right) \left(\frac{D}{\rm Mpc}\right)^2 \ , \tag{2.2}$$

where $F_{\rm CO(2\text{-}1)}$ is the intregrated CO(2-1) flux density.

2.4.3 NGC 1194

Molecular gas

The moment maps, PVD and integrated spectrum of NGC 1194 shown in Figure 2.2 suggest an edge-on, disturbed and lopsided central molecular gas disc well aligned with the maser disc. There are two large molecular gas concentrations, one extending north-west from the centre, the other farther out and disconnected to the south-east. Comparison to the SDSS r-band image in the upper-left panel of Figure 2.1 reveals the concentrations to be roughly aligned with the galaxy morphological major axis, while the composite *HST* image (F438W, F814W and F160W filters) in the lower-left panel of Figure 2.1 shows the molecular gas to be associated primarily with a weak irregular dust lane crossing the galaxy centre (with $PA_{\rm mor} \approx 160°$), while a much more prominent dust lane (offset to the south-west with $PA_{\rm mor} \approx 145°$) that seems to define part of a dust ring is apparently devoid of CO emission. This morphology and the first-moment map suggest the molecular

gas to be part of an irregular structure embedded within a roughly edge-on rotating disc, itself aligned with the large-scale galaxy disc. Unsurprisingly, the second-moment map reveals irregular velocity dispersions. The velocity dispersions are highest in the centre, but this may be due to beam smearing. They decrease to 10 – 20 km s^{-1} at the extremities of the distribution, typically associated with dynamically cold gas, and are comparable to the velocity dispersions of discs reported in other works (e.g. Davis et al., 2018; Smith et al., 2019; Lelli et al., 2022; Lu et al., 2022). Overall, our observations suggest a disturbed molecular gas distribution in a non-equilibrium state, possibly caused by an earlier (minor) merger event, a hypothesis supported by the twisted morphological position angle at large radii (see Fig. 11 of Läsker et al. 2016) as well as the existence of a detached H I cloud to the northwest of the main galaxy disc (Sun et al., 2013). Despite this, the maximum rotation velocity matches well that measured in H I (Sun et al., 2013).

As shown in the bottom-left panel of Figure 2.2, NGC 1194 is not detected in our JCMT CO(2-1) observations, which have a sensitivity of only 83 mJy per channel (while our synthesised ALMA integrated spectrum has a sensitivity of 1.3 mJy per channel on average, both based on the same channel width of 10 km s^{-1}). The ALMA integrated flux of 6.1 ± 0.1 Jy km s^{-1} yields a total molecular gas mass of (5.3 ± 0.1) × 10^7 $M_\odot$. Here and for the other two galaxies, the uncertainties quoted on the integrated flux and associated integrated mass are exclusively due to the noise in the integrated spectrum (see Section 2.4.1). They do not include potential systematic errors such as the ALMA flux calibration uncertainty (typically ≈ 10%), CO-to-molecule conversion factor uncertainty (typically ≈ 30%; Bolatto et al. 2013), galaxy distance uncertainty (typically ≈ 10%), etc. As the ALMA and JCMT FoVs only encompass ≈ 1 R_e around the galaxy centre, we have no information on the molecular gas beyond that region, and both the integrated flux and the associated integrated mass calculated here are likely lower limits of those quantities for the entire galaxy.

230-GHz continuum emission

The continuum map shown in the bottom-right panel of Figure 2.2 reveals a single compact 230-GHz continuum source at the centre of NGC 1194, most likely associated

Table 2.5: Properties of compact 230-GHz sources within the fields of view of our observations.

Galaxy	Property	Value
NGC 1194	R.A. (J2000)	$03^{h}03^{m}49\overset{s}{.}109$
	Dec. (J2000)	$-1°06'13\overset{''}{.}48$
	Flux (mJy)	1.73 ± 0.04
NGC 3393 (nucleus)	R.A. (J2000)	$10^{h}48^{m}23\overset{s}{.}47$
	Dec. (J2000)	$-25°09'43\overset{''}{.}5$
	Flux (mJy)	0.40 ± 0.04
	Spectral index	-0.18 ± 0.03
NGC 3393 (SW)	R.A. (J2000)	$10^{h}48^{m}23\overset{s}{.}40$
	Dec. (J2000)	$-25°09'44\overset{''}{.}1$
	Flux (mJy)	0.60 ± 0.04
	Spectral index	-0.8 ± 0.3
NGC 5765B (nucleus)	R.A. (J2000)	$14^{h}50^{m}51\overset{s}{.}52$
	Dec. (J2000)	$+5°06'52\overset{''}{.}2$
	Flux (mJy)	0.71 ± 0.08
NGC 5765B (SW)	RA (J2000)	$14^{h}50^{m}51\overset{s}{.}50$
	Dec. (J2000)	$+5°06'51\overset{''}{.}9$
	Flux (mJy)	0.28 ± 0.08

Notes: Source positions and integrated fluxes were measured using Gaussian fits. The spectral indices of NGC 3393 were measured by cross-identifying the sources with Very Large Array observations by Koss et al. (2015) and fitting power laws of the form $S \propto \nu^{\alpha}$ to the spectral energy distributions, where S is the integrated flux density, ν the frequency and α the spectral index.

with the AGN. Fitting this source with a 2D Gaussian using the `CASA` task `imfit` reveals it to be slightly spatially resolved (i.e. slightly larger than the synthesised beam). Its position and flux density derived from the Gaussian fit are listed in Table 2.5. This position is marginally consistent with that derived from maser astrometry (see Table 2.2). Another tentative more diffuse source is located $\approx 2\overset{''}{.}4$ south-west of the centre, with an integrated flux of $\approx$ 0.55 mJy.

2.4.4 NGC 3393

Molecular gas

The moments maps, PVD and integrated spectra of NGC 3393 shown in Figure 2.3 suggest a fairly regular but patchy molecular gas distribution, with little gas near the kinematic major axis and only faint diffuse gas in the very centre. There are two brighter structures in

the central region, one south-east of the centre (≈ 1.″5 or 360 pc from the centre), the other to the north-west (≈ 3.″3 or 790 pc from the centre), whose morphologies are reminiscent of (part of) a nuclear ring and/or spiral. These are also associated with increased velocity dispersions (40 – 60 km s^{-1}), that are otherwise ordinary (10 – 20 km s^{-1}). The velocity field is fairly regular on large scales, with $PA_{\rm kin} \approx 45°$, although a kinematic twist is present in the outer parts (most easily seen as a clear kink in the zero-velocity curve) and there are many small-scale disturbances. Finlez et al. (2018) discussed the observed CO(2-1) kinematics in great detail, along with the stellar and ionised-gas kinematics. To explain both the large-scale kinematics and that near the two brighter sources, they proposed a perturbation model driven by both a large-scale bar and a nuclear bar. The molecular gas detected at the largest radii (≈ 10″) forms an annulus or ring-like structure, that may be associated with spiral arms observed in the UV (see the lower-middle panel of Figure 2.1), and may thus trace recent star formation. Finally, the lack of molecular gas along the kinematic major axis may be due to photo-ionisation by the AGN/jets detected in continuum emission (see below), that are perpendicular to the accretion disc traced by maser emission (magenta lines in Figure 2.3).

As shown in the bottom-left panel of Figure 2.3, our JCMT CO(2-1) spectrum is in good agreement with our synthesised ALMA integrated spectrum at velocities above 3650 km s^{-1}, but the two differ at smaller velocities, with much lower JCMT fluxes. The ALMA first-moment map indicates that this could be accounted for if the JCMT had a pointing offset. Independent of this, despite the fact that our ALMA data do not have baselines shorter than 15 m, ALMA generally recovers more flux than the JCMT, likely because of the smaller FoV of the latter and the extended molecular gas distribution. The integrated flux of our ALMA CO(2-1) cube is 81.8 ± 0.4 Jy km s^{-1}, yielding a total molecular gas mass of (5.14 ± 0.02) × 10^8 M$_\odot$. As the ALMA FoV only encompasses ≈ 1.3 $R_{\rm e}$ and the molecular gas clearly extends to the FoV's edge, both the integrated flux and the associated integrated mass should again be considered lower limits of those quantities for the entire galaxy.

Our CO(3-2) JCMT spectrum is also in good agreement with our synthesised ALMA integrated CO(2-1) spectrum at velocities above 3720 km s^{-1}, but it again shows a

significant flux deficit at lower velocities. This could again be explained by a pointing offset. The integrated JCMT CO(3-2) flux of 52 ± 5 Jy km s^{-1} is thus both highly unreliable and likely a lower limit.

230-GHz continuum emission

The 230-GHz continuum map shown in the bottom-right panel of Figure 2.3 reveals two compact sources, one at the galaxy centre, consistent with the VLBI maser location, that we will refer to as the nuclear source, the other offset by ≈ 1.″0 or ≈ 240 pc south-west of the nucleus. Both sources are marginally spatially resolved, and the south-west source is ≈ 50% brighter than the nuclear source. There is also faint fuzzy emission north-east of the nucleus.

Based on X-ray emission, Fabbiano et al. (2011) reported a pair of SMBH/AGN separated by 150 pc (0.″6), much smaller than the separation of ≈ 240 pc between the two 230-GHz compact sources discussed above. Comparing the positions of the two X-ray sources in Figure 1 of Fabbiano et al. (2011), they appear to both be located in the emission tail of our nuclear source, both far away from the south-west compact source. Therefore, our two compact sources are unlikely to be Fabbiano et al.'s (2011) claimed dual SMBH/AGN. We also note that while Finlez et al. (2018) also disfavoured an SMBH/AGN pair, they misreported the location of the claimed second source in their Figure 4 and Section 4.3 which, according to Figure 1a of Fabbiano et al. (2011), should be north-east of the peak of the Very Large Array's (VLA) 8.4-GHz central source.

The nuclear source overlaps with component A discovered by Koss et al. (2015; also reported by Finlez et al. 2018) using VLA 8.4- and 4.9-GHz continuum observations, while the south-west compact source partially overlaps with their component B. A third source north-east of the centre was also reported by both Koss et al. (2015) as their component C and by Finlez et al. (2018). By carefully checking the spatial extent of component C, we conclude that the fuzzy emission detected here north-east of the nucleus also overlaps with it.

These three sources (nuclear source, south-west compact source and north-east fuzzy emission) can be attributed to the central AGN and (intrinsically) symmetric jets on

both sides of it. The south-west compact source is associated with the approaching jet and is thus significantly brighter than the north-east fuzzy emission (associated with the receding jet) due to Doppler-boosting (Koss et al., 2015). The integrated fluxes of the two compact sources are reported in Table 2.5, again derived using 2D Gaussian fits carried out with the `CASA` task `imfit`. Combining our measurements with those of Koss et al. (2015) at 8.4 and 4.9 GHz, we fit power laws of the form $S \propto \nu^{\alpha}$ to the spectral energy distributions, where S is the integrated flux density, ν the frequency and α the spectral index, and estimate that the nuclear source has a spectral index $\alpha = -0.18 \pm 0.03$ while the south-west compact source (i.e. the approaching jet) has $\alpha = -0.8 \pm 0.3$ (see Figure 2.5). These spectral indices are within the range of spectral indices of other nuclei and jets (e.g. Hovatta et al., 2014), and are consistent with self-absorbed optically thick synchrotron emission in the nucleus and optically thin synchrotron emission in the jet (see e.g. Ruffa et al., 2019a, 2022). We note however that we have neither matched our resolution to that of the VLA observations nor applied a 15 σ cut as done by Koss et al. (2015). These could lead to a bias in the spectral indices estimated.

2.4.5 NGC 5765B

Molecular gas

The CO(2-1) emission of NGC 5765B is very strong. The moment maps shown in Figure 2.4 show the typical morphology and dynamics of a barred disc galaxy, with emission particularly strong along two bisymmetric dust lanes (parallel to but offset from the optical bar; see the right column of Figure 2.1) as well as two bisymmetric nuclear spiral arms. The velocity field in turn shows a very strong kinematic twist beyond the dust lanes and thus the bar (most easily seen as a clear kink in the zero-velocity curve), and a milder kinematic twist in the centre within the nuclear spiral. We note that the sudden velocity jumps detected in the PVD within $\approx 2''$ on either side of the galaxy centre are not the signatures of Keplerian rotation around a putative SMBH, but rather arise from the bar and the twisted velocity map. As expected, the velocity dispersion map shows broad line widths ($\sigma \gtrsim 40$ km s^{-1}) due to beam smearing along the offset dust lanes, that are probably tracing bisymmetric shocks along the leading edges of the bar

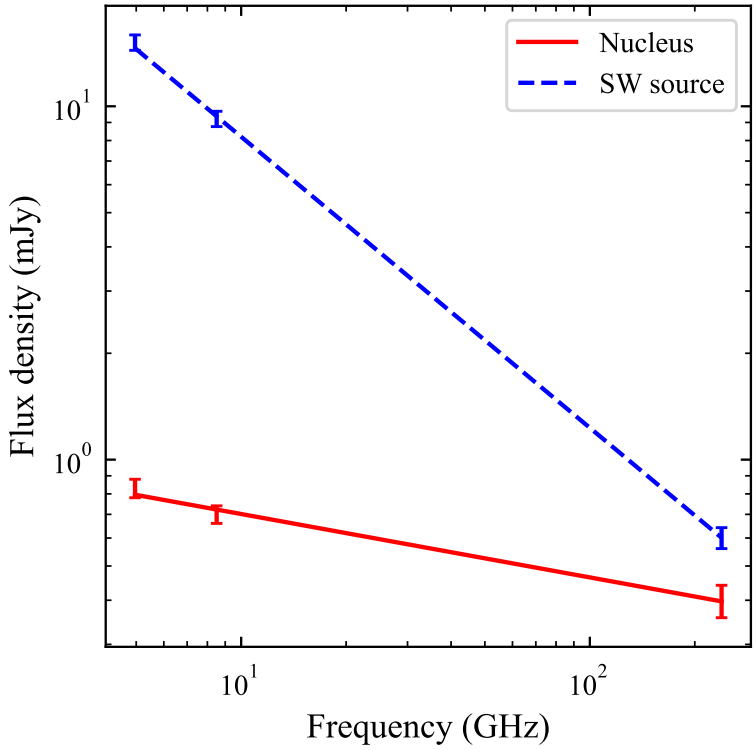

Figure 2.5: Radio – millimetre integrated continuum flux densities and power-law fits of the nuclear source (red) and south-west compact source (blue) detected in NGC 3393. The 8.4- and 4.9-GHz measurements are from Koss et al. (2015).

(see e.g. Athanassoula, 1992; Athanassoula & Beaton, 2006; Kim & Stone, 2012), and in the very centre, that may also harbour gas with intrinsically high turbulence due to AGN and/or star-formation feedback. There are also mildly increased line widths slightly beyond the end of the dust lanes (slightly leading). The gas elsewhere is dynamically cold ($\sigma < 20$ km s^{-1}) and follows a regular rotation pattern. We do nevertheless note a slight excess of molecular gas in the northern half of the galaxy, which may be related to the gravitational interaction with NGC 5765B's companion galaxy NGC 5765A. Another galaxy with a very similar barred morphology has recently been studied at a much higher spatial resolution (24 pc) as part of the WISDOM project (NGC 5806; Choi et al. 2023).

As shown in the bottom-left panel of Figure 2.4, our JCMT CO(2-1) spectrum (integrated flux density 186 ± 16 Jy km s^{-1}, corresponding to an integrated molecular gas mass of $(6.0 \pm 0.5) \times 10^9$ M$_\odot$) is in good agreement with our synthesised ALMA integrated spectrum (216.2 ± 0.4 Jy km s^{-1} and $(6.94 \pm 0.01) \times 10^9$ M$_\odot$). The slight

difference is likely due to the primary beam of the JCMT being slightly smaller than the total extent of the molecular gas detected with ALMA. Due to the relatively large distance of this galaxy, the ALMA primary beam reaches $\approx 1.8\ R_{\rm e}$, well beyond the total extent of the molecular gas detected, so all the molecular gas of NGC 5765B has probably been detected. The JCMT CO(3-2) spectrum is very similar to the CO(2-1) spectrum, the small differences probably reflecting minor excitation and/or distribution differences.

230-GHz continuum emission

The 230-GHz continuum map shown in the bottom-right panel of Figure 2.4 reveals one bright nuclear compact source (taking the VLBI source as the galaxy centre), a fainter compact source $\approx 0\farcs4$ ($\approx$ 200 pc) to the south-west of the centre and fuzzy extended emission to the north-west of the centre. Considering their locations, compactness and relative orientation (perpendicular to the maser disc), the two compact sources are likely due to the AGN (the off-centre source perhaps tracing a young jet). The fuzzy emission to the north-west partially overlaps with high–surface brightness and/or high–velocity dispersion regions in the zeroth- and second-moment maps. It may be dust emission, but nothing is detected on the opposite side of the galaxy despite a bisymmetric molecular gas distribution. Multi-band radio observations should constrain the spectral indices and therefore help reveal the origin of these sources.

2.5 Potential for SMBH Mass Measurements

Based on the detailed descriptions of the previous section, we now discuss the potential of each galaxy for an SMBH mass measurement using CO kinematics and future higher angular resolution ALMA observations ($\sim 0\farcs01$).

NGC 1194 has a narrow, lopsided and disturbed molecular gas distribution (see Section 2.4.3) that would prevent any robust dynamical modelling. In any case, it has very little molecular gas (see Figure 2.2), and the faintness of the CO(2-1) emission would result in impractically long exposure times with any synthesised beam much smaller than the current one. For a quantitative estimate, we take the brightest pixel across the central synthesised beam and all channels of the current datacube (with a flux of

2.95 mJy beam^{-1} at 4030 km s^{-1}), assume a homogeneous molecular gas distribution within it and adopt a smaller synthesised beam of 0.″045 required to marginally spatially resolve the predicted angular radius of the SMBH SoI ($\theta_{\rm SoI}$ = 0.″050; see Table 2.1). Requiring a signal-to-noise ratio $S/N = 5$ per synthesised beam and 10 km s^{-1} channels, we estimate using the ALMA Observing Tool (OT) that the observations would require a total observing time of $\approx$ 70 days.

Another uncertainty is that while the gas kinematics is consistent with a regular rotating disc at the current angular resolution, it is possible that at higher angular resolutions the very centre (at the scale of the SMBH SoI) would be disturbed or have a much lower CO surface brightness (e.g. a central hole), as is the case in several galaxies (e.g. Davis et al., 2018; Smith et al., 2019; Ruffa et al., 2023b). This concern of course applies to all galaxies, those discussed here and others.

NGC 3393 has a fairly regular molecular gas distribution and kinematics at large spatial scales (see Section 2.4.4), but there are many sub-structures and kinematic disturbances at small scales, and Finlez et al. (2018) required both a large-scale bar and a nuclear bar to model the kinematics. Such kinematic complexity would make it extremely difficult to robustly infer an SMBH mass through dynamical modelling. This difficulty would be compounded by the faintness of the CO(2-1) emission in the very centre and the lack of gas along the kinematic major axis (see Figure 2.3), the regions that best constrain the SMBH mass. In any case, for a central peak intensity of 2.38 mJy beam^{-1} at 3630 km s^{-1}, and requiring the smallest synthesised beam currently provided by ALMA (0.″02) to attempt to spatially resolve the predicted $R_{\rm SoI}$ ($\theta_{\rm SoI}$ = 0.″013; see Table 2.1), estimating the required ALMA observation time as above results in a total of $\approx$ 100 years.

The molecular gas distribution and kinematics of NGC 5765B are typical of those of barred disc galaxies (see Section 2.4.5). While this would make it challenging to model the large-scale kinematics, with sufficient spatial resolution it may be possible to model what appears to be a decoupled central disc (within the nuclear spiral and inner kinematic twist). The high velocity dispersions in the very centre are consistent with such a fast-rotating disc. However, while having relatively bright CO(2-1) emission, with a peak central intensity of 27.4 mJy beam^{-1} at 8190 km s^{-1}, the small angular scale required to

resolve the predicted $R_{\rm SoI}$ ($\theta_{\rm SoI} = 0\farcs013$; see Table 2.1) leads to an impossible integration time. Indeed, requiring a synthesised beam of $0\farcs02$ (the smallest currently available) and estimating the required ALMA observation time as above results in a total of ≈ 80 days.

Overall, because primarily of the impossibly long observation times required, and to a lesser extent the disturbed gas kinematics, none of our three targets is ultimately suitable for an SMBH mass measurement using ALMA. Of course, we have assumed here that CO is the most abundant cold molecular gas tracer in these three galaxies, and that observing CO(2-1) yields the best balance between S/N and angular resolution, but we cannot rule out the possibility that another cold molecular gas tracer (e.g. higher CO transition or higher-density tracer) might be better suited to measure the SMBH masses in these galaxies. In addition, we should not ignore an unlikely yet important hypothetical scenario in line with the motivation of such cross-checking endeavour where maser measurements may underestimate SMBH masses. In this case, molecular gas observations with poorer angular resolutions (and thus shorter integration times) than previously discussed may still be able to yield reliable SMBH mass measurements.

Apart from the intrinsic faintness of CO(2-1) in NGC 1194 and NGC 3393, the long observation times are primarily driven by the extremely small $\theta_{\rm SoI}$ required, as the observation time scales with the negative fourth power of $\theta_{\rm SoI}$ at a given surface brightness. In turn, the small $\theta_{\rm SoI}$ have primarily two causes. First, the maser method mostly probes low-mass SMBHs ($M_{\rm BH} \sim 10^7$ M$_\odot$, lower than most successful SMBH mass measurements using cold molecular gas), yielding small $R_{\rm SoI}$. Second, because of the scarcity of masers, maser-hosting galaxies are on average rather distant, much farther than most galaxies with existing SMBH mass measurements (the few nearby potential targets considered in Section 2.3.1 did not satisfy the other selection criteria), yielding small $\theta_{\rm SoI}$. To successfully cross-check the maser and cold molecular dynamics methods, maser-hosting galaxies that are both nearby and have regular dust/molecular gas distributions are required.

Although robust SMBH mass measurements with CO dynamics are unlikely with the maser galaxies discussed in this chapter, it is worth considering the possibility of obtaining upper limits of SMBH masses as they may be useful for various purposes such as confirming the offset of maser galaxies from the general $M_{\rm BH} - \sigma_\star$ relation reported

by Greene et al. (2016). Again, we mainly consider the gas kinematics and physical resolution. While the CO in NGC 1194 may follow pure regular rotation within the central $\lesssim 1''$, the misaligned and distorted gas distribution on larger scales would make it challenging to determine some other critical parameters of the dynamical modelling, e.g. the stellar mass-to-light ratio, inclination, and position angle. Therefore, the dynamical modelling is not promising, even for an upper limit of the SMBH mass. Meanwhile, despite the impractically long ALMA integration time required to resolve the SMBH SoI, it is not necessary to achieve such high resolution merely to derive an upper limit. As in the case of another galaxy, NGC 5208, a useful upper limit of the SMBH mass has been derived when the beam is larger than the (predicted) SMBH SoI by a factor of ten (Dominiak et al. in prep.). Thus, the beam size of the currently available data ($0\farcs26$, as compared to $\theta_{\rm SoI} = 0\farcs05$) may not be a major obstacle to deriving an upper limit. As for NGC 3393, the multiple kinematic kinks distributed in all regions of the gas disc would make it extremely challenging even just to derive an upper limit. Moreover, the difference between the beam size of the currently available data ($0\farcs50$) and the SoI ($0\farcs015$) is rather too large. Regarding NGC 5765B, the modelling of the gas kinematics may be possible, as discussed above. However, again, the current beam size of $0\farcs36$ is by a factor of 28 larger than the SoI, which would probably be too poor even for an upper limit. Nonetheless, with five hours of ALMA integration for example, the new data resolution can be improved to $0\farcs09$, which is by a factor of seven larger than the SoI. This may render an upper limit derivation feasible, if such new observations are obtained.

2.6 Links between disc properties and maser emission

The current ALMA observations can help uncover the relationship between the (central) molecular gas discs and masers. For example, all three galaxies studied here have a somewhat disturbed and/or clumpy molecular gas disc with a central mass concentration and likely non-circular motions.

To improve the number statistics and probe these trends further, we searched the literature for other published CO interferometric observations (i.e. moment maps) of galaxies in our parent sample of maser-hosting galaxies (Table 2.1). In addition to

the aforementioned NGC 1386 and Circinus in Section 2.3.1 (and the three galaxies presented in this chapter), there are publications concerning the galaxies NGC 1068, NGC 2273, NGC 4388 and NGC 4945. All except NGC 2273 show features similar to those of the three galaxies presented in this chapter. The CO(2-1) molecular gas in NGC 1386 has regular rotation on large scales (within $\approx$ 1 kpc in radius) but the centre ($\approx$ 220 pc in radius) is kinematically decoupled at a spatial resolution of 36 pc, leading to significant residuals from axisymmetric models (Ramakrishnan et al., 2019). Other kinematic kinks caused by the bar can also be seen in the CO(1-0) data presented by Zabel et al. (2019). These features resemble those of NGC 5765B. The molecular gas in the Circinus Galaxy consists of nuclear spiral arms (within $\approx$ 40 pc in radius) and a circumnuclear disc ($\approx$ 10 pc in radius), the latter showing a highly distorted velocity field at a spatial resolution of 3 pc (Izumi et al., 2018; Tristram et al., 2022). NGC 1068 has a ring-shaped deficit of molecular gas ($\approx$ 130 pc outer diameter) surrounding a CO-rich nucleus, and it shows strong distortions (at a resolution of 6 pc) in its velocity field both outside (i.e. beyond a radius of $\approx$ 200 pc) and within (i.e. within a radius of $\approx$ 15 pc) the ring-shaped deficit, presumably caused by AGN outflows (García-Burillo et al., 2019). The CO(2-1) kinematics in the central $\approx$ 500 pc in radius of NGC 2273 is almost perfectly regular at a spatial resolution of 90×72 pc^2, although the CO(2-1) distribution is similar to that of NGC 5765B, showing evidence of a molecular gas-rich nuclear spiral (Domínguez-Fernández et al., 2020). NGC 4388 has a molecular gas depression in the central $\approx$ 20 pc in radius as well as prominent kpc-scale molecular gas outflows, the latter causing significant kinematic disturbances (at 12-pc resolution) in the nucleus (i.e. within a radius of $\approx$ 40 pc; Domínguez-Fernández et al. 2020; García-Burillo et al. 2021). In NGC 4945, prominent outflows and bar-driven inflows of molecular gas are traced by CO(3-2) (Bolatto et al., 2021) and multiple dense-gas tracers (Henkel et al., 2018). The gas kinematics is highly disturbed within a radius of $\approx$ 250 pc at a resolution of 40 pc (see e.g. Figure 8 of Henkel et al. 2018), although a nuclear disc of $\approx$ 50 pc radius may be regularly rotating (see e.g. Figure 12 of Henkel et al. 2018).

Of the nine maser galaxies with spatially resolved CO observations discussed above, almost all have morphological irregularities and/or kinematic disturbances and/or

inflows/outflows, the only exception being NGC 2273 (that nevertheless shows potential bar-driven gas inflows). Although this sample is neither fully representative nor sufficiently large, the observations do suggest an emerging correlation between the properties of the central molecular gas disc and the existence of masers. It may be that a disturbed gas disc and/or gas inflows at the kiloparsec scale are necessary to form a very dense molecular gas concentration at the parsec scale, in turn triggering maser emission. Alternatively, it may be that AGNs with masers are likely to cause irregularities in the gas discs, potentially through interactions between jets and the ISM.

As masers mostly reside in Seyfert 2 AGN, to understand whether this emerging trend is exclusive to maser galaxies or is more generally associated with the whole Seyfert 2 galaxy population, we searched the literature for other (non-maser-hosting) Seyfert 2 galaxies with published interferometric observations of cold molecular gas. Stuber et al. (2021) reported a frequency of 53% of outflows in a sample of 19 AGN (mainly type 2), as part of the Physics at High Angular resolution in Nearby Galaxies (PHANGS) project. However, they did not discuss other non-circular motions. Alonso-Herrero et al. (2020) presented the zeroth-moment maps of 18 Seyfert galaxies (including 10 Seyfert 2) in their Figure 1. The sample was selected to have published mid-infrared spectral observations. All these galaxies have some morphological irregularities, such as non-axisymmetric gas distributions, off-centred peaks, holes/gaps and/or nuclear rings/spirals. This suggests that molecular gas irregularities are prevalent in the entire Seyfert 2 population. Nevertheless, the sample is still small in size, with unexplored potential biases, and critically the cold gas kinematics has not yet been explored.

Among publications with velocity maps available, all (non-maser-hosting) Seyfert 2 galaxies have features similar to those described in this work, e.g. Mrk 1066, NGC 7465 (Domínguez-Fernández et al., 2020), NGC 4968 and NGC 4845 (Bewketu Belete et al., 2021). However, the samples are even smaller in size and/or do not aim to be representative of all Seyfert 2 galaxies. Most publications concern a single object and aim to report non-circular motions in the first place.

Therefore, it is difficult to draw any statistical conclusion about how prevalent irregular kinematic features are in (non-maser-hosting) Seyfert 2 galaxies, to contrast with the maser

sample discussed in this section. In addition, the non-detection of masers in Seyfert 2 galaxies may well be due to inclination effects rather than the non-existence of masers. Thus, physical differences between maser-hosting and non-maser-hosting Seyfert 2 galaxies will be difficult to establish without large and carefully constructed samples of both.

All in all, while the above discussion is inconclusive, further investigation of the trend reported is warranted and desirable.

2.7 Summary and Conclusions

Our primary goal was to identify galaxies with existing megamaser SMBH mass measurements that are also promising targets for future measurements using high angular resolution ($\sim$ 0.″01) ALMA molecular gas observations, to cross-check the two methods. Considering all galaxies with a megamaser SMBH mass measurement, three promising galaxies were identified (NGC 1194, NGC 3393 and NGC 5765B) and new ALMA intermediate angular resolution ($\approx$ 0.″5) and JCMT single-dish observations were obtained. The main results are as follows.

1. NGC 1194 has an edge-on, disturbed and lopsided central CO(2-1) distribution dominated by two large components that appear associated with an irregular dust lane crossing the galaxy centre. The 230-GHz continuum emission is dominated by a single compact nuclear source.

2. NGC 3393 has fairly regular but patchy CO(2-1) emission, with little gas near the kinematic major axis and only faint diffuse emission in the very centre. There are also two brighter structures in the central region that are reminiscent of (part of) a nuclear ring and/or spiral. The velocity field has kinematic twists typical of (doubly) barred disc galaxies. The 230-GHz continuum emission is dominated by two compact sources. Combined with radio continuum flux densities from the literature, these reveal spectral indices typical of AGN/jets.

3. NGC 5765B has very bright CO(2-1) emission exhibiting the typical morphology and dynamics of a barred disc galaxy, with emission concentrated along two

bisymmetric offset dust lanes (probably tracing shocks) and two bisymmetric nuclear spiral arms, with associated kinematic twists in the velocity field and large line widths probably due to the shocks. The 230-GHz continuum emission is dominated by a compact nuclear source and extended diffuse emission on one side of the nucleus.

Overall, partially because of the disturbed molecular gas kinematics, but primarily because of the extremely long observation times required, none of the three galaxies is promising for a future SMBH mass measurement using molecular gas. These difficulties directly arise from the properties of maser-hosting galaxies: (i) frequent co-existence of masers and disturbed CO kinematics, as discussed in Section 2.6; (ii) relatively low SMBH masses ($\sim 10^7$ $M_\odot$), yielding small $R_{\rm SoI}$; and (iii) scarcity of masers, yielding typically large galaxy distances and thus small $\theta_{\rm SoI}$.

Apart from our three target galaxies, other candidates could emerge if the parent sample of maser-hosting galaxies were enlarged and/or the selection criteria used in this chapter were moderately relaxed. In particular, by observing (different molecular lines) at higher frequencies, the criterion of resolving the putative SMBH SoI with a $0\farcs01$ synthesised beam could be relaxed (although the observing times required are likely to remain impractically long). In practice, the order-of-magnitude estimate of an SMBH SoI adopted in this chapter (see Section 2.3.1) is also often smaller than actual measurements (e.g. Yoon, 2017).

Nonetheless, the new CO observations presented in this chapter have significantly added to the rather small number of spatially-resolved molecular gas studies of maser-hosting galaxies. A detailed morphological and kinematical examination of our three targets, as well as six other maser-hosting galaxies with analogous observations from the literature, has revealed a potential correlation between molecular gas disturbances and/or inflows/outflows and the existence of maser emission.

3

Giant molecular clouds of the lenticular galaxy NGC 1387

Contents

3.1 Introduction

Molecular gas is key to understanding star formation and galaxy evolution, but the giant molecular clouds (GMCs) of early-type galaxies (ETGs) have rarely been studied. Here we present analyses of the spatially resolved GMCs of the lenticular galaxy NGC 1387, exploiting high spatial resolution (0.″15 or 14 pc) ^{12}CO(2-1) line observations from the Atacama Large Millimeter/submillimeter Array. We identify 1285 individual GMCs and measure the fundamental properties (radius, velocity dispersion and molecular gas mass) of each with a modified version of the `CPROPStoo` package. Unusually for an ETG, the GMCs of NGC 1387 follow scaling relations very similar to those of the Milky Way (MW) disc and Local Group galaxy clouds, and most are virialised. GMCs with large masses and radii and/or small galactocentric distances have their angular momenta aligned with the large-scale galactic rotation, while other GMCs do not.

This chapter is arranged as follows. In Section 3.2, we provide details of the target and our data and create a GMC catalogue using a modified `CPROPStoo` package. In Section 3.3, we follow previous studies and measure the basic properties of the GMCs (size, velocity dispersion, molecular gas mass, etc) and compare them against the Larson relations of the MW, also comparing the gaseous and virial masses. In Section 3.4, we present a kinematic analysis constraining the origin of the internal rotation of the GMCs. In Section 3.5, we calculate the radial profile of the Toomre instability parameter and discuss a cloud-cloud collision model as the regulator of GMC properties. In Section 3.6, we discuss the steep radial gradients of GMC properties observed, which appear unique to NGC 1387. In Section 3.7, we discuss the similarities of the NGC 1387 and MW disc GMCs, and potential physical drivers. We summarise our results in Section 3.8.

3.2 DATA AND GMC IDENTIFICATION

3.2.1 Target overview

NGC 1387 is a nearby galaxy at a distance of 19.3 ± 0.8 Mpc, as measured from surface brightness fluctuations (Blakeslee et al., 2009). At this distance, 1″ corresponds to ≈ 94 pc. In this work, we adopt a systemic velocity[1] of 1285.1 km s^{-1}, as calculated in Section 3.2.4 and consistent within the galaxy redshift of 0.00434 (NASA/IPAC Extragalactic Database). NGC 1387 has a morphological type of SB0 (Sandage & Tammann, 1981; Ferguson, 1989; Buta et al., 2007), with a prominent bulge with an effective (half-light) radius $R_e = 4\farcs4$ at K_s band, a weak bar, a faint nearly circular ring with a radius of 6″, a stellar disc extending from ≈ 30″ to ≈ 90″ from the centre and no spiral arm (Laurikainen et al., 2006). Its total stellar mass is 4.70×10^{10} M$_\odot$, derived using a colour-dependent i-band mass-to-light ratio of 1.31 $(M/L)_{i,\odot}$ (Iodice et al., 2019a). The effective radius of its entire stellar component is 50.″1 in the B band (Ferguson, 1989; Sarzi et al., 2018) and 35.″5 in the r band (Iodice et al., 2019b). The stellar velocity dispersion reaches a maximum of ≈ 200 km s^{-1} at the galactic centre, while the luminosity-weighted average within the r-band effective radius is 143 km s^{-1} (Iodice et al., 2019b). NGC 1387 is a fast rotator (Iodice et al., 2019b).

Figure 3.1 shows an overview of NGC 1387 and its molecular gas content. An optical image (B-, V- and I-band composite) from the Carnegie-Irvine Galaxy Survey[2] (CGS; Ho et al. 2011) is shown in the left panel, while the right panels show unsharp-masked images from the *Hubble Space Telescope* (*HST*) Advanced Camera for Surveys (ACS) Wide Field Channel (WFC) F475W filter created with `scikit-image`[3] (van der Walt et al., 2014), with (bottom right) and without (top right) the CO(2-1) intensity contours overlaid (see Section 3.2.2). Those images clearly reveal that the molecular gas is in a regular disc perfectly co-spatial with a flocculent dust disc embedded within the bulge. Both discs are co-spatial with a kinematically decoupled stellar core (Iodice et al., 2019b), have sharp edges and occupy a roughly circular region of 10″ radius. This radius is ≈ 20% of the B-band effective radius, typical of Virgo Cluster ETGs

[1] We use barycentric velocities with radio convention throughout this chapter.
[2] https://cgs.obs.carnegiescience.edu/CGS/Home.html
[3] https://scikit-image.org

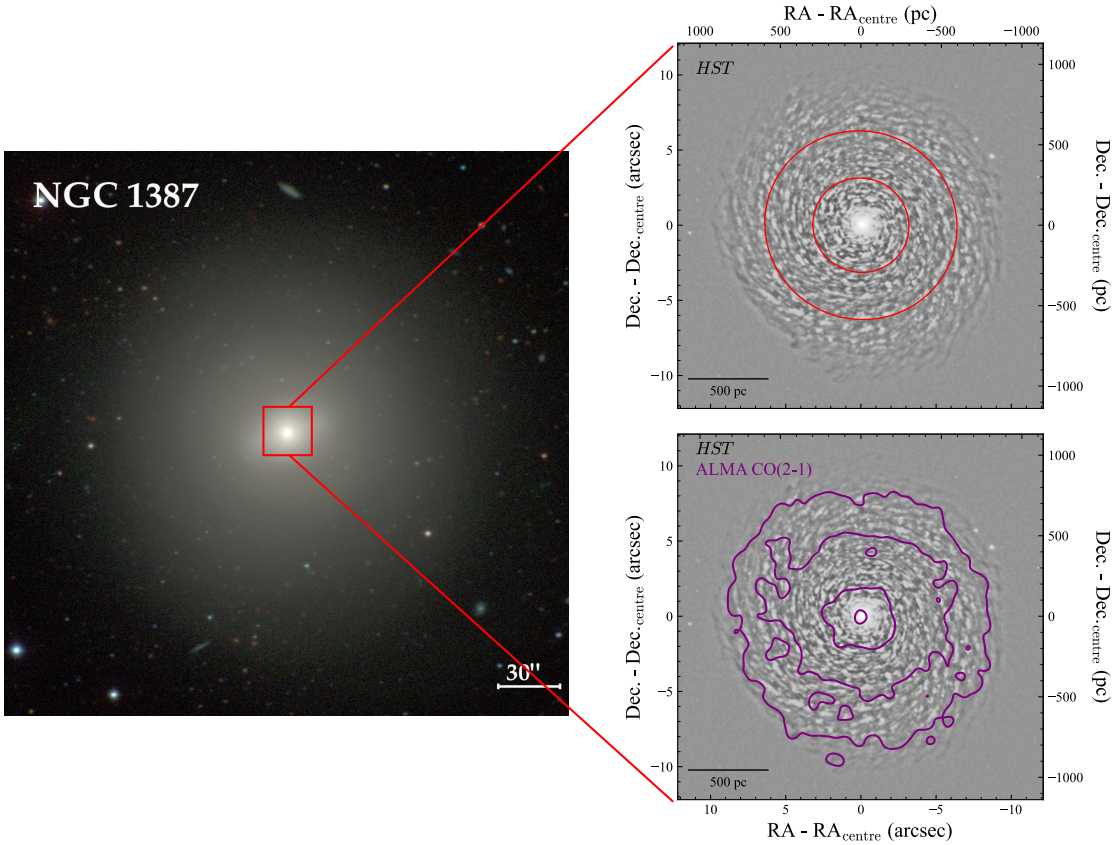

Figure 3.1: Overview of NGC 1387 and its molecular gas content. **Left:** optical image from the CGS survey. The galaxy bulge, bar, extended stellar disc and envelope are all clearly visible. **Top-right:** unsharp-masked *HST* ACS/WFC F475W image of the central region only, highlighting dust features. The red ellipses overlaid indicate the boundaries of the three regions defined in Section 3.2.4 and discussed in the text. **Bottom-right:** same unsharp-masked *HST* ACS/WFC F475W image, with the contours of the (smoothed) CO(2-1) total intensity map overlaid in purple (see Section 3.2.2). A scale bar is provided in each panel.

(Davis et al., 2013a). The red ellipses in the top-right panel divide the galaxy into three regions based on the molecular gas mass surface density profile; these regions are used later for our GMC analyses (see Section 3.2.4).

NGC 1387 (also known as FCC 184) belongs to the Fornax Cluster of galaxies and is the closest galaxy to the brightest central galaxy NGC 1399. Previous studies have found evidence of a gravitational interaction between these two galaxies in the stellar component (e.g. a stellar bridge and an overdensity of globular clusters; D'Abrusco et al. 2016; Iodice et al. 2016; Spiniello et al. 2018). The cluster environment can significantly affect the cold gas properties of galaxies. Recent observations revealed molecular gas discs smaller (once normalised by the size of the stellar component) than those of field galaxies, this for

both LTGs (Villanueva et al., 2022) and ETGs (Davis et al., 2013a). This is interpreted as a loss of angular momentum and subsequent inward migration of molecular gas due to ram-pressure stripping (Tonnesen & Bryan, 2009), which can also cause steep or truncated radial profiles of molecular gas mass surface density (Mok et al., 2017; Zabel et al., 2022) and affects star formation (Mok et al., 2016; Villanueva et al., 2022; Choi et al., 2022).

The cold molecular gas of NGC 1387 was first studied by Zabel et al. (2019) using ^{12}CO(1-0) (hereafter CO(1-0)) ALMA observations at an angular resolution of 2.″8. This revealed a smooth, symmetric and regularly rotating disc and several 3-mm continuum sources due to nuclear activity and dust. Zabel et al. (2019) report an integrated CO(1-0) flux of 83.3 ± 8.3 Jy km s^{-1} and we confirm that the CO(1-0) disc has the same spatial extent as the CO(2-1) disc (see Section 3.2.4 and Figure 3.2). We thus use CO(1-0) as the benchmark for the total molecular gas of NGC 1387. Throughout this chapter, we adopt a constant CO-to-H_2 conversion factor $X_{\mathrm{CO(1-0)}} = 2 \times 10^{20}$ cm^{-2} (K km s^{-1})$^{-1}$ (or equivalently a CO-to-molecular gas conversion factor $\alpha_{\mathrm{CO(1-0)}} = 4.3$ M$_\odot$ (K km s^{-1} pc^2)$^{-1}$; Bolatto et al. 2013). Using equation 3 of Bolatto et al. (2013), the total molecular gas mass is 3.2×10^8 M$_\odot$ or 0.7% of the total stellar mass, similar to ETGs both in and outside the Virgo Cluster (Young et al., 2011), and on the lower end of Virgo Cluster galaxies in the Virgo Environment Traced in CO survey (primarily LTGs; Brown et al. 2021). The (inclination-corrected) mean molecular gas mass surface density of the molecular gas disc is 104 M$_\odot$ pc^{-2}.

No atomic hydrogen (H I) was detected in both the H I Parkes All Sky Survey and using the Australia Telescope Compact Array, the latter providing the more stringent upper limit of 3×10^7 M$_\odot$ (Loni et al., 2021). Optical spectra and emission-line ratio analyses with the Baldwin, Phillips & Terlevich (BPT; 1981) diagram indicate that the stars and the molecular gas of NGC 1387 are co-rotating, and the centre of the galaxy is a low-ionisation nuclear emission-line region (Iodice et al. 2019b; Zabel et al. 2020). The BPT analysis also identified star-forming regions as well as composite regions in NGC 1387. The star-formation rate derived from the Hα emission line luminosity is reported to be in the range of 0.008 (considering only star-forming regions) to 0.082 M$_\odot$ yr^{-1} (also including composite regions; Iodice et al. 2019b). At X-ray wavelengths (energy range 0.3 – 8 keV), Liu (2011)

reported a point source associated with NGC 1387 with a luminosity of 3.22×10^{39} erg s^{-1}. The total 1.4-GHz radio power is 1.8×10^{20} W Hz^{-1} (Brown et al., 2011).

3.2.2 ALMA data

Observations were carried out with the ALMA 12-m array under project 2016.1.00437.S (PI: Davis) on 4 Nov. 2016, 21 Dec. 2016 and 7 Sept. 2017, for a total on-source time of 37.3 min. Observations were also obtained with the 7-m Atacama Compact Array (ACA) under project 2016.2.00053.S (PI: Liu) on 28 Jul. 2017, for a total on-source time of 17.1 min. These observations provide shorter spacings, therefore improving flux recovery. The baselines range from 9 to 7552 m after combining all observations, with a maximum recoverable scale of 28.″4. For the 12-m array, the ALMA correlator (band 6) was configured with one spectral window centred on the systemic velocity of the galaxy (CO(2-1) rest frequency of 230.538 GHz), with a bandwidth of 1.875 GHz ($\approx$ 2450 km s^{-1}) and channels of 488 kHz ($\approx$ 0.6 km s^{-1}). The remaining three spectral windows were used to observe the continuum, if any, each with a bandwidth of 2 GHz and channels of 15.625 MHz. For the ACA, one spectral window was also centred on CO(2-1) but with a bandwidth of 2 GHz ($\approx$ 2610 km s^{-1}) and channels of 977 kHz ($\approx$ 1.3 km s^{-1}). The remaining three windows for continuum detection again each had a bandwidth of 2 GHz and channels of 15.625 MHz.

Using the Common Astronomy Software Applications (`CASA`; CASA Team et al. 2022), we re-ran the standard calibration pipeline. After masking out channels with emission, the continuum (assumed constant with frequency) was fitted in the *uv* domain and subtracted from each track separately. We then combined all tracks and used Briggs weighting (Briggs, 1995) with a robustness parameter of 1.0 and no taper or clipping to image the data. This was chosen to achieve a physical resolution better than the characteristic size of GMCs while maintaining adequate sensitivity. The final data cube has a synthesised beam with major and minor axes of $\theta_{\rm maj} \times \theta_{\rm min} = 0.''167 \times 0.''136$ (15.6×12.7 pc^2) full-widths at half-maximum (FWHM), with a position angle of 89.°6 (measured from north through east). We adopt a 0.″04 pixel size to sufficiently sample the synthesised beam. We also bin the raw data spectrally to obtain a final 2 km s^{-1} channel width, sufficient to

spectrally resolve most GMCs. Interactive cleaning was carried out with the Hogbom algorithm (Högbom, 1974) implemented in CASA to a depth of 1.5 mJy beam^{-1} (slightly higher than the root-mean-square, RMS, noise level; see below). In each channel, an emission mask used for cleaning (denoted 'mask$_{\rm clean}$') was carefully created by visual inspection, manually adjusting a draft mask generated by the automatic masking algorithm AUTO-MULTITHRESH (Kepley et al., 2020). This cube (hereafter the 'uncorrected' cube) has a uniform RMS noise $\sigma_{\rm RMS}$ = 1.11 mJy beam^{-1} (1.12 K) per 2 km s^{-1} channel. Primary beam (PB) correction was then applied, producing our final 'corrected' cube. The fields of view of both cubes are $\approx 30''$, corresponding to the diameter of the area with a PB response ≥ 0.2 at the observed frequency. Although this covers only the bulge region of NGC 1387, it does encompass the entire CO extent.

The continuum emission was also imaged (and primary-beam corrected). A point source is detected at the centre of the galaxy, most likely a low-luminosity active galactic nucleus (LL-AGN), with a flux of 1.20±0.04 mJy and a position of RA = $03^{\rm h}36^{\rm m}57\overset{\rm s}{.}0333\pm$ 0.0001, Dec. = $-35°30'23\overset{''}{.}6790 \pm 0.0009$ (J2000.0). We adopt this position as the centre of the galaxy. There is also an extended source $10\overset{''}{.}3$ north-west of the galaxy centre.

3.2.3 *HST* image and stellar mass distribution

We model the stellar mass distribution of NGC 1387 using a multi-Gaussian expansion (MGE; Emsellem et al. 1994) constructed using the MGE_FIT_SECTORS package[4] of Cappellari (2002). We use an *HST* Wide Field Camera 3 F160W filter image and a constant stellar mass-to-light ratio of 0.97 $(\mathrm{M/L})_{\mathrm{F160W},\odot}$, derived by Dominiak et al. (2024) by fitting the CO gas kinematics with the publicly available package Kinematic Molecular Simulation (KinMS[5]; Davis et al. 2013a). The best-fitting inclination is $13\overset{\circ}{.}6$ and the best-fitting position angle $243\overset{\circ}{.}9$. The resulting 3D stellar-mass model and circular velocity curve $v_{\rm circ}(R)$ will be used in the kinematic study of the GMCs (Section 3.4) and the Toomre parameter calculation (Section 3.5).

[4] https://www-astro.physics.ox.ac.uk/~cappellari/software/#mge
[5] https://github.com/TimothyADavis/KinMS

3.2.4 Moment maps and region definition

We use the moment-masking technique to generate the moment maps (see Figure 3.2), which is based on Dame (2011) and implemented in the python package `pymakeplots`.[6] We start with defining line-free channels to be those outside 1200–1370 km s^{-1} and line-free spaxels to be those outside a $20'' \times 20''$ box, based on visual inspection of the datacube. We then smooth the uncorrected cube (i.e. the cube before PB correction) with a 3D Gaussian kernel. Its FWHMs in the two spatial dimensions are both twice that of the synthesised beam major axis and the kernel's standard deviation width in the spectral dimension equals two channels. Because of smoothing, real emission should remain significant while noise should largely vanish. We create a mask (denoted '$\mathrm{mask_{RMS}}$') including all the pixels of this smoothed uncorrected cube with an amplitude greater than five times the RMS noise measured in line-free channels of this cube. We then select pixels from the (unsmoothed) corrected cube within this mask to create moment maps. Maps of the uncertainties of the moments are created using the python package `Uncertainties`[7] based on σ_{RMS} (corrected by respective PB responses along different lines-of-sight) and standard error propagation.

In the top-left panel of Figure 3.2, the zeroth-moment (integrated-intensity) map shows that the large-scale molecular gas distribution has a high filling factor and the molecular gas disc is fragmented into a very large number of small clumps. This morphology is reminiscent of the flocculent spiral arms seen at optical wavelengths (Figure 3.1). There is also a small central hole ($\approx 0\farcs2$ in radius). In the top-middle panel of Figure 3.2, the first-moment (intensity-weighted mean line-of-sight velocity) map reveals an extremely regular rotating molecular gas disc, with no evidence of non-circular motions. In the top-right panel of Figure 3.2, the second-moment (intensity-weighted line-of-sight velocity dispersion) map shows that the molecular gas velocity dispersion gradually decreases away from the galaxy centre. The enhancement along the minor axis and some of the central peak are most likely due to beam smearing. The morphology and kinematics (but not the central hole) of the molecular gas disc are ideal for measuring the mass of

[6] https://pypi.org/project/pymakeplots/
[7] https://pythonhosted.org/uncertainties/

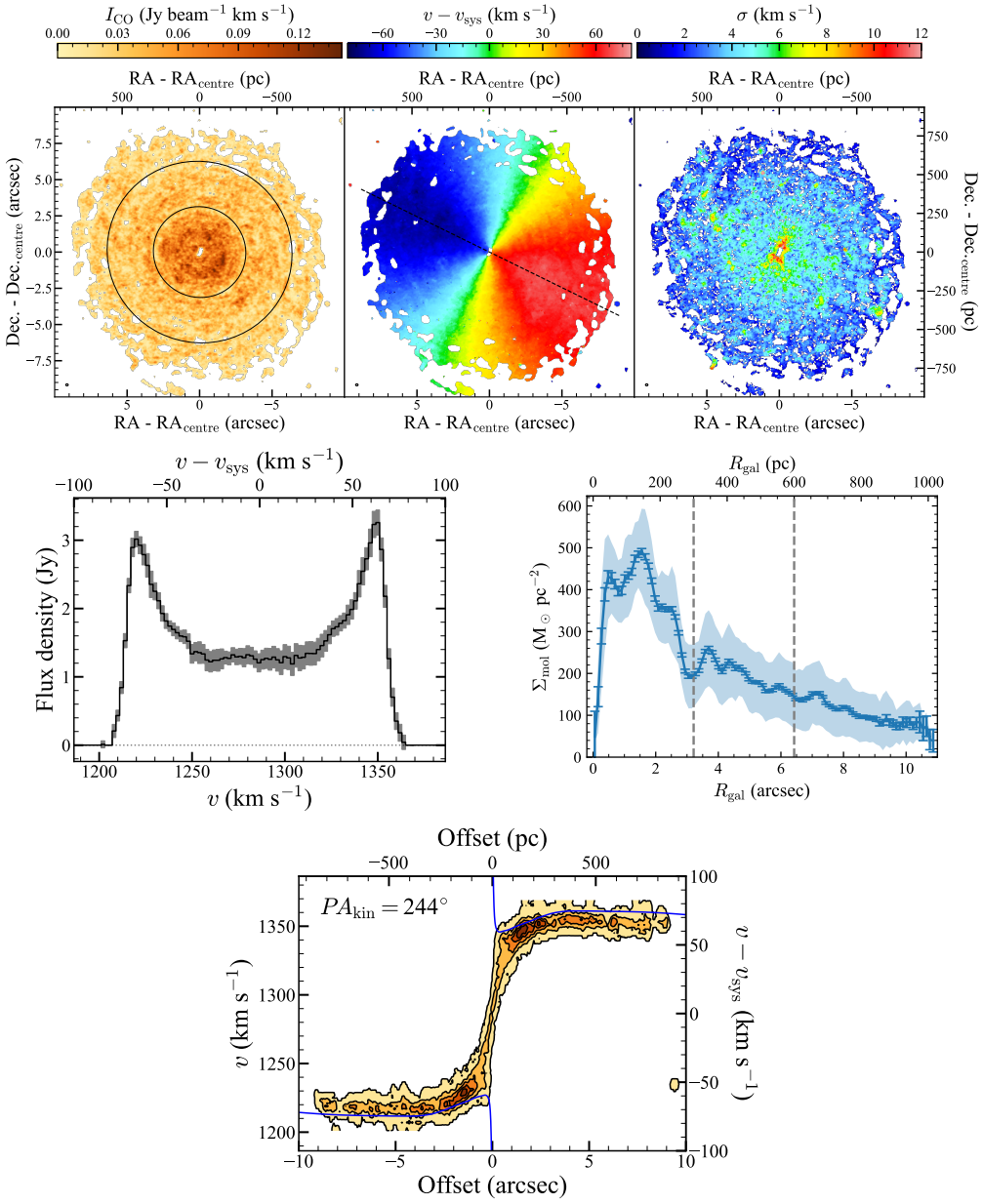

Figure 3.2: Molecular gas distribution of NGC 1387. **Top:** CO(2-1) zeroth (integrated-intensity), first (intensity-weighted mean line-of-sight velocity) and second (intensity-weighted line-of-sight velocity dispersion) moment maps. The black ellipses in the left panel indicate the boundaries of the three regions defined in Section 3.2.4. The dashed line in the middle panel indicates the kinematic major axis. The synthesised beam is shown in the bottom-left corner of each panel as a black ellipse. The small central holes in the maps (showing up as white due to absence of values) are caused by the central deficit of gas (see Section 3.2.4). **Middle-left:** spatially integrated CO(2-1) spectrum, corrected per channel to effectively reach infinite cleaning depth (see Section 3.2.4). 1σ uncertainties are shown as grey shading. **Middle-right:** inclination corrected molecular gas mass surface density radial profile. Error bars indicate the 1σ uncertainty on the mean of each radial bin, while the blue-shaded region shows the scatter (standard deviation) within each radial bin. The grey dashed vertical lines again indicate the boundaries of the three regions defined in Section 3.2.4. **Bottom:** rotation curve. The measured position-velocity diagram (along the kinematic major axis) is in the orange-shaded contours while the blue curves show the theoretical circular velocity (see Section 3.2.3).

a putative central supermassive black hole, as done by Dominiak et al. (2024), where the position-velocity diagram of the molecular gas disc is also presented.

To accurately recover the total flux and the flux density in the synthesised spectrum, we apply the formula in Appendix A.2 in Jorsater & van Moorsel (1995) to correct for the finite cleaning depth effect, which could cause a bias in flux due to the different normalisations of the dirty beam and the Gaussian clean beam. Using another datacube cleaned to 3.0 mJy beam^{-1}, along with the main datacube, for the aforementioned formula, channel by channel, we effectively derive the flux density (and thus the total flux) at infinite cleaning depth. With that formula applied, we also gradually enlarge mask$_{\rm RMS}$ to encompass more faint diffuse emission using the python routine `scipy.ndimage.binary_dilation`[8] until the derived total flux stops significantly increasing. This happens roughly at an enlargement of 40 pixels ($\approx$ 11 beams or 150 pc), adopted for the flux recovery and the enlarged mask is denoted mask$_{\rm RMS,large}$. We also use mask$_{\rm RMS,large}$ to generate the synthesised spectrum (corrected to infinite cleaning depth channel by channel) shown in the bottom-left panel of Figure 3.2. It reveals the classic 'double-horn' feature of a rotating disc. Due to the masking scheme, the uncertainty of the integrated flux in each channel is calculated in a rather complicated manner: for each line channel, we take the associated two-dimensional (2D) mask, independently sum every line-free channel of the corrected cube over that mask, calculate the standard deviation of those sums, and adopt that standard deviation as the uncertainty of that line channel. The total spatially integrated CO(2-1) flux, corrected to infinite cleaning depth, of NGC 1387 is 255 $\pm$ 3 Jy km s^{-1} (assuming standard error propagation for a sum). The absolute flux calibration of ALMA is however only accurate to $\approx$ 10%, which translates to an additional systematic error of $\approx$ 10% on every channel and thus the spatially integrated flux. Using the CO(1-0) integrated flux of Zabel et al. (2019), we derive a CO(2-1)/CO(1-0) line ratio of 0.77 ± 0.08 in brightness temperature units. This is consistent with the 1σ range of nearby massive disc galaxies (0.50 – 0.83; Leroy et al. 2022). The flux-weighted mean velocity calculated from this spectrum, 1286.4 ± 0.4 km s^{-1}, is adopted as the systemic velocity of the galaxy.

[8] https://docs.scipy.org/doc/scipy/reference/generated/scipy.ndimage.binary_dilation.html

The azimuthally averaged inclination corrected molecular gas mass surface density radial profile ($\Sigma_{\rm mol}(R_{\rm gal})$, where $R_{\rm gal}$ is the galactocentric distance) is shown in the bottom-right panel of Figure 3.2. The error bars indicate the 1σ uncertainty on the mean in each radial bin (propagated from the zeroth-moment map), while the blue-shaded region shows the scatter (standard deviation) within each radial bin. The central hole is reflected by the sharp drop in the central few radial bins.

Molecular gas and GMCs in different regions of the same galaxy can exhibit significantly different properties (e.g. Freeman et al., 2017; Sun et al., 2020b). In NGC 1387, we thus divide the molecular gas disc into three regions: an inner region ($R_{\rm gal} < 300$ pc), an intermediate region ($300 < R_{\rm gal} < 600$ pc) and an outer region ($R_{\rm gal} > 600$ pc). These boundaries are based on a visual inspection of the zeroth-moment map and reflect significant changes in the molecular gas mass surface density radial profile. Although the exact location of the second boundary at 600 pc is somewhat arbitrary, it does not affect the results discussed in the following sections.

The rotation curve (in the form of a position-velocity diagram, PVD, along the kinematic major axis) is also shown in Figure 3.2 (orange-shaded contours in the bottom panel), as a useful diagnostics of the gas disc kinematics. The rotation curve rises rapidly within $R_{\rm gal} \lesssim 100$ pc and then flattens out at a LoS-projected velocity of ≈ 70 km s^{-1}. The theoretical circular velocity curve, $v_{\rm circ}$, derived from stellar mass modelling (see Section 3.2.3) is shown as the blue curves. In comparison, $v_{\rm circ}$ shows the predicted Keplerian rise of velocity towards the galactic centre due to the supermassive blackhole while the PVD centre converges to zero velocity owing to beam smearing. In the rest part of the galaxy, $v_{\rm circ}$ is very close to but slightly higher than the observed CO rotation curve because of the small but non-zero velocity dispersion of CO providing dynamical support for the gas disc in the galaxy's gravitational potential well, making the observed rotational velocity slightly lower than the pure rotation–based prediction, $v_{\rm circ}$.

3.2.5 GMC identification

With the corrected cube as input, we adopt a modified version of the `CPROPStoo` package (Rosolowsky & Leroy, 2006; Liu et al., 2021) for GMC identification and property

measurements. First, CPROPStoo uses a mask to identify regions of real emission, which is a slightly manually enlarged one based on 'mask$_{\rm clean}$' to encompass faint diffuse emission. Within this mask, it then identifies pixels above $2\sigma_{\rm RMS}$, accretes neighbouring pixels above $1.5\sigma_{\rm RMS}$ and requires those regions to have an area larger than 32 pixels (roughly twice the synthesised beam area) to create 'islands' regarded as real emission. These parameters were selected to ensure that almost all diffuse emission is retained while keeping the noise low. As the current channel width of 2 km s^{-1} is comparable to the smallest line width of the gas disc (see Figure 3.2), we do not require any minimum number of channels for island identification.

Within these islands, CPROPStoo identifies local maxima and their uniquely associated spaxels (i.e. pixels brighter than the merging contour level with adjacent local maxima) as the seeds of GMCs. It then compares these maxima and associated spaxels with a minimum area, a minimum spectral width, a minimum contrast $\Delta T_{\rm min}$ between the highest and the lowest intensity and a minimum convexity $S_{\rm min}$ (enforced to prevent individual GMCs from having too much sub-structure; Lin et al. 2003). A more detailed description of the methodology can be found in Liu et al. (2021). To avoid significant bias toward small structures when a small minimum area is used, the local maximum search cycles through a range of minimum areas from 160 ($\approx$ 10 synthesised beam areas) to 16 ($\approx$ 1 synthesised beam area) spaxels, with a step size of 16 spaxels. The remaining spaxels in the islands (i.e. those not uniquely associated with a single local maximum) are assigned to clouds using a 'friend-of-friend' CLUMPFIND algorithm (Rosolowsky & Leroy, 2006; Liu et al., 2021). In the smallest minimum area search cycle (i.e. 16 spaxels), the aforementioned cloud criteria are checked after the spaxel assignment, while during all previous cycles, the criteria are checked using only uniquely associated spaxels. We set the minimum spectral width to be 2 channels, the minimum contrast to be 2 K ($\approx$ 1.8 $\sigma_{\rm RMS}$) and the minimum convexity to be 0.50.

These parameters were chosen via trial and error. After each trial, we examined the GMCs identified to verify that most had reasonable structures and most over-densities were indeed identified as GMCs. Different GMC identification results (with different $\Delta T_{\rm min}$ and $S_{\rm min}$) are presented in Appendix A, confirming that all reasonable sets of

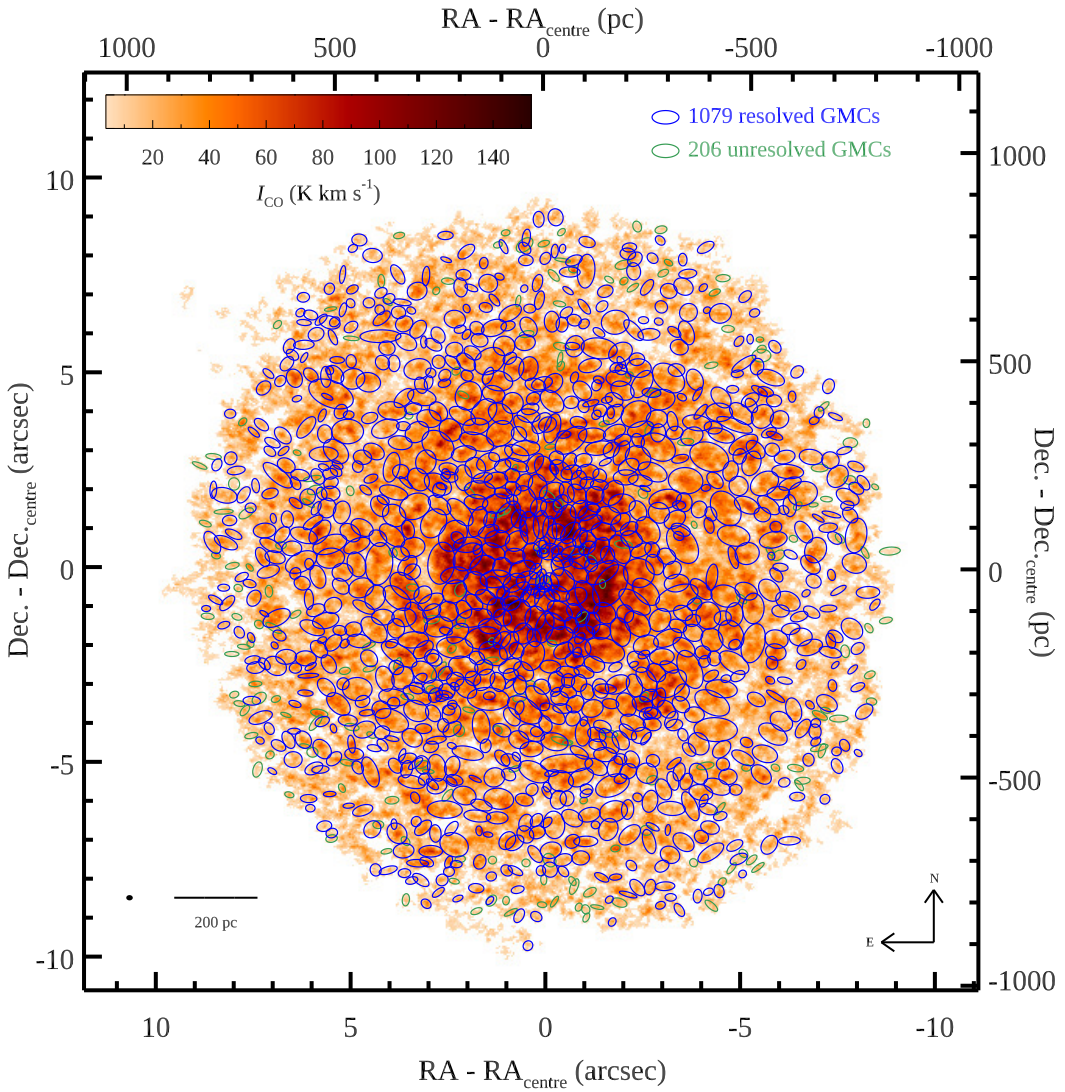

Figure 3.3: GMCs identified by `CPROPStoo`, schematically overlaid on the zeroth-moment map as ellipses. There are 1079 spatially and spectrally resolved GMCs (blue ellipses) and 206 unresolved GMCs (green ellipses). The synthesised beam is shown in the bottom-left corner as a black filled ellipse. A scale bar is also shown in the bottom-left corner.

parameters yield similar GMC properties and do not significantly alter the results discussed in the following sections.

The final GMC catalogue can be visualised in Figure 3.3, where the 1079 spatially and spectrally resolved GMCs and the 206 unresolved GMCs are schematically overlaid on the zeroth-moment map. For a GMC to be considered resolved, both its deconvolved radius and its deconvolved line width (see Section 3.3) must be larger than the instrumental resolution (half of the synthesised beam size and half of the channel width, respectively).

3.3 GMC properties

We measure the properties of each GMC in the same manner as Liu et al. (2021) and references therein (e.g. Rosolowsky & Leroy, 2006). Briefly, the GMC radius R_c is the geometric mean of the deconvolved intensity-weighted second moment in each direction (σ_x, σ_y), scaled by a factor $\eta = 1.9$. This factor η relates the GMC radius R_c (in terms of its outmost truncation boundary) and the spatial second moment. The value of 1.9 is adopted to keep consistency with previous works, where it was empirically calibrated (Solomon et al., 1987; Rosolowsky & Leroy, 2006). The GMC line width $\sigma_{obs,los}$ is measured from the stacked spectrum of each GMC and is deconvolved to account for the finite channel width. The GMC molecular gas mass M_{gas} is calculated from its total CO(2-1) luminosity ($L_{CO(2-1)}$) assuming the aforementioned global CO(2-1)/CO(1-0) line ratio, a standard CO-to-molecule conversion factor $\alpha_{CO(1-0)} = 4.3\ M_\odot\ (K\ km\ s^{-1}\ pc^2)^{-1}$ (yielding an effective $\alpha_{CO(2-1)} = 5.62\ M_\odot\ (K\ km\ s^{-1}\ pc^2)^{-1}$) and our assumed distance to NGC 1387. The molecular gas mass surface density of each GMC is simply $\Sigma_{gas} \equiv M_{gas}/\pi R_c^2$. It is not corrected for the cloud's inclination angle as a spherical geometry is assumed. An extrapolation is applied when measuring σ_x, σ_y, $\sigma_{obs,los}$ and $L_{CO(2-1)}$, whereby each quantity is measured as a function of the intensity threshold and extrapolated to zero intensity (equivalent to having infinite sensitivity). The uncertainty of each quantity is derived from 1000 bootstrap realisations of the pixels of each GMC. The potential systematic uncertainties are not included in the reported errors. The effects of confusion/crowding are discussed below.

As NGC 1387 is nearly face-on, the LoS confusion (i.e. multiple GMCs located along the same LoS) should be minimal for the thin molecular gas disc. More generally, when two GMCs are too close to each other in the sky plane (i.e. crowding) to be separated apart, we may identify two (or more) GMCs as a single one and thus potentially over-estimating the size, mass, and velocity dispersion of the GMC population. In terms of individual regions, the inner region has the highest surface number density of GMCs (see Figure 3.3) so that spatial crowding may be the most severe, but also the highest LoS velocity dispersion (see Figure 3.2) so that GMCs are more likely separable in the velocity

dimension to alleviate crowding. It is thus difficult to estimate the relative (and also absolute) severity of crowding across the regions unless simulation-aided tests are carried out. Although we cannot rule out the bias caused by confusion/crowding in our catalogue, it is not expected to be severe due to the high resolutions of the data in both dimensions (spatial and spectral), as GMC identification is done in 3D. Furthermore, if two GMCs are indeed spatially overlapping, it is conceptually equivalent to regarding them as one GMC with substructures. After all, the molecular ISM is a nested hierarchical structure with no particularly special physical scale, as discussed more in Chapter 4. In addition, we imposed the requirement of a convexity threshold to minimise the substructures in our identified GMCs (see Section 3.2.5). Our measurements and results do not change significantly across varied convexity thresholds, as tested in Appendix A. Therefore, we conclude the confusion/crowding effects should not jeopardise the credibility of our analyses.

The GMCs identified and their measured properties are listed in Table 3.1. For each GMC, additional properties listed include the (intensity-weighted) central position, (intensity-weighted barycentric) systemic velocity ($V_{\rm bc}$), brightness temperature of the brightest pixel ($T_{\rm max}$), internal velocity gradient ($\omega_{\rm obs}$), projected position angle of the angular momentum vector ($\phi_{\rm rot}$) and (deprojected) galactocentric distance ($R_{\rm gal}$), where the kinematic parameters $\omega_{\rm obs}$ and $\phi_{\rm rot}$ will be discussed in Section 3.4. To keep consistency with previous publications, the uncertainties of quantities measured with `CPROPSTOO` (i.e. $R_{\rm c}$, $\sigma_{\rm obs,los}$, $L_{\rm CO(2-1)}$ and $M_{\rm gas}$) are the median absolute deviation (MAD), which is the default output of the package. Other uncertainties (i.e. those of $\omega_{\rm obs}$ and $\phi_{\rm rot}$) are quoted at the 1σ level. The uncertainty of the adopted distance D to NGC 1387 is not propagated through the tabulated uncertainties of the measured quantities. This is because an error on the distance translates to a systematic (rather than random) scaling of some of the measured quantities (no effect on the others), i.e. $R_{\rm c} \propto D$, $L_{\rm CO(2-1)} \propto D^2$, $M_{\rm gas} \propto D^2$, $\omega_{\rm obs} \propto D^{-1}$ and $R_{\rm gal} \propto D$.

Table 3.1: GMC catalogue.

ID	RA (h:m:s)	Dec. (° : ′ : ″)	V_{bc} (km s^{-1})	R_c (pc)	$\sigma_{obs,los}$ (km s^{-1})	$L_{CO(2-1)}$ (10^4 K km s^{-1} pc^2)	M_{gas} (10^5 M$_\odot$)	T_{max} (K)	ω_{obs} (km s^{-1} pc^{-1})	ϕ_{rot} (degree)	R_{gal} (pc)
1	3:36:57.252	−35:30:21.60	1208.5	14 ± 26	1 ± 2	1 ± 2	0.6 ± 0.9	5.5	0.13 ± 0.02	21 ± 16	316
2	3:36:57.242	−35:30:21.29	1208.7	12 ± 12	3 ± 3	1.1 ± 0.5	0.6 ± 0.3	5.4	0.08 ± 0.02	134 ± 14	328
3	3:36:57.519	−35:30:21.70	1211.5	11 ± 15	-	1.4 ± 0.3	0.8 ± 0.2	8.4	-	-	585
4	3:36:57.500	−35:30:21.11	1212.0	10 ± 42	3 ± 3	1.1 ± 0.7	0.6 ± 0.4	4.6	0.10 ± 0.02	57 ± 15	584
5	3:36:57.663	−35:30:22.30	1213.1	12 ± 31	-	2 ± 3	1.2 ± 1.5	5.2	-	-	732
6	3:36:57.374	−35:30:21.95	1214.7	7 ± 16	4 ± 2	2.1 ± 0.6	1.2 ± 0.3	6.6	0.075 ± 0.008	14 ± 9	422
7	3:36:57.444	−35:30:21.71	1213.9	-	1.0 ± 1.3	0.6 ± 0.7	0.3 ± 0.4	4.4	-	-	503
8	3:36:57.474	−35:30:21.20	1215.1	16 ± 13	3 ± 2	3 ± 2	1.9 ± 1.0	8.7	0.125 ± 0.008	−49 ± 5	554
9	3:36:57.428	−35:30:21.09	1214.6	14 ± 5	5 ± 2	3.1 ± 0.6	1.7 ± 0.4	7.8	0.107 ± 0.007	12 ± 4	511
10	3:36:57.487	−35:30:18.62	1213.5	10 ± 20	1.8 ± 1.4	1.1 ± 1.2	0.6 ± 0.7	6.6	0.06 ± 0.02	142 ± 24	703
...	...	...	...	...	...	...	...	...	...	...	...
1285	3:36:56.827	−35:30:27.01	1361.7	-	2 ± 2	2 ± 2	1.0 ± 0.9	5.4	-	-	394

Notes: Measurements of M_{gas} assume a CO(2-1)/CO(1-0) line ratio of 0.77 ± 0.08 (in brightness temperature units) and a standard CO-to-molecule conversion factor $\alpha_{CO(1-0)} = 4.3$ M$_\odot$ (K km s^{-1} pc^2)$^{-1}$. To keep consistency with previous publications, the uncertainties of quantities measured in `CPROPSTOO` (i.e. R_c, $\sigma_{obs,los}$, $L_{CO(2-1)}$ and M_{gas}) are the median absolute deviation, which is the default output of the package. Other uncertainties (i.e. those of ω_{obs} and ϕ_{rot}) are quoted at the 1σ level. As noted in the text, the uncertainty of the adopted distance D to NGC 1387 was not propagated through the tabulated uncertainties of the measured quantities. This is because an error on the distance translates to a systematic (rather than random) scaling of some of the measured quantities (no effect on the others), i.e. $R_c \propto D$, $L_{CO(2-1)} \propto D^2$, $M_{gas} \propto D^2$, $\omega_{obs} \propto D^{-1}$ and $R_{gal} \propto D$. Table 3.1 is available in its entirety in machine-readable form in the electronic edition.

3.3.1 GMC property distributions

The most fundamental properties of GMCs are R_c, $\sigma_{obs,los}$ and M_{gas} (or Σ_{gas}). Figure 3.4 shows their distributions, for resolved (both spatially and spectrally) GMCs only and each region separately (colour coded). Gaussian fits are overlaid in matching colours. The means (standard deviations) of the fits are $\langle R_c \rangle$ = 20 pc (7 pc), $\langle \sigma_{obs,los} \rangle$ = 3.5 km s^{-1} (1.5 km s^{-1}), $\langle \log(M_{gas}/M_\odot) \rangle$ = 5.5 (0.4) and $\langle \log(\Sigma_{gas}/M_\odot\ pc^{-2}) \rangle$ = 2.4 (0.2).

There are some variations across the three regions. The strongest trend is that all four quantities decrease with radius, i.e. on average each quantity is the highest in the inner region and the lowest in the outer region (except for R_c in the inner and intermediate regions). Kolmogorov-Smirnov (KS) tests[9] are performed for the distributions in every pair of the three regions for each of these five quantities. All tests show significant differences at above five-sigma levels, except for a two-sigma difference of $\alpha_{obs,vir}$ between the inner and intermediate regions and a consistency (at 68% confidence level) of R_c between the inner and intermediate regions. These radial gradients will be quantified and discussed in more detail in Section 3.6. The mean R_c (20 pc) is only slightly larger than the synthesised beam size of 14 pc, so there might still be a tendency to identify GMCs of approximately such size, despite the range of scales probed.

The distributions of R_c and M_{gas} are overall slightly larger than those of the GMCs in the ETG NGC 4429, but the distribution of $\sigma_{obs,los}$ is overall slightly smaller (Liu et al., 2021). The GMC molecular gas mass surface densities (Σ_{gas}) have a wide distribution with a standard deviation of 0.2 dex. This is different from the presumed constant mass surface density of MW and Local Group GMCs (Larson, 1981), but similar to the distribution of the NGC 4429 GMCs (Liu et al., 2021).

3.3.2 Mass spectra

The distribution of GMC masses can help reveal the GMC formation and evolution mechanisms (e.g. Rosolowsky, 2005; Colombo et al., 2014; Freeman et al., 2017). Figure 3.5 shows the mass spectra (i.e. the cumulative mass distribution functions) of

[9]The python implementation is used, available at https://docs.scipy.org/doc/scipy/reference/generated/scipy.stats.kstest.html.

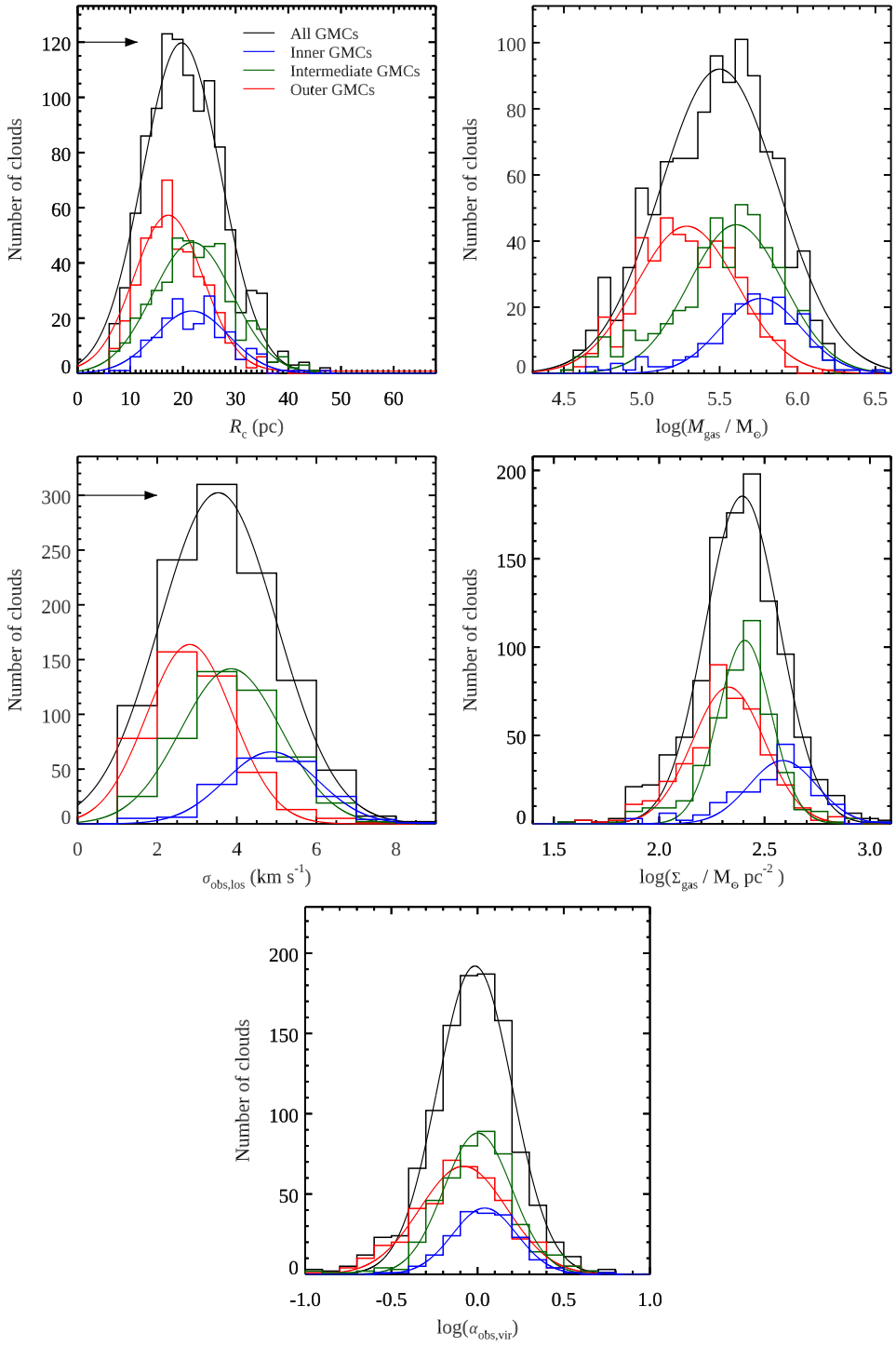

Figure 3.4: Distributions of the five fundamental GMC properties R_c (top-left), M_{gas} (top-right), $\sigma_{obs,los}$ (middle-left), Σ_{gas} (middle-right) and $\alpha_{obs,vir}$ (bottom). Only (spatially and spectrally) resolved GMCs are included, and the different regions are shown in different colours (black for the entire sample). Gaussian fits are overlaid in matching colours. The spatial and spectral resolutions are indicated by arrows in the panels of R_c and $\sigma_{obs,los}$, respectively. For R_c, the arrow length is $\eta\sqrt{\sigma_{maj}\sigma_{min}}$ = 11.4 pc, where the standard deviation of the synthesised beam major (minor) axis is $\sigma_{maj\,(min)} = \theta_{maj\,(min)}/2.35$. For $\sigma_{obs,los}$, the arrow length is the channel width of 2 km s^{-1}.

the NGC 1387 GMCs, where both resolved and unresolved GMCs are included, again for each region separately (colour coded). Horizontal error bars show the uncertainty of each GMC mass at the location where it contributes to the distribution. Although these are not strictly the uncertainties of the cumulative mass distribution functions, they provide a useful illustration of the uncertainties. We estimate the completeness limit of our data by adopting the common estimator $M_{\rm min} + 10\delta_{\rm M}$, where the first term is the minimum resolved GMC mass in our catalogue, 3.5×10^4 M$_\odot$, and $\delta_{\rm M}$ is the uncertainty induced by noise ($\delta_{\rm M} = 1.48\,MAD \times 2\Delta v \times \alpha_{\rm CO(2-1)} \times A_{\rm beam} = 9.9 \times 10^3$ M$_\odot$, where $MAD = 1.32$ K is the median absolute deviation of the whole corrected cube, the factor of 1.48 converts MAD to the commonly quoted standard deviation, $A_{\rm beam} = 225$ pc^2 is the area of the synthesised beam and $2\Delta v = 4$ km s^{-1} is the minimum spectral width of the GMCs). Our mass completeness limit is therefore estimated to be 1.3×10^5 M$_\odot$.

For each mass spectrum, we fit (in logarithmic space) the part above the mass completeness limit with both a single power law (dotted lines in Figure 3.5) and a broken power law (dashed lines in Figure 3.5). The two functions have the following forms, respectively:

$$\log\left(N(>M_{\rm gas})\right) = \log\left(\frac{M_{\rm gas}}{M_0}\right)^{\gamma+1},$$

$$\log\left(N(>M_{\rm gas})\right) = \log N_0 + \log\left(\left(\frac{M_{\rm gas}}{M_0}\right)^{\gamma+1} - 1\right),$$

where $N(>M_{\rm gas})$ is the number of GMCs with a mass higher than $M_{\rm gas}$, γ is the power-law slope, M_0 is the normalisation of the single power law but the characteristic cut-off mass of the broken power law and N_0 serves as the normalisation of the broken power law. The power-law index ($\gamma + 1$) is normally negative. Therefore, in the broken power law, $M_{\rm gas}$ must be smaller than M_0 for the formula to be meaningful. A truncation occurs when $M_{\rm gas}$ approaches M_0 and $\log\left(N(>M_{\rm gas})\right)$ decreases more quickly than a single power law. As can be seen in Figure 3.5, the advantage of the broken power law is that it can better reproduce the spectra at the high-mass ends, while the disadvantage is that the best-fitting slope is more sensitive to the few highest-mass bins than a single power-law fit. In fact, due to this sensitivity, and to reasonably match the totality of the spectra,

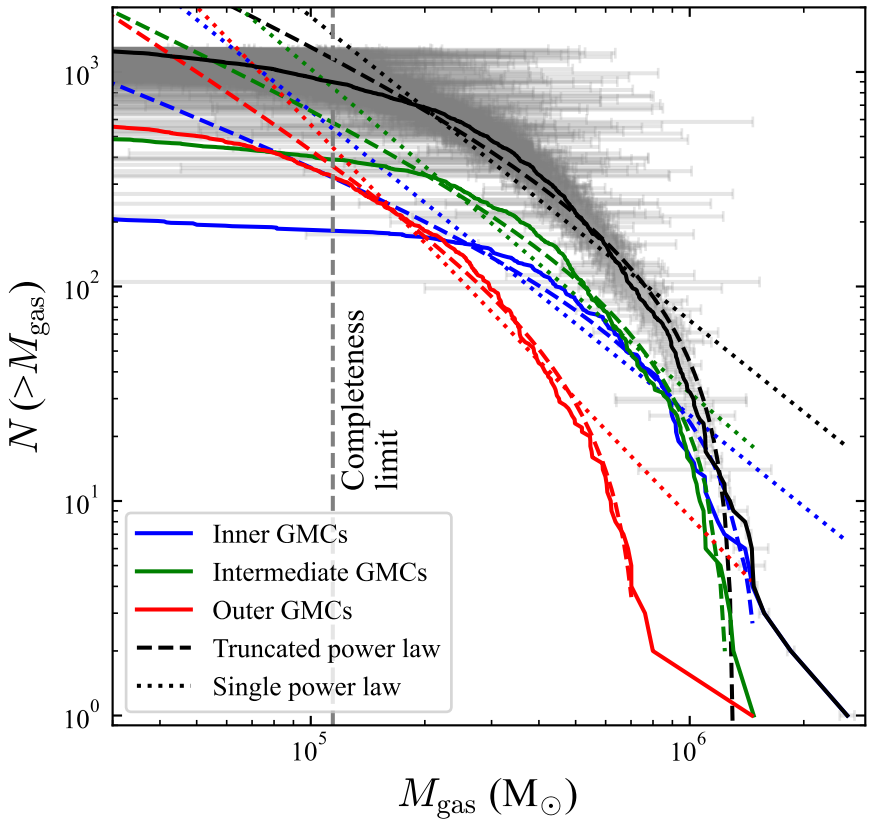

Figure 3.5: Mass spectra (i.e. cumulative mass distribution functions) of NGC 1387 GMCs. Both resolved and unresolved GMCs are included, and the different regions are shown in different colours (black for the entire sample). Best-fitting single power laws (dotted lines) and truncated power laws (dashed lines) are shown in matching colours. The nine most massive GMCs were excluded from the fit for the whole sample and the three most massive GMCs for each individual region, to avoid sensitivity to these few most massive bins. Grey horizontal error bars show the MAD uncertainty of each GMC mass at the location where it contributes to the distribution. The grey vertical dashed line indicates our mass completeness limit.

before fitting we remove the nine most massive GMCs from the whole sample and the three most massive GMCs from each individual region (for both functions).

The best fitting parameters are listed in Table 3.2. As demonstrated by Figure 3.5, the truncated power laws always match the mass spectra better than the single power laws, especially at the high-mass ends. Although the truncated power law is more suitable for this galaxy, we still present results of both function forms, following the convention in the literature (e.g. Rosolowsky, 2005) and for a more comprehensive comparison with previous publications. These truncations possibly indicate a cessation of active mass accumulation at the high-mass ends, but they could also be due to a selection bias towards

GMCs of radii similar to the synthesised beam size. Regarding the different regions, the best-fitting parameters (of the truncated power law) are all significantly different across regions, echoing the significant differences revealed by the KS test in Section 3.3.1. Although the four most massive GMCs are located in the inner region (blue curves), the intermediate region has roughly the same number of GMCs with $M_{\rm gas} > 10^6$ M$_\odot$ as the inner region. The inner-region GMCs have the shallowest power-law slopes while the outer-region GMCs have the steepest, irrespective of the function used. As expected, the slopes of the truncated power laws are always shallower than those of the single power laws. The best-fitting truncated power-law slope of the whole GMC sample is -1.820 ± 0.013. This is between the slope of inner MW GMCs (-1.6 ± 0.1, where 'inner' only includes those GMCs closer to the MW centre than the Sun) and outer MW GMCs (-2.2 ± 0.1, where 'outer' only includes those GMCs farther away from the MW centre than the Sun; Rice et al. 2016). In fact, the slope of the NGC 1387 GMCs has a similar radial trend, steepening from ≈ -1.7 in the inner region to ≈ -2.1 in the outer region. The best-fitting slope of the whole GMC sample of NGC 1387 is slightly steeper than that of the overall mass spectrum of Local Group GMCs (≈ -1.7; Blitz et al. 2007), it is shallower than that of the ETG NGC 4429 (-2.18 ± 0.21; Liu et al. 2021), and it is much shallower than that of another ETG NGC 4526 (-2.39 ± 0.03; Utomo et al. 2015). These comparisons are summarised in Table 3.3. The cut-off mass of the truncated power-law fit of the whole sample is $(1.533 \pm 0.004) \times 10^6$ M$_\odot$, similar to that of the outer MW GMCs ($(1.5 \pm 0.5) \times 10^6$ M$_\odot$; Rice et al. 2016) but much smaller than that of the inner MW GMCs ($(1.0 \pm 0.2) \times 10^7$ M$_\odot$; Rice et al. 2016). The cut-off mass in NGC 4429 ($(8.8 \pm 1.3) \times 10^5$ M$_\odot$; Liu et al. 2021) is lower than that of the NGC 1387 GMCs, but that in NGC 4526 ($(4.12 \pm 0.08) \times 10^6$ M$_\odot$; Utomo et al. 2015) is higher. These comparisons are summarised in Table 3.4. Overall, the NGC 1387 GMC mass spectra are quite similar to that of MW disc GMCs, with some variations at different galactocentric distances.

3.3.3 Larson relations

Nearly all previous GMC studies have used the Larson relations (Larson, 1981) as the common yardstick against which to gauge GMC properties. Figure 3.6 shows the Larson

Table 3.2: Best-fitting parameters of NGC 1387 GMC mass spectra.

	Single power law		Truncated power law		
	γ	M_0 (10^6 $M_\odot$)	γ	M_0 (10^6 $M_\odot$)	N_0
All GMCs	-2.42 ± 0.02	23.3 ± 1.2	-1.820 ± 0.013	1.533 ± 0.004	180 ± 5
Inner-region GMCs	-2.42 ± 0.05	11.4 ± 1.2	-1.67 ± 0.05	1.82 ± 0.02	69 ± 8
Intermediate-region GMCs	-2.51 ± 0.03	11.6 ± 0.8	-1.82 ± 0.02	1.487 ± 0.006	95 ± 5
Outer-region GMCs	-2.83 ± 0.03	3.8 ± 0.2	-2.13 ± 0.02	0.873 ± 0.004	50 ± 2

Notes: The fitting parameters are described in Section 3.3.2. Due to the sensitivity of the truncated power-law function to the few highest-mass bins, and to reasonably match the totality of the spectra, the nine most massive GMCs of the whole GMC sample were excluded from the fit and the three most massive GMCs of each individual region (for both functions). Uncertainties are quoted at the 1σ level.

Table 3.3: Slope comparison between NGC 1387 and other galaxies.

Galaxy (region)	Slope (descending order)	Reference
MW (inner)	-1.6 ± 0.1	Rice et al. (2016)
NGC 1387 (inner)	-1.67 ± 0.05	This work
Local Group (overall)	-1.7	Blitz et al. (2007)
NGC 1387 (overall)	-1.820 ± 0.013	This work
NGC 1387 (inter.)	-1.82 ± 0.02	This work
NGC 1387 (outer)	-2.13 ± 0.02	This work
NGC 4429 (overall)	-2.18 ± 0.21	Liu et al. (2021)
MW (outer)	-2.2 ± 0.1	Rice et al. (2016)
NGC 4526 (overall)	-2.39 ± 0.03	Utomo et al. (2015)

Notes: For NGC 1387 GMCs, the truncated power law slopes are adopted for comparison.

Table 3.4: Cut-off mass comparison between NGC 1387 and other galaxies.

Galaxy (region)	Cut-off mass (10^5 $M_\odot$; descending order)	Reference
MW (inner)	100 ± 20	Rice et al. (2016)
NGC 4526	41.2 ± 0.8	Utomo et al. (2015)
NGC 1387 (inner)	18.2 ± 0.2	This work
NGC 1387 (overall)	15.33 ± 0.04	This work
NGC 1387 (inter.)	14.87 ± 0.06	This work
MW (outer)	15 ± 5	Rice et al. (2016)
NGC 1387 (outer)	8.73 ± 0.04	This work
NGC 4429	8.8 ± 1.3	Liu et al. (2021)

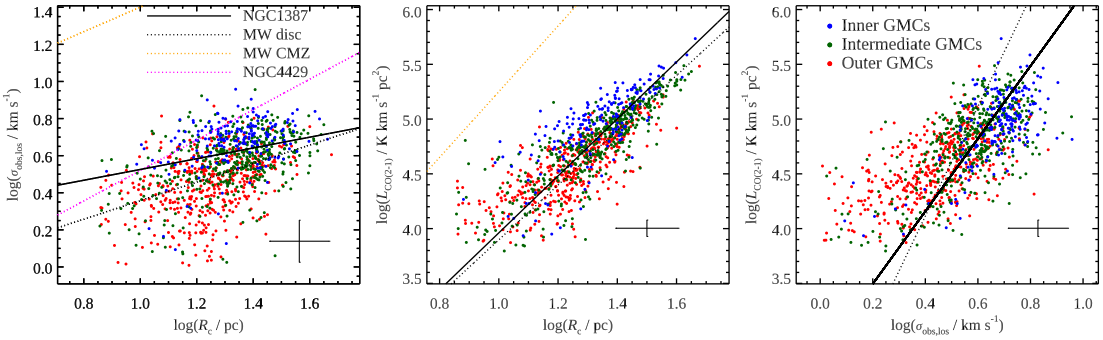

Figure 3.6: Larson relations of the resolved GMCs of NGC 1387. **Left:** size – line width relation. **Middle:** size – luminosity relation. **Right:** line width – luminosity relation. The GMCs of the different regions are shown in different colours. Solid lines show the best-fitting power-law relations of all the GMCs, while the black dotted lines show the Larson relations of the MW disc GMCs, the orange dotted lines those of the MW CMZ GMCs, and the magenta dotted line those of the ETG NGC 4429. The median MAD error bar is shown in the bottom-right corner of each panel.

relations of the resolved GMCs of NGC 1387. GMCs from different regions of NGC 1387 are shown in different colours. The left panel shows the size – line width relation, thought to be a signature of the turbulence within GMCs. The middle panel shows the size – luminosity relation (equivalent to a size – molecular gas mass relation, as we are assuming a constant mass conversion factor), providing insight into the internal structures of GMCs. The right panel shows the line width – luminosity relation (again equivalent to a line width – molecular gas mass relation), the GMC analogue of the Faber-Jackson relation of galaxies (Solomon et al., 1987). These three relations together constitute the GMC 'fundamental plane', but only two out of the three relations are independent as they are mathematically related.

The GMCs from different regions of NGC 1387 occupy slightly different areas of parameter space, consistent with the slight regional variations of GMC properties illustrated in Figure 3.4. In the size – line width relation, the inner-region GMCs (blue data points) occupy primarily the top-right portion of the distribution, at slightly larger sizes and velocity dispersions than the intermediate-region GMCs (green data points). The outer-region GMCs (red data points) have a distribution that is much more extended than that of the inner-region and intermediate-region GMCs, and is centred at smaller sizes and velocity dispersions. The trends are similar in the other two Larson relations. For each relation, we fit a power law to both the entire resolved GMC population and that

in each region. The fits are carried out in logarithmic space. The best-fitting relations of the entire population are shown as the black solid lines in Figure 3.6, where they can be compared to those of the MW disc GMCs (black dotted lines; Solomon et al. 1987; Heyer et al. 2009), CMZ GMCs (orange dotted lines; Kauffmann et al. 2017; Li & Zhang 2020), and the ETG NGC 4429 (magenta dotted line; Liu et al. 2021). The best-fitting parameters are listed in Table 3.5.

Table 3.5: Larson relation best-fitting parameters.

	Size – line width relation			Size – luminosity relation			Line width – luminosity relation		
	Slope	Normalisation	Correlation coefficient	Slope	Normalisation	Correlation coefficient	Slope	Normalisation	Correlation coefficient
All GMCs	0.29 ± 0.11	0.24 ± 0.15	0.47	2.60 ± 0.11	1.4 ± 0.2	0.82	3.3 ± 0.4	2.8 ± 0.3	0.70
Inner-region GMCs	0.07 ± 0.13	0.6 ± 0.2	0.31	2.2 ± 0.2	2.0 ± 0.3	0.78	3.3 ± 1.3	2.7 ± 0.9	0.50
Intermediate-region GMCs	0.4 ± 0.2	0.0 ± 0.2	0.43	2.3 ± 0.2	1.7 ± 0.3	0.87	4.3 ± 1.0	2.3 ± 0.6	0.60
Outer-region GMCs	0.3 ± 0.4	0.1 ± 0.5	0.39	2.4 ± 0.3	1.6 ± 0.4	0.77	3.6 ± 1.0	2.8 ± 0.5	0.57

Notes: Uncertainties are quoted at the 1σ level.

For the whole GMC population, the Spearman correlation coefficients of the resolved GMCs of NGC 1387 are weak (0.47) for the size – line width relation, strong (0.82) for the size – luminosity relation and moderate (0.70) for the line width – luminosity relation. The correlation coefficients of the GMCs of the different regions considered separately are almost always weaker, suggesting that the aforementioned systematic differences between the different regions contribute to creating the correlations when they are considered together. In other words, the galactocentric distance gradients of the three basic GMC parameters (R_c, $\sigma_{obs,los}$ and $L_{CO(2-1)}$) are significant. This will be shown more clearly in Section 3.6.

In all panels of Figure 3.6, the resolved GMCs of NGC 1387 follow the trend of the MW disc GMCs quite well, in terms of both slope and normalisation. In turn, this implies that they are unlike those of most other ETGs, which typically have velocity dispersions higher than those of MW disc GMCs at any given size (Liu et al., 2021) and luminosity (Utomo et al., 2015). Despite the fact that all of the NGC 1387 GMCs are located within its bulge, the properties of these GMCs deviate significantly from those of the CMZ GMCs. The size – line width relation of the NGC 1387 GMCs even has a shallower slope (0.29 ± 0.11) than that of the MW disc (0.5 ± 0.1) or Local Group (0.6 ± 0.1) GMCs. This is rather unique and will be discussed in light of a GMC collision model in Section 3.5. When considering the regions separately, the Larson relation best-fitting parameters can vary significantly. Specifically, the inner-region GMCs have an extremely flat size – line width relation with a slope of 0.07 ± 0.13, again contrary to the MW in which the CMZ GMCs have a much steeper size – line width relation (0.66 ± 0.18). The variation of the normalisation again mostly reflects the galactocentric distance gradients.

3.3.4 Virial parameter

We estimate the virial parameters $\alpha_{obs,vir}$ of the resolved GMCs of NGC 1387. The virial parameter is defined as the ratio of the virial mass (i.e. the dynamical mass assuming virial equilibrium $M_{obs,vir}$; MacLaren et al. 1988) and the molecular gas mass of a GMC, yielding

$$\alpha_{obs,vir} \equiv \frac{M_{obs,vir}}{M_{gas}} = \frac{\sigma^2_{obs,los} R_c / b_s G}{M_{gas}} , \tag{3.1}$$

where G is the gravitational constant and the geometric parameter b_s is taken to be $1/5$, corresponding to a homogeneous spherical mass volume density distribution (and allowing to compare to most previous works on GMCs).

Figure 3.7 shows the comparison of the virial masses and the molecular gas masses of the resolved GMCs of NGC 1387. GMCs from different regions of NGC 1387 are shown in different colours, as in previous figures. Although the GMCs from different regions occupy slightly different mass ranges, they generally follow the same trend. A power-law fit (carried out in logarithmic space) yields a best-fitting power-law index (i.e. a slope) of 0.84, suggesting that the estimated GMC virial masses are very similar to the molecular gas masses. Indeed, the distribution of the virial parameters of the resolved GMCs of NGC 1387 is shown in the inset of Figure 3.7, and 80% of the GMCs have $0.5 < \alpha_{\rm obs,vir} < 2$. The resolved GMCs of NGC 1387 thus appear to be nearly perfectly virialised ($\alpha_{\rm obs,vir} = 1$), with some scatter. A Gaussian fit to the log-normal distribution of $\alpha_{\rm obs,vir}$ yields a mean virial parameter $\langle\alpha_{\rm obs,vir}\rangle = 1.0$ with a standard deviation of $^{+0.6}_{-0.4}$. This is very similar to that of the MW disc (Heyer & Dame, 2015) and Local Group (e.g. Rosolowsky et al., 2003; Rosolowsky, 2007; Hirota et al., 2011) GMCs, but is lower than that of the ETG NGC 4429 GMCs ($\langle\alpha_{\rm obs,vir}\rangle = 4.0$; Liu et al. 2021). Compared with the empirical threshold of $\alpha_{\rm obs,vir} = 2$ for a gravitationally bound cloud (Kauffmann et al., 2013), the $\alpha_{\rm obs,vir}$ distribution indicates that, on average, the resolved GMCs of NGC 1387 are virialised and gravitationally bound. When GMCs are separated by regions in Figure 3.4, there is a marginal decreasing trend of $\alpha_{\rm obs,vir}$ from the inner region to the outer region.

We note however that this interpretation only considers the internal gravitational force of the GMCs. Other factors such as magnetic fields, external pressure and galaxy forces are not included in the above calculation of $\alpha_{\rm obs,vir}$. The virial parameter also suffers from a systematic uncertainty of about 30% associated with the CO-to-molecular gas conversion factor (Bolatto et al., 2013). In fact, Zabel et al. (2019) used a metallicity-dependent CO-to-H_2 conversion factor, yielding $X_{\rm CO} = (1.1\pm0.7)\times10^{20}$ cm^{-2} (K km s^{-1})$^{-1}$ for NGC 1387, a factor of roughly two smaller than ours, which would lead to virial parameters $\alpha_{\rm obs,vir}$ larger than ours by the same factor of roughly two. Nonetheless, given the large uncertainty

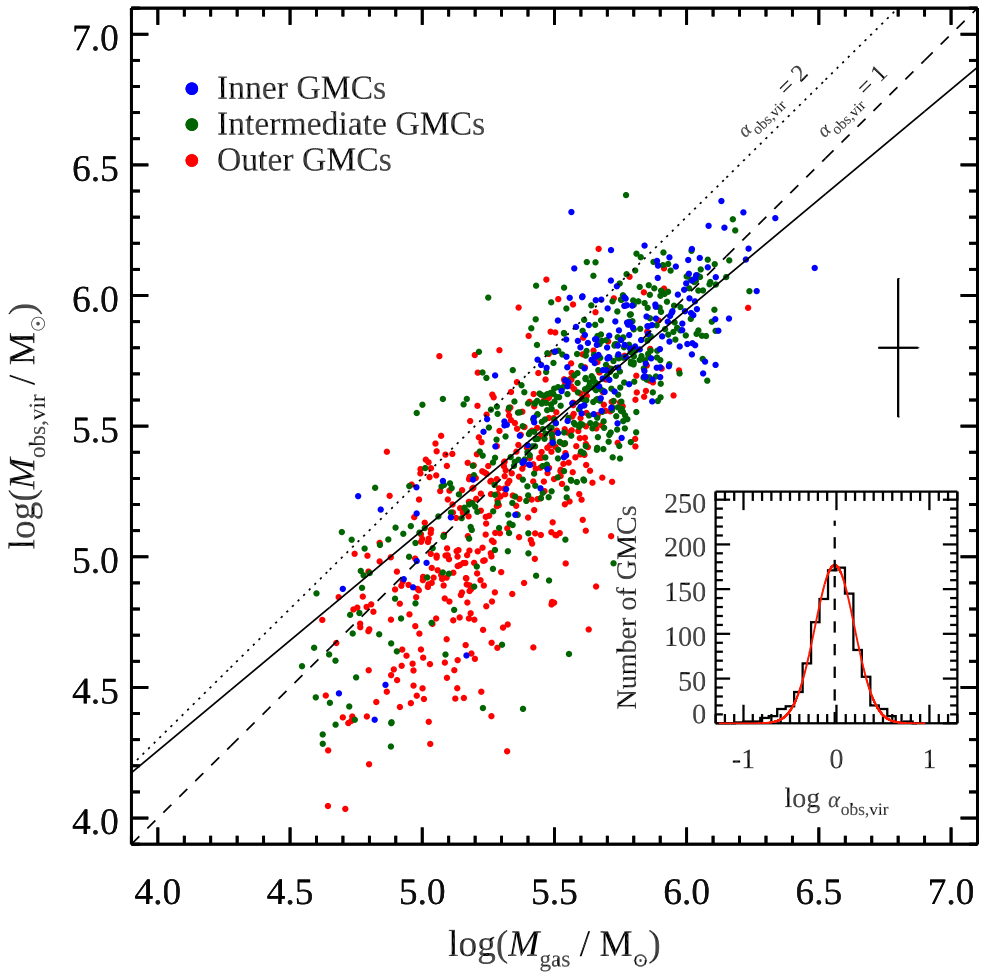

Figure 3.7: Correlation between the virial masses and the molecular gas masses of the resolved GMCs of NGC 1387. The GMCs of the different regions are shown in different colours. The solid line shows the best-fitting power-law relation, while the dashed and dotted diagonal lines show the $1:1$ ($\alpha_{obs,vir} = 1$) and $2:1$ ($\alpha_{obs,vir} = 2$) relations, respectively. The median MAD error bar is shown in the centre-right of the panel. The distribution of $\log(\alpha_{obs,vir})$ (black histogram) with a log-normal fit overlaid (red solid line) is shown in the inset. The dashed vertical line shows the mean of the log-normal fit.

of the gas-phase metallicity, and the resulting large uncertainty of the metallicity-dependent conversion factor, the two conversion factors are still in marginal agreement.

3.4 Origin of velocity gradients in GMCs

3.4.1 Galactic rotation and turbulence

We now aim to constrain the origin of the internal kinematics of the GMCs of NGC 1387, in particular, whether it is inherited from the large-scale galactic rotation. In the ETGs

NGC 4526 and NGC 4429, the internal GMC rotation is aligned with the large-scale velocity field, suggesting that shear (i.e. galactic rotation) drives the observed internal GMC rotation (see e.g. Figs. 7 and 8 of Liu et al. 2021). Following the same approach, we measure the internal rotation of each GMC by fitting a plane to its first-moment map, weighted by intensity (i.e. the zeroth-moment map). The fitting function is thus $v(x, y) = ax + by + c$, where (x, y) are the positions on the sky and a, b and c are free parameters. The projected angular velocity (i.e. the magnitude of the projected velocity gradient) is then $\omega_{\rm obs} = \sqrt{a^2 + b^2}$, and the projected position angle (measured from north through east) of the rotation axis is $\phi_{\rm rot} = \tan^{-1}(b/a)$.

We show the projected angular velocity vectors of the resolved GMCs of NGC 1387 overlaid on the isovelocity contours (i.e. the velocity field) in Figure 3.8 (only half the GMCs, randomly selected, are shown for clarity). To calculate the isovelocity contours, we input the mass model described in Section 3.2.3 to the `mge_vcirc` routine of the `Jean Anisotropic Modelling` (`JAM`) package[10] (Cappellari, 2020), and then used the `kinms_create_velField_oneSided` routine of the `KinMS` package to create the line-of-sight velocity map.

In Figure 3.8, the projected angular velocity vectors do not align significantly with the large-scale galactic rotation, as traced by the isovelocity contours. Dividing the GMCs into prograde (black arrows in Figure 3.8) and retrograde (dark grey arrows), based on the angle between each cloud's projected angular velocity vector and the local isovelocity contour (and adopting an angle of 90° as the threshold), the fraction of prograde clouds is larger than that of retrograde clouds in all three regions (and thus overall), although that fraction never approaches unity. In addition, there is a slightly larger fraction of prograde GMCs in the inner region ($141/195 = 72\%$) than in the intermediate region ($278/448 = 62\%$) and outer region ($256/436 = 59\%$) of the galaxy. This suggests that the inner-region GMCs couple best with the large-scale galactic rotation, and we elaborate on this in Section 3.4.4.

In Figure 3.9, the measured $\omega_{\rm obs}$ and $\phi_{\rm rot}$ are compared with modelled quantities ($\omega_{\rm mod}$ and $\phi_{\rm mod}$), where the latter is measured in an identical manner but using a model data cube with circular velocity $v_{\rm circ}(R)$. As a result, $\phi_{\rm mod}$ is along the local isovelocity

[10] https://pypi.org/project/jampy/

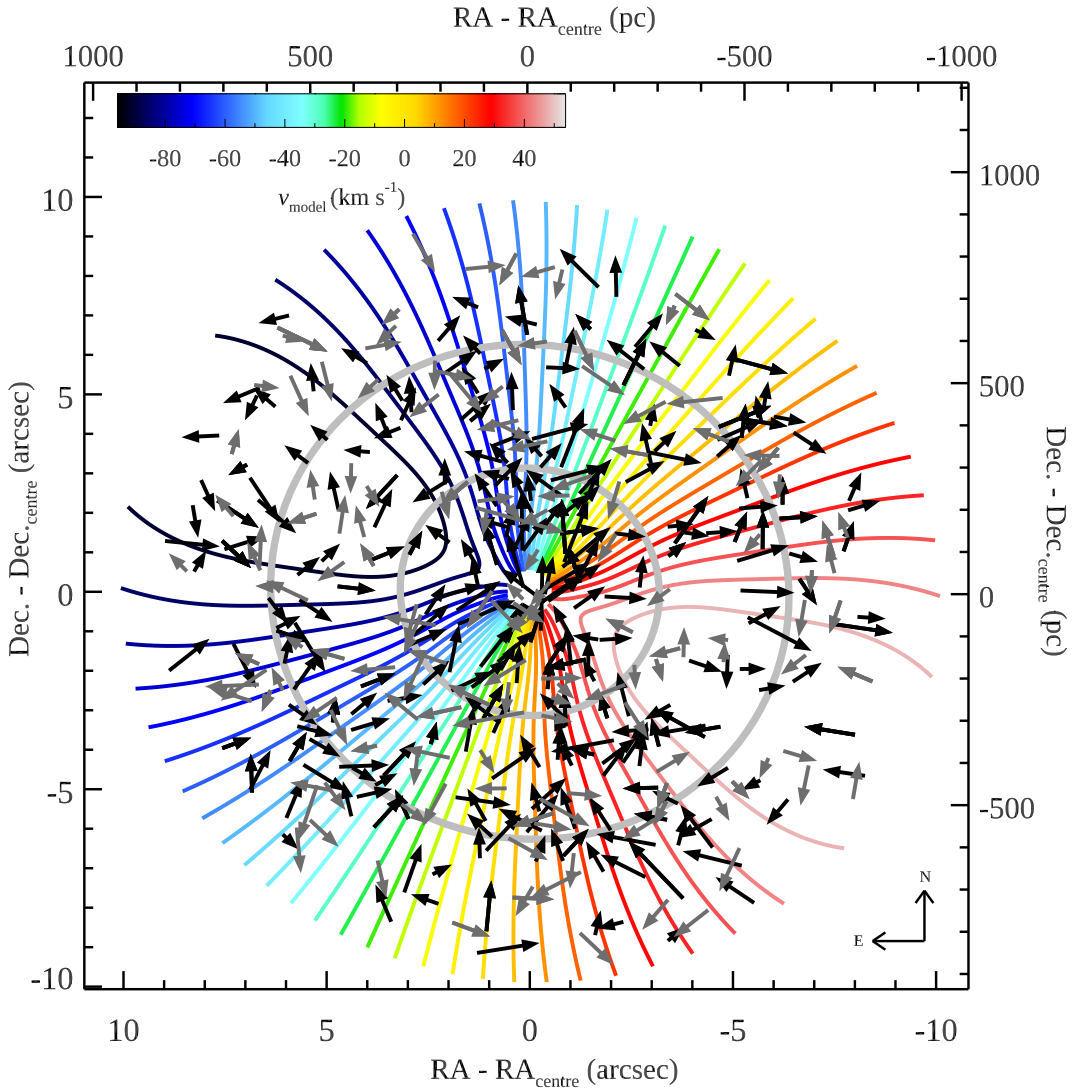

Figure 3.8: Projected circular velocity field of NGC 1387 ($v_{\rm model}$; coloured isovelocity contours). The projected angular momentum vectors of half of the resolved GMC of NGC 1387 (randomly selected; for clarity) are overplotted as arrows. Black arrows indicate prograde GMCs while dark grey arrows indicate retrograde GMCs, and the length of each arrow is proportional to $\omega_{\rm obs}$. The pale grey ellipses indicate the boundaries of the three regions defined in Section 3.2.4.

contour while $\omega_{\rm mod}$ is the magnitude of the expected velocity gradient. As can be inferred from the left panel of Figure 3.9 by comparing the three different regions, $\omega_{\rm mod}$ decreases with increasing galactocentric distance. All GMCs with $\omega_{\rm mod} > 0.55$ km s^{-1} are within the central region of $R_{\rm gal} < 100$ pc. Vice versa, 80% of GMCs at $R_{\rm gal} < 100$ pc have $\omega_{\rm mod} > 0.55$ km s^{-1}. This is due to a higher density of isovelocity contours in the central parts of the galaxy, partially resulting from the line-of-sight projection. Most importantly, in both panels of Figure 3.9, there is no significant correlation between the observed and modelled quantities. This is true for both the whole sample and the GMCs of individual regions only. The few GMCs with drastically large discrepancies between $\omega_{\rm mod}$ and $\omega_{\rm obs}$ (bottom-right corner of the top-left panel) result from the large $\omega_{\rm mod}$ and the rather average $\omega_{\rm obs}$. It shows the velocity gradients of these central GMCs may be decoupled from the disc rotation. It is worth noting that beam smearing may cause underestimates in the observed velocity gradients. While this effect does not directly alter the velocity of any pixels (or the largest velocity difference) within a GMC, it increases the spatial size and thus decreases the velocity gradient. Given the criteria of a resolved GMC (deconvolved radius larger than half of the beam size), beam smearing can cause the velocity gradient to be underestimated by a factor of up to 1.9. Thus, this can only be a minor reason for the large discrepancy (by a factor of $\approx$ 5–15) seen in these GMCs. The physical interpretation of kinematic decoupling of these GMCs is still robust. The inner-region GMCs (blue data points) may have a weak positive correlation, but almost all inner-region GMCs have $\omega_{\rm obs} < \omega_{\rm mod}$. We come back to this sub-population of GMCs in Section 3.4.4.

One caveat of studying the internal GMC kinematics of NGC 1387 is the near–face on orientation. If the origin of the velocity gradient is indeed the shear effect, the highest magnitude should be seen when the gas disc is edge-on. At a disc inclination of only 13.°6, the projected predicted velocity gradients of GMCs are on average $\omega_{\rm mod} = 0.10$ km s^{-1} (median). By multiplying $\omega_{\rm mod}$ and $2R_{\rm c}$, we calculate the median expected LoS velocity difference within GMCs to be 3.7 km s^{-1}. At a channel width as well as velocity resolution of 2 km s^{-1}, this expected velocity difference caused by shear is only marginally resolved.

An alternative potential origin for the internal velocity gradients of GMCs is turbulence. Given the limited spatial resolution of our data, we can not currently measure the internal

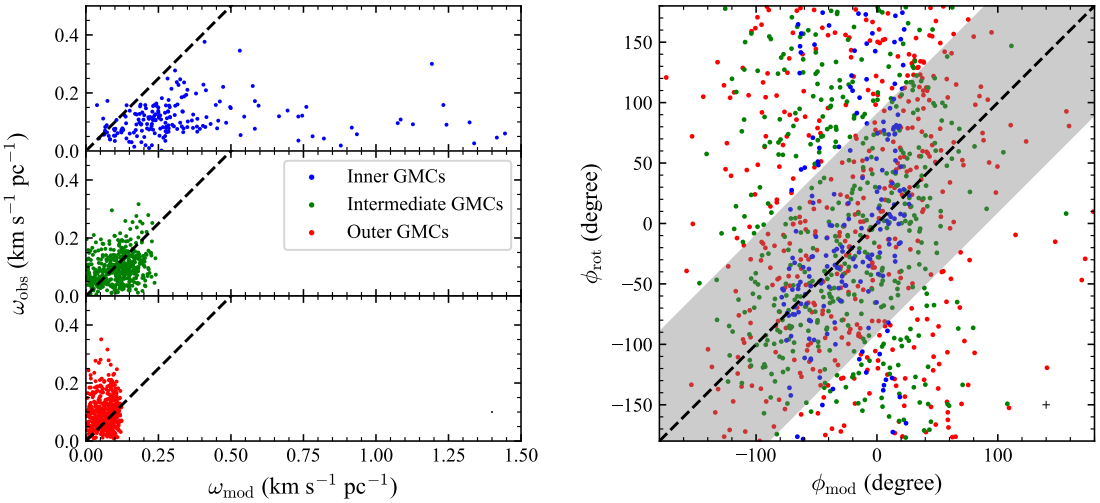

Figure 3.9: Comparison of the observed and modelled projected GMC angular velocity magnitudes $\omega_{\rm obs}$ (left panel) and position angles $\phi_{\rm rot}$ (right panel) of the resolved GMCs of NGC 1387. The GMCs of the different regions are shown in different colours. The dashed lines show the 1 : 1 relations. The grey shaded region in the right panel indicates an angular difference $\leq 90°$, which we adopt to define prograde clouds (conversely for retrograde clouds). The median 1σ uncertainty is shown as an error bar in the bottom-right corner of each panel (barely visible in the left panel).

turbulence of the clouds. The velocity gradients caused by turbulence can however be estimated in simulations, and Burkert & Bodenheimer (2000) report $(\omega_{\rm obs}/{\rm km\ s^{-1}\ pc^{-1}}) = 1.6(R_{\rm c}/0.1\ {\rm pc})^{-1/2}$. The expected $\omega_{\rm obs}$ caused by turbulence for GMCs of the sizes observed in NGC 1387 is thus $0.1 - 0.2$ km s^{-1} pc^{-1}, of the same scale as the measured $\omega_{\rm obs}$. Turbulence might thus be at the origin of the observed GMC velocity gradients of NGC 1387, although further evidence is required to confirm this.

3.4.2 Tidal radii

To further understand the potential impacts of external (i.e. the galaxy's) gravity on the clouds, we estimate the tidal radii $R_{\rm t}$ of the resolved GMCs of NGC 1387, defined as the distance from each GMC centre where the shear velocity due to differential galactic rotation is equal to the escape velocity of the GMC (Gammie et al., 1991; Tan, 2000). We adopt a simplified form from equation (52) of Liu et al. (2021), which assumes a spherical galaxy mass distribution:

$$R_{\rm t} = \left(\frac{G}{2A^2}\right)^{1/3} M_{\rm gas}^{1/3}\ , \tag{3.2}$$

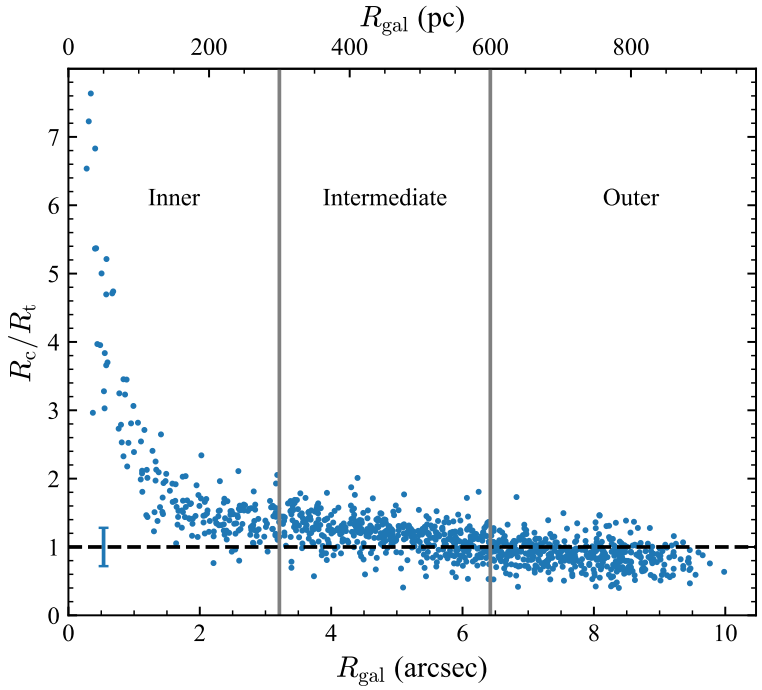

Figure 3.10: Measured GMC size to predicted tidal radius ratios ($R_{\rm c}/R_{\rm t}$) of the resolved GMCs of NGC 1387, as a function of GMC galactocentric distance $R_{\rm gal}$. The black horizontal dashed line indicates $R_{\rm c} = R_{\rm t}$ and also shows the median MAD uncertainty of $R_{\rm c}/R_{\rm t}$ as a vertical error bar in the bottom-left corner. The pale grey vertical lines indicate the boundaries of the three regions defined in Section 3.2.4.

where A is Oort's constant A evaluated at the galactocentric distance of the GMC.

The measured GMC size to predicted tidal radius ratios ($R_{\rm c}/R_{\rm t}$) of the resolved GMCs of NGC 1387 are shown as a function of GMC galactocentric distance $R_{\rm gal}$ in Figure 3.10. Overall, most GMCs have sizes similar to their tidal radii, suggesting that most GMCs are too dense for galactic shear to have a significant impact. In other words, most clouds are dominated by self-gravity rather than external gravity, although it could be that the cloud sizes have been limited by external gravity in the first place (thus driving $R_{\rm c}/R_{\rm t}$ to 1). These results are consistent with the virial parameters estimated in Section 3.3.4 and the kinematic analyses presented in Section 3.4.1, showing that most GMCs are decoupled from the large-scale galactic velocity field.

Figure 3.10 however also reveals a strong trend with galactocentric distance, whereby the inner-region GMCs essentially all have $R_{\rm c} > R_{\rm t}$, and their $R_{\rm c}/R_{\rm t}$ ratio increases rapidly with decreasing galactocentric distance. This primarily arises from rapidly increasing

A (i.e. shear) and thus rapidly decreasing R_t with decreasing galactocentric distance, as R_c varies little with R_{gal} (see Figure 3.4). This suggests that external gravity is more important than self-gravity for the inner-region GMCs, and that its importance decreases with increasing galactocentric distance, as expected. In turn, this suggests that the inner-region GMCs can not be gravitationally bound (although they could be bound by other forces). While the virial parameters of the inner-region GMCs are indeed higher than those of the clouds farther out (see Figure 3.4), they remain overall modest, only a few inner-region clouds having $\alpha_{obs,vir} > 2$. The implications for the gravitational boundedness of the inner-region clouds arising out of the R_c/R_t ratio analysis and the virial parameters thus appear contradictory. The concept of R_t is based on the assumption that the entire GMC follows the galactic circular velocity field. Throughout Section 3.4, we see this assumption does not hold for GMCs of NGC 1387, and more specifically not for the subsample of GMCs with $R_c > R_t$ (see Section 3.4.4). This may explain the limited predicting power of R_t regarding cloud boundedness indicated by $\alpha_{obs,vir}$.

3.4.3 Galactic rotation and GMC velocity gradients

Although the observed internal velocity gradients of GMCs discussed in Section 3.4.1 appear to arise primarily from internal turbulence, the fraction of prograde clouds is significantly greater than 50% in all three regions, so the contribution of the large-scale galactic rotation to the gradients is potentially non-negligible. We try to quantify this contribution in this sub-section, and follow Utomo et al. (2015) and Liu et al. (2021) by estimating the 'gradient-subtracted velocity dispersion' $\sigma_{gs,los}$ of each cloud, arguably a better tracer of internal GMC turbulence than $\sigma_{obs,los}$.

The quantity $\sigma_{gs,los}$ is estimated with the intention to remove the contribution of ordered internal bulk rotation from $\sigma_{obs,los}$. All the spectra of a given GMC along different lines of sight are thus shifted (according to their mean velocities) to a common systemic velocity before being stacked for the measurement of (the now gradient-subtracted) $\sigma_{gs,los}$. Under the assumption that internal GMC bulk motions arise purely from large-scale galactic circular rotation, the quadratic difference can be expressed as

$$\sigma^2_{obs,los} - \sigma^2_{gs,los} \approx b_e R_c^2 \left[\Omega^2 \sin^2\theta + (\Omega - 2A)^2 \cos^2\theta\right] \sin^2 i \qquad (3.3)$$

(see equations 19, 20, and B23 of Liu et al. 2021), where i is the disc inclination, θ the azimuthal angle of the GMC in the galaxy plane and Ω the galactic circular angular velocity evaluated at the galactocentric distance of the GMC (i.e. $v_{\rm circ}(R_{\rm gal})/R_{\rm gal}$). The geometric parameter $b_{\rm e}$ is again taken to be $1/5$, corresponding to a homogeneous mass volume density distribution (and allowing to compare to most previous works on GMCs).

By comparing the measured and modelled differences $\sigma^2_{\rm obs,los} - \sigma^2_{\rm gs,los}$, we can assess the contribution of the large-scale galactic circular rotation to the GMC velocity gradients. Figure 3.11 shows this comparison for all resolved GMCs of NGC 1387. Different panels show the same measurements with different colour coding ($R_{\rm gal}$, $M_{\rm gas}$ and $R_{\rm c}$). The overall distribution shows at best a very weak positive correlation between the observed and modelled quantities, far from the one-to-one line expectation. However, larger, more massive GMCs at small galactocentric distances tend to be closer to the one-to-one line. This suggests that the GMCs of this particular sub-sample have their velocity gradients dominated by large-scale galaxy rotation, while most other GMCs are dominated by internal turbulence, in agreement with the $R_{\rm c} - R_{\rm t}$ comparison discussed in Section 3.4.2.

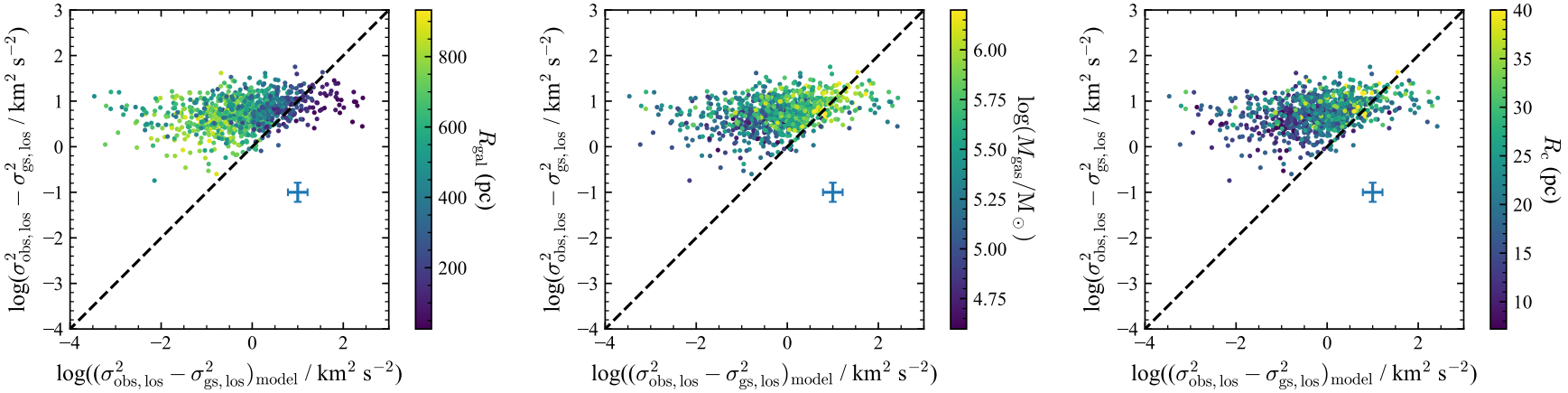

Figure 3.11: Comparison of the observed and modelled differences $\sigma^2_{\rm obs,los} - \sigma^2_{\rm gs,los}$ for the resolved GMCs of NGC 1387. From left to right, different panels show the same measurements with different colour coding: $R_{\rm gal}$, $M_{\rm gas}$ and $R_{\rm c}$. The dashed lines show the 1 : 1 relations. The median MAD error bar is shown in the central-right region of each panel.

We note that the limited spectral resolution (channel width of 2 km s^{-1}) of the data could cause a bias to the measured $\sigma_{obs,los}$ and thus $\sigma^2_{obs,los} - \sigma^2_{gs,los}$ (without affecting the modelled $\sigma_{gs,los}$). This bias is hard to quantify, but it should be more pronounced for smaller $\sigma_{obs,los}$ and thus smaller $\sigma^2_{obs,los} - \sigma^2_{gs,los}$.

3.4.4 GMC sub-samples

Although the overall GMC population of NGC 1387 does not seem to be significantly affected by the large-scale galactic rotation, a specific sub-sample (primarily large and massive inner-region GMCs) does seem to be. Using clues from the previous sub-sections, we thus construct three specific GMC sub-samples to test this possibility, requiring $R_c > 30$ pc, $M_{gas} > 10^6$ $M_\odot$ and $\Sigma_{gas} < \Sigma_{shear}$, respectively, where $\Sigma_{shear} = 4A^2R_c/3\pi G$ is the minimum surface mass density required to be remain bound against shear (Liu et al., 2021). The latter criterion selects low-surface density GMCs, which are more susceptible to galactic shear and thus more likely to align with the large-scale galactic rotation. We also separate the GMCs by galactocentric distance in all the following comparisons, using $R_{gal} = 300$ pc (the boundary between the inner region and the intermediate region) as the threshold (all the thresholds were determined via trial and error, based on the tentative trends discussed in the previous sub-sections). In Figure 3.12, we thus revisit the comparisons discussed in Sections 3.4.1 and Section 3.4.3 for these three sub-samples.

The first row of Figure 3.12 shows the sub-sample of large resolved GMCs ($R_c > 30$ pc). A positive correlation exists between the observed and modelled quantities of inner-region GMCs ($R_{gal} < 300$ pc, blue data points) in the left panel, although most data points are still slightly lower than the 1 : 1 line. If the two outliers with $\omega_{mod} > 0.8$ km s^{-1} pc^{-1} are ignored, the Pearson correlation coefficient (r_p) is 0.81, indeed indicating strong correlation. In the middle panel, most inner-region GMCs are close to the 1 : 1 line, with only a few outliers. With the same two GMCs excluded as before, r_p is 0.44, indicating weak correlation. In the right panel, the inner-region GMCs are distributed roughly horizontally, with a weak correlation of $r_p = 0.47$. The large GMCs of the intermediate region and the outer region ($R_{gal} > 300$ pc) do not show such a strong agreement between the observations and the circular rotation model, in any of the three panels.

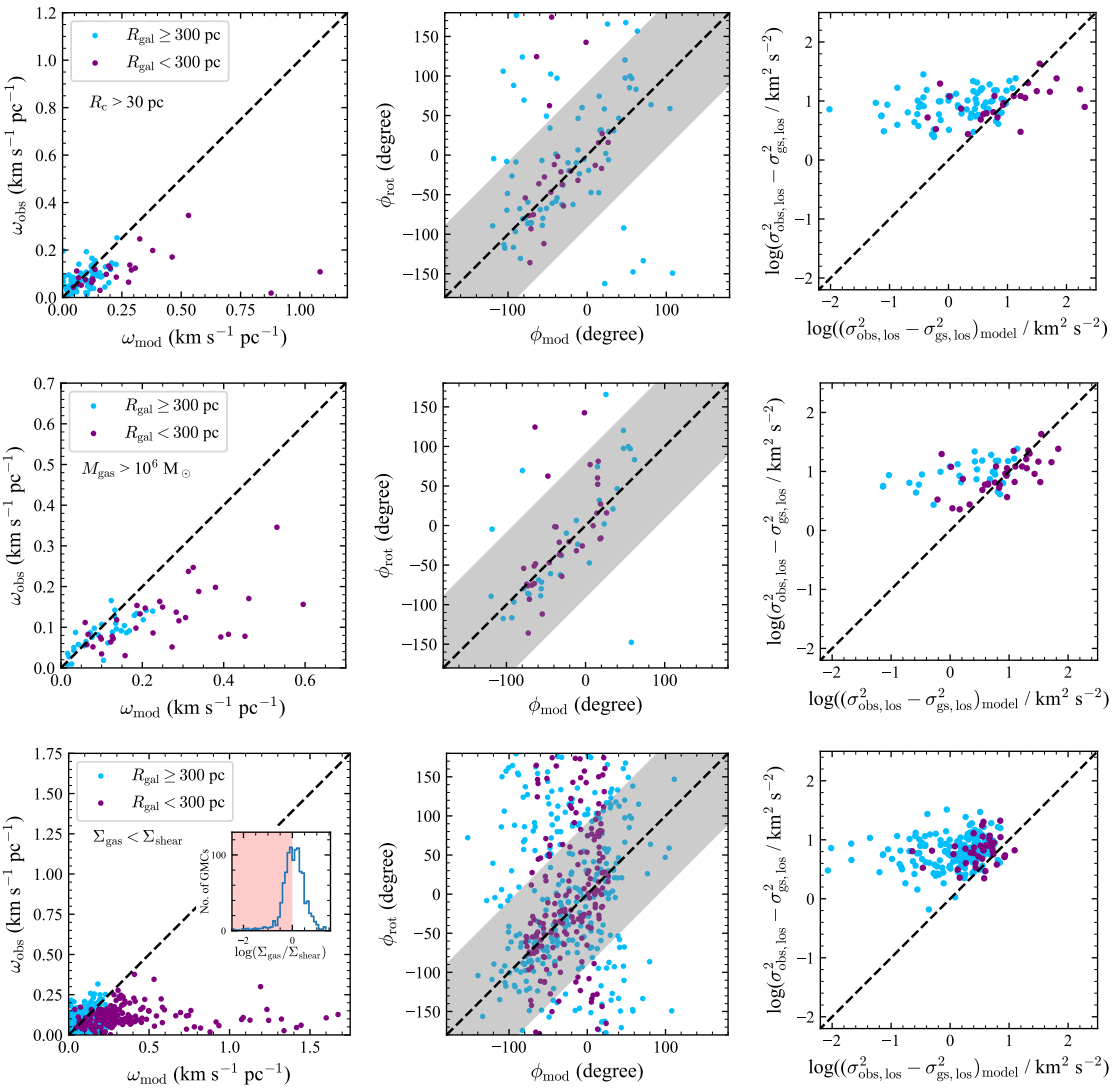

Figure 3.12: Comparison of the observed and modelled GMC quantities ω_{obs} (left column), ϕ_{rot} (middle column) and $\sigma^2_{obs,los} - \sigma^2_{gs,los}$ (right column), for three resolved GMC sub-samples of NGC 1387: $R_c > 30$ pc (top row), $M_{gas} > 10^6$ M$_\odot$ (middle row) and $\Sigma_{gas} < \Sigma_{shear}$ (bottom row). The inset in the bottom-left panel shows the distribution of the (logarithm of the) $\Sigma_{gas}/\Sigma_{shear}$ ratio of all the resolved GMCs of NGC 1387. Only the GMCs in the pink-shaded region ($\Sigma_{gas} < \Sigma_{shear}$) are plotted in the panels of this row. The data points are colour-coded according to the GMC galactocentric distance (purple, $R_{gal} < 300$ pc; blue, $R_{gal} \geq 300$ pc). The black dashed lines show the 1 : 1 relations. The grey shaded regions in the middle column indicate an angular difference $\leq 90°$, which we adopt to define prograde clouds (conversely for retrograde clouds). Note the different axis ranges among panels in the first column.

The second row of Figure 3.12 shows the sub-sample of massive resolved GMCs ($M_{\rm gas} > 10^6$ M$_\odot$). There is a positive correlation in all three panels for all galactocentric distances. In the left two panels, the four $r_{\rm p}$ are in the range of 0.57–0.78. As for the third panel, the inner-region GMCs are again in slightly better agreement ($r_{\rm p} = 0.59$) than the other massive GMCs ($r_{\rm p} = 0.46$). Most importantly, these correlations are much stronger than those of the entire GMC sample discussed in the previous sub-sections.

The third row of Figure 3.12 shows the sub-sample of resolved GMCs with $\Sigma_{\rm gas} < \Sigma_{\rm shear}$. There is no correlation between the observed and modelled quantities in any of the three panels and at any galactocentric distance. The measured $r_{\rm p}$ is at most 0.31 (ϕ comparison for inner GMCs), corresponding to a very weak correlation at best.

We also tested resolved GMC sub-samples with $\Sigma_{\rm gas} < 100$ M$_\odot$ pc^{-2}, $\Sigma_{\rm gas} > 500$ M$_\odot$ pc^{-2}, small $\sigma_{\rm obs,los}$, large $\sigma_{\rm obs,los}$ and $R_{\rm c} > R_{\rm t}$ (not shown in Figure 3.12). No correlation exists for any of these sub-samples. In particular, the absence of a correlation for the $R_{\rm c} > R_{\rm t}$ sub-sample suggests that although the discussion concerning the tidal radii in Section 3.4.2 is physically justified, further investigation of this aspect is required.

In summary, we see emerging correlations between GMC internal rotation and large-scale galactic circular rotation primarily for the most massive ($M_{\rm gas} > 10^6$ M$_\odot$) resolved GMCs of NGC 1387, but to a lesser extent also for the largest ($R_{\rm c} > 30$ pc) and/or inner ($R_{\rm gal} < 300$ pc) GMCs (though the innermost GMCs with $R_{\rm gal} < 100$ pc decouple from large-scale galactic rotation, as discussed in Section 3.4.1). The requirement of small $R_{\rm gal}$ can be interpreted as the requirement of high A indicating large shear, for which one expects stronger GMC coupling with galactic rotation. For the other two requirements, more massive GMCs simply tend to be larger (and vice-versa), and larger GMCs are more affected by shear ($\Sigma_{\rm shear} \propto R_{\rm c}$). As a GMC evolves, the (de-)coupling of its internal velocity gradients from galactic rotation is a competition between galactic shear and processes such as gas disc fragmentation (involving gravitational collapse; Juárez et al. 2019), gas accretion (Rawat et al., 2024), GMC mergers (Skarbinski et al., 2023), and stellar feedback (Nonhebel et al., 2024). The former imprints galactic differential rotation to the GMC, while all the latter generate random motions. To reveal the evolutionary path of a GMC, the relative strengths and timescales of these processes must be explored.

3.5 Toomre parameter and cloud-cloud collision model

Since we have demonstrated in Section 3.4 that the majority of the resolved GMCs of NGC 1387 (except those with $R_{\rm gal} < 300$ pc) are not significantly influenced by the large-scale galaxy rotation and shear, we now explore another mechanism potentially regulating GMC properties, i.e. cloud-cloud collisions. Liu et al. (2022) showed that where the Toomre instability parameter is below its critical threshold of unity, the disc is unstable and cloud-cloud collisions prevail in NGC 404.

The Toomre parameter

$$Q \equiv \frac{\kappa \sigma_{\rm disc}}{\pi G \Sigma_{\rm mol}} \tag{3.4}$$

(e.g. Toomre, 1964; Binney & Tremaine, 2008), where κ is the epicyclic frequency (calculated from the circular velocity curve) and $\sigma_{\rm disc}$ is the azimuthally averaged molecular gas disc velocity dispersion (calculated from the second-moment map). Even though the circular velocity curve is largely determined by the stellar contribution to the gravitational potential, this formulation only accounts for the surface mass density of the molecular gas, thus ignoring that of the stellar component. As the stars in the inner parts of NGC 1387 are likely to be distributed in a rather thick spheroidal component, rather than in a thin disc coplanar with the molecular gas disc, adding their contribution to Q would be non-trivial. Nevertheless, the resulting Q should formally be considered an upper limit (as any additional component will only lower Q; e.g. Wang & Silk 1994).

Figure 3.13 shows the Q radial profile of NGC 1387 (blue curve). Q is high in the inner region (at least partially due to beam smearing leading to overestimated velocity dispersions), but it generally decreases with galactocentric distance, primarily due to decreases of κ and $\sigma_{\rm disc}$ rather than $\Sigma_{\rm mol}$. At $R_{\rm gal} \gtrsim 500$ pc, Q remains below ≈ 1.5, close to the critical threshold of unity. Even ignoring the stellar component, the molecular gas disc is thus close to being gravitationally unstable and having a tendency to fragment in that region. In turn, this means that cloud-cloud collisions could be important in the outer half of the molecular gas disc. The bump in the Q radial profile at $R_{\rm gal} \approx 300$ pc is due to the narrow dip of $\Sigma_{\rm mol}$ at the same galactocentric distance (see the bottom-right panel of Figure 3.2), so we do not discuss this feature further.

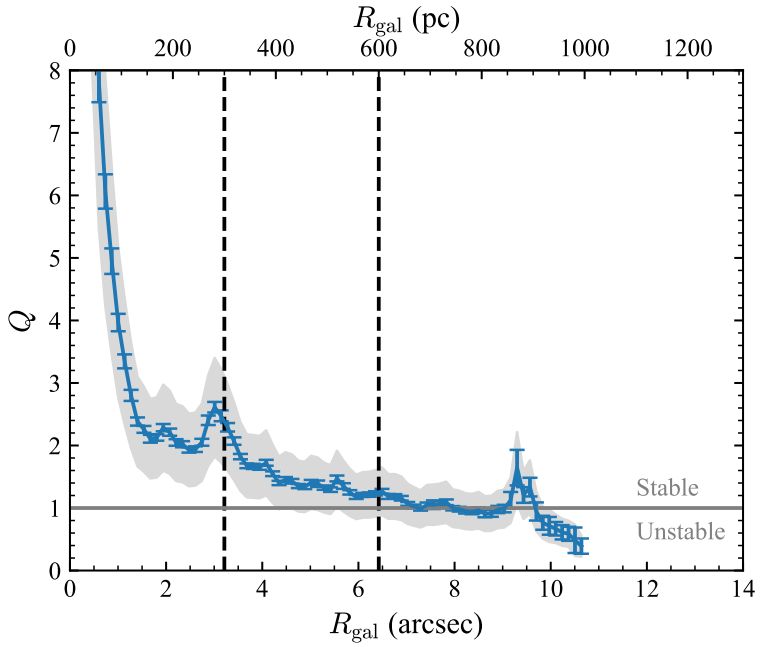

Figure 3.13: Radial profile of the Toomre instability parameter Q (blue curve) of NGC 1387. Error bars are 1σ uncertainties propagated from the measurement uncertainties, while the shaded regions include an additional 30% uncertainty to account for the CO-to-molecular gas conversion uncertainty. The black dashed vertical lines indicate the boundaries of the three regions defined in Section 3.2.4. The grey horizontal solid line indicates $Q = 1$.

Although Q is nowhere low enough to provide decisive support for the cloud-cloud collision model, one prediction of the model is that the slope of the size – line width relation is 1/3 (equation 18 of Liu et al. 2022). The best-fitting slope of 0.29 ± 0.11 for all the resolved clouds of NGC 1387 (see Table 3.5) is smaller than that of MW disc (0.5 ± 0.1; Solomon et al. 1987) and Local Group GMCs (0.6 ± 0.1; Bolatto et al. 2008), but it is in perfect agreement with that predicted from cloud-cloud collisions.

3.6 Radial gradients of GMC properties

As pointed out before (Sections 3.3.1 and 3.3.3), most properties of the resolved clouds of NGC 1387 reveal galactocentric distance (i.e. radial) gradients. This is not the case for previously studied ETGs (e.g. NGC 4526, Utomo et al. 2015; NGC 4429, Liu et al. 2021). Figure 3.14 shows the four fundamental properties $R_{\rm c}$, $M_{\rm gas}$, $\sigma_{\rm obs,los}$ and $\Sigma_{\rm gas}$ (see Figure 3.4) as a function of galactocentric distance. The blue data points show individual resolved GMCs, while the red lines show azimuthal averages in galactocentric distance

bins of width 100 pc. For the averages, only measurements larger than their uncertainties are considered. All properties peak near the centre at $R_{\rm gal} \approx 150$ pc ($R_{\rm c}$ at a slightly larger galactocentric distance), with a sharp drop in the innermost radial bin and a steady decrease with increasing galactocentric distance. Considering the $R_{\rm c}$ and $M_{\rm gas}$ trends, we interpret the decrease of $\Sigma_{\rm gas}$ from ≈ 150 to 550 pc to be primarily driven by $M_{\rm gas}$, while the flattening of $\Sigma_{\rm gas}$ beyond that is driven by the simultaneous decrements of $R_{\rm c}$ and $M_{\rm gas}$. The range of molecular gas mass surface densities of the resolved clouds ($2.1 \lesssim \log(\Sigma_{\rm gas}/{\rm M}_\odot\ {\rm pc}^{-2}) \lesssim 2.5$) is within that of the central molecular gas mass surface densities of barred LTGs (see the left panel of Fig. 2 of Sun et al. 2020b), both higher than the $\Sigma_{\rm gas}$ distribution of unbarred LTGs, consistent with NGC 1387 being weakly barred (this despite the vastly different spatial resolutions; 120 pc in Sun et al. 2020b).

3.7 Similarities with the MW disc

Recent studies have shown that GMCs in extragalactic environments (especially in ETGs; Utomo et al. 2015; Liu et al. 2021) do not follow the MW disc or Local Group Larson relations, which were long thought to be universal. In light of this, the GMCs of NGC 1387 are surprisingly similar to those of the MW disc, suggesting a more varied and complex regulation of GMC properties. Apart from galaxy morphological type (almost certainly a proxy for more relevant physical properties), we thus explore here other possible regulators of GMC properties.

Recent star formation may be one such regulator, as stellar winds and supernovae mechanically inject energy and thus turbulence into the surrounding interstellar medium. Zabel et al. (2020) studied the star-formation rates (SFRs), indicated by Hα emission, and star-formation efficiencies (SFEs) of a sample of galaxies including NGC 1387 as part of the Fornax3D project. While their data cover out to $R_{\rm gal} \approx 15$ kpc, Hα emission is only detected in the central $R_{\rm gal} \lesssim 1$ kpc, very similar to the spatial extent of the cold molecular gas. BPT analysis identified low-ionisation nuclear emission-line regions located roughly in the central $R_{\rm gal} \lesssim 250$ pc, star-forming blobs patchily distributed in a ring region at $R_{\rm gal} \approx 700$ pc, and composite emission mechanism in most other regions. The integrated SFR of NGC 1387 is in the range from 0.008 ${\rm M}_\odot\ {\rm yr}^{-1}$ (using Hα flux from star-forming

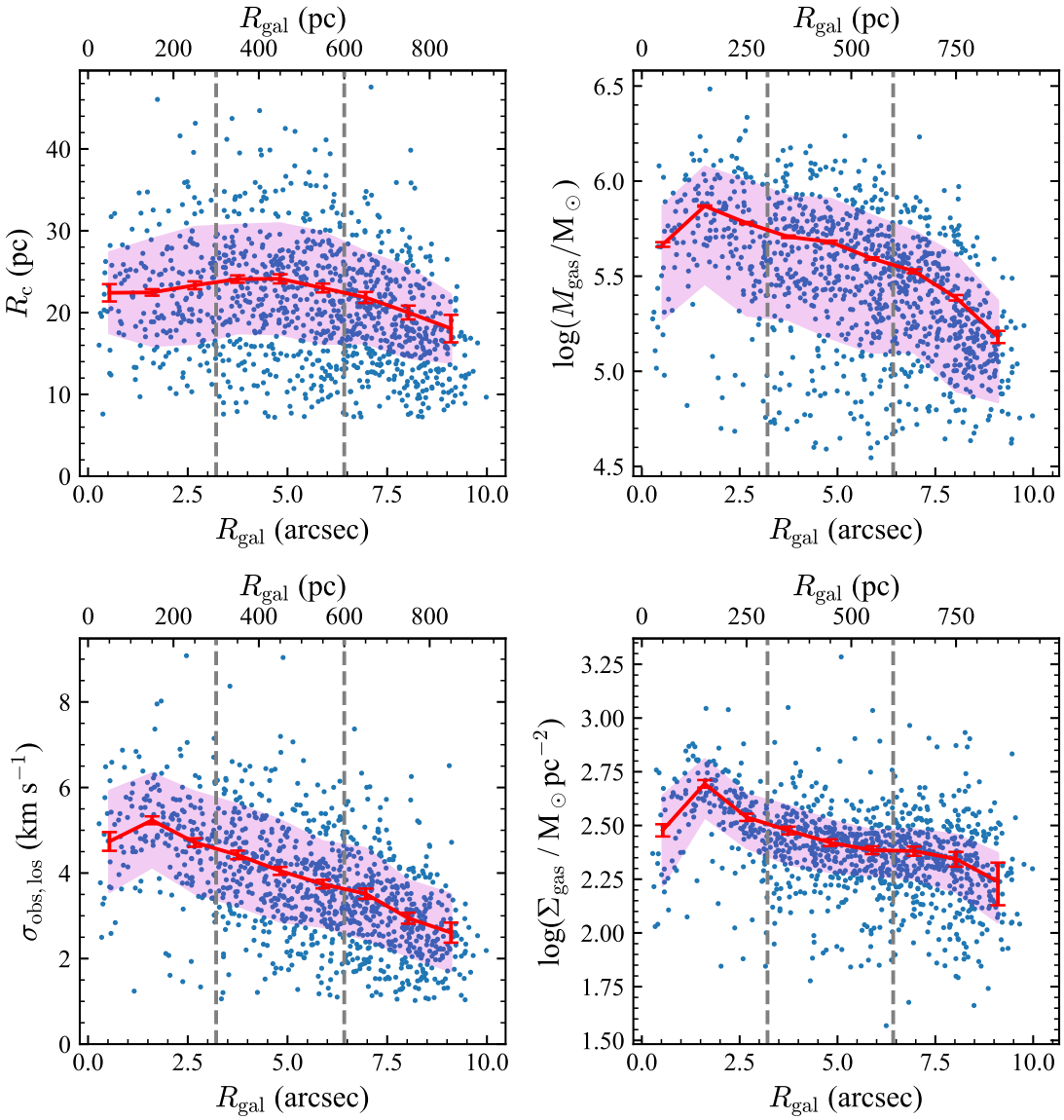

Figure 3.14: Properties of the resolved GMCs of NGC 1387 as a function of galactocentric distance: R_c (top-left), M_{gas} (top-right), $\sigma_{obs,los}$ (bottom-left) and Σ_{gas} (bottom-right). Data points are shown in blue, azimuthal averages in red. For the averages, only measurements larger than their uncertainties are considered. Error bars indicate the MAD uncertainty on the mean of each radial bin, while the magenta-shaded regions show the scatter (standard deviation) within each radial bin. The grey dashed vertical lines indicate the boundaries of the three regions defined in Section 3.2.4.

regions only) to 0.082 $M_\odot$ yr^{-1} (using Hα flux from both star-forming and composite regions). It is thus much smaller than that of the MW (1.65 ± 0.19 $M_\odot$ yr^{-1}; Licquia & Newman 2015), which has a total stellar mass ($(6.08 \pm 1.14) \times 10^{10}$ $M_\odot$; Licquia & Newman 2015) similar to that of NGC 1387, and it is 1.8 dex below the star-formation main sequence of the local universe (given the total stellar mass of NGC 1387; Elbaz et al. 2007). Using the total molecular gas mass, the SFE of NGC 1387 is in the range $-10.6 \lesssim \log(\mathrm{SFE/yr^{-1}}) \lesssim -9.6$, corresponding to depletion times $\tau_{\rm dep}$ of 4–41 Gyr, and the specific star-formation rate (sSFR) is in the range $-12.8 \lesssim \log(\mathrm{sSFR/yr^{-1}}) \lesssim -11.8$. In the $\tau_{\rm dep}$ – sSFR diagnostic diagram of Saintonge et al. (2011), NGC 1387 would be located in the region of high $\tau_{\rm dep}$ and small sSFR, along with other ETGs. These parameters and comparisons indicate that the SFR of NGC 1387 is consistent with its early-type morphology and its star formation can not be the driver of its MW disc-like GMC properties. A more comprehensive study of the suppression of star formation in NGC 1387 is however desirable to explore any potential causal link.

The gas-phase metallicity is another potential regulator of GMC properties, as metals serve as coolants of GMCs and affect processes such as the fragmentation of the gas disc (e.g. Hocuk & Spaans, 2010). With Very Large Telescope Multi Unit Spectroscopic Explorer data from the Fornax3D project, and using the Dopita et al. (2016) calibration, we estimate the median gas-phase metallicity of star-forming regions (identified through standard emission-line ratio diagnostic diagrams) to be $12 + \log(\mathrm{O/H}) = 9.07$, 0.4 dex above solar metallicity. Compared with the mass-metallicity relation shown in Fig. 1 of Lara-López et al. (2022), who use the same metallicity calibration, at a total stellar mass of 4.7×10^{10} $M_\odot$ the gas-phase metallicity of NGC 1387 is 0.25 dex larger than that of the general trend, and it is also higher than the MW metallicity (e.g. Balser et al., 2011).

ETGs are generally located at the high-mass and high-metallicity end of the mass-metallicity relation, with a scatter of about 0.3 dex (see Fig. 9 of Griffith et al. 2019 and references therein), suggesting that NGC 1387 is just a typical ETG in term of metallicity. Furthermore, the gas-phase metallicity of galaxies is largely determined by the origin of the gas, i.e. either high-metallicity gas recycled from stellar mass loss or low-metallicity gas accreted from dwarf galaxies. For NGC 1387, judging from its

location near the centre of the Fornax Cluster, its deficit of atomic gas and the perfect kinematic alignment between cold gas and stars (see Section 3.2.1), the origin of its cold gas is almost certainly internal, in line with the analyses of cluster ETGs of Davis et al. (2011). Thus, the early-type classification, the metallicity and the likely origin of the molecular gas of NGC 1387 are all consistent with each other, although they do not provide an explanation of the GMC properties. In addition, the cluster-centre environment, which NGC 1387 resides in, normally changes a galaxy towards the ETG-end of many properties rather than makes them similar to the MW or other LTGs (e.g. Davis et al., 2013a; Mok et al., 2017; Villanueva et al., 2022). A related but converse example is the ETG NGC 5128 (Centaurus A), which harbours externally accreted cold molecular gas and exhibits LTG-like GMC properties (Miura et al., 2021).

A third potential regulator we consider is the slope (power-law index β) of the spatial power spectrum of the CO zeroth-moment map, which has been used to characterise turbulent cascades and gas fragmentation (e.g. Elmegreen & Scalo, 2004). In fact, the high clumpiness of the gas disc in NGC 1387 was one of the major motivations of this work. It guarantees the existence of GMCs, unlike most other ETGs with a more smooth disc and few identifiable GMCs (e.g. NGC 524, Lu et al., 2024). The power-law index should reflect this feature. In Gensior et al. (2023), the power-law index of the CO disc of NGC 1387 is measured to be 2.09 ± 0.14, among seven other observed ETGs with a range of β from 2.05 to 3.02 and four observed LTGs with β from 2.45 to 2.81. NGC 1387 is thus at the lowest end of the β distribution of all observed galaxies in Gensior et al. (2023), not typical of either the ETG population or the LTGs. Compared with a sample of simulated galaxies from Gensior et al. (2023), $\beta = 2.09$ of NGC 1387 is in the middle of those of ETG-like ones (≈ 2.5) and LTG-like ones (≈ 1.8). In any case, the number of galaxies with a robustly measured β is still small, preventing strong constraints on the general distribution of β across the Hubble sequence, and it is of course possible that other physical drivers simultaneously determine both β and the GMC properties.

Lastly, the near–face on inclination may be the reason for the MW-like GMC properties. As mentioned before, galactic rotation induces velocity gradients in GMCs and thus increases the observed velocity dispersion. When such a contribution is removed and

only turbulence-induced velocity dispersion remains, the virial parameter of the ETG NGC 4429 changes from ≈ 4.0 (observed value) to ≈ 1.3 (after correction; Liu et al. 2021). The latter is already very close to the typical LTG virial parameters. At the low inclination of NGC 1387 and small (projected) galaxy rotation velocities, it may be natural for GMC velocity dispersions (and resultant virial parameters) to show similarly low values as LTGs. In addition, turbulence-induced velocity dispersions may be anisotropic (e.g. Hansen et al., 2011) and thus the observed quantities would depend on the inclination angle. The resolved cloud–scale studies of ETGs to this day are far too few to test such a dependency on inclination. Further observations and simulations are needed to explore this possibility.

3.8 Summary and conclusions

We obtained high-resolution (≈ 0.″17 × 0.″14 or 16 × 13 pc^2 spatially, 2 km s^{-1} spectrally) ALMA observations of the central region of the lenticular galaxy NGC 1387, with a sensitivity of 1.09 mJy beam^{-1} (1.11 K). We identified 1285 GMCs, 1079 of which are spatially and spectrally resolved, with a modified version of the `CPROPStoo` software. We measured the basic properties of the GMCs (radius R_c, line-of-sight velocity dispersion $\sigma_{obs,los}$, molecular gas mass M_{gas}, and molecular gas mass surface density Σ_{gas}), probed the inferred GMC mass spectra, Larson relations and virial parameters, and investigated the origin of the GMCs' internal rotation (including large-scale galactic rotation, gravitational instabilities and cloud-cloud collisions). All of these properties were compared to those of GMCs in other galaxies. Our key findings are summarised below.

- The means (standard deviations) of the basic properties of the resolved GMCs of NGC 1387 are: $\langle R_c \rangle$ = 20 pc (7 pc), $\langle \sigma_{obs,los} \rangle$ = 3.5 km s^{-1} (1.5 km s^{-1}), $\langle \log(M_{gas}/M_\odot) \rangle$ = 5.5 (0.4) and $\langle \log(\Sigma_{gas}/M_\odot\ pc^{-2}) \rangle$ = 2.4 (0.2). The distributions are similar to those of the GMCs of NGC 4429, one of the few ETGs with GMCs studied at a similar physical resolution.

- The mass spectrum (i.e. the cumulative probability distribution function of GMC mass) of NGC 1387 has a slope of −1.8 (best-fitting truncated power law),

comparable to that of MW disc GMCs. The cut-off mass of 1.5×10^6 $M_\odot$ indicates a lack of high-mass GMCs.

- The Larson relations and virial parameters of the NGC 1387 GMCs are also very similar to those of MW disc GMCs, despite the galaxy's early-type morphology. This shows that not all ETG GMCs deviate from the MW scaling relations. A few physical parameters are discussed to potentially explain such a similarity. The power spectrum index and the inclination angle are identified as possible.

- Overall, the internal rotation of the GMCs does not seem to arise from the large-scale circular rotation of the galaxy (e.g. through shear and tides). The prograde fraction of all resolved GMCs is nevertheless high (63%), with a slight decrease from the inner region (72%) to the outer region (59%), and as expected massive and/or large GMCs at small galactocentric distances do appear to be better coupled to the large-scale galactic rotation.

- The Toomre instability parameter $Q \lesssim 1.5$ in the outer half of the molecular gas disc, indicating that cloud-cloud collisions could be effective in that region. The shallow slope of the size – line width relation (0.29 ± 0.11) is as expected from cloud-cloud collisions.

Throughout this chapter, we have assumed spherical geometry for GMCs. While there are detected deviations in other galaxies and a large body of literature on molecular gas morphologies (e.g. Ragan et al., 2014; Liu et al., 2021, and Section 4.5.4), the analyses and conclusions in this chapter should still be robust despite the simple spherical assumption. The basic parameters $M_{\rm gas}$ and $\sigma_{\rm obs,los}$ are not affected by the geometry assumption while $R_{\rm c}$, $\Sigma_{\rm gas}$, and $\alpha_{\rm obs,vir}$ can be regarded as effective or average values without any obvious biases. We note that $R_{\rm c}$ is robust as the sky-plane size only, with little information on the LoS-direction size of the GMCs. With the near–face on orientation of NGC 1387, $R_{\rm c}$ is dominated by the gas disc–plane size, which may be larger (by a factor of ≈ 2) than the size vertical to the gas disc (i.e. GMC scale height; Liu et al. 2021). This does not fully explain the discrepancy between NGC 1387 and other ETGs in the

Larson relations, and even makes the discrepancy in the virial parameter larger. As for the kinematic analyses in Section 3.4, the geometry assumption may fold into the beam smearing effect discussed in Section 3.4.1. A highly elongated filamentary molecular cloud may suffer a high magnitude of beam smearing in its minor (i.e. transverse) axis, in terms of a high ratio between the observed and intrinsic lengths. This means the observed velocity gradient ($\omega_{\rm obs}$) might suffer from a higher degree of underestimation than discussed in Section 3.4.1. More quantitative discussion or confirmation of this effect require higher-resolution observations and/or simulations. In Sections 3.4.2 to 3.4.4, the measurements of both $R_{\rm t}$ and $\sigma^2_{\rm obs,los} - \sigma^2_{\rm gs,los}$ can be regarded as effective or average values. The derivation of both quantities make use of the circular velocity curve (and its derived curves of A and Ω), which is estimated at the centre of each GMC. The deviation of A and Ω between the GMC centre and other pixels should be negligible given the small physical scales of the GMCs, and such deviation is not particularly concerning GMC geometry. The measurement of $R_{\rm t}$ also makes use of $M_{\rm gas}$, which is not affected by the assumed geometry. All other quantities analysed in this chapter does not concern the GMC geometry assumption.

4

HNCO molecular gas dendrogram of the Milky Way Central Molecular Zone

Contents

4.1 Introduction

CMZs are extreme environments with a high concentration of (dense) molecular gas. They drive galaxy evolution through either enhancing or suppressing star formation, as well as stellar and AGN feedbacks. The CMZ of our own MW is the most extensively studied, yet many mysteries of gas cloud/clump properties and star formation remain to be solved. The ongoing ACES project, an ALMA large programme of the MW CMZ, offers substantially improved spatial and spectral resolutions compared to previous surveys to advance our knowledge on many aspects of the CMZ. To capture the hierarchical nature of the ISM, this work utilises the dendrogram algorithm `Astrodendro` to identify molecular gas structures across a wide range of physical scales (1–100 pc), traced by HNCO (4–3)[1] in the ACES data and by a few other lines together with HNCO in the Mopra CMZ survey. We compare the size-linewidth relation obtained from ACES with those from the Mopra survey and the literature. We also investigate the morphology and dynamic states of gas structures under the influence of shear/tidal forces and magnetic fields.

This chapter is arranged as follows. Section 4.2 introduces the basics of cold molecular gas observations used in this work, i.e. the Mopra CMZ survey and ACES. Section 4.3 describes the methodology to identify gas structures from the datacubes and to measure structure properties. Section 4.4 presents the gas structure catalogue from the Mopra survey and analyses the size-linewidth relation. Section 4.5 discusses the structure catalogue properties from ACES, in terms of an updated size-linewidth relation, the virial parameter, and shear and magnetic field effects on structure morphology. We discuss these results in the context of the turbulence level and structure-property regulator in Section 4.6, and conclude in Section 4.7.

The presentation of the Mopra analyses before the ACES ones are helpful in the following aspects. (i) The Mopra data and catalogue set a reliable benchmark. While the ACES data are superior in resolutions, their interferometric nature inevitably brings

[1]For simplicity, the transition is mentioned once at the first occurrence of each line and omitted for the rest of the chapter where applicable, unless another transition is discussed and explicitly specified.

about challenges in data reduction and risk of interferometric artefacts, especially for such an early-release version of the dataset used in this thesis. Having a chapter from the Mopra data, with a small portion already published by other groups as a cross-validation, provides a firm starting point in studying the gas structures in the MW CMZ and extending the analyses to ACES data. (ii) Once the fidelity of the ACES data is confirmed by reproducing Mopra results, it is valuable to directly examine the new capabilities enabled by the ACES resolutions, as discussed in Sections 4.5.2 and 4.6.1. As one of the initial works from the ACES project, such a direct comparison with a previous survey is a desirable showcase. (iii) The Mopra data have a wider field of view, covering a few more major clouds in the MW CMZ than the ACES data. The Mopra survey also observes a multitude of important molecular lines, while all other lines than HNCO of the ACES survey are still undergoing data reduction and not yet available. The comparison between different lines, as discussed in Section 4.4.3, as well as the wider spatial coverage of the Mopra data provide useful physical insights.

4.2 Observations

4.2.1 Mopra

Mopra is a 22-m single-dish millimetre telescope. The Mopra CMZ survey was carried out from 2007 to 2009. It has an area of 2.5×0.5 degree^2, including the brightest components of the CMZ such as Sgr A, Sgr B2, Sgr C, and G1.6-0.025. The (round) beam size is $39''$ (or 1.5 pc, assuming a distance of 8 kpc of the CMZ throughout the thesis; Gravity Collaboration et al. 2019). It mapped 20 spectral lines within 85.3–93.3 GHz in the 3-mm band using the 8-GHz Mopra Spectrometer (MOPS) digital filter bank and the Mopra Monolithic Microwave Integrated Circuit (MMIC) receiver. The raw channel width is 0.27 MHz (or 0.9 km s^{-1}). The smoothed and publicly available version we use has an effective spectral resolution of 1.07 MHz (or 3.6 km s^{-1}), Nyquist sampled with 0.54-MHz (or 1.8 km s^{-1}) channels. Further details about the Mopra CMZ survey are described in Jones et al. (2012). In this work, we use five lines from it: primarily HNCO, and secondarily HCN (1-0), N_2H^+ (1-0), HCO^+ (1-0), and HC_3N (10-9).

4.2.2 ALMA

We use ACES data, which is an ALMA cycle-8 large programme (2021.1.00172.L; PI: Longmore) targeted at the CMZ. The observations went from October 2021 to March 2023, with 120 hours of the 12-m Array, 360 hours of the 7-m Array, and 700 hours of the Total Power (TP) Array. The field of view (FoV) of ACES is a non-rectangular shape spanning Galactic Longitude (l) from $-0.^{\circ}6$ to $0.^{\circ}9$ and Galactic Latitude (b) from $-0.^{\circ}3$ to $0.^{\circ}2$, with an observed area of 0.43 degree^2, which is shown by the red curve in the upper panel of Figure 4.1. The whole FoV is divided into 45 'fields' (mostly rectangular) and corresponding member observation unit sets (MOUSs). Data reduction is carried out with the Common Astronomy Software Applications (`CASA`; CASA Team et al. 2022). Each field is individually imaged first and then stitched together. In the overlapping regions of more than one field, the weighted average of the intensity is adopted to minimise noise and the weightings are based on PB responses. While the imaging uses the mosaic mode in `CASA tclean`, in this chapter we use 'mosaic' to refer to the whole FoV of all the 45 fields. All ALMA data products mentioned in this chapter are PB-corrected (unless otherwise specified). Due to the slight overlapping between adjacent fields, a high-noise edge of an individual field (due to the lower PB response at the edges) becomes a 'low-noise trench' (lower in noise by a factor of $\lesssim \sqrt{2}$ than the inner region of a field) in the whole mosaic where an adjacent field's edge overlaps with that edge. We call this an 'inner edge'. The outermost rim of the whole mosaic remains high in noise and we call this an 'outer edge'.

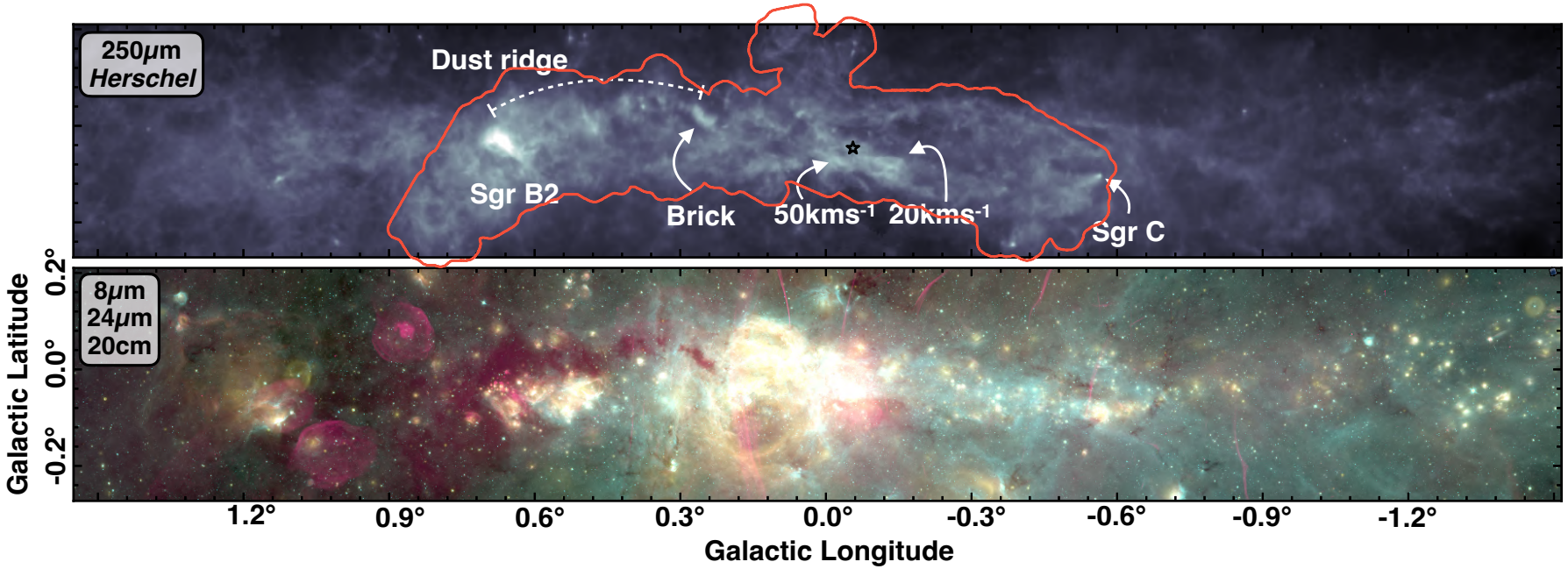

Figure 4.1: MW CMZ overview. Adapted from Henshaw et al. (2023) and references therein. The upper panel is *Herschel* observation at 250 μm in the background with the ACES FoV overlaid in the red curve. Annotations are provided for a few prominent regions and molecular clouds (the hollow black star showing Sgr A*). The lower panel is a three colour composite image of 8 μm (green; *Spitzer*), 24 μm (yellow; *Spitzer*), and 20 cm (red; MeerKAT).

A whole-mosaic HNCO datacube imaged from the 7-m observations feathered by the TP images is produced as part of an internal data release. This work uses this datacube, denoted ACES '7mTP' data. The synthesised beam size[2] (i.e. the spatial resolution) is $22'' \times 16''$ (or 0.84×0.63 pc^2) at a position angle of $-79°$.[3]

The imaging of the 12-m observations (to be combined with 7-m and TP observations; denoted the ACES '12m7mTP' data) is still being experimented with and processed, and will be made public in due course (ACES Collaboration in prep.). The resolutions of individual fields range from $1\farcs2$ to $2\farcs5$. This work will be extended in future works to benefit from the full spatial resolution.

ACES has six spectral windows in ALMA Band 3 (in the order of increasing frequency): two medium-width windows covering 86.0–86.5 and 86.7–87.1 GHz, two narrow windows covering 60-MHz bandwidth (≈ 200 km s^{-1}) centred on the rest frequencies of HNCO ($\nu_{\rm rest} = 87.925$ GHz) and HCO$^+$ ($\nu_{\rm rest} = 89.189$ GHz), and two broad windows covering 97.7–99.5 and 99.6–101.4 GHz. For HNCO, the spectral resolution as well as the final channel width after binning is 61 kHz (or 0.2 km s^{-1}). Because the default setup of the narrow spectral window (i.e. from -100 to 100 km s^{-1}) cannot capture the full velocity range of the CMZ emission, 21 fields are manually shifted in velocity by +30, +40, or -30 km s^{-1}, as illustrated in Figure 4.2. This uses a priori knowledge of where the emission is in 3D[4] to make the most of the ALMA spatial-spectral coverage. With this differential spectral setup, the spatial coverage in each channel also varies. The three manual velocity shifts create six transitions in spatial coverage across all channels. Additionally, since different MOUSs are observed at different times, the change in Earth velocity creates additional tiny velocity shifts (on the order of a few 0.2 km s^{-1} channels) and in turn many additional spatial coverage transitions. This feature leads to a special treatment in noise estimate and structure identification, detailed in Sects. 4.2.3 and 4.3.

A brief comparison between the Mopra CMZ survey and the ACES is presented in Table 4.1.

[2]We use the full-width at half-maximum (FWHM) of a beam as its size throughout the chapter, unless explicitly specified otherwise.

[3]All angles in this thesis are measured from Galactic north through east.

[4]3D refers to position-position-velocity in this chapter.

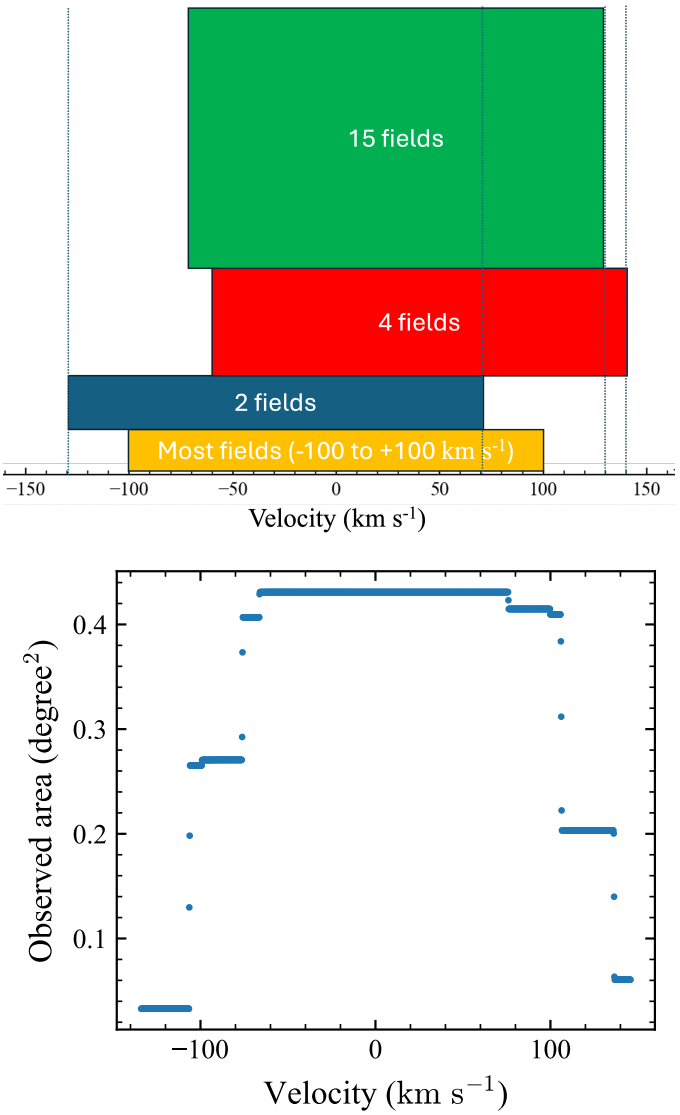

Figure 4.2: ACES FoV variation across channels. The designed (upper panel) and the observed (lower panel) spatial coverages of ACES across channels.

4.2.3 Noise estimate and moment maps

We use moment maps as a representation of data quality as well as an analysis tool for large-scale gas distribution and kinematics. To select pixels for the map generation (and for the dendrogram construction in Section 4.3), we first need a noise estimate corresponding to each voxel in the datacube. In principle, measuring the root-mean-square (RMS) within a 3D running box can provide such an estimate assuming real emission is properly masked out before the RMS calculation and the box is small enough to be locally representative. However, this approach is computationally too expensive for the scope of data sizes of

Table 4.1: Characteristics of Mopra CMZ survey and ACES.

	Mopra	ACES 7mTP
Spatial resolution (″)	39	19
Spatial resolution (pc)	1.5	0.73
Field of view (degree^2)	1.25	0.43
Galactic Longitude (l) range	$-0.^\circ7$ – $1.^\circ8$	$-0.^\circ6$ – $0.^\circ9$
Galactic Latitude (b) range	$-0.^\circ3$ – $0.^\circ2$	$-0.^\circ3$ – $0.^\circ2$
Spectral coverage (GHz)	85.3 – 93.3	86.0 – 101.4 (with gaps)
HNCO cube spectral resolution (km s^{-1})	3.6	0.2
HNCO cube median RMS noise (mK)	46	35

Notes: The characteristics above the dashed line apply to the entire survey (i.e. all lines and continuum) while those below are very specific to the HNCO datacube. Having said that, the spatial resolution (θ) also depends on the frequency (f; $\theta \propto f^{-1}$) and thus on the specific line of interest. The quoted spatial resolution value is measured at the HNCO frequency.
The spatial resolution of ACES (geometric average of the beam axes) is for the whole mosaic datacubes. Those for individual fields of ACES are typically 60% (in 1D) better (i.e. smaller). The ACES 12m7mTP dataset is still being experimented with and processed (ACES Collaboration in prep.), thus not listed here.
The field of view (FoV) of ACES is not a rectangle but the Mopra one is.

ACES and the balance between those two mutual-exclusive assumptions is difficult to achieve. Thus, we adopt a 'half-local-half-global' approach to estimate the local noises using the python routine `scNoiseRoutines`[5] from the PHANGS collaboration. It first masks out emission voxels in the datacube and generates a noise map by calculating the RMS along the spectral dimension. It then folds in (by multiplication) the normalised spectral variation of the noise using the RMS calculated in each channel, and ultimately outputs a 3D noise cube. With this procedure, the median value in the Mopra HNCO noise cube is 46 mK, consistent with the $\approx$ 50 mK reported by Jones et al. (2012).

For the ACES data (and not for the Mopra data), due to the spectral offset of many fields explained in Section 4.2.2 and Figure 4.2, the (spatial) outer edges are at different locations in different chunks of channels. One outer edge (with high noise) in one channel could be at the same lines-of-sight of an inner edge (with low noise) in many other

[5] https://github.com/akleroy/phangs_imaging_scripts/blob/master/phangsPipeline/scNoiseRoutines.py

channels. Such spatial-and-spectral variation of noise cannot be accurately captured by the aforementioned routines. Thus, we trim away outer edges, with the python routine `scipy.ndimage.binary_dilation`,[6] in all channels before going through the procedure above. The spatial extent of the trimming is chosen to be 1′. This trims the FoV to a position corresponding to 80% response of the ACA PB and is roughly the width of the 'low-noise' trench in the overlapping regions of any two adjacent fields. As a result, 10% of the observed voxels are trimmed away. Although it is not ideal to lose data, this is the most efficient way regarding computation time and storage space when working with the whole ACES mosaic, and the trimmed data are noisy edges anyway. With this procedure, the median value in the ACES HNCO noise cube (after trimming) is 35 mK.

For the moment maps as well as the maximum brightness map, we adopt a procedure based on the moment-masking technique of Dame (2011). For ACES data, we smooth the datacube with a 3D Gaussian kernel. Its standard-deviation widths in the two spatial dimensions are both twice that of the beam major-axis FWHM and that in the spectral dimension equals five channels (i.e. $\approx$ 1 km s^{-1} for five channels). For Mopra data, as the channel width is already 1.8 km s^{-1}, we do not apply spectral smoothing, and the spatial smoothing is also twice the Mopra beam size. Assuming the size of the smoothing kernel is comparable to the spatial extent of faint diffuse emission (i.e. below the sigma threshold before smoothing), all real emission should remain or become significant after smoothing while noise should be largely suppressed. We estimate the 3D noise cube of this smoothed datacube with the procedure explained above. We select voxels with an amplitude greater than five times its corresponding RMS and use these voxels in the original datacube (with the full resolutions) to create the moment maps.

We show the 0$^{\rm th}$-, 1$^{\rm st}$-, and 2$^{\rm nd}$-moment maps as well as the maximum brightness ($T_{\rm max}$) map in Figures 4.3 and 4.4, for Mopra and ACES data respectively. The internal holes of the 1$^{\rm st}$- and 2$^{\rm nd}$-moment maps are due to none selected pixels along those lines-of-sight (LoSs), for which zeros are filled in (only) for the 0$^{\rm th}$-moment and $T_{\rm max}$ maps. The prominent molecular clouds annotated in Figure 4.1 are clearly visible in the $T_{\rm max}$ and 0$^{\rm th}$-moment maps. The better spatial resolution of the ACES 7mTP data than

[6] https://docs.scipy.org/doc/scipy/reference/generated/scipy.ndimage.binary_dilation.html

the Mopra data can already be appreciated to some extent. The 1st- and 2nd-moment maps show the complex structure and kinematics of the CMZ. A detailed study of the position-velocity diagram combined with simulations will reveal insights into the geometry and gas inflow in the CMZ, which is a major goal of the ACES project. The 1st-moment map also reflects the asymmetry of both surveys' FoVs around the MW dynamic centre, i.e. Sgr A*, which further results from the asymmetric distribution of gas. The large values in the 2nd-moment map (> 10 km s^{-1}) are a combination of the prevalent LoS confusion of gas in the CMZ and elevated turbulence.

4.3 Dendrogram construction

4.3.1 Structure identification

In Chapter 3, the cloud identification pipeline `CPROPStoo` is adopted, which is based on local maxima and surrounding-pixel assignment. While it yields a reasonable and robust cloud catalogue, there is a scale bias in the identified structures towards the beam size, as discussed a few times in Chapter 3. In this chapter, to better capture the nested hierarchical structure of the ISM (especially given the higher complexity of structures in the MW CMZ than in NGC 1387 studied in Chapter 3) and to take advantage of the larger spatial dynamic range of the ACES survey (than the NGC 1387 data in Chapter 3), we adopt the dendrogram algorithm for structure identification, which is implemented in the python package `Astrodendro`.[7] Compared to most other structure identification algorithms, the main feature of dendrogram is the non-unique pixel assignment to structures. Instead of a catalogue of standalone structures that do not overlap with each other, the dendrogram catalogue is a nested tree of structures where higher-level structures are also part of their parental lower-level structures.

`Astrodendro` iterates from the highest-intensity pixel to the lowest (that is still above the noise level defined by the user, denoted 'min_value'), define a 'leaf' to be pixels uniquely associated with one local maximum that are at least 'min_delta' higher in brightness than the merging-contour level with its adjacent local maxima and have at

[7]We used the developer version available at https://github.com/dendrograms/Astrodendro.

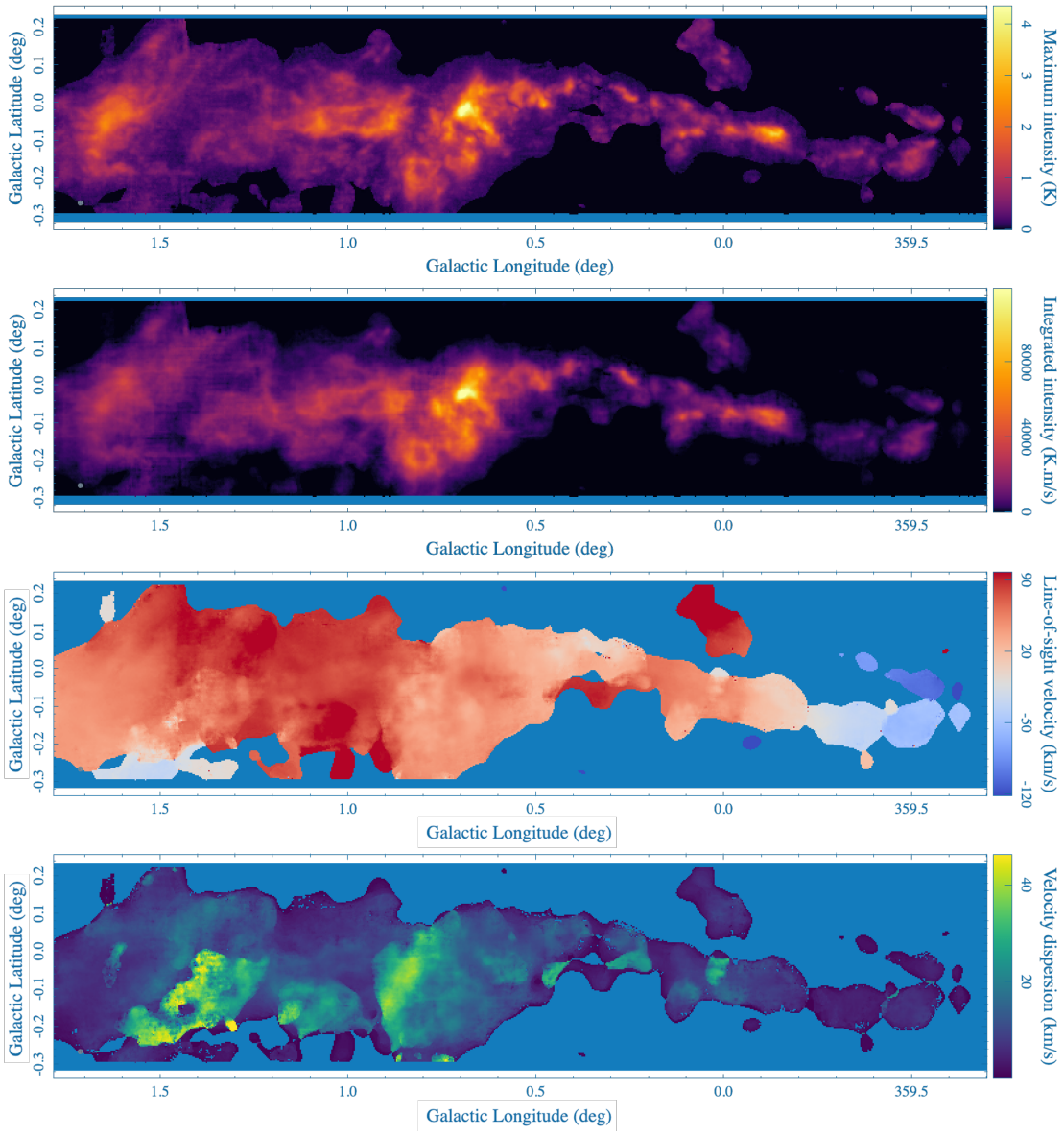

Figure 4.3: Moment maps of Mopra data. From top to bottom: maximum intensity, integrated intensity (i.e. 0^{th} moment), LoS mean velocity (1^{st} moment), and LoS velocity dispersion (2^{nd} moment).

least 'min_npix' pixels, and label all other levels of structures as 'branches' (such as a set including multiple neighbouring leaves). There can be an arbitrary number of levels of branches in a dendrogram during the process of joining new leaves or branches at different merging intensity levels into the dendrogram. For a more detailed description, see Rosolowsky et al. (2008). Intuitively, the lowest-level structures are also called 'trunks' in `Astrodendro`; these are mostly branches but also include a small fraction of leaves in the case of single-level structures. In this chapter, we use 'branch' to

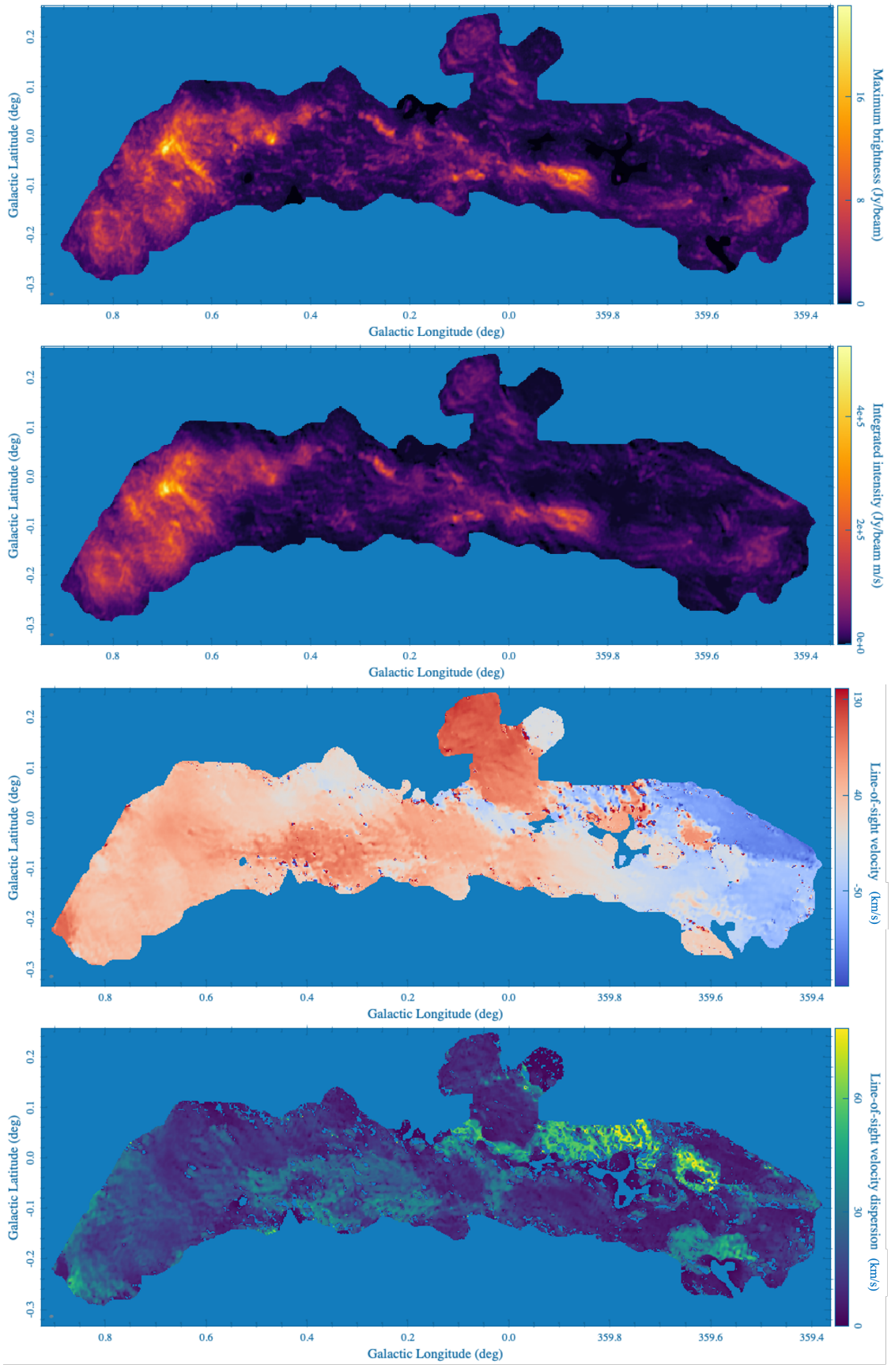

Figure 4.4: Moment maps of ACES data. The same as Figure 4.3 but for the ACES data.

exclusively refer to intermediate-level branches (that are not trunks), to be compared with 'trunks' and 'leaves' in analyses.[8]

Now, we decide on the input parameters for `Astrodendro`. As `Astrodendro` only takes a single value of min_value to set the noise threshold and the ACES cube has strongly varying noise, we input a detection significance cube to `Astrodendro`. It is constructed by dividing the original datacube by its corresponding noise cube created in Section 4.2.3 (with the 'outer edge removal step' implemented). We then set min_value = 5, which effectively requires a 5σ detection significance threshold for any pixel to be considered for the dendrogram. Additionally, we make use of the smoothed cubes (also explained in Section 4.2.3) to further increase the purity of the identification process. Before passing the significance cube to `Astrodendro`, we remove pixels whose intensity in the smoothed datacube is lower than five times its corresponding noise (estimated from the smoothed cube). As for the other threshold parameters, we set min_delta = 5 and min_npix to be twice the spaxel number within a beam (which can be interpreted as a beam-sized structure across two spectral channels, for example, but note the fact that `Astrodendro` does not require a certain pixel count in any individual dimension).

The choice of min_value = 5 and min_delta = 5 are rather conservative as we aim for a high-purity catalogue (instead of high completeness). Our goal is to identify potential physical drivers of gas structure properties and thus a catalogue with minimal false positive structures can provide higher credibility in the physical correlations we may detect. As for individual categories of structures, both high thresholds would result in fewer leaves than using lower thresholds; the high min_value would also reduce the number of trunks in the case of the single-level structures; the high min_delta would also reduce the number of branches as there would be cases where multiple structures were seen as a single one. Given the high sensitivity of the ACES data, all of these effects are expected to be minor. We also do not put high emphasis on the relative structure numbers of different categories until a further Spectral Clustering for Interstellar Molecular Emission Segmentation (SCIMES;[9] Colombo et al. 2015) analysis is done in the future.

[8] Single-level structures appear in both the trunk and the leaf categories.

[9] https://scimes.readthedocs.io/en/latest/

Apart from the adopted procedure described above, we have also tested two alternative approaches: (i) input a datacube without PB correction to `Astrodendro` and (ii) input the original datacube to `Astrodendro` and then prune away structures based on local noise levels (also estimated with `scNoiseRoutines`). Such tests are carried out on an individual field of the ACES data, i.e. the '41/ao' field containing the Brick Cloud. The procedure in use is also run on this field for comparison. The resulting catalogues from all three methods are quite similar in terms of both the visual impression from browsing through the identified structures and the number of structures.

However, the two alternatives have their respective drawbacks. Regarding alternative (i), although the datacube without PB correction is theoretically a flat-noise cube, such an expectation only takes the primary beam into account, but not interferometric artefacts (such as residual sidelobes and negative bowls). As a comparison, in the adopted procedure, the noise estimation method can, to some extent, capture such spatial and spectral variation of noise caused by artefacts. In addition, producing a non-PB-corrected cube for the ACES whole mosaic is not a trivial task, and for the Mopra single-dish data, the PB correction is irrelevant and not the cause of the varying noise. Regarding alternative (ii), although this method inputs a physical datacube (rather than a statistical cube as in the adopted procedure), the preliminary catalogue before pruning is overwhelmed by false detections in terms of the number of structures. Only about 20% of the leaves remain after pruning. Such a method would cast strong uncertainty on the final catalogue, sensitively depending on the choice of the pruning threshold, etc. Furthermore, pruning a dendrogram can cause conceptual difficulty if a leaf itself is deemed valid but its parental branch is pruned away. Therefore, we have demonstrated the efficacy of the adopted procedure from this comparative testing.

4.3.2 Property measurements

Physical properties of the identified structures are measured under the bijection scheme, i.e. considering the full intensities of assigned pixels without extrapolation (Rosolowsky et al., 2008). The 3D position of a structure is reported in Galactic Longitude (l), Galactic

Latitude (b), and velocity in the Kinetic Local Standard Rest frame ($V_{\rm LSRK}$), and measured from the detection significance–weighted mean of those of all pixels.

The radius of a structure ($R_{\rm s}$) is calculated from the spatial area (assuming a spherical geometry) and then deconvolved by half of the beam FWHM (as an approximate beam radius). The linewidth ($\sigma_{\rm s}$) is the detection significance–weighted second moment of velocities deconvolved by the standard deviation of the spectral resolution element, which is 'spectral_resolution/$\sqrt{2\pi}$' as suggested by Rosolowsky & Leroy (2006). This formula converts the width of a top-hat function to the standard deviation of a Gaussian with the same area and height. The standard deviations of the spatial and spectral resolution elements are assigned as uncertainties of $R_{\rm s}$ and $\sigma_{\rm s}$ for all structures, respectively.

The peak intensity ($T_{\rm max}$) of a structure is reported in brightness temperature unit (K) and its uncertainty is the RMS noise of the peak-intensity pixel extracted from the noise cube. The luminosity of a structure (e.g. $L_{\rm HNCO}$) is reported in the unit of K km s^{-1} pc^2 using the distance of 8 kpc. The uncertainty is calculated by the root-total-square of corresponding pixels in the noise cube, multiplied by the square root of the pixel number per beam to account for spatial correlation.

The (morphological) position angle ($\phi_{\rm m}$) is the direction of the major axis, i.e. the direction with the greatest elongation of a structure in the sky plane, measured from Galactic north through east. The direction perpendicular to that is the minor axis. The axis ratio (q) is the detection significance–weighted second spatial moment in the direction of the minor axis ('minor_sigma') over that of the major axis ('major_sigma'). Similarly, we use the standard deviation of the beam's major axis as the uncertainty of 'minor_sigma' and 'major_sigma', and use standard error propagation to derive the uncertainty of q.

We regard a structure as resolved only if $R_{\rm s}$ and $\sigma_{\rm s}$ are larger than the instrumental resolution (i.e. half of the beam FWHM and half of the spectral resolution, respectively). Unresolved structures are still likely to be real. They exist in the catalogue due to the crowdedness in the CMZ and the fact that `Astrodendro` does not specify a minimum size in any dimension (but only imposes a total pixel count threshold). Considering the high min_value in use, the expected fake structures from noise should be at most one

per cent of the catalogue (based on the numbers of independent resolution elements in the cubes and the numbers of identified structures in Sections 4.4 and 4.5).

However, some of the properties of the unresolved structures may not be trustworthy. R_s and σ_s are directly affected. We only show the unresolved structures in the histograms of R_s and σ_s to show their relative distributions to the whole catalogue, but we remove the values of R_s (or σ_s) for spatially (or spectrally) unresolved structures from the tables of structure properties. In other figures, they are plotted as limits. T_{max} and L_{HNCO} should be unaffected. As for morphological analyses with q and ϕ_m, we only keep the spatially resolved structures. Also, other quantities derived from R_s and/or σ_s naturally only apply to structures whose R_s and/or σ_s are resolved.

4.4 Mopra dense-molecular dendrogram catalogues

The resulting dendrogram catalogue from the Mopra HNCO data contains 129 structures (including 13 single-level structures): 75 leaves, 46 (intermediate-level) branches, and 21 trunks. The catalogue is visualised in Figure 4.5 by overlaying contours of structures on top of the 0^{th}-moment map. It is clear all significant emission is classified into structures and a higher number of structure levels occur in brighter and more complex regions. There are 13 structures deemed unresolved, all due to the spectral criterion.

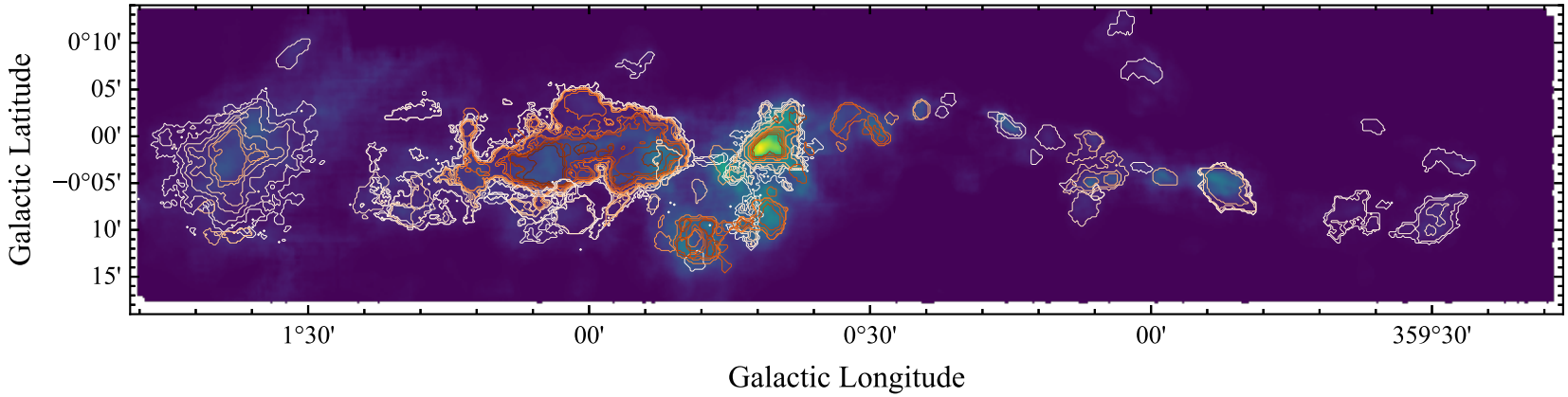

Figure 4.5: Mopra HNCO catalogue. Identified dendrogram structures (contours) from the Mopra HNCO cube overlaid on the 0^{th}-moment map of the Mopra HNCO data. The contour for each structure is made from the specific channel containing its peak intensity. The darker orange the contour is, the higher level the structure is.

Table 4.2: Mopra HNCO catalogue.

ID	l	b	$V_{\rm LSRK}$	$R_{\rm s}$	$\sigma_{\rm s}$	$L_{\rm HNCO}$	$T_{\rm max}$	q	$\phi_{\rm m}$	Category
	(° : ′ : ″)	(° : ′ : ″)	(km s^{-1})	(pc)	(km s^{-1})	(K km s^{-1} pc^2)	(K)		(degree)	
1	−00:32:37	−00:02:50	−103.2	4.6	4.8	319 ± 3	1.00 ± 0.04	0.3 ± 0.2	82	single
2	−00:23:45	+00:00:59	−77.7	2.4	2.1	46.1 ± 1.2	0.57 ± 0.05	0.6 ± 0.6	73	single
3	−00:30:27	−00:08:47	−55.9	6.9	6.2	1172 ± 5	1.09 ± 0.03	0.6 ± 0.2	131	trunk
4	−00:30:42	−00:08:40	−55.5	5.6	5.2	820 ± 3	1.09 ± 0.03	0.5 ± 0.2	144	branch
5	−00:27:16	−00:09:52	−58.5	1.5	3.2	33.3 ± 0.8	0.61 ± 0.04	0.6 ± 0.8	103	leaf
6	−00:29:45	−00:09:57	−55.5	1.4	2.0	39.7 ± 0.5	1.07 ± 0.04	0.7 ± 0.9	50	leaf
7	−00:30:38	−00:08:08	−57.2	2.2	-	75.2 ± 0.7	1.09 ± 0.03	0.8 ± 0.6	26	leaf
8	−00:20:25	−00:08:12	−28.4	7.4	5.6	495 ± 3	0.95 ± 0.03	0.5 ± 0.2	95	trunk
9	−00:20:12	−00:08:04	−28.0	5.8	4.9	318 ± 2	0.95 ± 0.03	0.4 ± 0.2	106	leaf
10	−00:23:38	−00:09:24	−34.0	1.8	2.2	34.9 ± 1.0	0.64 ± 0.05	0.9 ± 0.9	163	leaf
...	...	...	...	...	...	...	...	...	...	...
129	+01:09:53	−00:06:35	126.3	2.0	2.8	36.4 ± 1.1	0.57 ± 0.05	0.6 ± 0.6	102	single

Notes: Measurements of these properties are detailed in Section 4.3. Only spatially (or spectrally) resolved structures have $R_{\rm s}$ (or $\sigma_{\rm s}$) values. Uncertainties of $R_{\rm s}$ and $\sigma_{\rm s}$ are communally assumed to be the standard deviation of the spatial and spectral resolution elements, which are 0.64 pc and 1.4 km s^{-1}, respectively. q and $\phi_{\rm m}$ are reported only for spatially resolved structures. In the Category Column, 'Branch' refers to non-trunk branches only, slightly different from the original definition in `Astrodendro`, and 'Single' refers to single-level structures, which are regarded as both leaves and trunks.

4.4.1 Fundamental properties of HNCO structures

Properties of identified structures are measured according to Section 4.3 and tabulated in Table 4.2. Histograms of the fundamental properties of HNCO structures are shown in Figure 4.6. For the radius, leaves are exclusively small (< 6 pc) while both branches and trunks spread a much larger range (up to 28 pc). Despite the definition of trunks, only a few of them (three in this case) are at the largest end of structures, harbouring many large branches. All three categories peak at the lowest end of ≈ 1 pc, but all structures are spatially resolved. Besides, all the 13 single-level structures, which comprise more than half of the trunk category (13/21), are rather small (1.4–4.9 pc).

The maximum brightness, luminosity, and linewidth distributions all show a similar feature in that the leaf population is smaller in these properties than the branch population while the trunk population always spreads a wide range. The maximum brightness distribution of leaves (and trunks) also steadily increases towards smaller values, similar to the radius distributions. These similarities are partially due to the general correlations between these four quantities, among which the size-linewidth relation is elaborated in Section 4.4.2. The nesting behaviour is most clearly seen at the highest end of the

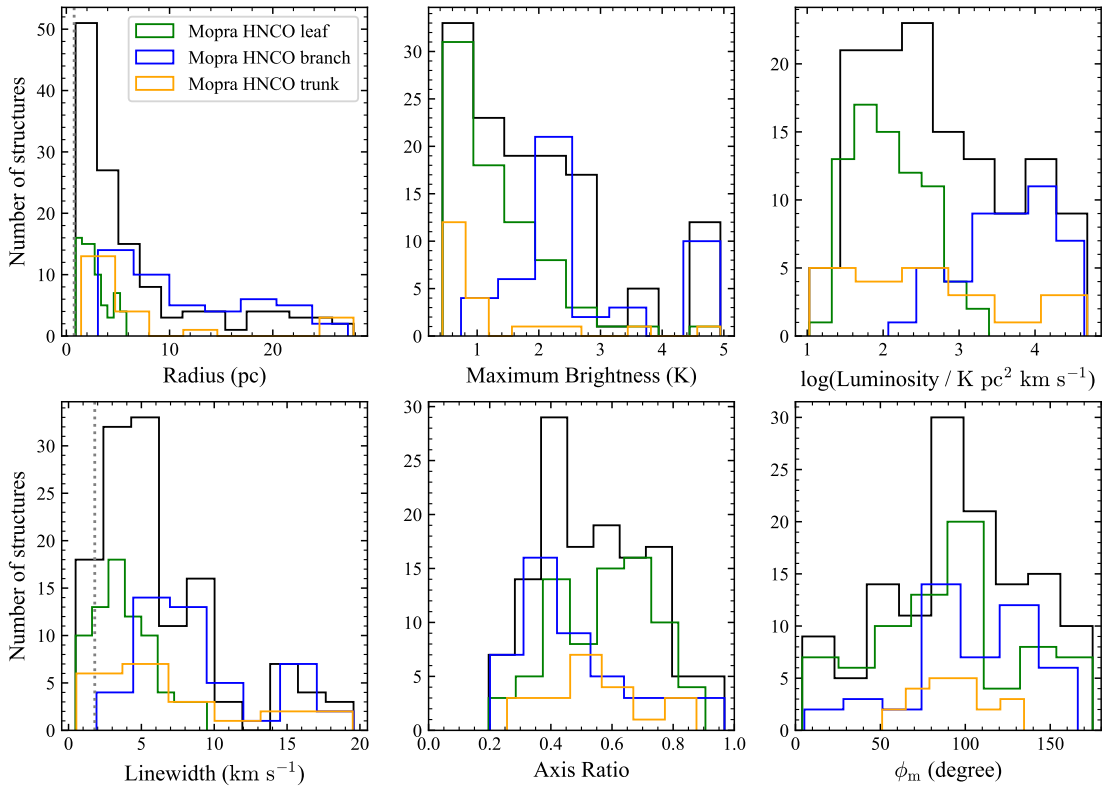

Figure 4.6: Fundamental property distributions of Mopra HNCO catalogue. From left to right and then upper to lower: radius, maximum brightness, luminosity, linewidth, axis ratio, and morphological position angle. The three categories are shown in the three different colours indicated by the legend while the overall distributions are shown in black. The vertical grey dotted lines in the panels of radius and linewidth are the resolution threshold, i.e. half of the beam FWHM and half of the spectral resolution, respectively.

maximum brightness distribution. The brightest pixel (of 4.9 K) occurs in one leaf and one trunk, with ten branches as intermediate levels sharing it.

As for the axis ratio, leaves tend to be slightly rounder (i.e. q closer to unity) than branches, potentially because leaves are more affected by the round beam, as they are (on average) smaller in intrinsic sizes. But still, the majority of leaves have an axis ratio below 0.8, although they do have larger uncertainties in q than branches and trunks. The trunks, again, have a broad distribution in q. The morphological position angle (ϕ_m) distribution of the leaves slightly peaks at around 90°. This may be a tentative hint of shear effects posing an elongation along the Galactic plane rather than in the vertical direction. The branch ϕ_m distribution shows two peaks at about 90° and 140°. The trunk distribution of ϕ_m also centres at 90° but has a much narrower range than that of the leaves.

Only the largest few trunks are biased by the overall gas distribution in the CMZ (i.e. constrained to a spatial extension along the Galactic plane), and the rest are interesting to study further (most of which are standalone single-level structures).

4.4.2 Size-linewidth relation

The Larson scaling relations are a powerful tool to understand the dynamical state of a molecular cloud (Larson, 1981). Among them, the size-linewidth relation reveals the turbulence level at a given spatial scale. In Figure 4.7, the resolved (both spatially and spectrally) structures of the Mopra observation (in blue symbols) clearly form a linear correlation, with a rather high Pearson correlation coefficient of 0.73. Among the three categories, leaves and branches closely follow the same trend with leaves occupying the lower-end of both quantities. Trunks have a broad distribution, generally encompassing the other two populations. This comparison will be further discussed in Section 4.5.2 with ACES data. The string of structures (one trunk and many branches harboured in that trunk) in the range of 10–30 pc and 5.5–10 km s^{-1} shows another example of hierarchically nested structures of the 1.1-Degree Cloud Complex. More specifically, nearby local intensity maxima in that cloud are each identified as a leaf, and then gradually joined together to form increasingly larger (and higher linewidth) branches at decreasing merging-contour intensities. On a separate note, a few trunks (star symbol) in the plot have a leaf (dot) right at its centre. These are the so-called single-level structures, which appear in both leaves and trunks by our definition. They are standalone emission structures in the CMZ not having any significant sub-structures so as not to form any additional branch level. These are worth detailed study in the future.

This correlation is compared to a few other catalogues and relations from the literature. The red squares show the N_2H^+ dendrogram structures from Shetty et al. (2012). N_2H^+ is regarded as the gold-standard dense gas tracers, only observable (at this spatial resolution) in the MW due to its faintness (e.g. Caselli et al., 2002; Bergin & Tafalla, 2007). The two populations generally occupy the same parameter space with similar scatters, but the N_2H^+ population is very slightly higher in linewidth at a given radius. The difference might partially arise from the slightly different procedures in constructing and plotting

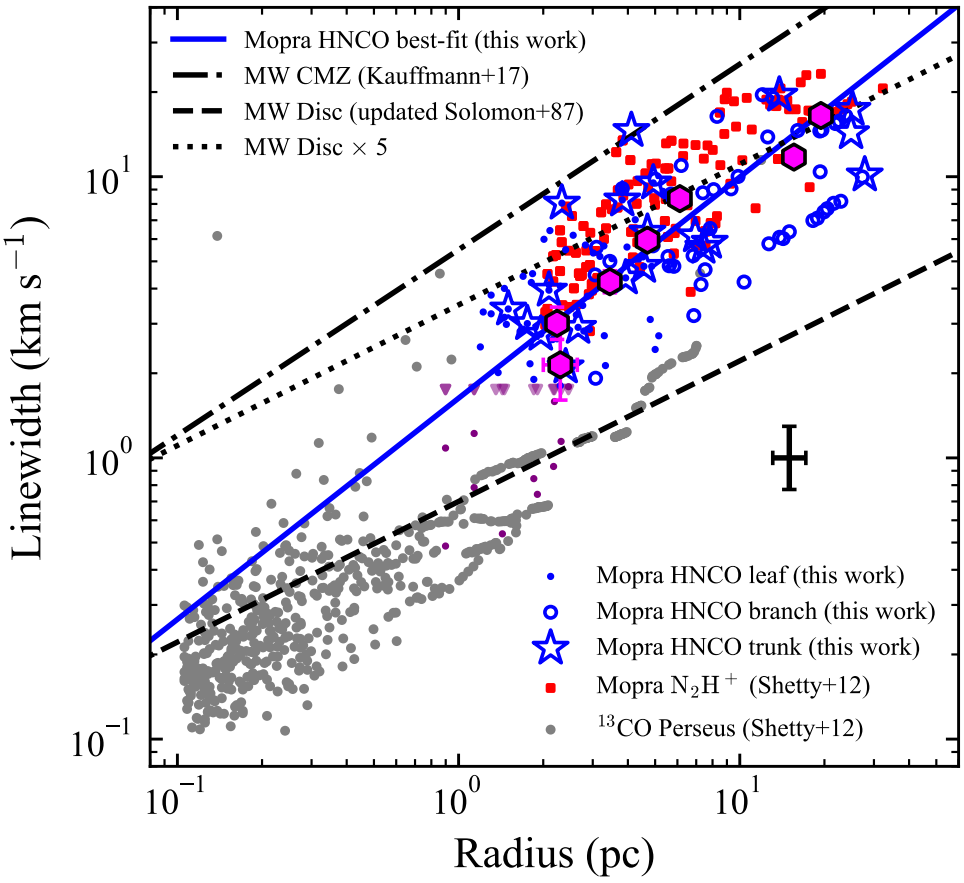

Figure 4.7: Mopra HNCO size-linewidth relation. Blue symbols show the resolved leaves (dots), branches (open circles), and trunks (stars) of the Mopra HNCO catalogue. The median log-space error of all resolved structures is shown as the black errorbar in the middle-right. The large magenta hexagons are binned (using linewidth as the independent variable) medians of resolved structures with propagated errors shown in the errorbars (some too small to be visible), all categories combined. Unresolved ones from this catalogue are shown both using their measured values (purple dots) and the upper limits at the resolving threshold (purple triangles). The Mopra N_2H^+ CMZ catalogue and the ^{13}CO Perseus catalogue from Shetty et al. (2012) are shown in red squares and grey dots, respectively. The solid blue line is the best-fitting relation of the Mopra HNCO catalogue. The dash-dotted black line is the MW CMZ relation from Kauffmann et al. (2017). The dashed black line is the MW Disc relation from Solomon et al. (1987) updated by Heyer et al. (2009). The dotted line is multiplying the MW Disc relation by five (in linear space) proposed by Shetty et al. (2012).

the dendrogram. For example, they input the datacube to `Astrodendro` rather than the detection significance cube used in this work, affecting both structure identification and quantity measurements. Also, they do not deconvolve the size or linewidth. To avoid methodology differences, a comparison with the same pipeline is presented in Section 4.4.3, where the same results will be seen. The ^{13}CO (used as a dense gas tracer) dendrogram structures in the Perseus Galactic Molecular Cloud (in grey points; Shetty et al., 2012), follow the MW disc relation with a slope of 0.5 from Solomon et al. (1987) updated by Heyer et al. (2009), in the dashed black line.

The best-fitting formula (the blue solid line) of the Mopra correlation is

$$\log \sigma_{\rm s} = (0.78 \pm 0.08) \times \log R_{\rm s} + (0.22 \pm 0.10) \ , \tag{4.1}$$

with 0.2 dex scatter (i.e. RMS of the residual on $\log(\sigma_{\rm s}/{\rm km\ s^{-1}})$). The fitting uses the python package `Linmix`[10] based on the algorithm of Kelly (2007). It is likelihood-based Bayesian statistics with Markov chain Monte Carlo (MCMC) sampling. The unresolved structures omitted in the fitting are shown by purple dots in Figure 4.7. They can also be considered as having upper limits in linewidth, the value of which is the spectral-resolving threshold we set (shown by purple triangles, corresponding to purple dots one by one). Due to this censorship of the sample, other methods such as least χ^2 or orthogonal distance regression would be biased. As all structures are spatially resolved but some are spectrally unresolved, we use linewidth as the independent variable and radius as the dependent variable in the fitting. Since censorship happens only in the dimension of the independent variable, such likelihood-based fitting is unbiased (Kelly, 2007). In addition, the fitting is done with binned data as input, shown in large magenta hexagons, rather than individual data points. This is because the data points at the lower end of the independent variable (i.e. linewidth) have large log-space errors, and this severely affects the stability and quality of the fitting. Within each bin of the independent variable, the median values of both quantities are used in the fitting (so as to mitigate the influence of outliers, compared to the mean estimator), with errors of the medians propagated from the original data points' errors. These smaller errors of the binned data guarantee the fitting quality. Last

[10] https://github.com/jmeyers314/linmix?tab=readme-ov-file

but not least, the fitting is in the ten-base logarithm space (rather than the linear space) to avoid a bias of dominance of the points at the higher end of the dependent variable.

This best-fitting relation is significantly higher in both the slope and the normalisation than the MW Disc relation. Shetty et al. (2012) got the same slope of 0.78 ± 0.18 from their N_2H^+ fitting and the lowest slope of 0.62 ± 0.19 for HCN among the other tracers (both are 1σ uncertainties adapted from their Table 2). As they did not study the HNCO line, there is no direct comparison. Nonetheless, they conservatively argued their relation (considering the rather large range of slopes from all tracers) is still consistent with the MW Disc relation but used five times its normalisation (the dotted black line) to match their data. The normalisation of our fitting indeed agrees well with both their N_2H^+ structures and the line of 'MW Disc ×5', but the MW Disc slope is arguably not as good a fit as the blue line to the HNCO structures. On the other hand, our slope based on the Mopra catalogue is closer to (and even steeper than) that of 0.66 ± 0.18 reported by Kauffmann et al. (2017). This result will be compared to the ACES result in Section 4.5.2 and further discussed in Section 4.6.2.

4.4.3 Comparison among different molecular-gas tracers

To fully take advantage of the broad and homogeneous line coverage of the Mopra dataset, we carry out the same procedure detailed in Section 4.3 to four other lines: HCN, N_2H^+, HCO^+, and HC_3N. HCN is used for external galaxies as a reasonable replacement of N_2H^+ in tracing dense gas (e.g. Gao & Solomon, 2004a; Jiménez-Donaire et al., 2019; Stuber et al., 2023b). The N_2H^+ dendrogram is now constructed with the same procedure as HNCO and other lines to avoid pipeline differences compared to Shetty et al. (2012). HCO^+ (Graciá-Carpio et al., 2006) and HC_3N Mills et al. (2018) are newly adopted dense gas tracers .

For display clarity, we carry out kernel density estimations for the dendrogram of each line (including all three categories of resolved structures). The resulting comparison is presented in Figure 4.8, where the (smallest possible) contours representing the dendrograms each tightly enclose 80% of the structures. All five lines are in general agreement in the occupation of the parameter space and the size-linewidth trend. Apart

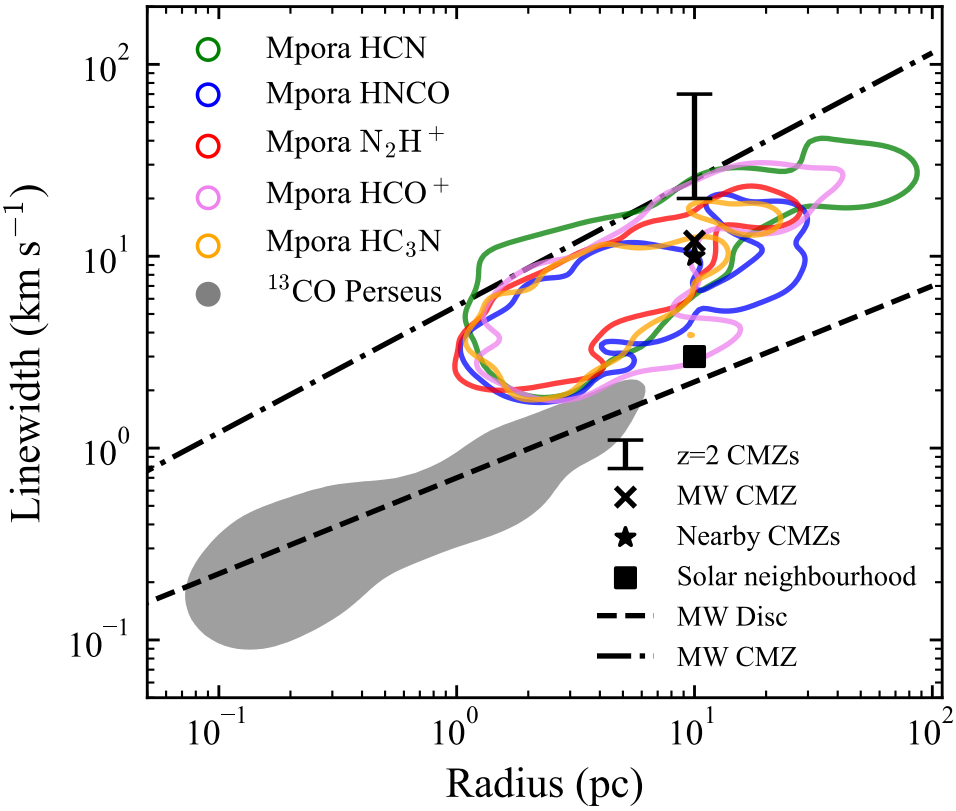

Figure 4.8: Mopra size-linewidth relations of multiple tracers. Each of the tracer's catalogues is shown by the smallest possible contour tightly encompassing 80% of the data points, with an assigned colour indicated by the legend. The dashed and dash-dotted lines are the same as in Figure 4.7. The four black symbols show the characteristic linewidths at 10-pc for z = 2 CMZs (range symbol), the MW CMZ (cross), nearby CMZs (star), and the solar neighbourhood (square), all from Henshaw et al. (2023).

from the MW Disc relation, the MW Disc Perseus Cloud (both from Shetty et al., 2012), and the MW CMZ relation from Kauffmann et al. (2017) as in Figure 4.7, we also add a few representative linewidth scales at 10-pc spatial scale from Henshaw et al. (2023), measured in the solar neighbourhood (square symbol), nearby CMZs (star symbol), MW CMZ (cross symbol), and cosmic-noon CMZs at z=2 (range symbol). All the contours in this work show good consistency with the CMZs in the MW and the local universe.

4.5 ACES HNCO dendrogram catalogue

The resulting dendrogram catalogue from the ACES HNCO data contains 2751 structures (including 130 single-level structures): 1463 leaves, 1243 (intermediate-level) branches,

and 175 trunks. The catalogue is visualised in Figure 4.9 and tabulated in Table 4.3. There are 584 unresolved structures, all due to the spatial criterion.

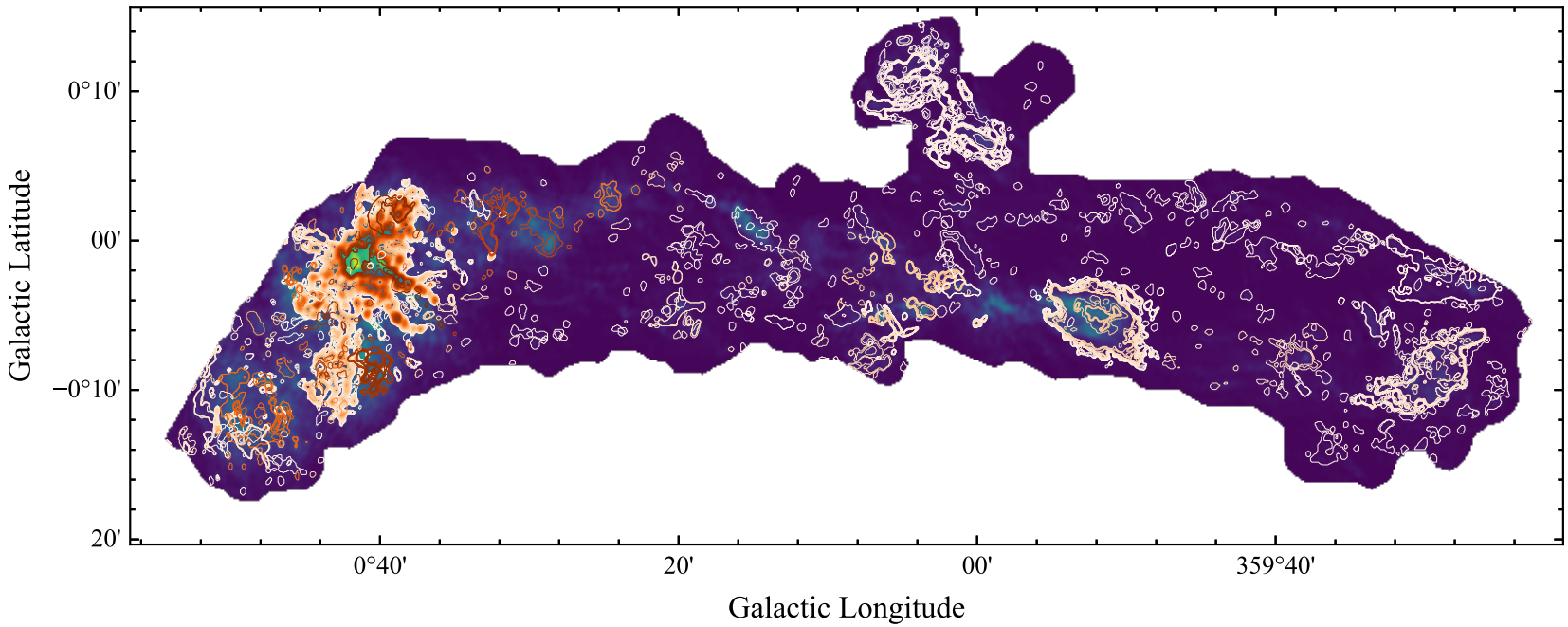

Figure 4.9: ACES HNCO catalogue. The same as Figure 4.5, but for the ACES HNCO catalogue. For clarity, only the trunks and randomly selected 20% of other structures are plotted.

Table 4.3: ACES HNCO catalogue.

ID	l	b	$V_{\rm LSRK}$	$R_{\rm s}$	$\sigma_{\rm s}$	$L_{\rm HNCO}$	$T_{\rm max}$	q	$\phi_{\rm m}$	Category
	(° : ′ : ″)	(° : ′ : ″)	(km s^{-1})	(pc)	(km s^{-1})	(K km s^{-1} pc^2)	(K)		(degree)	
1	−00:27:46	−00:01:11	−92.31	9.5	12.62	1246.0 ± 0.6	2.11 ± 0.02	0.17 ± 0.03	70	trunk
2	−00:28:53	−00:01:30	−94.75	8.0	10.36	1055.8 ± 0.5	2.11 ± 0.02	0.17 ± 0.04	66	branch
3	−00:27:50	−00:01:13	−92.43	9.1	12.52	1193.8 ± 0.6	2.11 ± 0.02	0.17 ± 0.03	70	branch
4	−00:28:54	−00:01:31	−94.76	7.8	10.37	1042.3 ± 0.5	2.11 ± 0.02	0.17 ± 0.04	66	branch
5	−00:28:57	−00:01:32	−94.81	7.5	10.31	1004.8 ± 0.5	2.11 ± 0.02	0.17 ± 0.04	66	branch
6	−00:28:58	−00:01:32	−94.83	7.4	10.29	997.4 ± 0.5	2.11 ± 0.02	0.17 ± 0.04	66	branch
7	−00:28:59	−00:01:32	−94.86	7.2	10.24	973.3 ± 0.4	2.11 ± 0.02	0.17 ± 0.04	66	branch
8	−00:35:46	−00:03:25	−120.45	-	1.62	0.73 ± 0.02	0.78 ± 0.05	-	-	leaf
9	−00:29:00	−00:01:33	−94.91	7.0	10.14	944.6 ± 0.4	2.11 ± 0.02	0.17 ± 0.04	66	branch
10	−00:29:00	−00:01:33	−94.87	7.1	10.19	949.9 ± 0.4	2.11 ± 0.02	0.17 ± 0.04	66	branch
...	...	...	...	...	...	...	...	...	...	...
2751	+00:40:38	−00:01:42	144.24	-	1.14	0.73 ± 0.03	0.84 ± 0.06	-	-	single

Notes: The same as Table 4.2 but for the ACES HNCO dendrogram catalogue. The communal uncertainties of $R_{\rm s}$ and $\sigma_{\rm s}$ are 0.31 pc and 0.080 km s^{-1}, respectively.

4.5.1 Fundamental properties

Histograms of structure properties are shown for the ACES HNCO dendrogram catalogue in Figure 4.10. In comparison with the Mopra version in Figure 4.6, radius and maximum brightness distributions are very similarly showing an increasing profile towards smaller values and the hierarchically nested structures at the high-value ends. Different from the case of Mopra, 584 structures are spatially unresolved in the ACES catalogue. Although this makes the exact profile at the small-radius end less constrained, the general increasing trend should still be valid. Future work with the full 12m resolution of ACES data will extend the spatial-resolving power further down to $\approx$ 0.1 pc.

As for the luminosity and the linewidth, similar to the Mopra distributions, branches are marginally larger than leaves as a population. But different from the Mopra histograms, where trunks have a mostly uniform and broad distribution, the ACES trunk distributions significantly peak at the lower end of both quantities, similar to where the leaf distributions peak.

The distributions of the axis ratio and the position angle are very similar among the three categories of structures, and the q of all of them peaks far away from unity, which indicates significant elongation. The position angle distribution of the trunks is much wider than that from the Mopra data. It is worth noting the ACES beam is not round but rather has an instrumental axis ratio of 0.72 at a position angle of 101°. As there is no concentration of structures at these values in the histograms, it is safe to

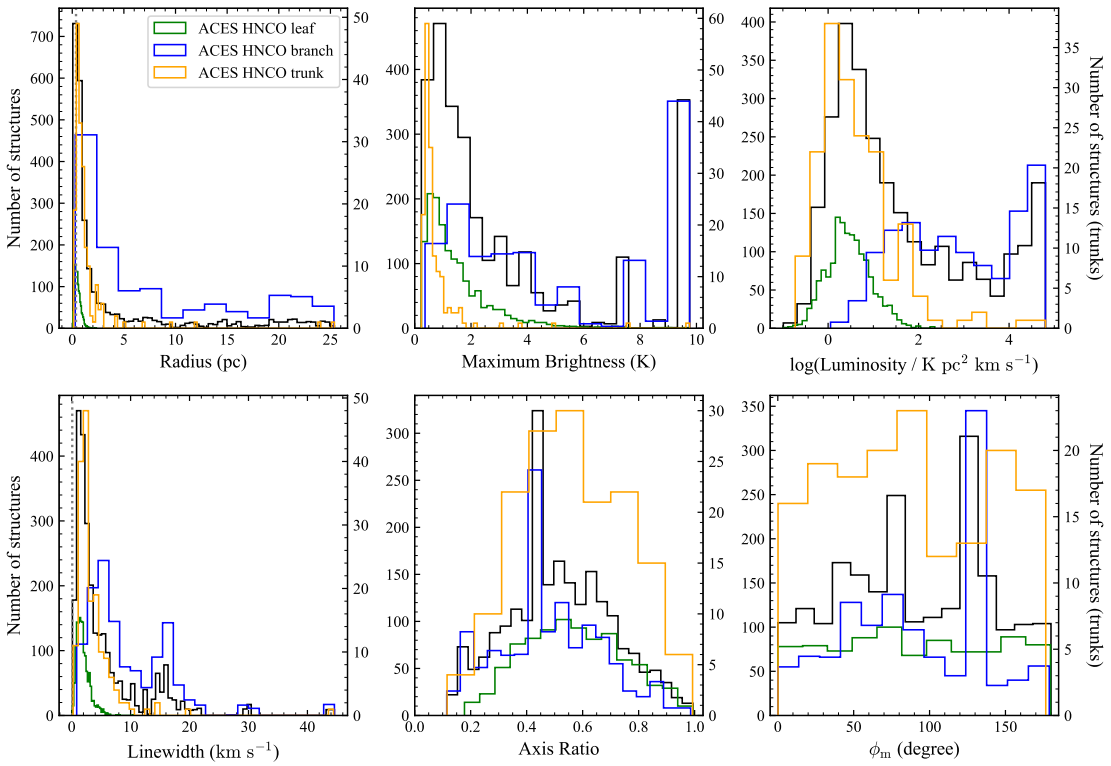

Figure 4.10: Fundamental property distributions of ACES HNCO catalogue. The same as Figure 4.6 but for the ACES HNCO dendrogram. For clarity, the trunk distributions in all panels are shown on a separate y-scale on the right.

state the spatially resolved structures of the dendrogram catalogue (even for the leaf category) are not severely affected by the beam ellipticity. The narrow spike of the branch population in both quantities ($q \approx 0.42$ and $\phi_m \approx 130°$) comes from the nested structures at Sgr B2. Due to its brightness, a constant min_delta level for 'hierarchy slicing' inevitably yields many more structures here than in other regions of the CMZ. As part of future work, utilising the algorithm and python package of SCIMES should be able to avoid such arbitrariness in dendrogram construction and provide a more coherent and physically driven ISM segmentation.

4.5.2 Size-linewidth relation

As done to the Mopra catalogue, we again use the size-linewidth relation to study the dynamical state of structures in the ACES HNCO dendrogram. Figure 4.11 shows the comparison between the ACES and Mopra dendrograms in the R_s-σ_s space. The contours with two different colours (corresponding to the two dendrograms) shown in all panels

are again the smallest enclosing curves of 80% of structures (only resolved structures are considered). The three panels separately show the different categories. In the parameter space probed by both surveys, the two dendrograms are in good agreement. The major difference (i.e. the several Mopra structures in the range of 10–30 pc and 5.5–10 km s^{-1} that are absent in ACES) comes from the 1.1-Degree Cloud Complex outside the ACES FoV. At the higher ends of both quantities, many branch structures form a few 'strings' of structures. This is again an example of nested ISM explained in Sections 4.4.1 and 4.4.2. At the lower ends of both quantities, the ACES survey shows the power of much better resolutions in both dimensions. Many more reliable structures are detected, mostly categorised as leaves. Similarly to the Mopra case, the leaf and branch populations are well separated in the parameter space while the trunks encompass both of them. In fact, most of the trunks at the lower ends of both quantities are standalone single-level structures.

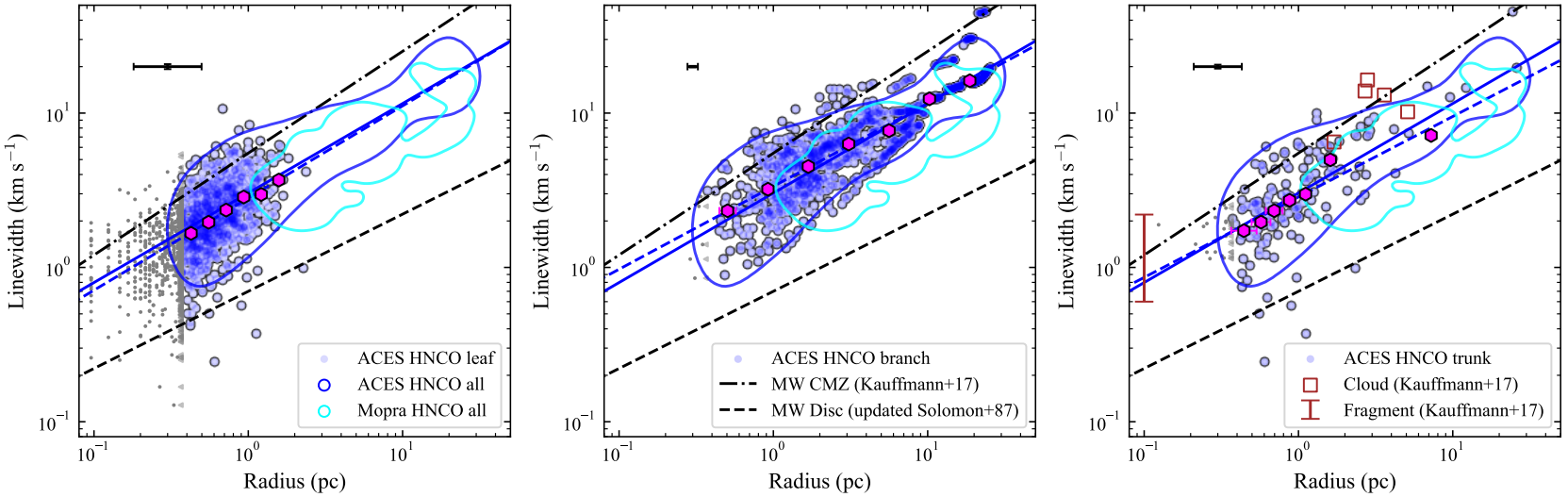

Figure 4.11: ACES HNCO size-linewidth relation. Resolved leaves, branches, and trunks of the ACES HNCO dendrogram are shown as blue-shaded circles from the left to the right panel, respectively. The darker blue indicates the higher number density of data points in the parameter space. The median log-space error of resolved structures in each category is shown as the black errorbar in the top-left corner of each panel. The large magenta hexagons are binned (using size as the independent variable) medians of resolved structures in each category (corresponding to each panel) with propagated errors shown in the errorbars (mostly too small to be visible). Unresolved ones are shown both using their measured values (grey dots) and the upper limits at the resolving threshold (grey triangles). The blue and cyan contours across all panels show the overall distributions of ACES and Mopra (resolved) structures, respectively, by tightly encompassing 80% of the data points. The solid blue line in all panels is the best-fitting relation of the overall (resolved) ACES HNCO catalogue while each dashed blue line shows that of the specific category in each panel. The dashed and dash-dotted black lines are the same as in Figure 4.7. The brown range symbol and brown hollow squares in the right panel are the 'fragments' and 'entire clouds' in Kauffmann et al. (2017).

Table 4.4: ACES HNCO size-linewidth relation fitting results.

Category	Slope	Normalisation	Scatter	r_p
All structures	0.58 ± 0.02	0.482 ± 0.014	0.17	0.90
Leaves	0.60 ± 0.05	0.450 ± 0.011	0.19	0.44
Branches	0.54 ± 0.02	0.525 ± 0.014	0.15	0.89
Trunks	0.52 ± 0.07	0.46 ± 0.03	0.23	0.69

Notes: The fitting parameters are defined as $\log \sigma_s = k \log R_s + b$, where k is the slope and b is the normalisation. Scatter is the RMS of the fitting residuals of $\log(\sigma_s/\mathrm{km\ s^{-1}})$. r_p is the Pearson correlation coefficient.

Best-fitting parameters of the size-linewidth relations, along with the scatter (i.e. residual RMS of $\log(\sigma_s/\mathrm{km\ s^{-1}})$) and the Pearson correlation coefficient, are plotted as dashed blue lines in each panel and summarised in Table 4.4. Following the same principles as in the Mopra fitting, we use the radius as the independent variable to achieve unbiased fitting with `Linmix`, as all ACES structures are spectrally resolved but some only have unresolved radii (grey dots) interpreted as upper limits (grey triangles). All other steps are the same as in the Mopra fitting. In the leaf panel (and the other two panels as well), it is a good sign for the fitting robustness that the best-fitting line (blue dashed line) using only resolved structures also extrapolates through the middle of the unresolved ones (grey dots).

The leaves have the weakest correlation coefficient of 0.44 with an intermediate scatter of 0.19 dex among the three categories while the trunks' trend has the largest scatter of 0.23 dex with an intermediate correlation coefficient of 0.69. The scatter of the trunk relation comes mainly from the low-radius end (which is roughly the entire range of leaf radii) while the higher correlation coefficient of trunks is largely due to its larger dynamic range than that of the leaves. The branch population has the tightest correlation (among the three categories) with the lowest scatter of 0.15 dex and the highest r_p of 0.89, since it has as large a dynamic range as the trunks' and does not suffer from the low-radius-end scatter. The overall relation has r_p of 0.90, also owing to the large dynamic range from the combination of the three categories.

The slopes of the different categories range from 0.52 for the trunks to 0.60 for the leaves, but this range is almost fully within the uncertainty. All of them, as well as the overall slope of 0.58 (plotted as the blue solid line in all panels), are lower than

(but still statistically consistent with) past findings of the MW CMZ with a slope of 0.66 ± 0.18 (Kauffmann et al., 2017), which is plotted as the black dash-dotted line in all panels. The normalisation of the branches is slightly higher than the others, but all of them are significantly lower than $0.74^{+0.07}_{-0.09}$ of Kauffmann et al. (2017). We have also added the 'fragments (of clouds)' (a brown range) and the 'entire clouds' (brown hollow squares) from Kauffmann et al. (2017) to the trunk panel in Table 4.4, from which they derived their size-linewidth relation. This comparison will be further discussed in Section 4.6.2. Compared to the MW Disc relation (plotted as the black dashed line Solomon et al., 1987; Heyer et al., 2009), the best-fitting trends of all categories are higher in both the slope and the linewidth values at any given radius, although a few single-level structures are located around the MW Disc trend.

4.5.3 Virial parameter

The virial parameter is another useful metric in judging the dynamical state of a structure. It is defined as the ratio of the virial mass (i.e. the dynamical mass assuming virial equilibrium $M_{\rm vir}$; MacLaren et al. 1988) over the (luminous) molecular gas mass of a structure ($M_{\rm s}$), yielding

$$\alpha_{\rm s} \equiv \frac{M_{\rm vir}}{M_{\rm s}} = \frac{\sigma_{\rm s}^2 R_{\rm s}/b_{\rm s}{\rm G}}{M_{\rm s}} \ , \tag{4.2}$$

where G is the gravitational constant and the geometric parameter $b_{\rm s}$ is taken to be $1/5$, corresponding to a homogeneous and spherical mass volume density distribution. We use the typical density of gas traced by HNCO and the structure radius $R_{\rm s}$ to calculate $M_{\rm s}$, assuming a uniform spherical distribution of gas mass. We adopt the HNCO density derived from radiative transfer modelling in the CMZ M0.8-0.2 Ring of $10^{4.2}$ cm^{-3} with 1 dex of uncertainty (Nonhebel et al., 2024). Again, only resolved structures are used in this analysis. The resulting $\alpha_{\rm s}$ distribution is shown in the left panel of Figure 4.12. The trunks and leaves occupy the same range, which peaks at roughly $\alpha_{\rm s} = 3 - 6$. The branches are, on average, lower and have double peaks at $\alpha_{\rm s} \approx 0.5, 3$. The theoretical threshold of virialisation, only considering gravity but not ISM ambient pressure, magnetic fields, etc., is $\alpha_{\rm s} = 1$ (plotted as the vertical grey dashed line). The

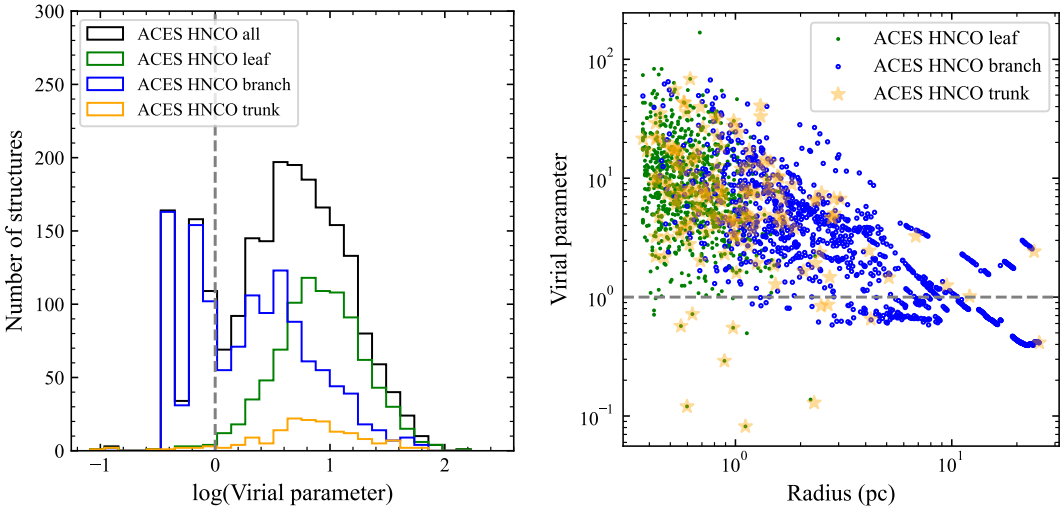

Figure 4.12: ACES HNCO viral parameter. *Left:* the histogram of the virial parameter of the resolved ACES HNCO structures, colour-coded by categories indicated in the legend. *Right:* virial parameter vs. radius, for resolved ACES HNCO structures. The grey dashed lines in both panels indicate virial equilibrium at $\alpha_s = 1$.

empirical threshold of structure boundedness is $\alpha_s = 2$ or $\log \alpha_s = 0.3$. Judging by these criteria, the majority of leaves and trunks are unbound and super-virial structures while a substantial fraction of branches are bound and/or virialised.

This difference may partly result from our calculation of α_s. We assume a constant density and a spherical geometry for all structures. Thus, effectively, $\alpha_s \propto (\sigma_s/R_s)^2$. Due to the sub-linear slope (i.e. smaller than unity) in the size-linewidth relation, α_s is negatively correlated with R_s. Branches, on average, have larger R_s than the other categories, and thus have lower α_s. Such behaviour can be seen in the negative correlation in the right panel of Figure 4.12, where the majority of structures below $\alpha_s = 1$ are those nested branch structures at the high-R_s end. As for trunks, while they also scarcely cover the high-R_s regime of the relation and these few trunks show up low in α_s, they also contribute six (single-level) structures below $\alpha_s = 1$ at the low-R_s end. These are the outliers to the size-linewidth relation seen in Figure 4.11 with very low linewidths similar to the MW Disc level.

Although the assumptions behind the α_s calculation and the uncertainty of our input density of 1 dex could affect the results, the total mass summed from all trunks is 5.6×10^7 $M_\odot$. This is consistent with the dust-derived total mass, within the uncertainty

of dust opacity assumption (Longmore et al., 2013). This seems to indicate the calculation of M_s (and thus α_s) is reasonable.

4.5.4 Elongation and orientation

The morphology of a molecular structure can embed information of its formation and evolution history. We study the elongation and orientation (measurements explained in Section 4.3) of the dendrogram structures and test the following two factors as the potential regulators of these properties: galactic shear and magnetic field.

Shear and tidal effects

Strong differential rotation, typical in the deep gravitational field of the bulge region of a galaxy, can tear a molecular cloud apart through shear and tidal effects. This has been shown to dominate cloud properties both in MW observations (Henshaw et al., 2019) and in external galaxy observations (e.g. Liu et al., 2021), as well as in simulations (Petkova et al., 2023).

With strong shear and tidal effects, gas structures are expected to be elongated along the orbit-tangential and the orbit-radial directions, respectively, both in the Galactic plane. Thus, the morphological position angle should be aligned with the Galactic Longitude direction rather than the Galactic Latitude direction, i.e. ϕ_m close to 90°. As for axis ratio, stronger shear/tidal effects should result in a lower q (i.e. farther from a circular geometry of $q = 1$), especially when the major axis indeed aligns with Galactic Longitude (and in turn the minor axis with Galactic Latitude). With the (spatially) resolved structures in the ACES HNCO dendrogram, Figure 4.13 examines such a potential correlation between q and ϕ_m. The magenta curve is the running mean of the blue data points in each panel. The grey dashed vertical line indicates $\phi_m = 90°$. In the middle panel of branches, there is a tentative trend that q is lower at $\phi_m \approx 90°$. In other words, we regard both low q and $\phi_m \approx 90°$ as signs of strong shear/tidal influence on the structure, and we find coexistence (or correlation) between these two signs, which is further interpreted as a support of shear/tidal effects. A similar but weaker trend can be seen for the trunks (in the right panel) but such a trend is much weaker (if any) for the leaves (in the left panel). As for structures

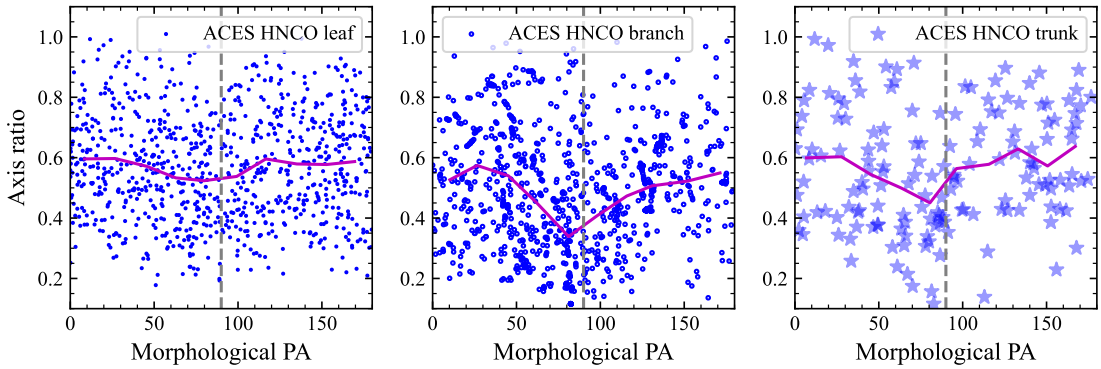

Figure 4.13: ACES axis ratio vs. morphological position angle. Different panels show different categories of resolved ACES HNCO structures, as indicated in the legends. The magenta curves are the running mean of the data points in each panel. The vertical dashed lines indicate $\phi_{\rm m} = 90°$.

with large q and $\phi_{\rm m}$ far from 90°, the signature of shear/tidal effects may have been washed out by other factors and/or other mechanisms may dominate, to be discussed below.

We further investigate this tentative signal with more physically motivated sub-samples instead of the dendrogram categorisation. Figure 4.14 shows the result of dividing the dendrogram by size (the upper row) and on-sky location (the lower row), still requiring the resolving criteria.

The size ranges for 'small', 'medium', and 'large' structures are: 0.37–1, 1–5, and 5–25.4 pc, respectively. 0.37 and 25.4 pc are simply the smallest and the largest $R_{\rm s}$; 1 and 5 pc are often used as empirical size boundaries between cores, clumps, and clouds though such separation has some arbitrariness in light of the nested hierarchical ISM. These boundaries also ensure roughly equal numbers of structures in each range and slightly modifying the boundaries does not affect any conclusions below.

It is apparent the large structures have a strong preference for small q at $\phi_{\rm m} \approx 90°$ as well as a large q at other angles. Apart from the proposed interpretation of shear/tidal effects, we examine whether the overall ring-like distribution of gas largely along the Galactic Longitude in the CMZ may also play a role. The typical height of the CMZ (and also the vertical extent of the ACES FoV designed to match it) is roughly 10′ or 23 pc. This is comparable to the largest structures in the catalogue, so the majority of structures in the upper right panel of Figure 4.14 are not constrained in the vertical extent by large-scale CMZ gas distribution. This is also confirmed by visual inspection.

Therefore, this correlation should be attributed to shear effects. This trend is much weaker (if any) for the small and medium structures. This may indicate a typical scale (larger than 5 pc) where shear/tidal effects dominate.

In the lower row of Figure 4.14, the dendrogram is divided by the Galactic Longitude: $|l| < 0.^{\circ}3$, $0.^{\circ}3 < |l| < 0.^{\circ}6$, and $|l| > 0.^{\circ}6$.[11] The motivation is to select structures by their orbital positions. We expect the on-sky morphology is most affected by the shear effect when a gas structure is moving transversely (in other words, when its location is on the LoS toward the dynamic centre). On the other hand, the tidal effect plays a major row when a structure is moving along the LoS (in other words, when the LoS to the structure is tangential to its orbit). Given the large hole around Sgr A* in the CMZ (Henshaw et al., 2023), most structures (within the ACES FoV) should be roughly at the same radius and on the same orbit, alleviating potential LoS confusion from multiple orbits. Nonetheless, the tidal effect is more difficult to detect than the shear effect for the following reason. The longitude coverage of ACES is only as far as $0.^{\circ}9$ (and only $-0.^{\circ}6$ on the other side), slightly beyond Sgr B2. It is unknown how many structures are moving along their LoSs to make the tidal effect most visible.

Reading from Figure 4.14, the inner structures (lower left panel) show a strong correlation of low q and $\phi_{\rm m} \approx 90^{\circ}$. No correlation is seen in the other two subsamples. This indicates significant shear effect but the tidal effect is not detected.

Magnetic field

Another potential driving factor of cloud morphology is the magnetic field ($\boldsymbol{B}$). Paré et al. (2024) presented the CMZ polarisation observation from the Stratospheric Observatory for Infrared Astronomy (SOFIA) High-resolution Airborne Wideband Camera plus (HAWC+) instrument as part of the Far-InfraREd Polarimetric Large-Area CMZ Exploration (FIREPLACE) survey. They found an alignment of magnetic field pseudo-vectors with the morphology of many prominent CMZ clouds (such as the Brick, Three Little Pigs, etc.). Here, we use the publicly available FIREPLACE data to further investigate this correlation. The spatial resolution of FIREPLACE is $19.''6$, almost the same as the 7mTP

[11] This division assumes the dynamic centre of the MW is at $l = 0$. The small offset in reality is insignificant to the analyses here.

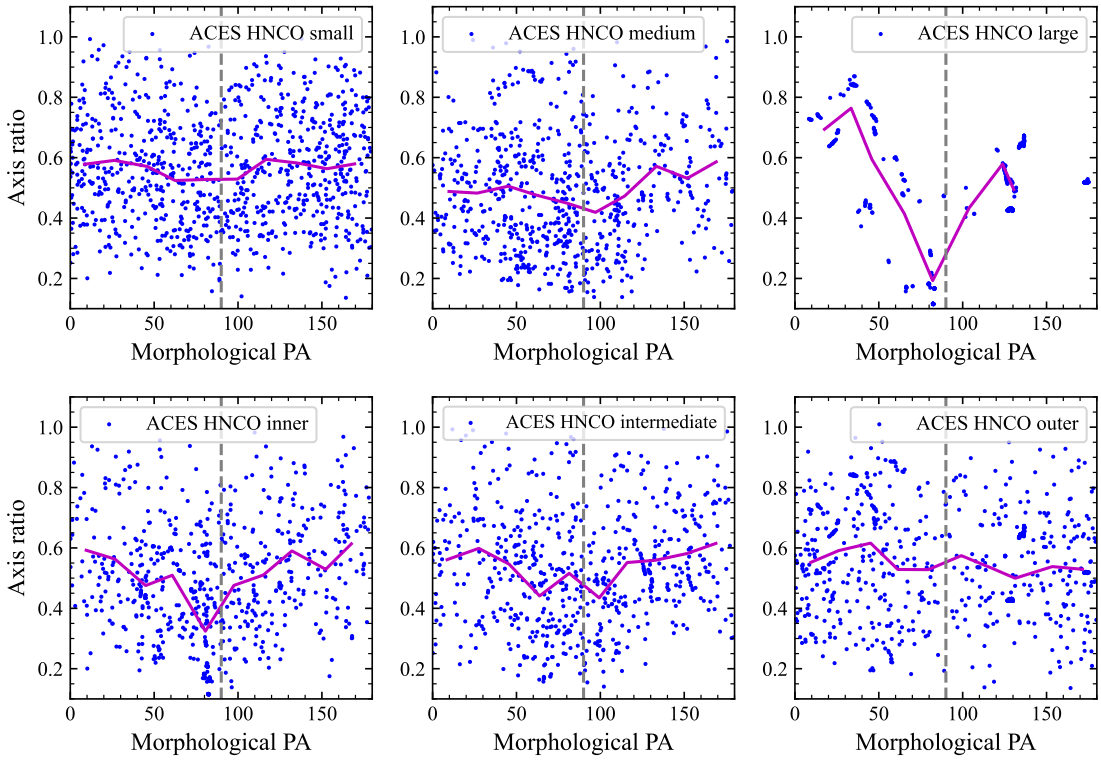

Figure 4.14: ACES structure morphology of subsamples. The same as Figure 4.13 but for physically motivated subsamples instead of structure categories. *Upper row:* small (left panel; 0.37 pc $< R_s <$ 1 pc), medium (middle panel; 1 pc $< R_s <$ 5 pc), and large (right panel; 5 pc $< R_s <$ 25.4 pc) structures. *Lower row:* inner (left panel; $|l| < 0.^\circ3$), intermediate (middle panel; $0.^\circ3 < |l| < 0.^\circ6$), and outer (right panel; $|l| > 0.^\circ6$) structures.

HNCO data. After re-gridding FIREPLACE maps onto the ACES grid, we apply the same quality-control cut on a pixel basis as done in Paré et al. (2024), which requires detection significance of at least 200 on 214-μm intensity and of at least 3 on polarisation percentage, $f_{\rm pol}$, and $f_{\rm pol} < 50$ per cent.[12] Although FIREPLACE data do not have velocity information, we spatially match our identified structures to the FIREPLACE maps and assign the integrated intensity–weighted median of $f_{\rm pol}$ and the orientation angle of pseudo-vectors of $\boldsymbol{B}$, $\phi_{\boldsymbol{B}}$, to each structure.[13] We also measure a uniqueness fraction $f_{\rm unique}$ for each structure to gauge the LoS uniqueness/crowdedness. We take all LoSs of a structure to form a 2D mask and define $f_{\rm unique}$ as the ratio of this structure's

[12]The requirement of $f_{\rm pol} < 50$ per cent is inherited from Paré et al. (2024) but it does not make a difference when the other two are in place.

[13]The pixels that do not pass the quality-control cut are ignored for the weighted median (rather than assumed to be zero in $f_{\rm pol}$ or $\phi_{\boldsymbol{B}}$). The reason is obvious for the measurement of $\phi_{\boldsymbol{B}}$. As for $f_{\rm pol}$, not passing the cut does not indicate a near-zero $f_{\rm pol}$ but rather is due to faintness in 214-μm intensity and thus high uncertainties on $f_{\rm pol}$.

integrated intensity over the integrated intensity of all pixels that are identified into some structure (without repetition) and are within this 2D mask. The higher $f_{\rm unique}$ is, the more accurate $\boldsymbol{B}$-related measurements of structures should be. We impose a threshold of $f_{\rm unique} > 0.5$ for a structure to be considered in the following analyses.

If the magnetic field indeed regulates gas structure morphology, we would expect a correlation between the orientation ($\phi_{\rm m}$ and $\phi_{\boldsymbol{B}}$) and between structure elongation and the magnetic field strength. Figure 4.15 shows histograms of the orientation comparison, $|\phi_{\rm m} - \phi_{\boldsymbol{B}}|$.[14] In the left panel, all three structure categories show a peak at 0°, which indicates alignment between the gas structure elongation direction and the magnetic field orientation. Paré et al. (2024) also reported such alignment for a few prominent gas clouds (e.g. the Brick, Three Little Pigs, Sgr C). There are secondary peaks for all categories at $|\phi_{\rm m} - \phi_{\boldsymbol{B}}| \approx 60°$. That peak of the branches is largely driven by the high number of levels from the bright nested structures at Sgr B2, as mentioned in Section 4.5.1, where $\phi_{\boldsymbol{B}}$ is mostly $\approx 70°$. However, the leaves and the trunks are not affected by the high numbers of levels at bright structures, and yet they also show secondary peaks around $|\phi_{\rm m} - \phi_{\boldsymbol{B}}| \approx 60°$. These particular leaves and trunks at the secondary histogram peak are distributed pretty broadly across the ACES FoV with no obvious bias towards any particular prominent molecular cloud. This might indicate another characteristic angle difference between the magnetic field and gas structure morphology, in addition to the alignment with $|\phi_{\rm m} - \phi_{\boldsymbol{B}}| = 0°$.

The right panel of Figure 4.15 divides the dendrogram catalogue by Galactic Longitude. The left part ($l > 0.^\circ45$) is concentrated within $60 - 80°$, indeed from Sgr B2 and causing the branch peak at $|\phi_{\rm m} - \phi_{\boldsymbol{B}}| \approx 60°$. The central region ($-0.^\circ2 < l < 0.^\circ45$) has a very prominent concentration of structures around $|\phi_{\rm m} - \phi_{\boldsymbol{B}}| = 0°$. Although the right region ($l < -0.^\circ2$) also has a peak of 0° angle difference, its height is just a factor of ≈ 2 of the rest of the distribution, which is more or less flat. Comparing the central region and the right part, there is an indication that the alignment between gas morphology and the

[14]The FIREPLACE data only determine pseudo-vectors of the magnetic field, which give the orientation of the magnetic field line but not the exact direction along the line (out of the two possible directions). Thus, $\phi_{\boldsymbol{B}}$ has a period of 180°, the same as $\phi_{\rm m}$, and in turn $|\phi_{\rm m} - \phi_{\boldsymbol{B}}|$ ranges from 0 to 90°.

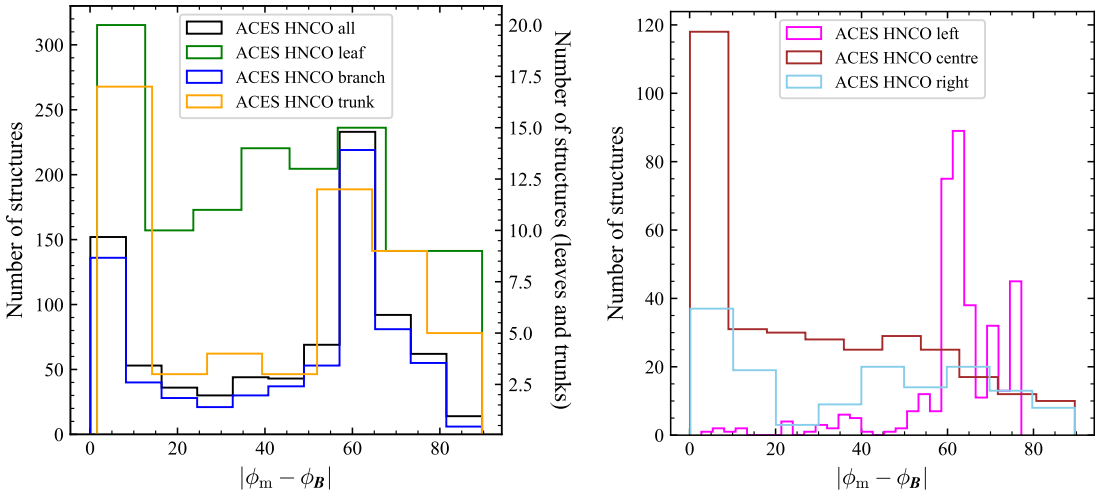

Figure 4.15: Distributions of structures' magnetic field orientation. *Left:* the distribution of $|\phi_m - \phi_B|$ of resolved structures in each category with colour-coding indicated in the legend and of the overall (resolved) catalogue in black. For clarity, leaves and trunks use a separate y-axis on the right. *Right:* the distribution of $|\phi_m - \phi_B|$ of resolved structures in the left (magenta; $l > 0.^\circ45$), central (brown; $-0.^\circ2 < l < 0.^\circ45$), and right regions (sky-blue; $l < -0.^\circ2$) of the ACES FoV.

magnetic field is most significant in the central part of the CMZ. This may be related to the shear effect, which is also more dominant in roughly that region than in outer regions.

We further examine the physical cause of such alignment between ϕ_m and ϕ_B in Figure 4.16. The left and middle panels respectively show the axis ratio q and the morphological position angle ϕ_m as predictor properties of $|\phi_m - \phi_B|$. Indeed, when q is lower than ≈ 0.4 and when ϕ_m is around 90°, $|\phi_m - \phi_B|$ becomes substantially lower. These correlations are related to the ones we analysed before, where we argue the shear effect is the potential cause of a lower q and $\phi_m \approx 90^\circ$. As for the further correlation with $|\phi_m - \phi_B|$ shown here, a possible interpretation is that the shear effect also regulates the orientation of the magnetic field to align with the Galactic plane. In this case, we would naturally also see good alignment between ϕ_m and ϕ_B in structures with low q and $\phi_m \approx 90^\circ$, for which structures the shear effect is strong.

An alternative interpretation is the magnetic field independently shapes gas morphology and makes gas structures elongate along the magnetic field lines. Thus, small $|\phi_m - \phi_B|$ and low q coexist. This interpretation does not quite yet explain the good alignment between ϕ_m and ϕ_B at $\phi_m \approx 90^\circ$.

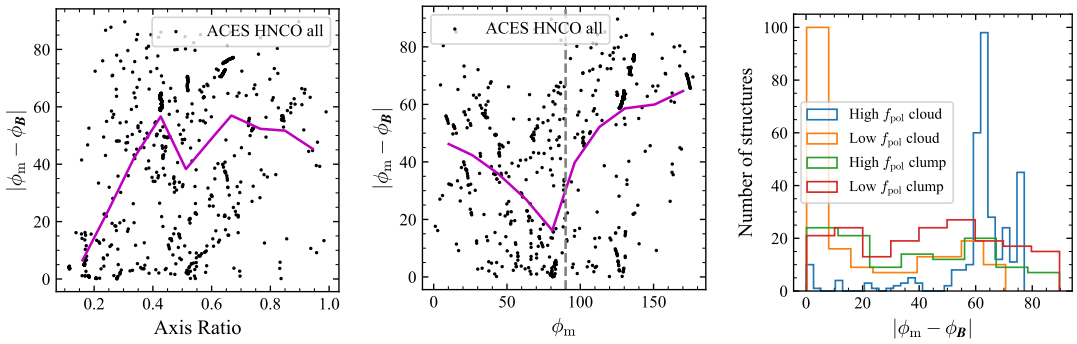

Figure 4.16: ACES structure magnetic field regulator. *Left panel:* $|\phi_m - \phi_{\boldsymbol{B}}|$ as a function of axis ratio; *middle panel:* $|\phi_m - \phi_{\boldsymbol{B}}|$ as a function of axis ratio ϕ_m; *right panel:* $|\phi_m - \phi_{\boldsymbol{B}}|$ histograms in four subsamples defined by polarisation percentage and radius ('clouds' with $R_s > 5$ pc, 'clumps' with $R_s < 5$ pc). All resolved ACES HNCO structures are included. The magenta curves in the left and middle panels are the running mean of the data points. The grey vertical dashed line in the middle panel indicates $\phi_m = 90°$.

To continue the examination of the regulation of the magnetic field on gas morphology, we adopt polarisation percentage as a proxy of the magnetic field strength. In the right panel of Figure 4.16, $|\phi_m - \phi_{\boldsymbol{B}}|$ is tested for a correlation with f_{pol} in subsamples of larger structures (denoted 'cloud'; $R_s > 5$ pc) and smaller structures (denoted 'clump'; $R_s < 5$ pc), inspired by Herrington et al. (2024). The threshold we use between high and low f_{pol} is 4.3 per cent, to balance the sub-sample sizes. While clumps have rather uniform/random distributions regardless of f_{pol}, cloud morphologies tend to be aligned to $\phi_{\boldsymbol{B}}$ (i.e. angle difference close to 0) under a weak $\boldsymbol{B}$ and become almost perpendicular to $\boldsymbol{B}$ (i.e. larger angle differences of 60°–80°) under a strong field. Although the latter is not exactly 90°, this trend is quite similar to what Herrington et al. (2024) reported from their simulation work. This transition of the alignment/orthogonality between ϕ_m and $\phi_{\boldsymbol{B}}$ can be interpreted as the transition of dominance from magnetic to gravitational support, along with other mechanisms (see Herrington et al., 2024, for a summary).

We note that the peak for high f_{pol} clouds (the blue histogram) is dominated by structures from Sgr B2 (as seen previously in other distributions). But even when the excessive structures (from Sgr B2) causing the peak of $\phi_m \approx 130°$ (in Figure 4.10) are excluded, this histogram of high f_{pol} clouds still peaks at $\approx 65°$ (less prominently though).

This also shows f_{pol} is a reasonable tracer of the magnetic field strength even when

it is measured as an integration along the LoS.[15]

4.6 Discussion

4.6.1 Comparison between Mopra and ACES

One key improvement of the ACES survey to the Mopra one is the better spatial resolution (by a factor of two with the 7mTP data used in this work and by a factor of at least 15 with the 12m7mTP data in processing) and the better spectral resolution (by a factor of 18 for the HNCO line used in this work and the HCO^+ line, or by 17%-53% for other lines).[16] At such higher resolutions, the sensitivity (in terms of cube median noise in Table 4.1) of the ACES 7mTP data is even slightly better than the Mopra data, thanks to the great sensitivity of ALMA and the large amount of allocated time.

The better resolution naturally results in a broader parameter space becoming reachable. Taking the size-linewidth relation in Section 4.5.2 as an example, ACES clearly extends the study of Mopra. Such good spectral resolution is also crucial for detecting sonic and thermal gas and the 12m resolution is important for studies of molecular cores (and other compact sources), both of which will be useful in constraining star formation theories. In the meantime, large-scale information of gas is still preserved. Although a factor of three smaller than the Mopra Survey FoV, the ACES FoV is sufficient in studying the overall gas geometry, kinematics, and the feeding mechanism of the CMZ as well as large-scale feedback signatures. This large dynamic range offered by the ACES survey will enable a better connection across scales and ultimately a bridge between physical drivers and observed phenomena.

4.6.2 Slope of the size-linewidth relation

In this work, we first get a steep slope of the size-linewidth relation from the Mopra HNCO catalogue of 0.78 ± 0.08, and then a flatter one of 0.58 ± 0.02 from the ACES HNCO catalogue. The difference between the two catalogues is most clearly seen in the

[15]The $f_{\rm unique}$ cut mainly affects the clump category but barely eliminates any cloud.

[16]This spectral comparison is based on the Mopra data version used in this work from the data release. Hanning smoothing was carried out during their data reduction to increase sensitivity, resulting in the effective spectral resolution of 3.6 km s^{-1}. See Section 4.2.1 and Jones et al. (2012) for more details.

middle (branch) panel of Figure 4.11. Ignoring the string of structures outside the ACES FoV explained in Section 4.5.2, the high-radius end of the Mopra catalogue has the same average linewidth as the ACES one, as the highest-radius bin shown by that magenta hexagon is in the centre of the cyan blob. However, at the low end of the Mopra catalogue, it almost lacks half of the high-linewidth structures, again seen by the comparison between the magenta hexagons and the cyan contour. This naturally yields a steep slope for the Mopra fitting. The Mopra FoV fully encompasses the ACES FoV (see Table 4.1), so the spatial coverage of the Mopra survey is not the reason. One possibility is this regime is close to both the spatial and the spectral resolution limits of Mopra, and thus the structure detection completeness may not be ideal. The poorer sensitivity (46 mK with 40″ beam for Mopra vs. 35 mK with 19″ beam for ACES) may also play a role. A detailed one-to-one cross-check between the two catalogues would reveal the full picture, but in any case, the ACES catalogue with better instrumental capabilities (spatial resolution, spectral resolution, and sensitivity) should be more trustworthy regarding catalogue completeness in this domain. In addition, by Bayesian inference, Shetty et al. (2012) concluded all the tracers they studied (i.e. N_2H^+, HCN, $H_{13}CN$, and HCO^+) from the Mopra survey yield rather large uncertainties in the best-fit size-linewidth relations (the combined 1σ confidence interval from all tracers of the best-fitting slope being 0.5–0.9), thus resulting in statistical consistency with our ACES result (and also our Mopra result).

Kauffmann et al. (2017) managed to probe smaller scales ($\approx$ 0.1 pc) with the Submillimeter Array (SMA) than the 7mTP ACES data presented in this chapter. Combining large-scale observations of entire clouds from the Atacama Pathfinder Experiment (APEX) and the *Herschel Space Telescope*, they reported a steep slope of 0.66 ± 0.18. In the right (trunk) panel of Figure 4.11, we compare their small-scale fragments (the brown range symbol) and large-scale clouds (brown hollow squares) with our HNCO population. Despite the uncertainties of both surveys on the small scale, our best-fitting relation goes through the range spread by their fragments. However, their large-scale clouds are systematically higher than our trunks (and our branches, on average) as well as the best-fitting relation (roughly by a factor of two). This is the main reason for the slope difference. This could be caused by the different tracers used to obtain the

linewidth, i.e. N_2H^+ (3-2) of their survey and HNCO of our catalogue. Although our Figure 4.8 shows the N_2H^+ (1-0) has very little difference from HNCO, this might not be true for N_2H^+ (3-2). It may also be due to the inhomogeneity of their measurements. They used *Herschel* dust observations to determine the sizes of their clouds and APEX single-dish observations for the linewidths. Aperture mismatch between the two can result in offsets in the size-linewidth parameter space. On the contrary, the ACES HNCO catalogue is from the same ALMA Large Programme, homogeneous in instrumental characteristics, observation set-ups, and data reduction. In principle, these two potential reasons could be further tested by a one-on-one cross-check of the catalogues in future work, especially with the SCIMES algorithm adopted. Another possibility is again the completeness of the structures probed. They only targeted several prominent clouds while the ACES catalogue (semi-blindly) surveys the CMZ contiguously. In this sense, the ACES catalogue is more representative of the gas dynamics in the CMZ.

All in all, the size-linewidth relation concluded by this study is

$$\log \sigma_s = (0.58 \pm 0.02) \times \log R_s + (0.482 \pm 0.014) \ , \tag{4.3}$$

It is still higher than the MW Disc relation, which is typical of all galaxy disc environments in the nearby universe (e.g. Bolatto et al., 2008), in both the slope and the normalisation, but the difference is smaller than previously thought.

4.6.3 Structure dynamical state

The ultimate goal of studying gas structure properties is to understand gas property regulation and predict star formation activities. All the properties we analyse have an indication for the potential for star formation. The linewidths of gas structures are almost always dominated by turbulence at the pc scale studied in this work. However, at smaller scales, stars form from dense cores of molecular gas where the velocity dispersion becomes (trans-)sonic and is dominated by thermal motions. Theoretically, assuming gas temperatures of 50 to 100 K, the pure thermal velocity dispersion using HNCO molecular mass is 0.10–0.14 km s^{-1} while, more relevantly, the dispersion with a mean free particle mass gives 0.4–0.6 km s^{-1} (Kauffmann et al., 2017). To aim for the latter range, the

extrapolation of our size-linewidth relation predicts cores at 0.03–0.06 pc of radius are on average sonic and thermal instead of turbulent. This is similar to the transitional scale in the turbulent power spectrum derived from the optically thin dust continuum emission in the Brick Cloud (Rathborne et al., 2015). This is also comparable to the ACES 12m7mTP resolution of individual fields (0.05–0.10 pc), which will be explored in future works.

Just with the current 7mTP data, ten resolved structures and 55 unresolved ones have a velocity dispersion below 0.6 km s^{-1}. They are outliers to the bulk of the size-linewidth relation and are located around the MW Disc relation, as briefly mentioned in Section 4.5.2. These structures also appear low in the virial parameter. These all indicate strong potential for star formation. These structures can be cross-correlated with the compact continuum catalogue (Wallace et al. in prep.) and chemical modelling from ACES ALMA data as well as young stellar objects identified from ancillary multi-wavelength data of the ACES collaboration to study gas core evolution at the early phase of star formation.

On the origin of turbulence, the slope of the size-linewidth relation remains very similar across the scales we probe without flattening or steepening. This universality implies the turbulence is inherited from the largest scales ($\gtrsim$ 30 pc) of the colliding ISM flows (Heyer & Brunt, 2004; Shetty et al., 2012). From the virial parameter analyses, larger structures ($\sim$ 10 pc) tend to be more virialised and thus stable while the majority of small-scale ($\sim$ 1 pc) structures seem to be rapidly evolving with $\alpha_s \approx 10$. This reveals a general picture of both the static part and the dynamic part of the CMZ ISM.

Regarding the specific physical drivers of gas structure properties, we find evidence that shear effects and magnetic fields shape gas structure morphologies, especially at the physical scale around 5–25 pc, as detailed in Section 4.5.4. To briefly recap, we use axis ratio to trace the elongation magnitude of gas structures, expect the morphological position angle to be aligned with the Galactic plane under shear effects, and use the angle difference $|\phi_m - \phi_{\boldsymbol{B}}|$ to test the regulation on gas morphology of magnetic fields. There is significant co-existence among low axis ratios, $\phi_m \approx 90°$, and low angle differences, especially for subsamples with larger radius and inner on-sky positions (tracing the transverse part of the orbit). This correlation among cloud morphology, the shear effect and the magnetic field could be a complex physical interplay. The shear effect in galactic centres is usually

expected to be strong due to the deep gravitational potential well and dominate the evolution of molecular clouds (e.g. Liu et al., 2021). The magnetic field and molecular gas can be coupled to each other and then co-evolve in their morphologies. Past studies have found toroidal magnetic fields form from coupling to the baryonic component of galaxies (Morris, 2015). More detailed studies are needed to fully disentangle this picture.

4.7 Summary and conclusions

This chapter presents early results from the ALMA Band-3 large programme ACES survey of the MW CMZ using the 7mTP version of HNCO data. The whole mosaic ACES HNCO datacube has a (non-rectangular) FoV of 0.43 degree^2 within $l = -0.^\circ6 - 0.^\circ9$ (210 pc) and $b = -0.^\circ3 - 0.^\circ2$ (70 pc), spatial resolution of 19″ or 0.73 pc, and spectral resolution of 0.2 km s^{-1}. We construct a dendrogram with 2751 molecular gas structures categorised into leaves, branches, and trunks. We measure their (deconvolved) radius, (deconvolved) linewidth, axis ratio, morphological position angle, etc. The spatial scale probed is from 0.4 pc to 25 pc (for resolved structures). The analyses below are built upon and compared with the earlier Mopra survey of the CMZ.

- ACES catalogue agrees well with the Mopra one in the overlapping FoV and significantly extends towards smaller spatial scales and smaller linewidths than Mopra.

- The ACES HNCO structures form a strong size-linewidth relation with $r_\mathrm{p} = 0.90$. The trend remains very similar across the spatial scales as well as different categories of structures. The best-fitting relation to all resolved structures is $\log \sigma_\mathrm{s} = (0.58 \pm 0.02) \times \log R_\mathrm{s} + (0.482 \pm 0.014)$. Both the slope and the normalisation are higher than that of the disc environment, but the difference is smaller than in previous studies.

- On gas structure morphology, low axis ratios (i.e. stronger elongation) and a morphological position angle (ϕ_m) around 90° (i.e. along the Galactic plane) tend to be concurrent. This correlation is the strongest among large ($R_\mathrm{s} > 5$ pc) and

inner structures ($|l| < 0.^{\circ}3$). These are interpreted as evidence of strong shear effects regulating gas structure morphology.

- Using the FIREPLACE data, we measure the LoS magnetic field angle ($\phi_{\boldsymbol{B}}$) and polarisation percentage. Using structures with a low level of LoS confusion, we find the distribution of the angle difference $|\phi_{\rm m} - \phi_{\boldsymbol{B}}|$ peaks at zero, especially for structures with low axis ratio and $\phi_{\rm m} \approx 90^{\circ}$, and for large structures ($R_{\rm s} > 5$ pc) under weak fields. This potentially reveals the interplay between magnetic field, gas structure morphology, and shear effect.

Overall, this study has found tentative evidence of mechanisms dominating gas structure properties and has demonstrated the great potential of the ACES survey (along with other synergistic datasets) to further enlighten us on this topic. As this is just the beginning of the investigation into gas structure properties and their potential for star formation with an early version of the ACES dataset, much more future work can/will be done along the following directions, for example: to utilise the full 12m resolution ($\sim$ 0.1 pc) of the ACES data to push the scale limit down to where thermal sonic gas may be prevalent; to compare the HNCO results with the other molecular lines and the continuum observed by ACES to further study the physical and chemical properties of these structures; to adopt the SCIMES clustering algorithm on top of the dendrogram algorithm to achieve more physically driven structure identification; to further study special structures such as single-level structures and nested structures to shed light on structure formation, growth, and evolution in the MW CMZ.

5 Summary

Contents

5.1 Conclusions

This thesis is focused on the cold molecular gas (cloud) properties of different types of galaxies at different physical scales. Chapter 2 started with an analysis of the kpc-scale (physical resolutions of $\approx$ 100 pc) molecular gas distributions and kinematics of three disc galaxies (two LTGs and one lenticular), all of which host a Sy 2 AGN and megamasers. Chapter 3 moved on to the resolved cloud–scale (resolution of 14 pc) analyses of the dynamical states and internal kinematics of the GMCs in the ETG NGC 1387. Chapter 4 provided a dense cold gas dendrogram analysis of the MW CMZ over a range of physical scales from sub-pc to 100 pc, and discussed potential physical drivers of the gas structures and properties.

This research has consolidated and extended our knowledge of molecular gas (clouds) in the following ways:

- The large-scale gas properties are largely determined by galaxies' environments and types. In the cluster environment typical for ETGs, atomic gas is depleted and molecular gas forms a much smaller and smoother disc than in LTGs. The nuclear activities, often present in LTGs, are also likely to have a strong impact on the gas morphology and kinematics. So do galaxy interactions and bar-induced non-axisymmetric potentials. Specifically for megamaser host galaxies, this thesis significantly increased the number of high-resolution studies of molecular gas distributions and kinematics. I also find that the prevalent disturbances and special kinematic features tend to be a systematic obstacle to using molecular gas to dynamically measure the central SMBH mass.

- GMC properties vary both across and within galaxy types. This thesis, for the first time, finds that ETGs can harbour GMCs with properties similar to those of LTG GMCs even when the ETG gas has an internal origin. The source of the turbulence of GMCs and the relation between GMC properties and star formation call for further studies of a larger sample of galaxies.

- With new observations of the MW CMZ at unmatched resolutions, presented by this thesis, I find new evidence to show that shear forces and magnetic fields are potential drivers of the gas properties at the (sub-)cloud scale.

Apart from new physical understanding, this series of projects has also showcased the advantages and limitations of different analysis tools. At the kpc scale, moment maps are traditional and powerful diagnostics to reveal the bulk distribution and motion of gas. At the 10-pc scale, structure identification algorithms such as `CPROPStoo`, with unique pixel assignments, are intuitive and straightforward. Across a range of scales from sub-pc to near kpc, hierarchical structure identification algorithms such as `Astrodendro` capture the nesting and fractal nature of the molecular ISM.

5.2 Future work

Despite the progress of this and other research in the field, many detailed yet fundamental questions remain to be solved. There is still much to learn about the complex interplay between multiple physical mechanisms impacting molecular gas and star formation in the extreme environment of galactic centres. Along the line of this work, a few promising ideas have emerged. I explore a few of them in detail below (Sections 5.2.1 to 5.2.3) and only briefly mention some others (Section 5.2.4).

5.2.1 Cloud internal kinematics

As discussed in Section 3.4, the velocity gradients of GMCs, potentially interpreted as GMC spins, can carry abundant information about their formation and evolution. Straightforwardly, the same measurement of the GMC velocity gradient can be done for a larger sample of galaxies. A metric to quantify the difference across galaxies would be the fraction of retrograde GMCs. Preliminarily, a wide range of retrograde fractions have already been found in: NGC 4429 of 1% (Liu et al., 2021), NGC 383 of 14% (private communication from Lijie Liu), NGC 1387 of 37% (Section 3.4), NGC 404 of 50% (private communication from Lijie Liu), and NGC 5064 of 67% (Liu et al. submitted). These fractions can be then compared with galaxy morphologies and other properties. Moreover, one can try to look for a critical spatial scale in each galaxy at which GMC spin starts to decouple from the large-scale kinematics of the gas disc. This critical scale may even be predicted from first-principle physics.

To further advance our understanding in that direction, cloud internal (or spin) specific angular momentum can be used as a powerful tool to unravel cloud evolution as well as to predict star formation. Specific angular momentum is defined as $\vec{j} \equiv (\int \vec{r} \times \vec{v}\ \mathrm{d}M)/M \approx (\int \vec{r} \times \vec{v}\ \mathrm{d}F)/F$, where the integration is over all pixels of a cloud, and $\vec{r}$ is the physical distance from the cloud centre, $\vec{v}$ the velocity, $\mathrm{d}M$ the mass in a pixel, $\mathrm{d}F$ the flux in a pixel, M the total mass of a cloud, and F the total flux of a cloud.

The $\vec{j} - M$ diagram in galaxy studies (i.e. the Fall relation; see Figure 5.1) was proposed by Fall (1983) and updated by e.g. Romanowsky & Fall (2012) and Hardwick et al. (2022). Early attempts to study the $\vec{j} - M$ relation for molecular clouds revealed

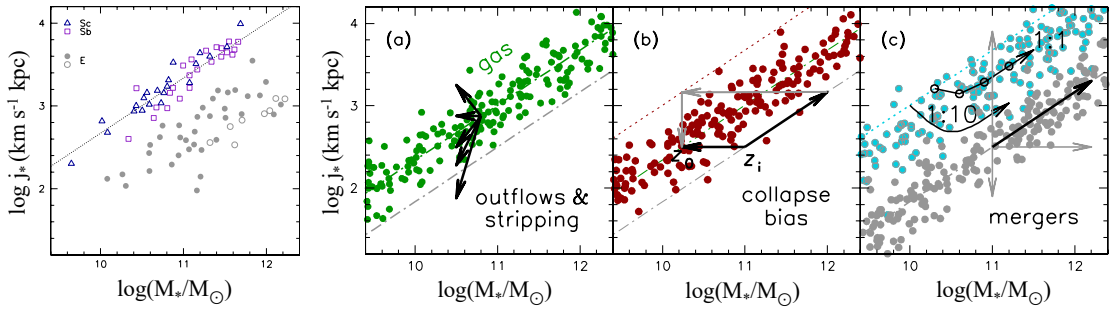

Figure 5.1: Demonstration of the Fall relation in galaxy studies, disentangling different evolutionary channels. All panels show the $\vec{j}_* - M_*$ diagram with diagonal lines showing $\vec{j}_* \propto M_*^{2/3}$. The first panel shows observed galaxies with clear separations across different galaxy categories labelled in the top-left corner. The other three panels show mock galaxies from an analytical model (except for grey points showing dark matter haloes). The movement of a galaxy on this diagram due to different evolutionary processes is illustrated by the arrows corresponding to the texts alongside. Adapted from Romanowsky & Fall (2012).

power-law slopes of 0.7 for MW disc clouds (Phillips, 1999) and 0.6 for M33 disc clouds (Rosolowsky et al., 2003). Theoretical works have also suggested retrograde orientation of $\vec{j}$ can be a signature for cloud-cloud collisions (e.g. Dobbs et al., 2011). However, due to observational limitations, no study has looked at $\vec{j}$ in CMZs.

One can measure both a total $\vec{j}$ as well as a radial growth curve (i.e. enclosed $\vec{j}$ vs cloud-centric radius R) for each cloud. The distribution of angular momentum for CMZ clouds can be compared with other physical quantities of clouds (e.g. cloud mass $M_{\rm gas}$, linewidth, size, virial parameter) and star formation (derived from ancillary data such as the Hα emission). On the $\vec{j} - M_{\rm gas}$ diagram, the regions occupied by the cloud population can reflect their evolutionary paths (see Figure 5.1 for an analogue from galaxy studies). $\vec{j}_{\rm enclosed}(R)$ can be studied in a similar manner as Figure 9 of Romanowsky & Fall (2012), where each object forms a track on the diagram, depicting the radial growth history and the dominant growth channel(s). Theoretical predictions for the cloud $\vec{j} - M_{\rm gas}$ relation can be provided by simulations. Several groups are working on realistic cloud simulations in ACES (e.g. Petkova et al., 2023), WISDOM (e.g. Gensior et al., 2023), and PHANGS (e.g. Jeffreson et al., 2024) .

5.2.2 Novel star formation rate indicator

Accurate estimates of SFRs are crucial to all studies connecting gas properties and star formation, as briefly seen throughout this thesis. In the context of this thesis, high angular resolution ($\sim 0\farcs1$, as in Chapter 3) is key to matching the interferometric millimetre observations of GMCs. Being lacking or even free of dust extinction is another major requirement of a high-accuracy SFR indicator. A few SFR indicators are commonly used, each with its pros and cons. (i) Hα emission tracing OB stars is a widely used one (e.g. Kennicutt, 1983), as shown in Chapter 3. However, it suffers significantly from dust extinction. Also, its achievable angular resolution is usually limited to $\approx 1''$ by atmospheric seeing at ground sites, although higher resolutions at $\sim 0\farcs1$ are possible with either adaptive optics or space-based telescopes. In addition, old stellar populations can also contribute to Hα emission, contaminating the SFR estimation (Yan & Blanton, 2012). (ii) The UV continuum luminosity comes directly from OB stars (e.g. Wilkins et al., 2012). It can only be observed from space (due to atmospheric absorption at UV wavelengths), which does offer high enough angular resolution thanks to the short wavelength, but it suffers from dust extinction even more severely than at optical wavelengths. (iii) The near-IR polycyclic aromatic hydrocarbon emission and recombination line emission (such as Paschen-α and Brackett-α) also directly trace the H II regions around massive stars (e.g. Lai et al., 2020; Pasha et al., 2020; Neufeld et al., 2024). Dust extinction is minimal at these long wavelengths. The recently launched *JWST* offers supreme resolutions of $\approx 0\farcs1$ at near-IR, while all other current IR facilities do not have matching resolutions to millimetre interferometry. (iv) The mid-/far-IR continuum luminosity comes from dust thermal emission, which is dust-processed stellar light. It has been used to indicate SFR either alone or in combination with UV continuum luminosity (e.g. Hao et al., 2011; Senarath et al., 2018). Yet again, achieving desired angular resolution is challenging, except for *JWST* (with $\approx 0\farcs2$ resolutions at mid-IR). (v) Radio continuum emission at $\sim$ 1 GHz traces synchrotron emission from supernova-induced cosmic rays and thus can also be used to calibrate recent SFR. Although angular resolution and dust extinction challenges do not apply to this method, the measured SFR is on a slightly different

timescale (between star formation and supernova explosion) and spatial scale (due to cosmic ray diffusion length of $\sim$ 1 kpc; e.g. Heesen et al. 2014).

As seen above, very few of the currently available SFR indicators meet the needs for measuring high-quality SFR on the scale of a GMC. On the other hand, it should be promising to further calibrate the radio continuum emission at 33 GHz as a better SFR indicator than traditional ones. This emission is dominated by free-free emission arising from electrons in the H II regions surrounding massive stars. It is thus a direct and accurate SFR indicator with clear theoretical understanding (see Condon, 1992, for a review). It also offers advantages such as no dust extinction, no contamination from old stellar populations, and high resolution ($\approx 0\farcs1$) thanks to radio interferometry. The contamination from other emission processes at 33 GHz is $\approx$ 10% in sources resolved on $<$ 0.5 kpc scales (e.g. Nikolic & Bolton, 2012; Murphy et al., 2015), which corresponds to $2''$ at the typical distance ($\approx$ 50 Mpc) of nearby galaxies.

Previous observations and applications of this indicator have been limited to nearby LTGs (e.g. Murphy et al., 2011). However, its characteristics are ideal for studying the elusive SFR of early-type galaxies, especially since traditional SFR indicators have suffered great difficulties in detecting the faint residual star formation in massive galaxies and/or ETGs.

5.2.3 Spectral line energy distribution modelling

As elaborated in Section 3.7, the ETG NGC 1387 has GMCs very similar to those of the MW Disc, which means they should have great potential for star formation. However, the SFE of NGC 1387 is as low as a typical ETG. The reasons for this must lie in some other GMC properties not probed by either this thesis or the currently available dataset.

Theories and simulations suggest that the star-formation efficiency (SFE) depends on four physical quantities: (1) Virial parameter $\alpha_{\rm vir}$; (2) Toomre instability parameter Q; (3) GMC's internal mass volume density distribution (normally characterised by a log-normal distribution); (4) sonic Mach number $\mathcal{M} \equiv \sigma_{\rm turb}/v_{\rm c}$, where $\sigma_{\rm turb}$ is the turbulence velocity dispersion and $v_{\rm c}$ is the speed of sound.

1. Virial parameter $\alpha_{\rm vir}$. The low SFEs of ETGs may be due to large GMC Virial parameters, as the gas in ETGs appears to be very turbulent, thus supporting GMCs against gravitational collapse and star formation (e.g. Gensior et al., 2020; Kim et al., 2021);

2. Toomre instability parameter Q. The low SFEs of ETGs may be caused by 'morphological quenching', whereby the deep potential wells of ETGs hold gas stable against star formation, i.e. $Q \gg 1$ (Martig et al., 2009, 2013);

3. GMC internal density distribution. The low SFEs of ETGs may be caused by the impact of dynamical processes on the internal density distributions of GMCs. For example, the stronger shear and tidal forces in ETGs may tear GMCs apart, making it more difficult to form dense clumps and/or cores for the same bulk/average mass density (e.g. Kim et al., 2021; Mac Low & Klessen, 2004; Meidt et al., 2018);

4. Mach number $\mathcal{M}$. The low SFEs of ETGs may be due to sonic Mach numbers $\mathcal{M}$ being lower than those of spirals, leading to less shock-induced compression and effectively resulting in higher star-formation density thresholds $\rho_{\rm crit}$ (Federrath & Klessen, 2012; Federrath et al., 2021).

Specifically for NGC 1387, the GMC virial parameters ($\alpha_{\rm vir} \approx 1$) are very similar to those of the MW disc and nearby spirals. The Toomre parameter of its gas disc ($Q \approx 1.5$ in the bulk of the disc) is close to the threshold ($Q = 1$) of instability and fragmentation dominance, even without considering stellar mass (which would lower Q). Also, the abundance of GMCs already identified indicates significant instability and fragmentation.

Therefore, the other two critical parameters should be investigated, (i) each GMC's internal density distribution, which can be characterised by the mean mass volume density ρ_0 and the width of the log-normal density distribution σ_ρ, and (ii) the GMC Mach number $\mathcal{M}$, that can be derived from the gas kinetic temperature as $\mathcal{M} \equiv \sigma_{\rm turb}/v_{\rm c} = 2.6 \left(\frac{\sigma_{\rm turb}}{\rm km\ s^{-1}}\right) \left(\frac{T_{\rm k}}{25\ \rm K}\right)^{-1/2}$ (Leroy et al., 2016), given $\sigma_{\rm turb}$ directly measurable from the observation. Several methods have been developed to probe these GMC properties. Ultra high–resolution (≈3 pc or 0.″03 at the distance of NGC1387) observation can directly probe

the internal density structure of GMCs. But such a small beam would require too much observation time. Dense-gas tracers have been used to measure dense-gas fractions (Gao & Solomon, 2004b). However, the low abundances of such molecules make it still too time-consuming to observe at GMC scales. Radiative transfer modelling usually requires multiple transitions to derive the kinematic temperature $T_{\rm k}$. However, traditional radiative transfer codes, such as `Radex`, are normally based on one-dimensional calculations (van der Tak et al., 2007), thus preventing a determination of the detailed GMC density distribution.

It should be promising to propose new GMC-scale (0.″2 or 20 pc) observations of multiple ^{12}CO lines in the ETG NGC1387 ($J_{\rm up} = 1 - 6$). Radiative transfer analyses of the observed transitions can be performed using the state-of-the-art three-dimensional (3D) radiative transfer code β`3D` (Liu et al., 2017). Compared to commonly used codes such as `Radex` and `Ratran`, β3D has the following advantages: (i) its 3D dimensionality, so that a unique set of temperature, density, abundance and velocity can be attributed to every grid cell in a 3D cube; (ii) its inclusion of IR-pumping; (iii) its novel line-tracing approach, which can be performed over a projected area along arbitrary viewing angles. By simultaneously deriving the width of the internal gas density distribution (σ_ρ) and kinetic temperature ($T_{\rm K}$) of each GMC in NGC1387, the ultimate goal is to disentangle different possible mechanisms underlying star-formation suppression in ETGs.

To identify how the CO spectral line energy distributions (SLEDs) might vary with the density distribution width σ_ρ and the kinetic temperatures $T_{\rm K}$ of the NGC1387 GMCs, β`3D` SLED models have been run for a typical GMC with a mean mass volume density $\rho_0 = 10\,{\rm M}_\odot\,{\rm pc}^{-3}$, a mean radius of 20 pc, and a turbulence velocity dispersion of $\approx 4\,{\rm km\,s}^{-1}$ (measured from velocity-gradient-subtracted linewidth). We then varied $T_{\rm k}$ ($20 - 100$ K; considering a typical range of normal galaxies, starbursts, and AGNs) and σ_ρ ($0 - 2$ dex) in a 3D cube with $20 \times 20 \times 20 = 8000$ cells, to encompass realistic GMC properties.

Our model predictions (private communication from Lijie Liu) for the CO SLEDs of a typical NGC1387 GMC are shown in Figure 5.2, where each panel shows the normalised SLED for a given set of input parameters. The SLEDs are sensitive to variations of both $T_{\rm k}$ and σ_ρ, which can thus be constrained from observations. In particular:

- The SLED peaks shift towards higher transitions with increasing $T_{\rm k}$ and/or σ_ρ;

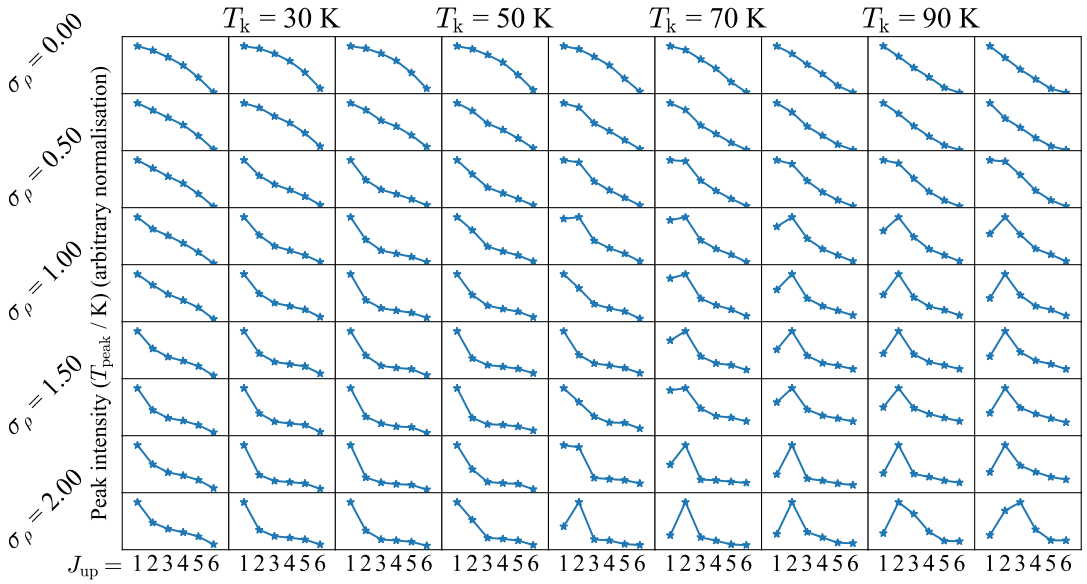

Figure 5.2: SLED predicted peak intensity T_{peak} of ^{12}CO lines in typical GMCs in NGC1387. Different panels correspond to different sets of input kinetic temperature T_k and density scatter σ_ρ. Normalisation in each panel is arbitrary since line ratios will be used to constrain the model.

- The SLED low-end slopes can break this degeneracy. For example, the line ratios of the first three transitions drastically change from the top-left to the bottom-right of Figure 5.2.

- The SLED high-end slopes can also help to break this degeneracy. For example, the high-end SLEDs tend to flatten out from the top-left to the bottom-right of Figure 5.2.

With multiple CO transitions measured for each individual GMC in NGC1387 and the β3D modelling results, the following goals can be achieved.

- Derive the optimal σ_ρ and T_k of each observed GMC. We will first measure the CO SLED of each GMC in NGC1387, and then derive T_k and σ_ρ (or equivalently the dense gas fraction) by comparing the observations to the β3D model predictions. We will then compare the T_k and σ_ρ distributions of the NGC1387 GMCs to previous observations and simulations of GMCs in the MW and nearby galaxies (e.g. Corbelli et al., 2018; Tang et al., 2018). This will directly reveal how these key GMC properties differ between ETGs and spirals. The spatial distributions

and radial profiles of σ_ρ and T_k across NGC1387 will also be compared with the existing SFE map (derived from archival VLT/MUSE Hα and the ALMA CO data), to look for correlations.

- Estimate the Mach number $\mathcal{M}$, critical density for star formation ρ_{crit} and fraction of gas above the critical density f_{crit}. $\mathcal{M}$ can be derived from each GMC velocity dispersion and T_k as described above. ρ_{crit} can be derived from $\mathcal{M}$ and T_k using Eq. 20 of Federrath & Klessen (2012). Given a log-normal gas density distribution of known ρ_0 and σ_ρ, $f_{crit} = P(\rho > \rho_{crit}|\rho \approx \mathcal{N}(\rho_0, \sigma_\rho))$. In turn, we will compare these derived quantities (and their spatial distributions) with observations and simulations in the literature, to establish how they may differ from those of the GMCs in the MW and nearby spirals (Ballesteros-Paredes, 2006).

- Reveal the physics that suppresses star formation in NGC1387 below GMC scales. With the above analyses, we can further disentangle the relative importance of different potential mechanisms to suppress star formation in NGC1387. Recalling the different scenarios discussed above, this can be simply illustrated. (i) If the σ_ρ are low at a fixed mean gas mass density ρ_0, then low dense-gas fractions are likely (i.e. scenario 3). This could further be due to stronger shear and/or tidal forces caused by the deeper gravitational potential wells of ETGs. (ii) If the T_k are high and thus the $\mathcal{M}$ low, then a high critical density for star formation in ETGs is likely (i.e. scenario 4). The quenching of the whole ETG population could of course arise from a combination of multiple simultaneous mechanisms. However, following a proof of concept, the method proposed in this study can be applied to a much larger sample of ETGs, and thus reveal the broader picture of quenching.

Overall, through SLED modelling probing *below* GMC scales, such a study will explore the detailed physics behind the suppression of star formation in the ETG NGC1387, as an important pioneering effort to understand the ETG population.

On a separate note, NGC 4429 also has an intriguing line ratio feature. More specifically, there is a difference between the spatial extent of CO(1-0) and CO(3-2) discs. The former has a diameter of 30″ in archival ALMA data (the same as the dust disc) while

the latter only 10″ with a sharp cut-off in intensity at the edge (Liu et al., 2021). This means a CO(3-2)/CO(1-0) ratio of zero at galactocentric radius of 5″–15″. The sharp cut-off also corresponds to a morphological transition in the dust disc (Davis et al., 2018). This has to be determined by some dominant physical mechanism worth exploring.

5.2.4 Others

- It is worth exploring the correlation between the existence of megamasers and the disturbed morphology and kinematics in Section 2.6 in a more systematic way. The cold molecular gas content of a larger sample of megamaser host galaxies, together with a well-constructed control sample of Sy 2 AGN galaxies without megamasers, need to be observed at $\approx$ 100 pc resolution. With this, a more robust statistical conclusion can be drawn on the physical interaction between megamasers and the ISM.

- The spatially resolved SFE of NGC 1387 can be studied with available ALMA and MUSE data. From emission line diagnostics, the spaxels dominated by star formation ionisation form a ring at a galactocentric radius of $\gtrsim$ 6″, which is adjacent to a stellar ring at 6″ reported by Laurikainen et al. (2006). This could reveal the inside-out growth of a nuclear stellar disc. A stellar population analysis similar to what has been done in the Time Inference with MUSE in Extragalactic Rings (TIMER) project (Gadotti et al., 2019) can be carried out.

- Quantifying and explaining the non-existence of GMCs in some galaxies. Following the example of NGC 524 (Lu et al., 2024), other galaxies especially ETGs can be examined using the same methodology. NGC 6753 seems to show similar non-existence of GMCs (private communication from Woorak Choi).

Appendices

A

Result robustness as a function of CPROPStoo parameters

The identification of GMCs from our adopted datacube has some arbitrariness in the choices of the CPROPStoo parameters. Indeed, as described in Section 3.2.5, several steps require manual input based on trial and error. Here, we quantify the changes to the main derived GMC properties when the two most important parameters are varied, and show that our results are robust against these choices.

We perform the same GMC identification and analyses for nine different sets of parameters. The minimum contrast ($\Delta T_{\rm min}$ = 1, 2 and 3 K) and minimum convexity ($S_{\rm min}$ = 0.45, 0.50 and 0.55) are varied while all other parameters are kept constant. The GMC identification results are shown in Figure A.1 and the GMC virial mass ($M_{\rm obs,vir}$) – molecular gas mass ($M_{\rm gas}$) comparisons are shown in Figure A.2 (along with the distributions of the virial parameters, $\alpha_{\rm obs,vir}$). The central panel of both figures shows the results for the set of parameters adopted in the main body of this paper. We note that the GMC identification is carried out in 3D (i.e. using the adopted datacube), so the visualisation of the GMC catalogues using the 2D zeroth-moment maps shown in Figure A.1 does not reflect the process perfectly.

As expected, Figure A.1 shows that the GMC catalogue using the strictest combination of parameters (top-right panel of each figure; $\Delta T_{\rm min}$ = 3 K and $S_{\rm min}$ = 0.55) has the

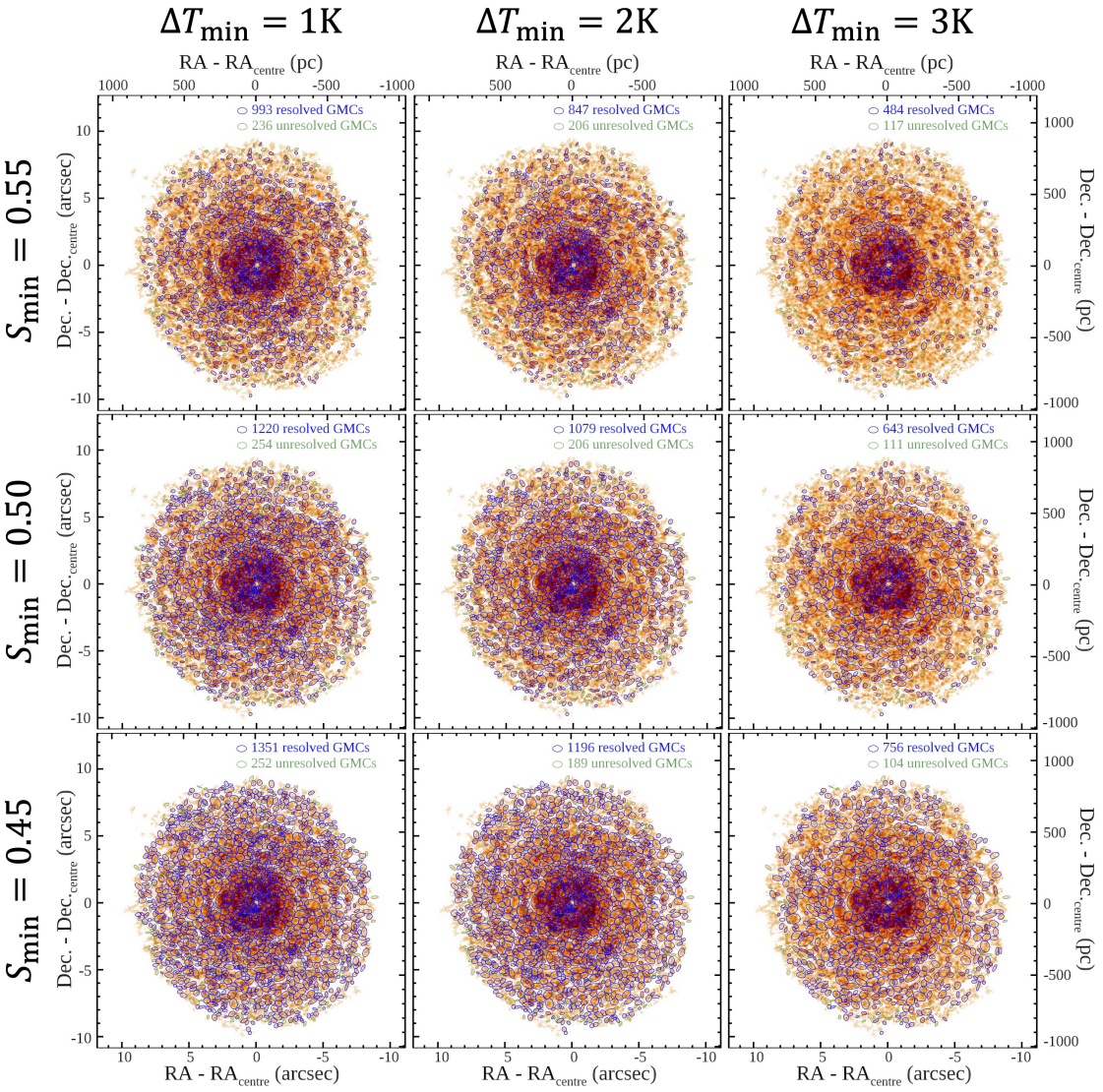

Figure A.1: GMC identification as a function of the CPROPStoo parameters $\Delta T_{\rm min}$ (from left to right: 1, 2 and 3 K) and $S_{\rm min}$ (from bottom to top: 0.45, 0.50 and 0.55). All panels are as Figure 3.3, with a few annotations removed for clarity. The central panel shows the results for the set of parameters adopted in the main body of this paper.

fewest GMCs (484 resolved and 117 unresolved GMCs), while the opposite combination (bottom-left panel of each figure; $\Delta T_{\rm min}$ = 1 K and $S_{\rm min}$ = 0.45) has the most GMCs (1351 resolved and 252 unresolved GMCs). A higher $\Delta T_{\rm min}$ leads to identify only the largest overdensities and fails to identify GMCs across the relatively smooth parts of the molecular gas disc. A higher $S_{\rm min}$ leads to the inclusion of slightly larger structures with more abundant sub-structures. A similar conclusion is reached by inspecting the moment maps of individual GMCs (not shown). The two parameters $\Delta T_{\rm min}$ and $S_{\rm min}$

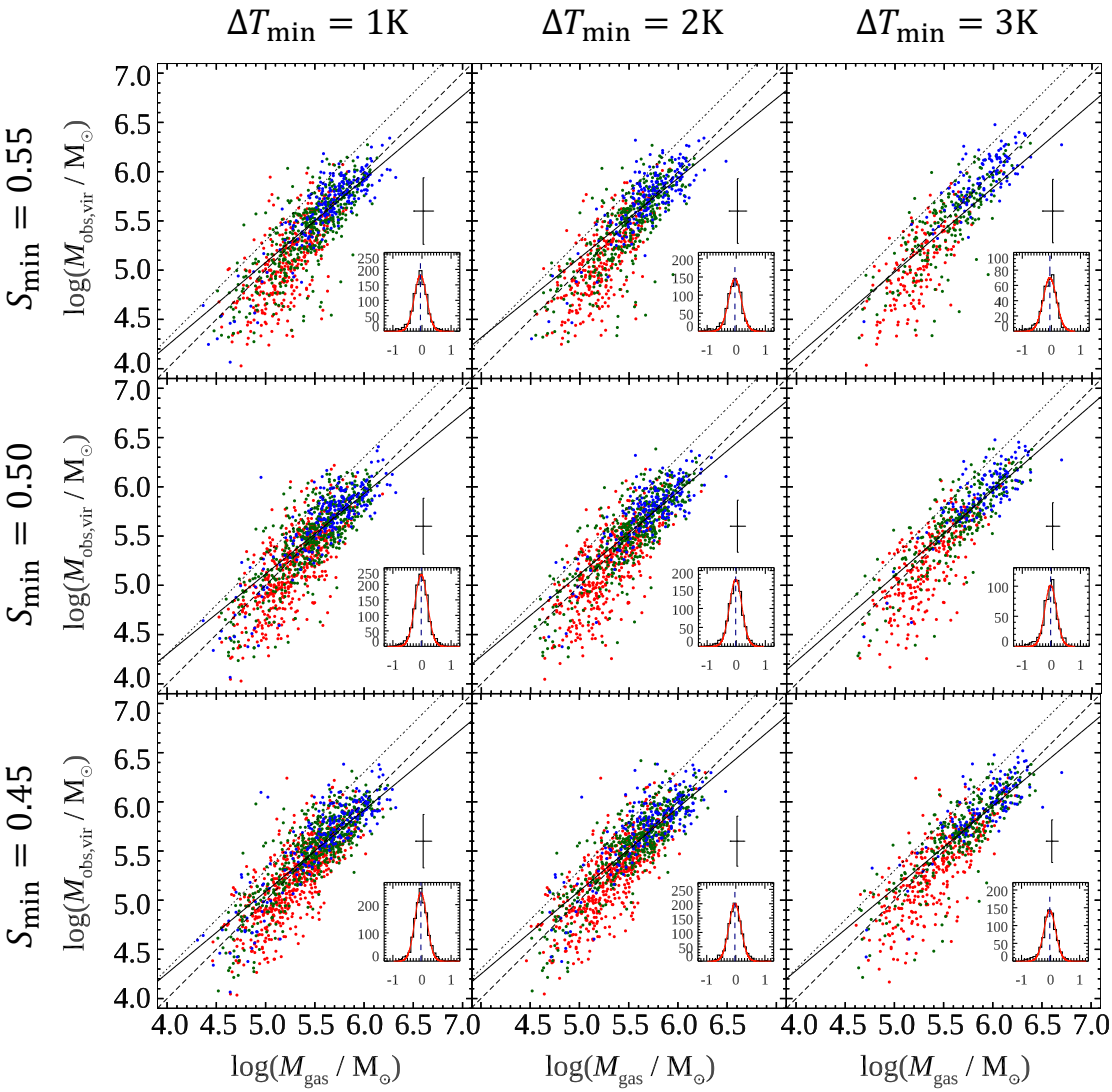

Figure A.2: As Figure A.1, but for the comparison of the GMC virial masses ($M_{\rm obs,vir}$) and molecular gas masses ($M_{\rm gas}$), as well as the distributions of the virial parameters ($\alpha_{\rm obs,vir}$). All panels are as Figure 3.7, with a few annotations removed for clarity.

are thus impacting the GMC identification in the manner expected.

Figure A.2 shows that the two masses $M_{\rm obs,vir}$ and $M_{\rm gas}$ correlate very well with each other for all sets of parameters, and the $\alpha_{\rm obs,vir}$ distributions are also all very similar, being centred around $\alpha_{\rm obs,vir} = 1$ with very similar scatters.

We also probed the robustness of the Larson relations for all nine sets of parameters. Considering the scatters, they all roughly agree with the MW disc GMC relations, although the best-fitting slopes and zero-points do vary a little. For example, the slope of the size – line width relation ranges from 0.18 to 0.44, all nevertheless flatter than

that of the MW disc GMCs (0.5).

Based on the tests in this appendix, we therefore conclude that, within reasonable ranges, the choice of the parameters used for the GMC identification does not affect our conclusions.

Bibliography

Abazajian K. N., et al., 2009, ApJS, 182, 543

Adelman-McCarthy J. K., et al., 2008, ApJS, 175, 297

Aird J., Coil A. L., Georgakakis A., Nandra K., Barro G., Pérez-González P. G., 2015, MNRAS, 451, 1892

Alam S., et al., 2021, Phys. Rev. D, 103, 083533

Albareti F. D., et al., 2017, ApJS, 233, 25

Alexander D. M., Hickox R. C., 2012, New A Rev., 56, 93

Allen M., Robinson G. W., 1977, ApJ, 212, 396

Alonso-Herrero A., et al., 2020, A&A, 639, A43

Alves J., Lombardi M., Lada C. J., 2007, A&A, 462, L17

Antonucci R., 1993, ARA&A, 31, 473

Athanassoula E., 1992, MNRAS, 259, 345

Athanassoula E., Beaton R. L., 2006, MNRAS, 370, 1499

Baade W., 1944, ApJ, 100, 137

Baldwin J. A., Phillips M. M., Terlevich R., 1981, PASP, 93, 5

Ballesteros-Paredes J., 2006, MNRAS, 372, 443

Ballesteros-Paredes J., Klessen R. S., Mac Low M. M., Vazquez-Semadeni E., 2007, in Reipurth B., Jewitt D., Keil K., eds, Protostars and Planets V. p. 63 (arXiv:astro-ph/0603357), doi:10.48550/arXiv.astro-ph/0603357

Balser D. S., Rood R. T., Bania T. M., Anderson L. D., 2011, ApJ, 738, 27

Bania T. M., 1977, ApJ, 216, 381

Barnes A. T., 2018, PhD thesis, Liverpool John Moores University, UK

Barnes A. T., et al., 2023, ApJ, 944, L22

Barth A. J., Boizelle B. D., Darling J., Baker A. J., Buote D. A., Ho L. C., Walsh J. L., 2016a, ApJ, 822, L28

Barth A. J., Boizelle B. D., Darling J., Baker A. J., Buote D. A., Ho L. C., Walsh J. L., 2016b, ApJ, 822, L28

Battersby C., et al., 2020, ApJS, 249, 35

Baumgartner W. H., Tueller J., Markwardt C. B., Skinner G. K., Barthelmy S., Mushotzky R. F., Evans P. A., Gehrels N., 2013, ApJS, 207, 19

Beifiori A., Courteau S., Corsini E. M., Zhu Y., 2012, MNRAS, 419, 2497

Bell E. F., de Jong R. S., 2000, MNRAS, 312, 497

Bergin E. A., Tafalla M., 2007, ARA&A, 45, 339

Berta S., Lutz D., Genzel R., Förster-Schreiber N. M., Tacconi L. J., 2016, A&A, 587, A73

Bewketu Belete A., et al., 2021, A&A, 654, A24

Binney J., Tremaine S., 2008, Galactic Dynamics: Second Edition. Princeton series in astrophysics, Princeton University Press, Princeton, New Jersey, USA

Blakeslee J. P., et al., 2009, ApJ, 694, 556

Blanton M. R., Moustakas J., 2009, ARA&A, 47, 159

Blitz L., Fukui Y., Kawamura A., Leroy A., Mizuno N., Rosolowsky E., 2007, in Reipurth B., Jewitt D., Keil K., eds, Protostars and Planets V. p. 81

Boizelle B. D., Barth A. J., Walsh J. L., Buote D. A., Baker A. J., Darling J., Ho L. C., 2019, ApJ, 881, 10

Boizelle B. D., et al., 2021a, ApJ, 908, 19

Boizelle B. D., et al., 2021b, ApJ, 908, 19

Bolatto A. D., Leroy A. K., Rosolowsky E., Walter F., Blitz L., 2008, ApJ, 686, 948

Bolatto A. D., Wolfire M., Leroy A. K., 2013, ARA&A, 51, 207

Bolatto A. D., et al., 2017, ApJ, 846, 159

Bolatto A. D., et al., 2021, ApJ, 923, 83

Bonnor W. B., 1957, MNRAS, 117, 104

Boselli A., Cortese L., Boquien M., Boissier S., Catinella B., Lagos C., Saintonge A., 2014, A&A, 564, A66

Braatz J. A., Condon J. J., Henkel C., Lo K. Y., Reid M. J., 2009, in astro2010: The Astronomy and Astrophysics Decadal Survey. p. 23

Briggs D. S., 1995, in American Astronomical Society Meeting Abstracts. p. 112.02

Broderick A. E., et al., 2022, ApJ, 935, 61

Brown M. J. I., Jannuzi B. T., Floyd D. J. E., Mould J. R., 2011, ApJ, 731, L41

Brown T., et al., 2021, ApJS, 257, 21

Burkert A., Bodenheimer P., 2000, ApJ, 543, 822

Buta R. J., Corwin H. G., Odewahn S. C., 2007, The de Vaucouleurs Atlas of Galaxies

CASA Team et al., 2022, PASP, 134, 114501

Calura F., Matteucci F., 2004, MNRAS, 350, 351

Cappellari M., 2002, MNRAS, 333, 400

Cappellari M., 2020, MNRAS, 494, 4819

Cappellari M., Verolme E. K., van der Marel R. P., Verdoes Kleijn G. A., Illingworth G. D., Franx M., Carollo C. M., de Zeeuw P. T., 2002a, ApJ, 578, 787

Cappellari M., Verolme E. K., van der Marel R. P., Verdoes Kleijn G. A., Illingworth G. D., Franx M., Carollo C. M., de Zeeuw P. T., 2002b, ApJ, 578, 787

Cappellari M., Neumayer N., Reunanen J., van der Werf P. P., de Zeeuw P. T., Rix H. W., 2009, MNRAS, 394, 660

Cappellari M., et al., 2011, MNRAS, 416, 1680

Carniani S., et al., 2024, arXiv e-prints, p. arXiv:2405.18485

Caselli P., Benson P. J., Myers P. C., Tafalla M., 2002, ApJ, 572, 238

Catinella B., et al., 2018, MNRAS, 476, 875

Chevance M., Krumholz M. R., McLeod A. F., Ostriker E. C., Rosolowsky E. W., Sternberg A., 2023, in Inutsuka S., Aikawa Y., Muto T., Tomida K., Tamura M., eds, Astronomical Society of the Pacific Conference Series Vol. 534, Protostars and Planets VII. p. 1 (arXiv:2203.09570), doi:10.48550/arXiv.2203.09570

Choi W., Kim C.-G., Chung A., 2022, ApJ, 936, 133

Choi W., et al., 2023, MNRAS, 522, 4078

Choi W., et al., 2024, MNRAS, 531, 4045

Chown R., et al., 2019, MNRAS, 484, 5192

Cohn J. H., et al., 2021, ApJ, 919, 77

Colombo D., et al., 2014, ApJ, 784, 3

Colombo D., Rosolowsky E., Ginsburg A., Duarte-Cabral A., Hughes A., 2015, MNRAS, 454, 2067

Combes F., Young L. M., Bureau M., 2007, MNRAS, 377, 1795

Combes F., Gupta N., Jozsa G. I. G., Momjian E., 2019, A&A, 623, A133

Concas A., Popesso P., 2019, MNRAS, 486, L91

Condon J. J., 1992, ARA&A, 30, 575

Cooke A. J., Baldwin J. A., Ferland G. J., Netzer H., Wilson A. S., 2000, ApJS, 129, 517

Corbelli E., Elmegreen B. G., Braine J., Thilker D., 2018, A&A, 617, A125

Cornwell T. J., 2008, IEEE Journal of Selected Topics in Signal Processing, 2, 793

Cortes P. C., Crutcher R. M., Shepherd D. S., Bronfman L., 2008, ApJ, 676, 464

Cretton N., Emsellem E., 2004, MNRAS, 347, L31

Crutcher R. M., Troland T. H., Goodman A. A., Heiles C., Kazes I., Myers P. C., 1993, ApJ, 407, 175

Currie M. J., Berry D. S., Jenness T., Gibb A. G., Bell G. S., Draper P. W., 2014, in Manset N., Forshay P., eds, Astronomical Society of the Pacific Conference Series Vol. 485, Astronomical Data Analysis Software and Systems XXIII. p. 391

D'Abrusco R., et al., 2016, ApJ, 819, L31

D'Onofrio M., Marziani P., Chiosi C., 2021, Frontiers in Astronomy and Space Sciences, 8, 157

Dabrowski I., 1984, Canadian Journal of Physics, 62, 1639

Dame T. M., 2011, arXiv e-prints, arXiv:1101.1499, arXiv:1101.1499

Dame T. M., et al., 1987, ApJ, 322, 706

Davies R. I., et al., 2006, ApJ, 646, 754

Davis T. A., et al., 2011, MNRAS, 417, 882

Davis T. A., et al., 2013a, MNRAS, 429, 534

Davis T. A., Bureau M., Cappellari M., Sarzi M., Blitz L., 2013b, Nature, 494, 328

Davis T. A., Bureau M., Onishi K., Cappellari M., Iguchi S., Sarzi M., 2017, MNRAS, 468, 4675

Davis T. A., et al., 2018, MNRAS, 473, 3818

Davis T. A., et al., 2020, MNRAS, 496, 4061

Davis T. A., et al., 2022, MNRAS, 512, 1522

Devereux N., Ford H., Tsvetanov Z., Jacoby G., 2003, AJ, 125, 1226

Dobbs C. L., Burkert A., Pringle J. E., 2011, MNRAS, 417, 1318

Domínguez-Fernández A. J., et al., 2020, A&A, 643, A127

Dominiak P., Bureau M., Liang F.-H., 2024, MNRAS, submitted

Donovan Meyer J., et al., 2013, ApJ, 772, 107

Dopita M. A., Kewley L. J., Sutherland R. S., Nicholls D. C., 2016, Ap&SS, 361, 61

Draine B. T., 2011, Physics of the Interstellar and Intergalactic Medium

Drehmer D. A., Storchi-Bergmann T., Ferrari F., Cappellari M., Riffel R. A., 2015, MNRAS, 450, 128

Dreyer J. L. E., 1953, New General Catalogue of Nebulae and Clusters of Stars (1888), Index Catalogue (1895), Second Index Catalogue (1908)

Elbaz D., et al., 2007, A&A, 468, 33

Elmegreen B. G., Scalo J., 2004, ARA&A, 42, 211

Emsellem E., Monnet G., Bacon R., 1994, A&A, 285, 723

Event Horizon Telescope Collaboration et al., 2019, ApJ, 875, L6

Fabbiano G., Wang J., Elvis M., Risaliti G., 2011, Nature, 477, 431

Fall S. M., 1983, in Internal Kinematics and Dynamics of Galaxies. pp 391–398

Federrath C., Klessen R. S., 2012, ApJ, 761, 156

Federrath C., et al., 2016, ApJ, 832, 143

Federrath C., Klessen R. S., Iapichino L., Beattie J. R., 2021, Nature Astronomy, 5, 365

Feldmeier-Krause A., Zhu L., Neumayer N., van de Ven G., de Zeeuw P. T., Schödel R., 2017, MNRAS, 466, 4040

Ferguson H. C., 1989, AJ, 98, 367

Ferrarese L., Merritt D., 2000, ApJ, 539, L9

Ferrière K., Gillard W., Jean P., 2007, A&A, 467, 611

Finlez C., Nagar N. M., Storchi-Bergmann T., Schnorr-Müller A., Riffel R. A., Lena D., Mundell C. G., Elvis M. S., 2018, MNRAS, 479, 3892

Florez J., et al., 2021, MNRAS, 508, 762

Förster Schreiber N. M., Wuyts S., 2020, ARA&A, 58, 661

Förster Schreiber N. M., et al., 2011, ApJ, 739, 45

Freeman P., Rosolowsky E., Kruijssen J. M. D., Bastian N., Adamo A., 2017, MNRAS, 468, 1769

Gadotti D. A., et al., 2019, MNRAS, 482, 506

Gammie C. F., Ostriker J. P., Jog C. J., 1991, ApJ, 378, 565

Gao Y., Solomon P. M., 2004a, ApJS, 152, 63

Gao Y., Solomon P. M., 2004b, ApJ, 606, 271

Gao F., et al., 2016, ApJ, 817, 128

Gao F., et al., 2017, ApJ, 834, 52

García-Burillo S., et al., 2019, A&A, 632, A61

García-Burillo S., et al., 2021, A&A, 652, A98

Garrod R. T., Widicus Weaver S. L., Herbst E., 2008, ApJ, 682, 283

Gebhardt K., Thomas J., 2009, ApJ, 700, 1690

Gebhardt K., et al., 2000, ApJ, 539, L13

Gebhardt K., Adams J., Richstone D., Lauer T. R., Faber S. M., Gültekin K., Murphy J., Tremaine S., 2011, ApJ, 729, 119

Gensior J., Kruijssen J. M. D., Keller B. W., 2020, MNRAS, 495, 199

Gensior J., Davis T. A., Bureau M., Kruijssen J. M. D., Cappellari M., Ruffa I., Williams T. G., 2023, MNRAS, 526, 5590

Giavalisco M., et al., 2011, ApJ, 743, 95

Ginsburg A., et al., 2016, A&A, 586, A50

Ginsburg A., et al., 2020, ApJS, 248, 24

González-Casanova D. F., Lazarian A., 2017, ApJ, 835, 41

Graciá-Carpio J., García-Burillo S., Planesas P., Colina L., 2006, ApJ, 640, L135

Gravity Collaboration et al., 2019, A&A, 625, L10

Green S., Montgomery J. A. J., Thaddeus P., 1974, ApJ, 193, L89

Greene J. E., Seth A., Lyubenova M., Walsh J., van de Ven G., Läsker R., 2014, ApJ, 788, 145

Greene J. E., et al., 2016, ApJ, 826, L32

Greenhill L. J., Moran J. M., Herrnstein J. R., 1997, ApJ, 481, L23

Greenhill L. J., et al., 2003, ApJ, 590, 162

Greenhill L. J., Tilak A., Madejski G., 2008, ApJ, 686, L13

Griffith E., Martini P., Conroy C., 2019, MNRAS, 484, 562

Hansen C. E., McKee C. F., Klein R. I., 2011, ApJ, 738, 88

Hao C.-N., Kennicutt R. C., Johnson B. D., Calzetti D., Dale D. A., Moustakas J., 2011, ApJ, 741, 124

Hardwick J. A., Cortese L., Obreschkow D., Catinella B., Cook R. H. W., 2022, MNRAS, 509, 3751

Hartquist T. W., Cameron A. G. W., 1977, Ap&SS, 48, 145

Hatchfield H. P., Sormani M. C., Tress R. G., Battersby C., Smith R. J., Glover S. C. O., Klessen R. S., 2021, ApJ, 922, 79

Haynes M. P., et al., 2018, ApJ, 861, 49

Heckman T. M., 1980, A&A, 87, 152

Heesen V., Brinks E., Leroy A. K., Heald G., Braun R., Bigiel F., Beck R., 2014, AJ, 147, 103

Henkel C., et al., 2018, A&A, 615, A155

Henshaw J. D., et al., 2019, MNRAS, 485, 2457

Henshaw J. D., Barnes A. T., Battersby C., Ginsburg A., Sormani M. C., Walker D. L., 2023, in Inutsuka S., Aikawa Y., Muto T., Tomida K., Tamura M., eds, Astronomical Society of the Pacific Conference Series Vol. 534, Protostars and Planets VII. p. 83 (arXiv:2203.11223), doi:10.48550/arXiv.2203.11223

Hernández-Gómez A., Sahnoun E., Caux E., Wiesenfeld L., Loinard L., Bottinelli S., Hammami K., Menten K. M., 2019, MNRAS, 483, 2014

Herrington N. P., Dobbs C. L., Bending T. J. R., 2024, MNRAS, 532, 1701

Herrnstein J. R., Moran J. M., Greenhill L. J., Trotter A. S., 2005, ApJ, 629, 719

Heyer M. H., Brunt C. M., 2004, ApJ, 615, L45

Heyer M., Dame T. M., 2015, ARA&A, 53, 583

Heyer M., Krawczyk C., Duval J., Jackson J. M., 2009, ApJ, 699, 1092

Hicks E. K. S., Malkan M. A., 2008, ApJS, 174, 31

Hirota A., Kuno N., Sato N., Nakanishi H., Tosaki T., Sorai K., 2011, ApJ, 737, 40

Ho L., 1999, in Chakrabarti S. K., ed., Astrophysics and Space Science Library Vol. 234, Observational Evidence for the Black Holes in the Universe. p. 157, doi:10.1007/978-94-011-4750-7_11

Ho L. C., Sarzi M., Rix H.-W., Shields J. C., Rudnick G., Filippenko A. V., Barth A. J., 2002, PASP, 114, 137

Ho L. C., Li Z.-Y., Barth A. J., Seigar M. S., Peng C. Y., 2011, ApJS, 197, 21

Hocuk S., Spaans M., 2010, A&A, 510, A110

Högbom J. A., 1974, A&AS, 15, 417

Hovatta T., et al., 2014, AJ, 147, 143

Hu G., Shao Z., Li L., 2023, ApJ, 950, 142

Hubble E. P., 1925, Popular Astronomy, 33, 252

Hubble E. P., 1926, ApJ, 64, 321

Hubble E. P., 1936, Realm of the Nebulae

Huré J. M., Hersant F., Surville C., Nakai N., Jacq T., 2011, A&A, 530, A145

Iglesias E., 1977, ApJ, 218, 697

Imanishi M., Saito Y., 2014, ApJ, 780, 106

Iodice E., et al., 2016, ApJ, 820, 42

Iodice E., et al., 2019a, A&A, 623, A1

Iodice E., et al., 2019b, A&A, 627, A136

Izumi T., Wada K., Fukushige R., Hamamura S., Kohno K., 2018, ApJ, 867, 48

Izumi T., et al., 2023, Science, 382, 554

Jackson J. M., Armstrong J. T., Barrett A. H., 1984, ApJ, 280, 608

Jeans J. H., 1902, Philosophical Transactions of the Royal Society of London Series A, 199, 1

Jeans J. H., 1928, Astronomy and cosmogony

Jeffreson S. M. R., Semenov V. A., Krumholz M. R., 2024, MNRAS, 527, 7093

Jenness T., Economou F., 2015, Astronomy and Computing, 9, 40

Jeter B., Broderick A. E., 2021, ApJ, 908, 139

Jeter B., Broderick A. E., McNamara B. R., 2019, ApJ, 882, 82

Jiménez-Donaire M. J., et al., 2019, ApJ, 880, 127

Jones P. A., et al., 2012, MNRAS, 419, 2961

Jørgensen J. K., Hogerheijde M. R., van Dishoeck E. F., Blake G. A., Schöier F. L., 2004, A&A, 413, 993

Jorsater S., van Moorsel G. A., 1995, AJ, 110, 2037

Juárez C., Liu H. B., Girart J. M., Palau A., Busquet G., Galván-Madrid R., Hirano N., Lin Y., 2019, A&A, 621, A140

Kabasares K. M., et al., 2022, ApJ, 934, 162

Karachentsev I. D., Makarov D. A., 1996, AJ, 111, 794

Kauffmann J., Pillai T., Zhang Q., 2013, ApJ, 765, L35

Kauffmann J., Pillai T., Zhang Q., Menten K. M., Goldsmith P. F., Lu X., Guzmán A. E., 2017, A&A, 603, A89

Kelly B. C., 2007, ApJ, 665, 1489

Kennicutt R. C. J., 1983, ApJ, 272, 54

Kennicutt Robert C. J., 1998, ApJ, 498, 541

Kepley A. A., Tsutsumi T., Brogan C. L., Indebetouw R., Yoon I., Mason B., Donovan Meyer J., 2020, PASP, 132, 024505

Keto E. R., Myers P. C., 1986, ApJ, 304, 466

Kim W.-T., Stone J. M., 2012, ApJ, 751, 124

Kim J.-G., Ostriker E. C., Filippova N., 2021, ApJ, 911, 128

Klitsch A., Davis T. A., Hamanowicz A., van de Voort F., Péroux C., Zwaan M. A., 2023, MNRAS, 523, L46

Koley A., Roy N., Momjian E., Sarma A. P., Datta A., 2022, MNRAS, 516, L48

Komatsu E., et al., 2009, ApJS, 180, 330

Kondratko P. T., et al., 2006, ApJ, 638, 100

Kondratko P. T., Greenhill L. J., Moran J. M., 2008, ApJ, 678, 87

Kormendy J., Ho L. C., 2013, ARA&A, 51, 511

Kormendy J., Kennicutt Robert C. J., 2004, ARA&A, 42, 603

Koss M. J., et al., 2015, ApJ, 807, 149

Koss M. J., et al., 2021, ApJS, 252, 29

Krajnović D., Cappellari M., de Zeeuw P. T., Copin Y., 2006, MNRAS, 366, 787

Kruijssen J. M. D., Longmore S. N., 2013, MNRAS, 435, 2598

Kruijssen J. M. D., Dale J. E., Longmore S. N., 2015, MNRAS, 447, 1059

Kuo C. Y., et al., 2011a, ApJ, 727, 20

Kuo C. Y., et al., 2011b, ApJ, 727, 20

Kuo C. Y., Braatz J. A., Reid M. J., Lo K. Y., Condon J. J., Impellizzeri C. M. V., Henkel C., 2013, ApJ, 767, 155

Kuo C. Y., et al., 2015, ApJ, 800, 26

Lacy J. H., Knacke R., Geballe T. R., Tokunaga A. T., 1994, ApJ, 428, L69

Lada C. J., Lada E. A., 2003, ARA&A, 41, 57

Lai T. S. Y., Smith J. D. T., Baba S., Spoon H. W. W., Imanishi M., 2020, ApJ, 905, 55

Lara-López M. A., et al., 2022, A&A, 660, A105

Larson R. B., 1981, MNRAS, 194, 809

Läsker R., Greene J. E., Seth A., van de Ven G., Braatz J. A., Henkel C., Lo K. Y., 2016, ApJ, 825, 3

Laurikainen E., Salo H., Buta R., Knapen J., Speltincx T., Block D., 2006, AJ, 132, 2634

Lee J.-E., Bergin E. A., Evans Neal J. I., 2004, ApJ, 617, 360

Lee J. H., Park C., Hwang H. S., Kwon M., 2024, ApJ, 966, 113

Lelli F., Davis T. A., Bureau M., Cappellari M., Liu L., Ruffa I., Smith M. D., Williams T. G., 2022, MNRAS, 516, 4066

Leroy A. K., et al., 2016, ApJ, 831, 16

Leroy A. K., et al., 2021, ApJS, 257, 43

Leroy A. K., et al., 2022, ApJ, 927, 149

Li G.-X., Zhang C.-P., 2020, ApJ, 897, 89

Lian J., et al., 2020, MNRAS, 497, 2371

Liang F.-H., et al., 2024, MNRAS, 527, 9343

Licquia T. C., Newman J. A., 2015, ApJ, 806, 96

Liepold E. R., Ma C.-P., Walsh J. L., 2023, ApJ, 945, L35

Lin G., Adiga U., Olson K., Guzowski J. F., Barnes C. A., Roysam B., 2003, Cytometry Part A: the journal of the International Society for Analytical Cytology, 56, 23

Lin L., et al., 2020, ApJ, 903, 145

Lin L., et al., 2022, ApJ, 926, 175

Liszt H. S., 2007, A&A, 476, 291

Liu J., 2011, ApJS, 192, 10

Liu L., et al., 2017, ApJ, 846, 5

Liu L., Bureau M., Blitz L., Davis T. A., Onishi K., Smith M., North E., Iguchi S., 2021, MNRAS, 505, 4048

Liu L., et al., 2022, MNRAS, 517, 632

Lo K. Y., 2005, ARA&A, 43, 625

Lodato G., Bertin G., 2003, A&A, 398, 517

Longmore S. N., et al., 2013, MNRAS, 429, 987

Loni A., et al., 2021, A&A, 648, A31

Loni A., et al., 2023, MNRAS, 523, 1140

Lu A., et al., 2022, MNRAS, 514, 5035

Lu A., et al., 2024, MNRAS, 531, 3888

Mac Low M.-M., Klessen R. S., 2004, Reviews of Modern Physics, 76, 125

MacLaren I., Richardson K. M., Wolfendale A. W., 1988, ApJ, 333, 821

Madau P., Dickinson M., 2014, ARA&A, 52, 415

Maiolino R., Mannucci F., 2019, A&A Rev., 27, 3

Martig M., Bournaud F., Teyssier R., Dekel A., 2009, ApJ, 707, 250

Martig M., et al., 2013, MNRAS, 432, 1914

Matteucci F., 2012, Chemical Evolution of Galaxies, doi:10.1007/978-3-642-22491-1.

Matteucci F., Chiappini C., 2005, PASA, 22, 49

McWilliam A., 1997, ARA&A, 35, 503

Meidt S. E., et al., 2018, ApJ, 854, 100

Messier C., 1781, Catalogue des Nébuleuses et des Amas d'Étoiles (Catalog of Nebulae and Star Clusters), Connoissance des Temps ou des Mouvements Célestes, for 1784, p. 227-267

Mills E. A. C., Ginsburg A., Immer K., Barnes J. M., Wiesenfeld L., Faure A., Morris M. R., Requena-Torres M. A., 2018, ApJ, 868, 7

Miura R. E., et al., 2021, MNRAS, 504, 6198

Mok A., et al., 2016, MNRAS, 456, 4384

Mok A., Wilson C. D., Knapen J. H., Sánchez-Gallego J. R., Brinks E., Rosolowsky E., 2017, MNRAS, 467, 4282

Molinari S., et al., 2010, PASP, 122, 314

Molinari S., et al., 2011, ApJ, 735, L33

Morris M. R., 2015, in Freeman K., Elmegreen B., Block D., Woolway M., eds, , Lessons from the Local Group: A Conference in honor of David Block and Bruce Elmegreen. p. 391, doi:10.1007/978-3-319-10614-4_32

Mukherjee D., Wagner A. Y., Bicknell G. V., Morganti R., Oosterloo T., Nesvadba N., Sutherland R. S., 2018a, MNRAS, 476, 80

Mukherjee D., Bicknell G. V., Wagner A. Y., Sutherland R. S., Silk J., 2018b, MNRAS, 479, 5544

Murphy E. J., et al., 2011, ApJ, 737, 67

Murphy E. J., et al., 2015, ApJ, 813, 118

Nagai H., et al., 2019, ApJ, 883, 193

Nair P. B., Abraham R. G., 2010, ApJS, 186, 427

Narayan R., Fabian A. C., 2011, MNRAS, 415, 3721

Neufeld C., et al., 2024, ApJ, 972, 156

Neumayer N., Cappellari M., Reunanen J., Rix H. W., van der Werf P. P., de Zeeuw P. T., Davies R. I., 2007, ApJ, 671, 1329

Ngeow C.-C., et al., 2015, AJ, 149, 66

Nguyen D. D., et al., 2020, ApJ, 892, 68

Nguyen D. D., et al., 2021, MNRAS, 504, 4123

Nguyen D. D., et al., 2022, MNRAS, 509, 2920

Nikolic B., Bolton R. C., 2012, MNRAS, 425, 1257

Nonhebel M., et al., 2024, A&A, 691, A70

North E. V., et al., 2019, MNRAS, 490, 319

Obreschkow D., Rawlings S., 2009, MNRAS, 394, 1857

Offner S. S. R., Clark P. C., Hennebelle P., Bastian N., Bate M. R., Hopkins P. F., Moraux E., Whitworth A. P., 2014, in Beuther H., Klessen R. S., Dullemond C. P., Henning T., eds, Protostars and Planets VI. pp 53–75 (arXiv:1312.5326), doi:10.2458/azu_uapress_9780816531240-ch003

Oh K., et al., 2018, ApJS, 235, 4

Onishi K., Iguchi S., Sheth K., Kohno K., 2015a, ApJ, 806, 39

Onishi K., Iguchi S., Sheth K., Kohno K., 2015b, ApJ, 806, 39

Onishi K., Iguchi S., Davis T. A., Bureau M., Cappellari M., Sarzi M., Blitz L., 2017, MNRAS, 468, 4663

Onken C. A., et al., 2007, ApJ, 670, 105

Oppenheimer M., Dalgarno A., 1975, ApJ, 200, 419

Padovani P., et al., 2017, A&A Rev., 25, 2

Paradis D., et al., 2010, A&A, 520, L8

Paré D., Butterfield N. O., Chuss D. T., Guerra J. A., Iuliano J. I., Karpovich K., Morris M. R., Wollack E. J., 2024, ApJ, 969, 150

Pasha I., Leja J., van Dokkum P. G., Conroy C., Johnson B. D., 2020, ApJ, 898, 165

Pastorini G., et al., 2007, A&A, 469, 405

Peebles P. J. E., 1968, ApJ, 153, 1

Pesce D. W., Braatz J. A., Condon J. J., Gao F., Henkel C., Litzinger E., Lo K. Y., Reid M. J., 2015, ApJ, 810, 65

Pesce D. W., et al., 2020, ApJ, 891, L1

Petkova M. A., et al., 2023, MNRAS, 525, 962

Phillips J. P., 1999, A&AS, 134, 241

Pjanka P., Greene J. E., Seth A. C., Braatz J. A., Henkel C., Lo F. K. Y., Läsker R., 2017, ApJ, 844, 165

Popesso P., Concas A., Morselli L., Rodighiero G., Enia A., Quai S., 2020, MNRAS, 496, 2531

Priestley F. D., Clark P. C., Glover S. C. O., Ragan S. E., Fehér O., Prole L. R., Klessen R. S., 2023, MNRAS, 526, 4952

Querejeta M., et al., 2016, A&A, 588, A33

Ragan S. E., Henning T., Tackenberg J., Beuther H., Johnston K. G., Kainulainen J., Linz H., 2014, A&A, 568, A73

Ramakrishnan V., et al., 2019, MNRAS, 487, 444

Rathborne J. M., et al., 2015, ApJ, 802, 125

Rawat V., et al., 2024, MNRAS, 528, 2199

Reid M. J., Braatz J. A., Condon J. J., Lo K. Y., Kuo C. Y., Impellizzeri C. M. V., Henkel C., 2013, ApJ, 767, 154

Remijan A., et al., 2019, ALMA Technical Handbook,ALMA Doc. 7.3, ver. 1.1, 2019, ALMA Technical Handbook,ALMA Doc. 7.3, ver. 1.1ISBN 978-3-923524-66-2, doi:10.5281/zenodo.4511522

Reynolds T. N., et al., 2022, MNRAS, 510, 1716

Rice T. S., Goodman A. A., Bergin E. A., Beaumont C., Dame T. M., 2016, ApJ, 822, 52

Ridley M. G. L., Sormani M. C., Treß R. G., Magorrian J., Klessen R. S., 2017, MNRAS, 469, 2251

Robertson B. E., et al., 2023, Nature Astronomy, 7, 611

Roman-Duval J., Heyer M., Brunt C. M., Clark P., Klessen R., Shetty R., 2016, ApJ, 818, 144

Romanowsky A. J., Fall S. M., 2012, ApJS, 203, 17

Rose T., et al., 2019, MNRAS, 489, 349

Rose T., et al., 2020, MNRAS, 496, 364

Rosolowsky E., 2005, PASP, 117, 1403

Rosolowsky E., 2007, ApJ, 654, 240

Rosolowsky E., Leroy A., 2006, PASP, 118, 590

Rosolowsky E., Engargiola G., Plambeck R., Blitz L., 2003, ApJ, 599, 258

Rosolowsky E. W., Pineda J. E., Kauffmann J., Goodman A. A., 2008, ApJ, 679, 1338

Ruffa I., et al., 2019a, MNRAS, 484, 4239

Ruffa I., et al., 2019b, MNRAS, 489, 3739

Ruffa I., Prandoni I., Davis T. A., Laing R. A., Paladino R., Casasola V., Parma P., Bureau M., 2022, MNRAS, 510, 4485

Ruffa I., et al., 2023a, MNRAS, 522, 6170

Ruffa I., et al., 2023b, MNRAS, 522, 6170

Sage L. J., Welch G. A., Young L. M., 2007, ApJ, 657, 232

Saglia R. P., et al., 2016, ApJ, 818, 47

Saintonge A., Catinella B., 2022, ARA&A, 60, 319

Saintonge A., et al., 2011, MNRAS, 415, 61

Saintonge A., et al., 2017, ApJS, 233, 22

Sakamoto S., Hasegawa T., Handa T., Hayashi M., Oka T., 1997, ApJ, 486, 276

Salpeter E. E., 1955, ApJ, 121, 161

Sandage A., Tammann G. A., 1981, A Revised Shapley-Ames Catalog of Bright Galaxies

Sarzi M., et al., 2018, A&A, 616, A121

Schinnerer E., Leroy A. K., 2024, arXiv e-prints, p. arXiv:2403.19843

Schmitt H. R., Donley J. L., Antonucci R. R. J., Hutchings J. B., Kinney A. L., 2003, ApJS, 148, 327

Schneider R., Maiolino R., 2024, A&A Rev., 32, 2

Schweizer F., 1990, in Wielen R., ed., , Dynamics and Interactions of Galaxies. pp 60–71

Scoville N., et al., 2014, ApJ, 783, 84

Senarath M. R., Brown M. J. I., Cluver M. E., Moustakas J., Armus L., Jarrett T. H., 2018, ApJ, 869, L26

Shapiro P. R., 1995, in Ferrara A., McKee C. F., Heiles C., Shapiro P. R., eds, Astronomical Society of the Pacific Conference Series Vol. 80, The Physics of the Interstellar Medium and Intergalactic Medium. p. 55

Shapiro K. L., Cappellari M., de Zeeuw T., McDermid R. M., Gebhardt K., van den Bosch R. C. E., Statler T. S., 2006, MNRAS, 370, 559

Shetty R., Glover S. C., Dullemond C. P., Klessen R. S., 2011, MNRAS, 412, 1686

Shetty R., Beaumont C. N., Burton M. G., Kelly B. C., Klessen R. S., 2012, MNRAS, 425, 720

Shirazi M., Brinchmann J., 2012, MNRAS, 421, 1043

Shull J. M., Smith B. D., Danforth C. W., 2012, ApJ, 759, 23

Simon D. A., Cappellari M., Hartke J., 2024, MNRAS, 527, 2341

Siopis C., et al., 2009, ApJ, 693, 946

Skarbinski M., Jeffreson S. M. R., Goodman A. A., 2023, MNRAS, 519, 1887

Skrutskie M. F., et al., 2006, AJ, 131, 1163

Smith M. D., et al., 2019, MNRAS, 485, 4359

Smith M. D., et al., 2021, MNRAS, 503, 5984

Snyder L. E., Buhl D., 1972, ApJ, 177, 619

Solomon P. M., Klemperer W., 1972, ApJ, 178, 389

Solomon P. M., Rivolo A. R., Barrett J., Yahil A., 1987, ApJ, 319, 730

Spiniello C., et al., 2018, MNRAS, 477, 1880

Stuber S. K., et al., 2021, A&A, 653, A172

Stuber S. K., et al., 2023a, A&A, 676, A113

Stuber S. K., et al., 2023b, A&A, 680, L20

Sun A.-L., Greene J. E., Impellizzeri C. M. V., Kuo C.-Y., Braatz J. A., Tuttle S., 2013, ApJ, 778, 47

Sun J., et al., 2018, ApJ, 860, 172

Sun J., et al., 2020a, ApJ, 892, 148

Sun J., et al., 2020b, ApJ, 901, L8

Tacconi L. J., Genzel R., Sternberg A., 2020, ARA&A, 58, 157

Tan J. C., 2000, ApJ, 536, 173

Tanaka K., Nagai M., Kamegai K., Iino T., Sakai T., 2018, ApJS, 236, 40

Tang X. D., et al., 2018, A&A, 611, A6

Teng Y.-H., et al., 2022, ApJ, 925, 72

Teng Y.-H., et al., 2024, ApJ, 961, 42

Thompson A. R., Moran J. M., Swenson George W. J., 2017, Interferometry and Synthesis in Radio Astronomy, 3rd Edition, doi:10.1007/978-3-319-44431-4.

Tideswell D. M., Fuller G. A., Millar T. J., Markwick A. J., 2010, A&A, 510, A85

Toba Y., et al., 2014, ApJ, 788, 45

Tonnesen S., Bryan G. L., 2009, ApJ, 694, 789

Toomre A., 1964, ApJ, 139, 1217

Toomre A., 1977, in Tinsley B. M., Larson Richard B. Gehret D. C., eds, Evolution of Galaxies and Stellar Populations. p. 401

Tremonti C. A., et al., 2004, ApJ, 613, 898

Tristram K. R. W., et al., 2022, A&A, 664, A142

Tumlinson J., Peeples M. S., Werk J. K., 2017, ARA&A, 55, 389

Turner B. E., 1974, ApJ, 193, L83

Turner B. E., Terzieva R., Herbst E., 1999, ApJ, 518, 699

Utomo D., Blitz L., Davis T., Rosolowsky E., Bureau M., Cappellari M., Sarzi M., 2015, ApJ, 803, 16

Verdoes Kleijn G. A., van der Marel R. P., Carollo C. M., de Zeeuw P. T., 2000, AJ, 120, 1221

Verdoes Kleijn G. A., van der Marel R. P., de Zeeuw P. T., Noel-Storr J., Baum S. A., 2002, AJ, 124, 2524

Villanueva V., et al., 2022, ApJ, 940, 176

Vollmer B., 2013, in Oswalt T. D., Keel W. C., eds, , Vol. 6, Planets, Stars and Stellar Systems. Volume 6: Extragalactic Astronomy and Cosmology. p. 207, doi:10.1007/978-94-007-5609-0_5

Wakelam V., et al., 2017, Molecular Astrophysics, 9, 1

Wallerstein G., 1962, ApJS, 6, 407

Walsh J. L., van den Bosch R. C. E., Barth A. J., Sarzi M., 2012, ApJ, 753, 79

Walsh J. L., Barth A. J., Ho L. C., Sarzi M., 2013, ApJ, 770, 86

Wang B., Silk J., 1994, ApJ, 427, 759

Wang F., et al., 2021, ApJ, 907, L1

Wang T., et al., 2023, arXiv e-prints, p. arXiv:2311.07653

White S. D. M., Rees M. J., 1978, MNRAS, 183, 341

Whitworth A. P., Jaffa S. E., 2018, A&A, 611, A20

Wilkins S. M., Gonzalez-Perez V., Lacey C. G., Baugh C. M., 2012, MNRAS, 427, 1490

Williams T. G., et al., 2023, MNRAS, 525, 4270

Wilson R. W., Jefferts K. B., Penzias A. A., 1970, ApJ, 161, L43

Wolf C., Wisotzki L., Borch A., Dye S., Kleinheinrich M., Meisenheimer K., 2003, A&A, 408, 499

Wolfire M. G., Vallini L., Chevance M., 2022, ARA&A, 60, 247

Yamauchi A., Nakai N., Sato N., Diamond P., 2004, PASJ, 56, 605

Yamauchi A., Nakai N., Ishihara Y., Diamond P., Sato N., 2012, PASJ, 64, 103

Yan R., Blanton M. R., 2012, ApJ, 747, 61

Yan Z., Jerabkova T., Kroupa P., 2017, A&A, 607, A126

Yoon I., 2017, MNRAS, 466, 1987

Young J. S., Scoville N. Z., 1991, ARA&A, 29, 581

Young J. S., et al., 1995, ApJS, 98, 219

Young L. M., Bureau M., Cappellari M., 2008, ApJ, 676, 317

Young L. M., et al., 2011, MNRAS, 414, 940

Zabel N., et al., 2019, MNRAS, 483, 2251

Zabel N., et al., 2020, MNRAS, 496, 2155

Zabel N., et al., 2022, ApJ, 933, 10

Zhang H., et al., 2024, MNRAS, 530, 3240

Zhao W., et al., 2018, ApJ, 854, 124

Zhao M., et al., 2024, ApJ, 967, 18

de Vaucouleurs G., de Vaucouleurs A., Corwin Herold G. J., Buta R. J., Paturel G., Fouque P., 1991, Third Reference Catalogue of Bright Galaxies

van den Bergh S., 1976, ApJ, 206, 883

van den Bosch R. C. E., 2016, ApJ, 831, 134

van den Bosch R. C. E., Greene J. E., Braatz J. A., Constantin A., Kuo C.-Y., 2016, ApJ, 819, 11

van der Tak F. F. S., Black J. H., Schöier F. L., Jansen D. J., van Dishoeck E. F., 2007, A&A, 468, 627

van der Walt S., et al., 2014, PeerJ, 2, e453